

Method development for the analysis of biochemical and paleo-environmental markers in speleothems

Dissertation

for attaining the Academic Degree of
“Doktor rerum naturalium” (Dr. rer. nat.)

of the Departments

08 – Physics, Mathematics, and Computer Science,

09 – Chemistry, Pharmaceutics, and Geosciences,

10 – Biology,

and University Medicine

of the Johannes Gutenberg University

by

Julia Homann

born 05.09.1994
in Bad Kreuznach



JOHANNES GUTENBERG
UNIVERSITÄT MAINZ

Max Planck Graduate Center 
mit der Johannes Gutenberg-Universität

Johannes Gutenberg-Universität with the Max Planck-Graduate Center

Mainz, July 2023

Faculty director: Prof. Dr. Eva Rentschler

1st supervisor: Prof. Dr. Thorsten Hoffmann

2nd supervisor: Prof. Dr. Denis Scholz

Date of Examination: 25.09.2023

I hereby declare that I wrote the dissertation submitted without any unauthorized external assistance and used only sources acknowledged in the work. All textual passages which are appropriated verbatim or para-phrased from published and unpublished texts as well as all information obtained from oral sources are duly indicated and listed in accordance with bibliographical rules. In carrying out this research, I complied with the rules of standard scientific practice as formulated in the statutes of Johannes Gutenberg University Mainz to insure standard scientific practice.

Mainz, July 2023

Julia Homann

*"A mind needs books like a sword needs a whetstone,
if it is to keep its edge."*

- Tyrion Lannister

*"Words are, in my not-so-humble opinion,
our most inexhaustible source of magic.
Capable of both inflicting injury, and remedying it."*

- Albus Dumbledore

Zusammenfassung

Klimaarchive wie Speläotheme, Eisbohrkerne, Sedimentkerne oder Baumringe enthalten wertvolle Informationen über lokale und globale klimatische Ereignisse. Sie können dazu verwendet werden, verschiedene Aspekte vergangener Umweltbedingungen zu rekonstruieren und so wiederum helfen, künftige Klimaänderungen vorherzusagen. Speläotheme eignen sich hervorragend als Klimaarchive, da sie über einen Zeitraum von bis zu 100.000 Jahren kontinuierlich wachsen können und ihr Alter mit Hilfe von U-Serien-Methoden absolut, genau und hochaufgelöst bestimmt werden kann. Etablierte Proxies (z.B. Isotopenverhältnisse oder Spurenelemente) werden zunehmend durch organische Biomarker ergänzt, die spezifischere Aspekte der Paläoumweltbedingungen wie Vegetationstyp, Feuerdynamik und Temperatur erfassen. Ziel dieser Arbeit war es, spurenanalytische Methoden für drei verschiedene Gruppen von biochemischen Proxies in Speläothemen zu entwickeln. Die Methoden wurden dann auf Realproben angewandt, um zeitliche Veränderungen in den Proxysignalen nachzuweisen und diese in Bezug auf Veränderungen der klimatischen und umweltbedingten Gegebenheiten zu interpretieren.

Im ersten Teil dieser Arbeit wurde eine elektrochemische Methode für die anodische Oxidation und den nachfolgenden Aufschluss von Lignin in Speläothemen entwickelt, um die entstehenden Ligninoxidationsprodukte (LOPs) als Paläo-Vegetationsmarker zu nutzen. Die LOPs wurden mit einem Ultra-Hochleistungs-Flüssigkeitschromatographiesystem analysiert, das mit einem hochauflösenden Massenspektrometer gekoppelt war. Die Methode erreichte vergleichbare oder sogar höhere LOP-Konzentrationen als die etablierten CuO- und CuSO₄-Oxidationsmethoden. Die Methode stellt ein neues Werkzeug für die Analyse und Rekonstruktion der Paläovegetation dar und hat das Potenzial, auch auf andere Klimaarchive und Matrices angewandt zu werden.

Im zweiten Teil wurden Levoglucosan, ein Verbrennungsanzeigender Anhydrozucker, und LOPs in einem Stalagmit analysiert, um die Feueraktivität und die Vegetationszusammensetzung in der California Coast Range während des 8.2 kyr-Ereignisses zu rekonstruieren. Erhöhte Levoglucosankonzentrationen deuten auf eine erhöhte Feueraktivität hin, während die veränderte LOP-Zusammensetzung auf eine Verschiebung hin zu einer stärker verholzten Vegetation während dieses Ereignisses schließen lässt. Wie stabile Kohlenstoff- und Calciumisotopenverhältnisse zeigen, gehen diese Veränderungen mit einer erhöhten Unbeständigkeit des Hydroklimas einher. Zusammengefasst deuten diese Daten darauf hin, dass Klimaschwankungen (Oszillationen zwischen extremer Nässe und Trockenheit) und Regenfälle in Kalifornien, die mit dem anthropogenen Klimawandel voraussichtlich zunehmen werden, im frühen Holozän eng miteinander verbunden waren.

Im letzten Teil wurde eine sequentielle Extraktion von pulverisierten Stalagmitproben durchgeführt, um diese auf 16 polyzyklische aromatische Kohlenwasserstoffe (PAKs) und drei Monosaccharidanhidride (MAs) zu untersuchen. Die Probenvorbereitung erfordert nur kleine Probemengen; die PAKs und MAs wurden mittels GC-MS beziehungsweise LC-HILIC-MS gemessen. Die Methode wurde an 10 Proben eines ~400 Jahre alten Stalagmiten aus der Cenote Ch'en Mul in Mayapan, der größten postklassischen Maya-Hauptstadt der Halbinsel Yucatán, angewendet. Es wurde eine starke Korrelation zwischen dem bedeutendsten MA

(Levoglucosan) und den nicht-alkylierten PAKs ($\Sigma 15$) festgestellt. Es wurden mehrere diagnostische PAK- und MA-Verhältnisse untersucht, und obwohl nicht alle als Paläobrandproxy geeignet waren, scheinen Verhältnisse, die PAKs mit MAs kombinieren, vielversprechende Hilfsmittel zu sein, um verschiedene Brandregime zu identifizieren und Rückschlüsse auf die Art des verbrannten Materials zu ziehen. In den 1950er und 1960er Jahren verdoppelten sich die Konzentrationen von Levoglucosan und $\Sigma 15$ im Vergleich zu anderen Zeiten in den letzten 400 Jahren, was auf eine größere Feueraktivität in Mayapan während dieser beiden Jahrzehnte schließen lässt. Die höheren Konzentrationen von Feuermarkern könnten auf die Rodung des Geländes und die Erkundung der Höhle durch Archäologen des Carnegie Institutes zurückzuführen sein.

Abstract

Climate archives like speleothems, ice cores, sediment cores, or tree rings hold valuable information about local and global climatic events. They can be used to reconstruct different aspects of past environments and thus in turn help to predict future climate change. Speleothems are ideally suited as climate archives since they can grow continuously over a period of up to 100,000 years and their age can be determined absolutely with high accuracy and high resolution using U-series methods. Established proxies (e.g. isotopic ratios or trace elements) are increasingly complemented by organic biomarkers that record more specific aspects of paleoenvironmental conditions like vegetation type, fire dynamics, and temperature. The aim of this work was to develop trace analysis methods for three different groups of biochemical proxies in speleothems. The methods were then applied to real samples to elucidate temporal changes in the proxy signals and interpret them in regards to changes in the climatic and environmental conditions.

In the first part of this work, an electrochemical method for the anodic oxidation and subsequent degradation of lignin in speleothems was developed to utilise the resulting lignin oxidation products (LOPs) as paleo-vegetation markers. LOPs were analysed using an ultra-high performance liquid chromatography system coupled to a high-resolution mass spectrometer. The method achieved comparable or even higher LOP concentrations than established CuO and CuSO₄ oxidation methods. The method represents a new tool for the analysis and reconstruction of paleo-vegetation and has the potential to be applied to other climate archives and matrices.

In the second part, levoglucosan, a combustion-sensitive anhydrosugar, and LOPs were analysed in a stalagmite, reconstructing fire activity and vegetation composition in the California Coast Range across the 8.2 kyr event. Elevated levoglucosan concentrations suggest increased fire activity while altered LOP compositions indicate a shift toward more woody vegetation during the event. These changes are concurrent with increased hydroclimate volatility as shown by carbon and calcium isotope proxies. Together, these records suggest that climate whiplash (oscillations between extreme wetness and aridity) and fire activity in California, both projected to increase with anthropogenic climate change, were tightly coupled during the early Holocene.

In the last part, a sequential extraction of pulverised carbonate samples was conducted to analyse them for 16 polycyclic aromatic hydrocarbons (PAHs) and three monosaccharide anhydrides (MAs). The preparation method requires only small sample sizes; PAHs and MAs were measured by GC-MS and LC-HILIC-MS, respectively. The method was applied to 10 samples from a ~400-year-old stalagmite from Cenote Ch'en Mul, at Mayapan, the largest Postclassic Maya capital of the Yucatán Peninsula. A strong correlation between the major MA (levoglucosan) and non-alkylated PAHs ($\Sigma 15$) was observed. Multiple diagnostic PAH and MA ratios were investigated and although not all were applicable as paleo-fire proxies, ratios that combine PAHs with MAs appear to be promising tools for identifying different fire regimes and inferring the type of fuel burned. In the 1950s and 1960s, levoglucosan and $\Sigma 15$ concentrations roughly doubled compared to other times in the last 400 years, suggesting greater fire activity at Mayapan during these two decades. The higher concentrations of fire

markers may be due to land clearance at the site and explorations of the cave by Carnegie Institution archaeologists.

Table of Contents

Zusammenfassung.....	I
Abstract.....	III
1. Introduction and theoretical background.....	1
1.1. Speleothems as paleoclimate archives.....	1
1.1.1. Formation.....	1
1.1.2. Dating.....	2
1.2. Established proxies.....	4
1.2.1. Stable isotopic ratios.....	4
1.2.2. Trace elements.....	5
1.3. Novel molecular proxies.....	7
1.3.1. Lignin as a vegetation proxy.....	7
1.3.2. Monosaccharide anhydrides as a biomass burning proxy.....	10
1.3.3. Polycyclic aromatic hydrocarbons as combustion proxies.....	12
1.4. Analytical methods.....	14
1.4.1. Solid phase extraction.....	14
1.4.2. Sample evaporation.....	15
1.4.3. High performance liquid chromatography.....	15
1.4.4. Gas chromatography.....	19
1.4.5. Mass spectrometry.....	20
2. Development of a method for anodic degradation of lignin for the analysis of paleo-vegetation proxies in speleothems.....	27
2.1. Abstract.....	28
2.2. Introduction.....	28
2.3. Results and Discussion.....	30
2.4. Conclusion.....	33
2.5. Experimental Section.....	33
2.6. Acknowledgements.....	36
3. Linked fire activity and climate whiplash in California during the early Holocene.....	37
3.1. Abstract.....	37
3.2. Introduction.....	37
3.3. Results.....	39
3.3.1. Stalagmite-based fire and vegetation proxies.....	39
3.3.2. Fire and vegetation proxies in the modern cave environment.....	41

3.4. Discussion	43
3.5. Methods.....	46
3.5.1. Statistical analysis of previously sampled proxy records.....	46
3.5.2. Chemicals and materials.....	46
3.5.3. Speleothem and modern calcite sample preparation.....	47
3.5.4. Levoglucosan Analysis	48
3.5.5. LOP Analysis.....	49
3.6. Data availability	49
3.7. Acknowledgments	49
3.8. Author contributions	50
3.9. Competing Interests Statement.....	50
4. Past fire dynamics inferred from polycyclic aromatic hydrocarbons and monosaccharide anhydrides in a stalagmite from the archaeological site of Mayapan, Mexico.....	51
4.1. Abstract.....	51
4.2. Introduction	52
4.3. Methods.....	53
4.3.1. Materials	53
4.3.2. PAH and MA extraction.....	55
4.3.3. PAH analysis.....	55
4.3.4. MA analysis.....	56
4.4. Results and discussion	57
4.4.1. Method validation	57
4.4.2. Speleothem MAs and PAHs	58
4.4.3. LEV and PAHs as indicators of fire activity at Cenote Ch'en Mul	63
4.5. Conclusions.....	63
4.6. Future Work.....	64
4.7. Data availability	65
4.8. Author contributions	65
4.9. Competing interests.....	65
4.10.Acknowledgements	65
5. Conclusion and outlook.....	67
6. References.....	71
7. Appendix	90
A. Supplementary material chapter 3	90
B. Supplementary material chapter 4	97

C.	Adaptation of CuSO ₄ digestion to other matrices.....	109
C.1.	Introduction	109
C.2.	Solid-liquid extraction prior to CuSO ₄ digestion	109
C.3.	Direct CuSO ₄ digestion	114
C.4.	Comparison and conclusion.....	117
D.	Levoglucosan in speleothems: An evaluation of various sample preparation methods	119
D.1.	Abstract.....	119
D.2.	Introduction	123
D.3.	Experimental.....	123
D.4.	Results and discussion	126
D.5.	Comparison.....	129
D.6.	Conclusion.....	130
E.	Further optimisation and validation of the levoglucosan extraction method and lignin digestion	131
E.1.	Silanisation of extraction vessels	131
E.2.	Extraction efficiency for different sample amounts	133
E.3.	Impact of extraction of levoglucosan on retrieved LOP concentration	134
F.	List of Abbreviations.....	137
G.	List of related publications and presentations.....	141
H.	Acknowledgments	143
I.	Curriculum vitae.....	145

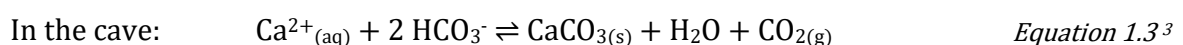
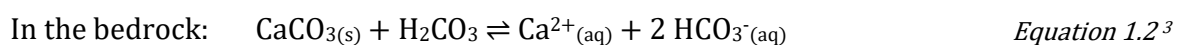
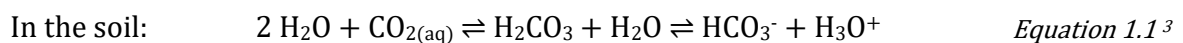
1. Introduction and theoretical background

1.1. Speleothems as paleoclimate archives

Speleothems, such as stalagmites, stalactites, and flowstones, are secondary carbonate deposits in caves that form in karst areas as a result of weathering of the bedrock (usually soluble rock types such as limestone CaCO_3 or dolomite $\text{CaMg}(\text{CO}_3)_2$). Speleothems are usually composed of calcareous the two most common are calcite and aragonite.^{1,2} Speleothems are ideally suited as climate archives since they can grow continuously over a period of up to 100,000 years and their age can be determined absolutely with high accuracy and high resolution using U-series methods.^{3,4} Most caves have a year-round stable climate which in addition to the generally sheltered conditions lead to reduced weathering of the speleothems. In addition, speleothems are usually chemically closed systems that do not change after deposition, so that trapped biomolecules are also preserved. Speleothems have a vast terrestrial scope which incorporates most ice-free landmass, and for this reason they are a valuable tool for reconstructing global and local climate events of the past.^{5,6}

1.1.1. Formation

The processes involved in the formation of speleothems are shown in Figure 1.1. In the soil, a high partial pressure of CO_2 ($p\text{CO}_2$) prevails due to the respiration of plants and the decomposition of organic matter. Rainwater absorbs the dissolved CO_2 from the soil and thus forms a solution of carbonic acid (H_2CO_3 ; Equation 1.1). The solution seeps through the soil into the epikarst zone and subsequently dissolves carbonate from the underlying karst rock until saturation with respect to Ca^{2+} is reached (Equation 1.2). Carbonate rocks are capable of storing and transmitting water through pores and fissures and are therefore called aquifers. As illustrated in Figure 1.1, the water table divides the bedrock into the overlying vadose and the lower phreatic zone. Often, the water level falls over time, leaving previously water-filled caves exposed and allowing new cavities to form in deeper layers of the bedrock. The saturated carbonate solution is able to pass through the aquifer until it hits a cavity where the $p\text{CO}_2$ is lower than in the surrounding rock due to ventilation. To reach a new equilibrium, CO_2 degasses from the solution. This leads to an increase in pH and the solubility of carbonate decreases. This shifts the equilibrium described by Equation 1.3 to the right and CaCO_3 precipitates from the now supersaturated solution and forms speleothems.^{1-3,7}



Various forms of speleothems are distinguished, with the most studied for paleoclimatology being flowstones formed under running water on the floor or wall, or dripstones. Flowstones form under the influence of a fissure or conduit flow and frequently cover large areas. The large extension often allows for duplicate sampling in the form of drill cores. In the case of dripstones, stalagmites growing from the floor upwards are usually preferred as paleoclimate archives over stalactites growing from the ceiling downwards, as they have a unambiguous stratigraphy (i.e. lower layers are younger) and often have a simpler geometry. Ideally, a stalagmite will only feature one continuous growth axis along which samples are taken. However, it is not uncommon for the growth axis to shift over time due to a positional change of the drip water. In addition, the calcite deposition can stop for extended periods of time based on the cessation of dripping or a change in the drip water chemistry. The discontinuation of dripping may be caused by climatic changes (e.g. the formation of permafrost above the cave) or by a change in the flow path. Sometimes dust or other residues are deposited on the surface of the speleothem during the absence of drip water; this then visually marks a hiatus.^{1,3}

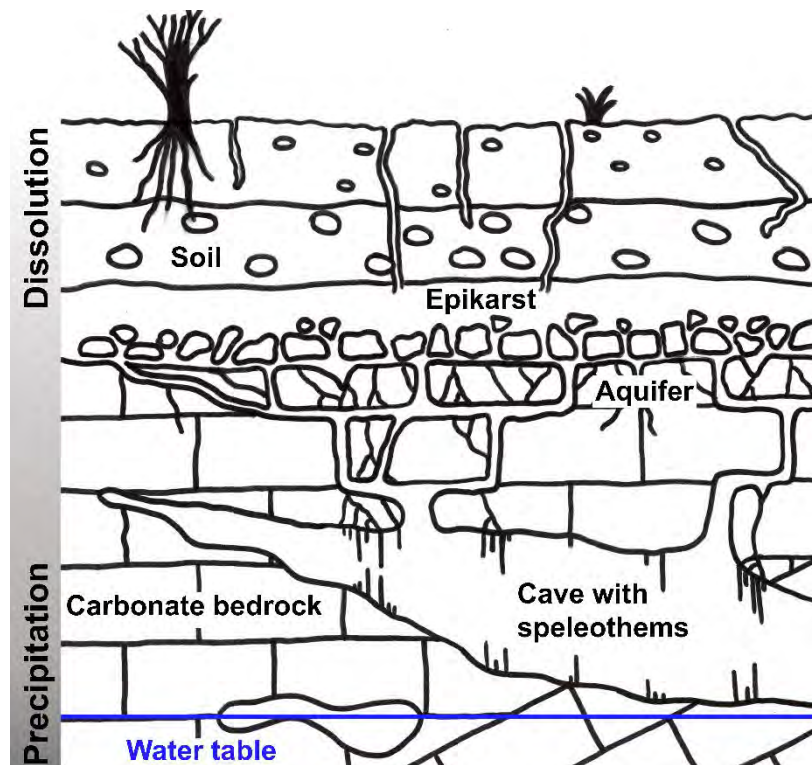


Figure 1.1. Schematic of the formation of speleothems and necessary chemical processes. Drawing produced after Fairchild et al. (2006).³

1.1.2. Dating

To make practical use of (paleo-)climate archives, it is necessary to date them precisely. The radiocarbon method (^{14}C) can be used to date speleothem samples to a limit of ca. 60,000 years^{8,9}, but U-series methods such as U/Th and U/Pb dating can provide longer timescales of

600,000 years – 20 million years respectively.^{4,10} Both of the latter methods are based on the radioactive decay of radionuclides within their decay chains.

In an undisturbed system, parent and daughter nuclides reach equilibrium after a few million years. $^{230}\text{Th}/\text{U}$ dating is based on the fractionation of parent (^{234}U and ^{238}U) and daughter (^{230}Th) nuclide and subsequent re-equilibration in the speleothem. The return to equilibrium allows the quantitative determination of time and thus the dating of the time of fractionation. The observed fractionation is a result of the different solubilities of U and Th. In nature, U occurs predominantly as water-soluble uranyl (UO_2^{2+}) and thus in the oxidation state +VI. Th, on the other hand, is mainly present in the oxidation state +IV and forms water-insoluble complexes. As a result, groundwater contains dissolved U but virtually no Th, meaning that initially, no Th is incorporated into a forming speleothem. Thus, ^{230}Th contained in speleothems should only be a result of U decay processes. Nevertheless, it is possible that, for instance, during a growth stop, Th attached to clay minerals is introduced into the speleothem. This initially present Th would result in a higher age of the corresponding growth layer. To avoid such a falsification, ^{232}Th is measured as well. ^{232}Th is not part of the decay series, but behaves in the same way as ^{230}Th and can therefore be used as a detritus indicator and to correct the raw ages.^{4,11}

To date individual layers of a speleothem, the degree to which the equilibrium has been restored is determined. Typically, several samples are dated along the growth axis of the speleothem. The carbonate samples are dissolved in acid, spiked with a mixture of artificial Th and U isotopes (^{229}Th , ^{233}U , and ^{236}U), and oxidised to eliminate organic contaminations. U and Th are separated on an anionic exchange column prior to measurement.¹² Nowadays, U and Th are mainly measured by multi-collector inductively coupled plasma mass spectrometry (MC-ICP-MS); this technique allows precise quantification at low detection limits.^{13–16} An age model is calculated from the U and Th concentrations, which ascribes an age to every measured proxy data point.⁴ Various algorithms are available for calculating the age model, such as StalAge¹⁷, OxCal¹⁸, and COPRA¹⁹. The algorithms differ in their required inputs and procedures in handling disruptions like hiatuses.

1.2. Established proxies

Signals archived in the speleothem may originate from the atmosphere (e.g. water, CO₂, and aerosols), the overlying soil and vegetation, the karstic aquifer, or the cave itself.³ Thus, they archive important climatic aspects of the environment such as mean annual temperature, rainfall variability, changes in atmospheric circulation, and vegetation transitions. To reconstruct these changes different features (proxies) are investigated. Typically measured parameters include stable isotope ratios (e.g. δ¹³C and δ¹⁸O), variations in trace element concentrations and ratios (e.g. Sr or Mg/Ca), growth-rate changes, and crystal form of the carbonate (i.e. calcite vs. aragonite).²⁰

1.2.1. Stable isotopic ratios

The most described stable isotopic ratios in speleothem science are δ¹³C and δ¹⁸O but other ratios are reported as well, e.g. δ²H, δ⁴⁴Ca, and ⁸⁷Sr/⁸⁶Sr. The δ-values refer to the ratio of the rare isotope to their more common isotope in relation to a standard material (Equation 1.4); δ values are expressed in per mil (‰). Isotopic ratios of Carbon and Oxygen are determined through dissolution of the carbonate in orthophosphoric acid and subsequent analysis of the formed CO₂ with an isotope-ratio mass spectromete. Alternative measuring techniques, especially used for the analysis of isotopes of other elements, include laser ablation (LA), thermal ionisation mass spectrometry, and MC-ICP-MS.^{3,20}

$$\delta^{18}\text{O} = \left(\frac{{}^{18}\text{O}/{}^{16}\text{O}_{\text{Sample}} - {}^{18}\text{O}/{}^{16}\text{O}_{\text{Standard}}}{{}^{18}\text{O}/{}^{16}\text{O}_{\text{Standard}}} \right) \cdot 1,000 \quad \text{Equation 1.4}^{21}$$

δ¹⁸O values of the drip water, and thus also δ¹⁸O values of the newly formed carbonate, records the weighted mean δ¹⁸O value of the meteoric water at the site, as long as isotopic equilibrium prevails. This is only the case, if speleothem growth is only due to degassing of CO₂ and not to evaporation of water. The latter would cause kinetic fractionation, thus altering the isotopic pattern. These conditions dominate in temperate locations, where a stable cave air temperature and high humidity levels in the cave are achieved. In arid and semi-arid sites however, this is often not the case, complicating the interpretation of δ¹⁸O values.²⁰ The δ¹⁸O value of meteoric water is influenced by the surface air temperature, the isotopic composition of the vapour source (i.e. body of water that the cloud water evaporated from), distance from the main vapour source, and amount of precipitation. Thus, δ¹⁸O values are usually used to study changes in global atmospheric circulation patterns (e.g. North Atlantic Oscillation and El Niño-Southern Oscillation), changes in the main vapour source of the site, and first order climatic events (e.g. Dansgaard-Oeschger events and the 8.2 kyr event). Local effects like heavy rainfall might also need to be considered for each site.^{1,20,21}

The δ¹³C values of speleothems are mainly affected by the δ¹³C values of the overlying soil which in turn is influenced by the soil respiration rate, the type and density of vegetation, and the dominant photosynthetic pathways of vegetation (C₃ versus C₄). In an open system, enough gaseous soil CO₂ is present during the dissolution of the host rock to allow for full carbon-exchange. The dissolved carbonate species (mainly bicarbonate; HCO₃⁻) will then only

reflect the isotopic composition of the soil CO₂. Under closed conditions, no gaseous soil CO₂ is available during dissolution and the $\delta^{13}\text{C}$ will be altered by the host rock's isotopic composition. In reality, most caves constitute partially closed systems so that the $\delta^{13}\text{C}$ is subject to multiple controls.^{7,20} In arid regions, large shifts in $\delta^{13}\text{C}$ can be caused by a change in the photosynthetic pathway of above ground vegetation (C₃ versus C₄). In temperate zones, higher $\delta^{13}\text{C}$ values can be due to high rainfall, leading to insufficient equilibration in the soil so that isotopically heavier atmospheric CO₂ is transported into the cave. Alternatively, higher $\delta^{13}\text{C}$ ratios may also be induced by overall drier conditions, resulting in evaporation of the dripwater or degassing of isotopically lighter CO₂ above the cave; the latter is referred to as prior calcite precipitation (PCP). A decrease in $\delta^{13}\text{C}$ can be ascribed to a gradual build-up of soil and resulting increase in soil activity and pCO₂, for example at the transition from a glacial to an interglacial period.^{7,20} To disentangle the various factors influencing $\delta^{13}\text{C}$, a combination with other proxies (e.g. $\delta^{18}\text{O}$, trace elements, or biomarkers) in a multi-proxy approach is sensible.

A more recent development is the analysis of clumped isotopes. For this the temperature dependant preference of heavy nuclides to bond with other heavy isotopes rather than lighter nuclides is utilised. For carbonate analysis, four different isotopologues of CO₂ can be observed: ¹²C¹⁶O₂ (mass 44), ¹³C¹⁶O₂ (mass 45), ¹²C¹⁸O¹⁶O (mass 46), and ¹³C¹⁸O¹⁶O (mass 47). The isotopologue with mass 47 shows the desired clumped isotopes (heavy isotopes of both C and O); its relative abundance is expressed as $\Delta 47$. The $\Delta 47$ is a function of the crystallisation temperature and can thus be used to derive paeo-temperatures.^{1,22-24}

Apart from the carbonate itself the isotopic composition of fluid inclusions within the speleothem tissue can also be investigated. Fluid inclusions are repositories of the dripwater from the time of calcification. They provide a direct link to the isotopic composition of the meteoric water at the time and can therefore be used to calculate paleo-temperatures. To enable their measurement, the speleothem is crushed while subject to mild heating to ensure only water from visible inclusion is released. Then, the $\delta^2\text{H}$ and $\delta^{18}\text{O}$ ratios of the water are determined.^{1,23,25}

1.2.2. Trace elements

Speleothems contain a range of trace elements that can be used as proxies for rainfall, temperature, soil conditions, fire occurrence, and other environmental conditions. The primary source of trace elements in speleothems is the dissolved bedrock; the dissolution is at its maximum where pCO₂ is highest. The atmosphere only plays a minor role as a source of trace elements in dripwater and speleothems. However, Sr and Si can originate from aeolian dust, NaCl, Sr, and Mg may be input by deposition of sea-salt aerosol, and sulphate can be a tracer of various atmospheric pollutants (e.g. volcanic activity or anthropogenic sources).²⁶

Trace elements can be incorporated into the growing speleothem in different ways; Ca²⁺ and CO₃²⁻ can be directly substituted in the crystal lattice by divalent ions with similar sizes (e.g. Mg²⁺, Sr²⁺, Ba²⁺, and SO₄²⁻). Other ions (e.g. Y³⁺, Na⁺, Br⁻, and PO₄³⁻) are preferentially integrated at defect sites where the exact ion size is of less importance. Single and triply

charged ions substitute as couples to preserve charge balance. Ions that are adsorbed to particles or are transported as colloids can be enclosed in small detrital particles or associated to sub-micron-sized organic colloids. This is most commonly found for elements complexed by organic matter, e.g. Mn^{2+} , Cu^{2+} , Ni^{2+} , Zn^{2+} , Pb^{2+} , and PO_4^{2-} . Lastly, sodium chloride can be dissolved in fluid inclusions.^{26,27}

Interpretation of trace element signals in speleothem is often difficult because of the different sources and processes responsible for availability and incorporation. One well studied event is the PCP; if PCP occurs, CaCO_3 precipitates from the solution prior to the studied speleothem drip-site. This results in an increase of the Sr/Ca and Mg/Ca ratios of the studied carbonate, often accompanied by an increased $\delta^{13}\text{C}$. As discussed above (Chapter 1.2.1), PCP is most likely due to a drier climate but can also be caused by a more efficient ventilation of the cave resulting in a lowered cave pCO_2 . Periods of high rainfall can be linked to an increase in elements that are transported through colloids or elements that are preferentially mobilised in reducing conditions like Mn^{2+} . P exhibits a seasonal signal as it is released into the soil through die-back of vegetation in autumn and is then flushed into the cave during the following season.²⁶

Fire impacts the soil rather than the bedrock, even though fissures can be formed during severe fires. A primary consequence of fire on soils is the reduction of pCO_2 as plant roots and bacterial communities are diminished; as a result, dissolution of bedrock is lessened, concentrations of bedrock-based elements (e.g. Ca, Mg, Sr) decrease, speleothem growth is reduced, and $\delta^{13}\text{C}$ values increase (i.e. enrichment in ^{13}C).²⁸⁻³¹ Elements that are normally bound in biomass (e.g. P, sulphate, and K) can be released through fire and are subsequently washed into the cave. Depending on the site, fire may either lead to more water-permeable soil or increased susceptibility to evaporation. In the first case, the increased water-flow results in a dilution of trace elements. In the second case, the augmented evaporation leads to a concentration of the present trace elements.^{28,30-35}

To disentangle the different influences involved at the investigated site, often a principal component analysis is carried out. This clusters together the examined proxies that are subject to the same controls.^{31,32,35,36}

In the past, analysis of trace elements in speleothems was often carried out using atom absorption spectroscopy or inductively coupled plasma optical emission spectroscopy. Due to the significantly improved detection limits, mainly (LA-)ICP-MS or microprobe techniques (e.g. secondary ionisation mass spectrometry and micro x-ray fluorescence) are used.^{3,26}

1.3. Novel molecular proxies

For a long time, mainly inorganic proxies were studied in speleothems. In more recent times, these established proxies are increasingly complemented by organic biomarkers that record more specific aspects of the paleoenvironmental conditions like vegetation type, fire dynamics, and temperature.³⁶⁻⁴⁰

A fairly non-specific proxy for climate and vegetation is luminescence, which is elicited by organic compounds with weakly bound electrons.^{6,38} Racemisation of amino acids is being investigated as an alternative dating method. However, this method is not very specific due to the variety of entry possibilities and more research is needed.⁶ Speleothems can also contain different bacterial membrane lipids, glycerol dialkyl glycerol tetraethers (GDGTs), which can be used as a paleo-thermometer (TEX₈₆ index).^{37,41-43} Low molecular weight fatty acids (C₁₂-C₂₀) are also of bacterial origin⁴⁴, while high molecular weight fatty acids (> C₂₀) originate from vascular plants and are considered as vegetation proxies.^{39,45} Similarly, longer chain *n*-alkanes (> C₂₀) are associated with leaf waxes and are therefore considered as indicators of higher plants.^{6,46,47}

While multiple proxies yield more general vegetational information like abundance or predominance of C₃ versus C₄ plants, a proxy that can be unambiguously linked to plants and give more detailed information on the vegetation composition would be essential to bettering the reconstruction of paleo-environments.³⁸

Another important aspect of past environments is the occurrence and dynamics of fires, whether natural or anthropogenic. It is well documented that aerosols in the atmosphere have a major influence on climate and climate change through various direct and indirect processes, e.g. light scattering or condensation on particles.⁴⁸ Combustion processes have been a source of large amounts of particles in the atmosphere since prehistoric times. The development of fire-sensitive proxies in paleoenvironmental archives can help elucidate interactions among climate, regional hydrology, vegetation, and fire activity.³²

1.3.1. Lignin as a vegetation proxy

Lignins are biopolymers that occur in all terrestrial plants and give them strength and stability through incorporation into the cell walls. After cellulose, lignins are the most abundant biopolymers and account for about 30 % of the organic carbon in the biosphere.^{49,50} The polymer is mainly composed of the three monomers shown in Figure 1.2: coumaryl alcohol, coniferyl alcohol and sinapyl alcohol. The monomers react with each other by radical polymerisation to form a three-dimensionally linked network similar to the partial structure shown in Figure 1.2.^{49,51}

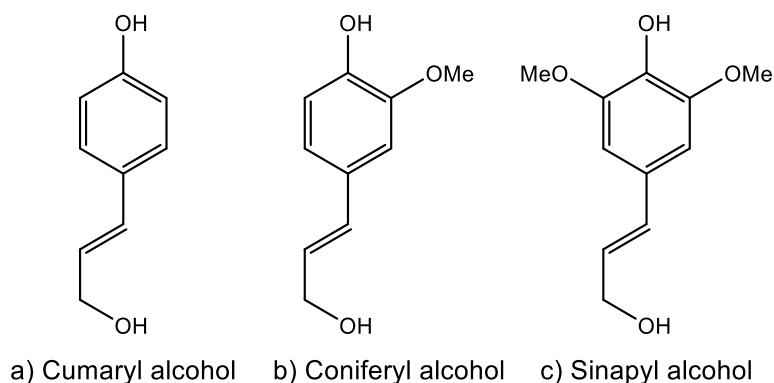


Figure 1.2. Molecular structures of the three main constituents of polymeric lignin. After Jex et al. (2014).⁵²

Due to the very stable bonds contained in the biopolymer, mainly aromatic six rings, carbon-carbon bonds, and ether bonds, it is only degraded very slowly by microorganisms. Therefore, it is possible that lignins are transported through the soil and are eventually stored in speleothems.⁵²

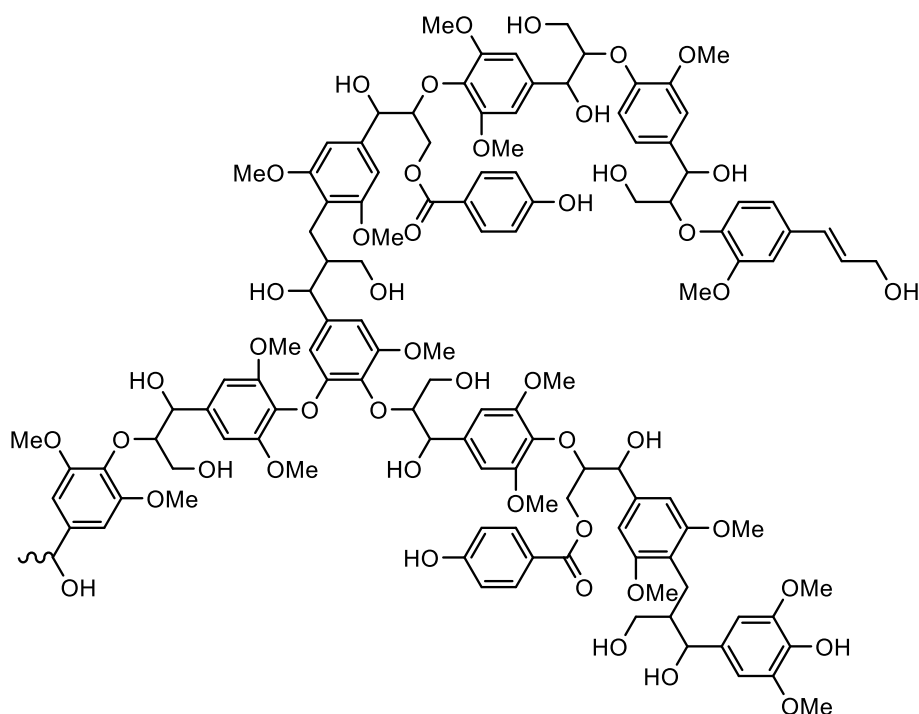


Figure 1.3. Example of a partial molecular structure of lignin. After Vanholme et al. (2010).⁵¹

To render the polymer accessible for analysis, it is digested by oxidation under basic conditions. Often, a digestion with copper (II) oxide (CuO) is used for this purpose, in which CuO acts as an oxidant and ammonium iron (II) sulphate ((NH₄)₂Fe(SO₄)₂) is used as an oxygen scavenger.⁵²⁻⁵⁵ An alternative digestion can be employed based on copper (II) sulfate (CuSO₄) and ascorbic acid.^{56,57} The advantage of the latter is that no toxic chemicals are used and that it is possible to work with solutions instead of solids. In both cases, the chemicals and the polymeric lignin are added to a sodium hydroxide solution and heated to 150 – 170 °C for a few hours in an inert gas atmosphere. The resulting monomeric units are described as lignin oxidation products (LOPs) and can be sorted into four groups based on their molecular

structures (Figure 1.4): the vanillyl (V), syringyl (S), cinnamyl (C) and *p*-hydroxyl (P) group.^{52,54}

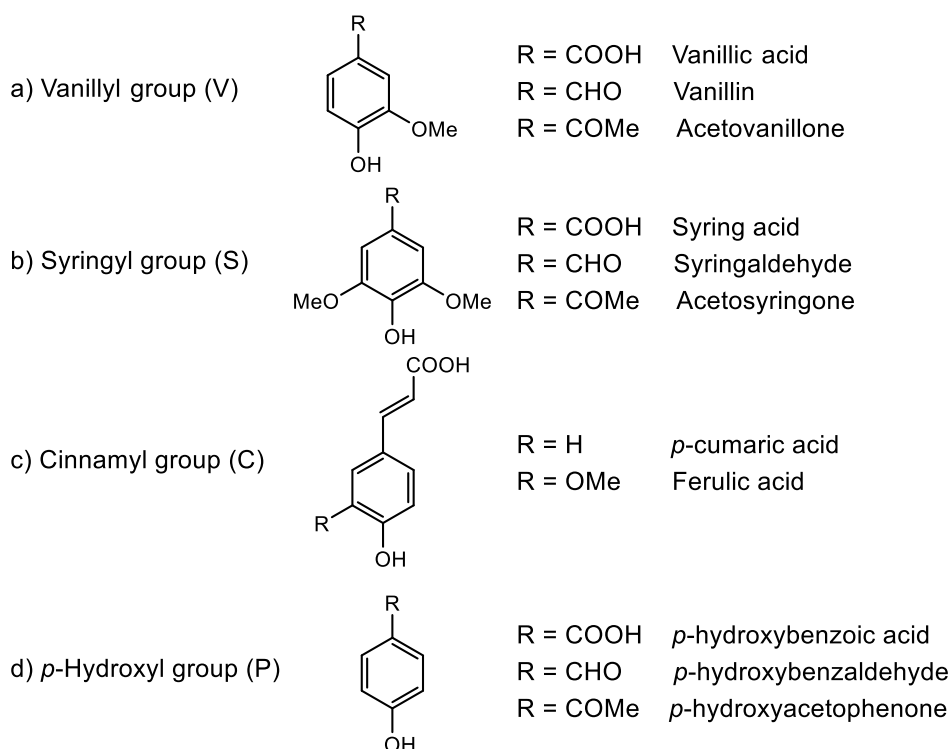


Figure 1.4. Classification of the LOPs based on their structural features. After Jex et al. (2014).⁵²

Lignins are particularly interesting as vegetation proxies because the structure of the polymer and thus the distribution of the oxidation products allow conclusions to be drawn about the origin of the polymer. Investigations of fresh plant parts by Hedges and Mann (1979) have shown that lignins from gymnosperms (bare-seeded plants, softwoods) and angiosperms (cover-seeded plants, hardwoods), as well as from herbaceous and woody plants, each have different monomer compositions.⁵⁴ The monomers of the S-group (syringic acid, syringaldehyde, and acetosyringone) only occur in significant amounts in angiosperms, while the C-group monomers (*p*-coumaric acid and ferulic acid) are only found in non-woody plant parts. The phenols of the V-group (vanillic acid, vanillin, and acetovanillone) are present in all parts of all vascular plants and are used to normalise the other two groups. By examining the C/V and S/V ratios, it is thus possible to draw conclusions about the type of plant material (see Figure 1.5).^{52,54}

The analytes of the *p*-hydroxyl group (*p*-hydroxybenzoic acid, *p*-hydroxybenzaldehyde and *p*-hydroxyacetophenone) can also originate from sources other than lignin and are therefore not interpreted as vegetation proxies.^{52,54}

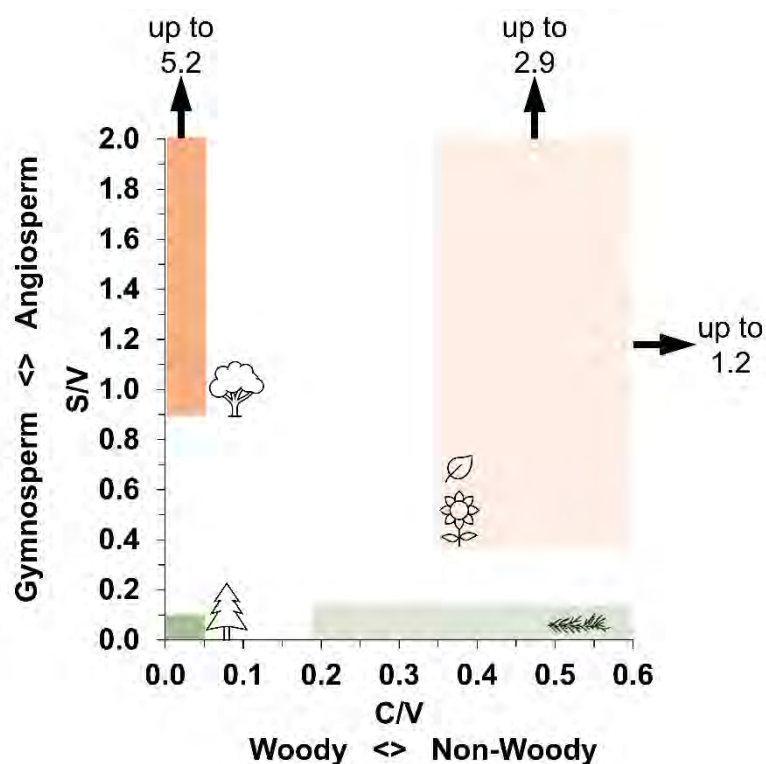


Figure 1.5. Scatter plot of the S/V vs. C/V ratios for the assignment of the source of a lignin. Indicated areas according to Hedges and Mann (1979).⁵⁴ Dark orange: woody angiosperms; light orange: non-woody angiosperm; dark green: woody gymnosperm; light green: non-woody gymnosperm. Drawing produced after Jex et al. (2014).⁵²

The application of lignin oxidation products for the reconstruction of paleo-vegetation has already been demonstrated some time ago in other paleoclimate archives such as peat and sediments.⁵² A study from Heidke et al. (2021)⁵⁸ found decreasing lignin concentrations in soil, drip water, and speleothems, respectively. However, as the relative vegetation signal (i.e. relative distribution within the S/V vs. C/V scatter plot) was preserved throughout the transport into the cave and the incorporation into the carbonate, the applicability of LOPs in speleothems was demonstrated.⁵⁸ The determination of lignins in speleothems, is still novel, but there are already some studies on which this work will build.^{36,45,53,57-59}

1.3.2. Monosaccharide anhydrides as a biomass burning proxy

Monosaccharide anhydrides (MAs) are formed only during the combustion of biomass at temperatures of 150 – 300 °C. The most abundant MA levoglucosan (1,6-anhydro- β -D-glucopyranose) is formed during the combustion of cellulose; the corresponding processes are shown in abbreviated form in Figure 1.6. Two further MAs, mannosan and galactosan (1,6-anhydro- β -D-mannopyranose and 1,6-anhydro- β -D-galactopyranose), are primarily formed from the pyrolysis of hemicellulose, a polymer which is composed of various monosaccharides.⁶⁰⁻⁶²

During combustion, the MAs are released into the particle phase either as a pure substance or adsorbed on soot particles. It was shown that the analytes are not photolytically decomposed

even in an oxidative environment (O_3 or NO_2), but reactions with hydroxyl radicals occur and stability decreases with increasing pH.^{61,63} Levoglucosan has an atmospheric lifetime of 2-26 days meaning that no hydrolysis occurs under the conditions prevailing in the atmospheric particle phase (aqueous environment, pH \sim 2).⁶³⁻⁶⁵ The circumstances are thus given that the anhydro sugars can be transported and deposited.⁶³

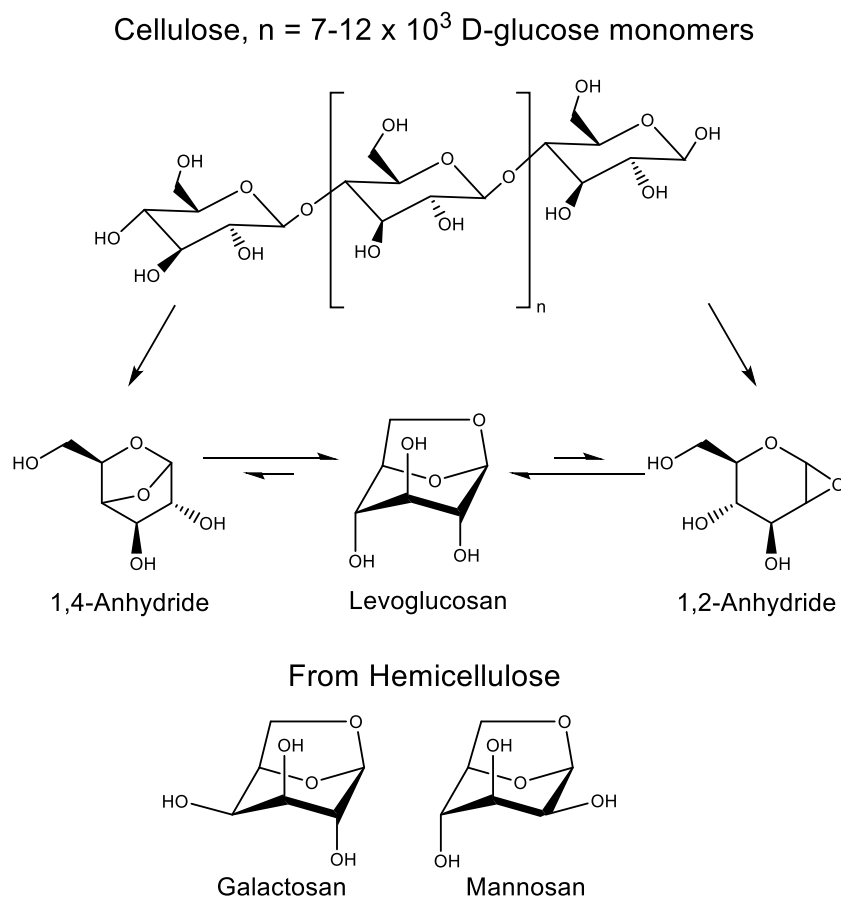


Figure 1.6. Schematic representation of the pyrolytic degradation of cellulose at $T > 150$ °C. Adapted from Elias et al. (2001).⁶⁰

Levoglucosan is primarily formed during the combustion of wood or other cellulosic biomass such as straw or leaves and is therefore suitable as a biomass burning marker. However, the concentration of levoglucosan has to be considered critically, as the emission is strongly dependent on fuel type, oxygen availability, and temperatures during pyrolysis.⁶⁶ Moreover, Fabbri et al. (2009)⁶⁷ and Yan et al. (2018)⁶² have recently shown that small amounts of levoglucosan are also produced during the combustion of (brown) coal. It is therefore recommended to employ the ratio of levoglucosan to its isomers mannosan and galactosan ($L/(G+M)$) to distinguish between combustion of coal and different types of biomass.^{62,67}

Levoglucosan has long been used as a combustion proxy in aerosols⁶⁸ and is also preserved in sediments^{60,69} and ice cores^{57,70} through particle deposition. Elias et al. (2001)⁶⁰ demonstrated that the concentration of levoglucosan in sediments correlates well with charcoal ($r = 0.81$), a general combustion marker. In a similar way, levoglucosan could also reach speleothems; this has been investigated in former studies that each detected all three isomers in speleothem samples.^{57,71,72} These results confirm that levoglucosan and its isomers

are preserved in speleothems and can provide new valuable palaeoclimatological information.

1.3.3. Polycyclic aromatic hydrocarbons as combustion proxies

Polycyclic aromatic hydrocarbons (PAHs) are a group of compounds that consist of two or more fused benzene rings that are products of incomplete combustion over a wide temperature range (200-700 °C)^{73,74} with both natural (e.g. biomass burning, volcanism, and oil seeps) and anthropogenic (e.g. combustion of fossil fuels, traffic) sources.^{75,76} The formation of the PAHs during pyrolysis has been mainly associated with Diels-Alder type reactions and the deoxygenation of oxygenated aromatic compounds.^{74,77-79}

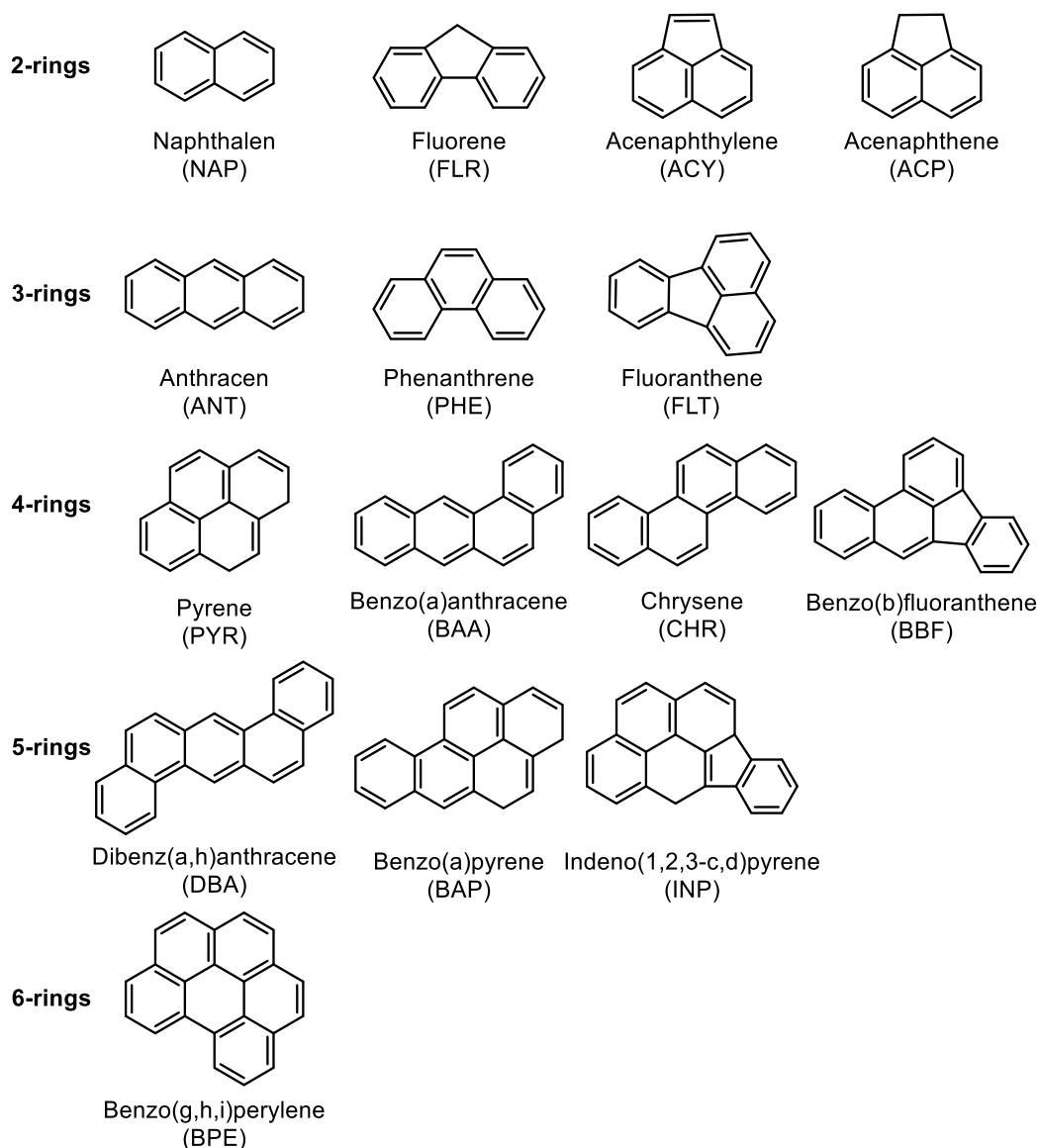
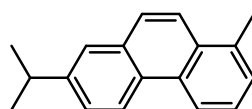


Figure 1.7. Molecular structures of 15 of the 16 priority PAH compounds as defined by the United States Environmental Protection Agency.⁸⁰ Not depicted is Benzo(k)fluoranthene.

PAHs are very persistent in the environment and are thus found ubiquitously, even in remote areas like the Arctic⁸¹, and have been described in many different environmental matrices like aerosols⁸², soil^{83,84}, peat⁸⁵, sediments^{86,87}, water⁸⁸, ice cores⁸⁹, and even speleothems^{90,91}. Due to their carcinogenic nature, some PAHs, e.g. the substances shown in Figure 1.7, are monitored in exhaust gases and wastewater.^{80,92,93}

The composition of PAH emissions is highly dependent on the combustion temperature, oxygen availability, gas phase resident time, and fuel type.⁷⁴ By studying the PAH profile and employing different PAH diagnostic ratios, it is possible to distinguish between different fuel types, to draw conclusions about the pyrolysis temperature, and determine whether the PAHs are derived from smoke or residues.^{86,87,94–97} Furthermore, some PAH compounds are unambiguous markers for the fuel source; for example, retene (Figure 1.8) is a unique marker for the combustion of gymnosperm biomass.^{98,99}



Retene (RET)

Figure 1.8. Molecular structure of retene, a molecular marker of gymnosperm combustion. After Ramdahl (1983).⁹⁸

Both, PAHs and MAs, have been reported as combustion markers and have been used in paleo-applications. Due to their different sources, formation processes, and physicochemical properties, the tandem analysis of these two groups of analytes is very promising. It opens up the possibility not only to detect the presence of fire but also to explore changes in fire regime (e.g. fire frequency, intensity, and fuel source). A joint analysis has so far only been reported in lake sediment cores^{100–102} but not for speleothems.

1.4. Analytical methods

The analytical procedures employed in this work encompass various sample preparation methods, such as solid phase extraction (SPE) and centrifugal evaporation. The samples are then measured using ultra-high performance liquid chromatography (UHPLC) or gas chromatography (GC) coupled to a high-resolution mass spectrometer (HRMS). The respective techniques are described in the following chapters.

1.4.1. Solid phase extraction

SPE is a widely used sample preparation technique that can be used for the preconcentration of an analyte in solution, matrix removal, or a solvent exchange, for example from an aqueous to an organic solvent. A polypropylene or glass cartridge holds a small amount of a solid phase material that is in between two frits. The solid phase is chosen according to the desired application and is mostly silica or polymer based but in recent times more specialised materials like graphitised carbon are available^{103–106}.

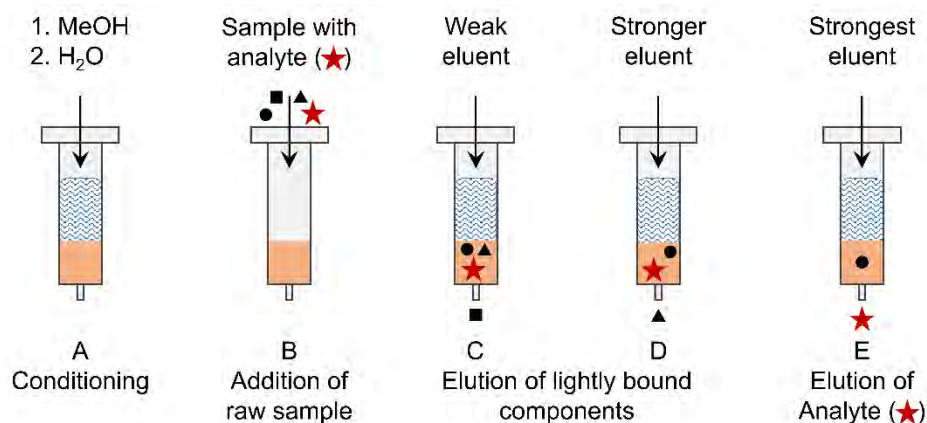


Figure 1.9. Schematic of a SPE procedure. Drawing produced after Harris et al. (2014).¹⁰³

A typical SPE procedure is illustrated in Figure 1.9 and starts with conditioning of the solid phase (A). The sorbent is first wetted with a solvent (here: Methanol, MeOH) to assure that the whole surface is covered in solvent and the functional groups are activated. Afterwards, the cartridge is equilibrated with another solvent that is matched to the sample matrix (here: H₂O). Subsequently, the sample solution is added to the cartridge (B) and the analyte and matrix components are adsorbed to the solid phase. To remove any undesired compounds, the cartridge can be washed with a weak eluent (C). This step can be repeated with a stronger eluent, if necessary (D). In a final step (E), the analyte is eluted with the strongest eluent. If the elution of the analyte is combined with a solvent exchange, the solid phase is dried before the final step to allow full sample recovery. Some components might stay bound to the solid phase, if the interaction with the sorbent is too strong.^{103,104}

1.4.2. Sample evaporation

If no sufficient retention or recovery can be reached with the available SPE materials, it might be necessary to evaporate the sample solution in order to concentrate the sample or isolate the analyte. To enter the gaseous state, a molecule needs to overcome the intermolecular interactions in the solution, the surface tension, and the vapor pressure above the surface. Evaporation can be enhanced by lowering any of these three values or by adding more energy into the system by heating.¹⁰⁷⁻¹⁰⁹

Often, nitrogen blowdown is used to facilitate the evaporation of small sample volumes of a few millilitres. A gentle stream of nitrogen is passed over the surface of the solution to accelerate the evaporation by reducing the partial pressure of solvent over the liquid. To avoid thermal degradation of analytes, this is carried out at room temperature or only slightly elevated temperature. However, volatile analytes may evaporate even at low temperatures especially if long evaporation times are required due to large sample volumes or high boiling points of the solvents.¹⁰⁷

Alternatively, a vacuum can be applied to the sample to decrease the boiling point of the liquid. However, the subsequent evaporation is often accompanied by bumping and foaming of the solution which can lead to sample loss and cross-contamination. This can be avoided by conducting the vacuum evaporation in a centrifuge; this process is called centrifugal evaporation. The sample vials are loaded into a centrifuge and rotated at high speed. The resulting centrifugal force moves denser particles towards the margins of the sample vessel while compounds of lesser density migrate towards the centre of rotation. The resulting pressure gradient ensures that the solution only boils at the surface, thus preventing foaming of the liquid. Centrifugal evaporation is suited for the evaporation of larger sample volumes (> 10 mL) and leads to high recovery rates due to minimal thermal degradation and degradation by oxygen.^{107,110,111}

1.4.3. High performance liquid chromatography

Chromatography is a versatile separation technique that is based on the repeated distribution of compounds between a mobile (gaseous or liquid) and a stationary (liquid or solid) phase. In liquid chromatography (LC), the mobile phase is a liquid of varying polarity and the stationary phase is composed of spherical microparticles which are either silica or polymer based. The surface of the particles is derivatised to allow the desired interactions with the analytes. The solid phase is tightly packed into a column through which the mobile phase is pumped; this results in a high back pressure.^{103,112} Newer columns are packed with sub 2 μm particles and operated at higher flow rates to reduce analysis time. However, this leads to increased back pressure; systems that can withstand these pressures of up to 1000 bar are referred to as ultra-high performance liquid chromatography (UHPLC).¹¹³

A high performance liquid chromatography (HPLC) system is comprised of eluent reservoirs, a pump, an injection system, a column with optional column oven, and a detector (Figure 1.10).^{103,112} In most cases, the detector is either a mass spectrometer (MS; see Chapter 1.4.5)

or a UV/Vis-Detector to analyse ionic species or absorbed light, respectively. The obtained signal is plotted against the time to produce a chromatogram.

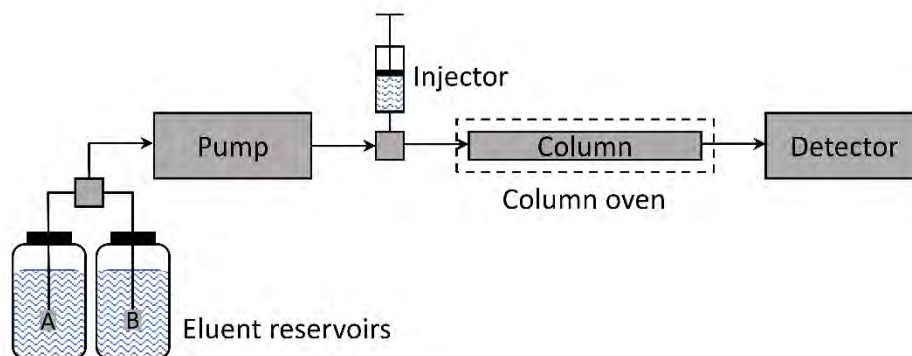


Figure 1.10. Schematic of a HPLC including two eluent reservoirs, a pump, the injector, a column with optional column oven, and a detector.

Different LC modes can be defined in dependence on the polarities of mobile and stationary phase. Originally, polar silica particles were used as stationary phase in combination with non-polar organic solvents as mobile phase; this setup is called normal phase LC (NP-LC). Here, apolar components will elute quickly while polar analytes show higher retention times. Over time, non-polar stationary phases were developed, like C₁₈ derivatised silica gels. These were employed in combination with aqueous eluents, to better retain apolar analytes. These methods are described as reversed phased LC (RP-LC). Of late, the necessity for a technique that is capable of separating highly polar compounds while also exhibiting a high sensitivity for electrospray ionisation mass spectrometry (ESI-MS; see Chapter 1.4.5.1) has arisen. Here, hydrophilic interaction chromatography (HILIC) is employed. For this method, polar stationary phases, similar to phases used in NP-LC, are used. The mobile phases, however, resemble the ones used in RP-LC and are mostly comprised of polar organic solvents like acetonitrile (ACN) and small amounts of aqueous buffers. Figure 1.11 illustrates the suitability of the different LC modes in relationship to the analyte polarity and the ESI-MS sensitivity. These two variables determine the choice of analysis method for a separation problem on hand.^{112,114–116}

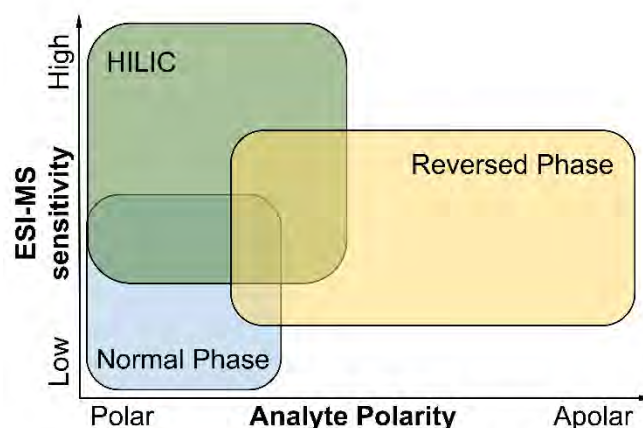


Figure 1.11. Analyte polarity and ESI-MS sensitivity of normal phase LC, reversed phase LC, and hydrophilic liquid interaction chromatography (HILIC). Drawing after Kahsay et al. (2014).¹¹⁶

In this work, RP-LC and HILIC have been employed. Therefore, these two methods will be discussed in more detail below. A special focus will be placed on the respective separation mechanisms of the column materials used.

1.4.3.1. Reversed phase chromatography

As already described, derivatised silica gels are predominantly used as stationary phases in the RP-LC. For this purpose, various non-polar residues are chemically bonded to the free silanol groups on the surface of the silica particles. In this work, a phase modified with pentafluorophenyl residues (PFP, Figure 1.12) was used.^{114,115}

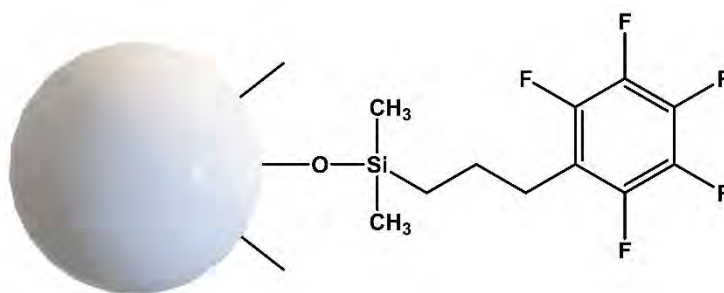


Figure 1.12. Schematic structure of a PFP phase. Drawing based on Przybyciel (2006).¹¹⁷

While pure hydrophobic interactions dominate in phases with alkyl groups, the phenyl structure and the more polar fluorine substituents of the PFP moiety enable further interaction mechanisms. The aromatic structure of the PFP group allows for π - π interactions making this phase especially suitable for the separation of aromatic compounds. Furthermore, silanol interactions increase the retention of basic analytes.^{117,118}

A mixture of an organic solvent and aqueous buffer is used as the mobile phase. To support the separation, the eluent composition is shifted from predominantly aqueous to higher organic proportions during the course of the analysis. This gradually increases the eluting power of the eluent and analytes strongly bound to the stationary phase are also eluted.¹¹⁵

1.4.3.2. Hydrophilic-interaction chromatography

Hydrophilic interaction chromatography (HILIC) was initially described as a variant of NP chromatography.¹¹⁹ HILIC uses polar stationary phases. Oftentimes, typical NP adsorbents such as pure silica gel or modified silica gel (e.g. diol, amine, or amide) are used, but in this work zwitter-ionic phases with quaternary ammonium, phosphoric acid, and sulfonic acid groups (Figure 1.13) were employed. The mobile phase is relatively nonpolar compared to the stationary phase and consists mostly of an organic solvent such as ACN (usually $\geq 70\%$), which is mixed with aqueous solutions. Often a residue-free evaporable salt such as ammonium formate or acetate is added to optimise the separation.^{103,120-123}

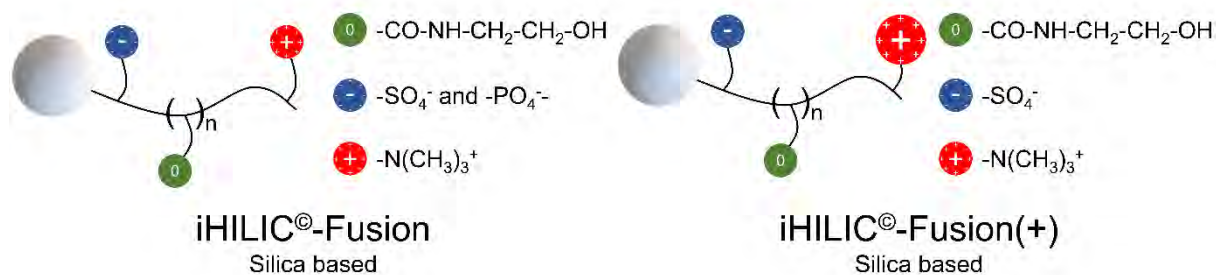


Figure 1.13. Schematic of the column phases used in this work: *iHILIC-Fusion* and *iHILIC-Fusion(+)*. Drawing produced after HILICON AB (2018).¹²³

The exact separation mechanism remains elusive; however, it is apparent that various mechanisms such as partitioning, adsorption; and electrostatic interaction come into play. For uncharged solutes, separation by partition is the predominant mechanism. It is based on the formation of an aqueous adsorption layer on the stationary phase, as a result of which a polarity gradient is formed between the stationary and mobile phases (Figure 1.14, left). Depending on the polarity of the analyte, it will preferentially reside in the immobilised aqueous layer or in the organic bulk-eluent; a distribution equilibrium is established. Because of this main mechanism, HILIC is sometimes considered a liquid-liquid chromatography technique.^{120,124–127}

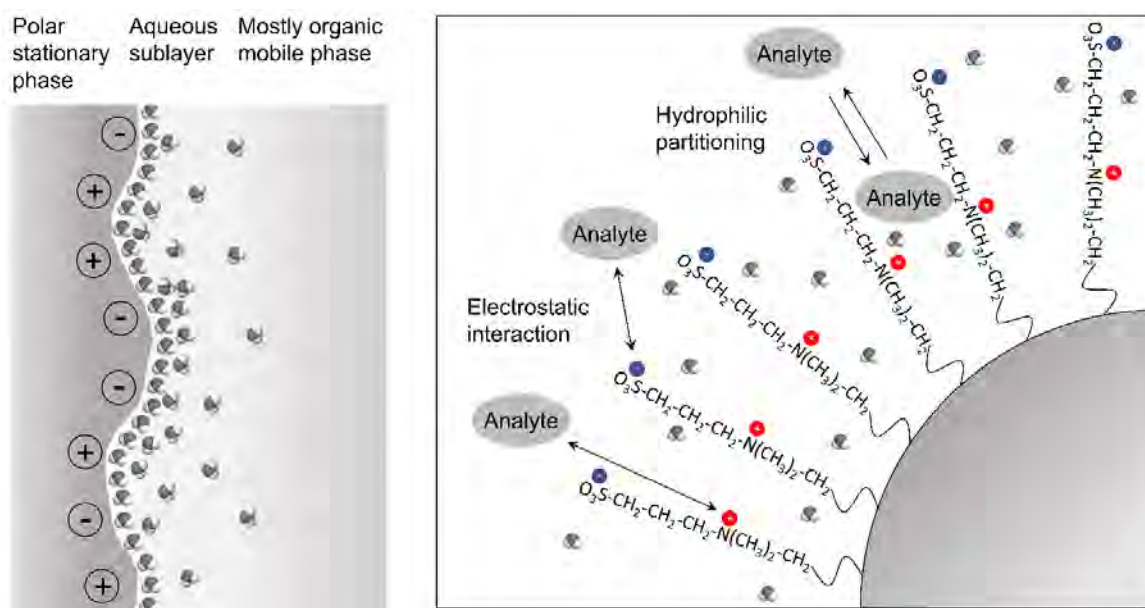


Figure 1.14. Left: Schematic of the polarity gradient between stationary and mobile phase by formation of an aqueous sublayer. Drawing produced after Jandera (2011).¹²¹ Right: Schematic of different interactions between analyte and stationary phase in HILIC. Drawing produced after Vogel (2012).¹²⁸

However, other processes will disturb the partitioning. Buffer salts contained in the eluent predominantly influence the electrostatic interactions of analyte and stationary phase. If they disturb the interaction, the retention is reduced, but it is also possible to reduce the repulsion between equal charges, which increases the retention. Likewise, charged stationary phases can interact with the solutes through coulomb interactions (Figure 1.14, right). The pH value of the eluent has no direct influence on the separation, but only on the charge of the analytes,

which determines the polarity and possible electrostatic interactions. Furthermore, RP retention on hydrophobic parts of bound ligands of the solid phase and specific adsorption of polar groups can be observed. In summary, it can be said that the exact separation mechanism and the resulting retention order is highly dependent on the analytes present and the separation system used.^{120,124–127}

1.4.4. Gas chromatography

In gas chromatography (GC), the mobile phase is comprised of an inert gas (e.g. Helium, Nitrogen, or Hydrogen) and an immobilised liquid is used as the stationary phase. A GC system is comprised of a gas cylinder holding the carrier gas (mobile phase), various pressure regulators and a flow control valve, an injection system (syringe, septum, and heated injector), a column that is coated with the stationary phase is contained within the column oven, and a detector (Figure 1.15). For carbon based analytes, flame ionisation detectors or MS systems are often employed for detection.^{103,112,129,130}

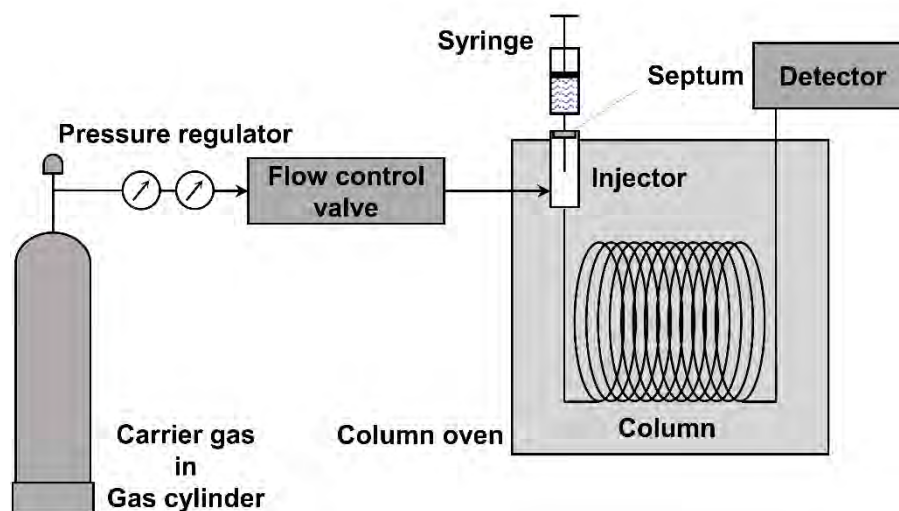


Figure 1.15. Schematic of a GC including a gas cylinder containing the carrier gas, pressure regulators, a flow control valve, an injection system, a column in a column oven, and a detector. After Otto (2014).¹¹²

During analysis, the sample is injected as a narrow band, vaporised, and transported through the column by the carrier gas; the individual components partition between the liquid stationary phase and the gas phase. Separation is achieved based on the analyte's relative vapour pressure and affinities to the stationary phase. Temperature programmes can be used to optimise separation and shorten analysis time. The temperature is increased during the measurement, which results in an increase in the vapour pressure of the analytes so that they elute more quickly. The detector monitors the gas stream as it leaves the column and produces the chromatogram.^{103,112,129,130}

Most current applications use fused-silica columns covered with a protective polyimide jacket to increase the stability of the column and protect it. Typical column inner diameters are 0.15 - 0.5 mm at 15 - 100 m column length. Remaining active sites of the column material are deactivated by high-temperature silylation. The liquid stationary phase is deposited in a thin

film (0.1 – 5 μm) on the inside of the column; such a design is called wall-coated open tubular. All coatings are characterised by high thermal and chemical stability and have a high boiling point / low vapour pressure. The stationary phases are often based on cross-linked polysiloxanes derivatised with appropriate residues. As is the case in LC, the principle of "like solves like" applies, so that -CN, -C=O or -OH residues are used for the separation of polar analytes, while phenyl residues or aliphatic hydrocarbons are used for non-polar targets. In the case of non-polar systems, the separation is based purely on differences in vapour pressure, while in polar systems dipole-dipole interactions between the analyte and the stationary phase also have an effect. In contrast to LC, there is no interaction between the mobile phase and the analyte.^{103,112,129}

1.4.5. Mass spectrometry

Mass spectrometry allows the determination of the mass-to-charge ratio (m/z) of electrically charged particles in the gas phase. The analytes are often transferred from the condensed phase to the gas phase beforehand. Figure 1.16 shows the schematic structure of an MS. Each MS requires an inlet system to transport the analytes into the ion source. Depending on the technique used, the sample inlet and ionisation may be under atmospheric pressure or low vacuum, while the rest of the MS requires high vacuum (10^{-5} – 10^{-11} mbar) to achieve a high mean free path. In the ion source, the analytes are converted into charged species by various procedures.¹¹²

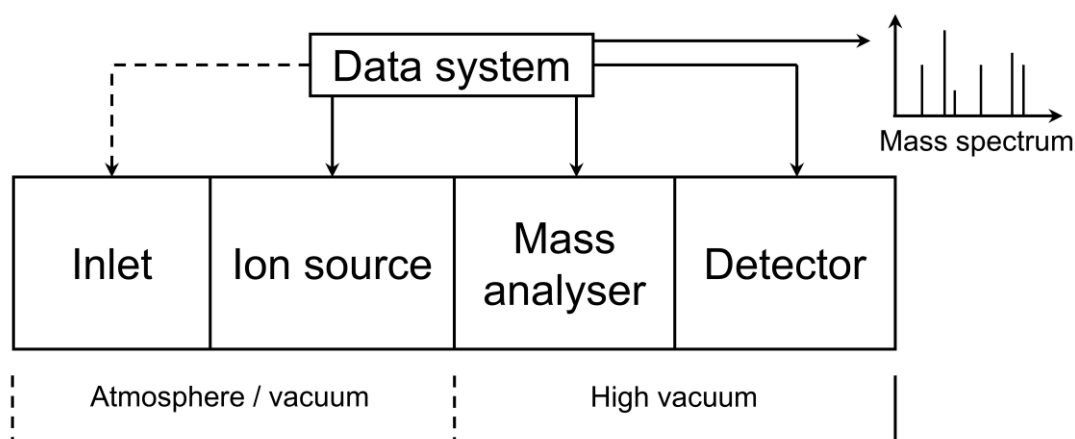


Figure 1.16. Schematic of the set-up of a mass spectrometer. Drawing produced after Otto (2014).¹¹²

The quality of the mass separation is called mass resolution R and is calculated according to Equation 1.5.

$$R = \frac{m}{\Delta m} \quad \text{Equation 1.5}^{112}$$

R : Mass resolution

m : Analysed mass

Δm : Distinguishable mass difference

Here, m describes the mass of an ion and Δm the mass difference, which can still be distinguished from m . High-resolution devices ($R > 50\,000$) can thus be used to calculate sum formulas from the determined m/z ratio. Other important parameters of a mass spectrometer are the analysable mass range and the measuring rate.^{112,131,132}

1.4.5.1. Electrospray ionisation

For electrospray ionisation (ESI), an analyte solution is finely nebulised under the influence of a strong electric field. Ions are released from the droplets of the aerosol, which can then be analysed in the MS. For this purpose, the sample solution is passed through a steel capillary to which a potential of 2-5 kV is applied. Due to the small diameter of the capillary, the resulting electric field is very strong, so that a redox reaction leads to a charge separation and an accumulation of positive or negative charge carriers (depending on the capillary's polarisation) on the surface of the meniscus. As shown in Figure 1.17 on the left, these are attracted by the counter electrode and the so-called Taylor cone is formed. In this, there rules an equilibrium of electric field and surface tension. With increasing distance from the tip of the capillary, the Taylor cone is destabilised and a fine liquid jet results. If the Coulomb repulsion of the surface charges exceeds the surface tension, the Rayleigh limit is reached, and the jet breaks up into individual droplets. Often the sputtering of the solution is supported by a stream of inert gas, e.g. N_2 , concentrically arranged around the capillary.^{103,131,133-136}

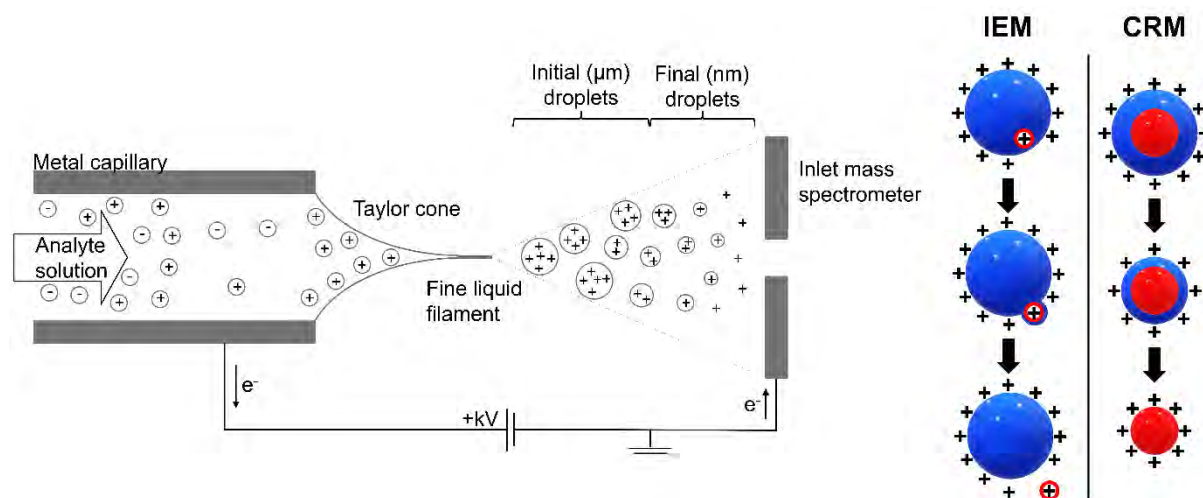


Figure 1.17. Left: Schematic of the processes taking place in an ESI-source. After Hunag et al. (1990), Kebarle and Tang (1993), and Konermann et al. (2013).¹³⁴⁻¹³⁶ Right: Schematic of the ion formation following the Ion Emission Model (IEM) and the Charge Residue Model (CRM). Drawing produced after Konermann et al. (2013).¹³⁶

Solvent evaporates from these relatively large droplets until the Rayleigh limit is reached again and microdroplets are formed in a Coulomb explosion that carry less than 2 % of the mass but about 15-25 % of the charge of the mother droplet. This process is repeated several times until the radii of the droplets are in the nano meter range. The formation of free ions from these highly charged nanodroplets can follow two different models, which are shown schematically in Figure 1.17 on the right. It is assumed that ions are formed from small, surface-active molecules according to the ion emission model (IEM).¹³⁷ Here, the emission of

individual ions from droplets with radii of about 8 nm competes with the further Rayleigh decay of the droplet. For large, spherical molecules, ion formation is observed according to the charge residue model (CRM)¹³⁸, in which the solvent evaporates completely from a droplet and only the ion remains in the gas phase. The ions are subsequently passed through an interface into the MS. This is a fine hole in the counter electrode or a heated transfer capillary. In the second case, the set-up is called heated ESI (HESI). Since the processes described so far take place under atmospheric pressure, the pressure is gradually reduced after the interface has passed through to achieve the high vacuum required for analysis.^{133,134,136-139}

ESI is a soft ionisation technique, which means that very little fragmentation of the ions occurs during ionisation. If the analyte is not already present as an ion in the solution, the actual ionisation is usually based on protonation or deprotonation of the ions in solution or in the gas phase; the quasimolecule ion with $[M+H]^+$ or $[M-H]^-$ (M: molecule) is observed in the mass spectrum. Because of this mechanism, analysis by ESI is limited to more polar molecules or those with high gas-phase acidity or basicity. Another characteristic of ESI is the occurrence of ion clusters (e.g. $[M+Na]^+$) and multiply charged ions. This makes molecules with very high absolute masses, such as proteins, accessible to mass spectrometers with a limited mass range. The greatest advantage of ESI is the very easy coupling to liquid chromatography, so that an MS can be used as a detector. Such a coupling is useful because analytes with the same mass cannot be distinguished in MS without prior chromatographic separation. Moreover, since different molecules exhibit different ionisation efficiencies by ESI, prior separation allows analytes with a low response to still be detected and not be suppressed by more readily ionised substances.^{133,136,139}

1.4.5.2. Electron ionisation

Electron ionisation (EI) describes the process of bombarding an analyte in the gas-phase with an electron beam of defined energy. This results in a transfer of energy, causing the analyte to ionise.¹⁴⁰

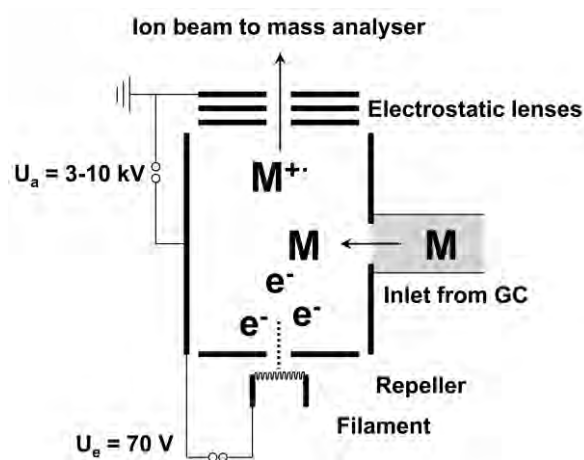


Figure 1.18. Schematic of the processes taking place in an EI-source. Drawing produced after Gross (2019).¹³¹

The electron source is comprised of a heated W- or Re-filament (Figure 1.18); the emitted electron beam is accelerated into the ion volume with voltage U_e , usually 70 V. To assure a high mean free path, the ion volume is kept at a vacuum of $\leq 10^{-6}$ mbar. The electrons collide with gaseous analyte molecules (M) that enter the ion volume through a sample inlet that is perpendicular to the ion beam. As the sample needs to be gaseous, a coupling of EI with GC suggests itself.^{103,112,131,140,141}

Upon impact of the electrons, the analytes are ionised resulting in the formation of molecule radical ions ($M^{\cdot+}$). Depending on the electron's energy, the molecule radical ion still retains excess energy from the collision, resulting in diverse fragmentation. The ions are then accelerated through a high voltage potential (U_a ; 3-10 kV), focused into an ion beam with electrostatic lenses, and transported to the mass analyser.^{103,112,131,140,141}

EI is considered a hard ionisation technique, meaning that it often generates multiple fragment ions for one analyte. Therefore, EI spectra often contain detailed structural information and can assist with the identification of unknown compounds. The standardised electron energy of 70 eV results in fingerprint-like spectra for each sample and analyte molecule that can often provide unambiguous target identification by library comparison.^{112,140,141}

1.4.5.3. Orbitrap mass analyser

The Orbitrap mass analyser has been commercially available since 2005 and the latest models can achieve resolutions of up to 1 000 000; thus, the Orbitrap is among the high-resolution mass spectrometers. Figure 1.19 schematically shows the setup of a Q-Exactive Hybrid Quadrupole Orbitrap mass spectrometer, which was used in this work.

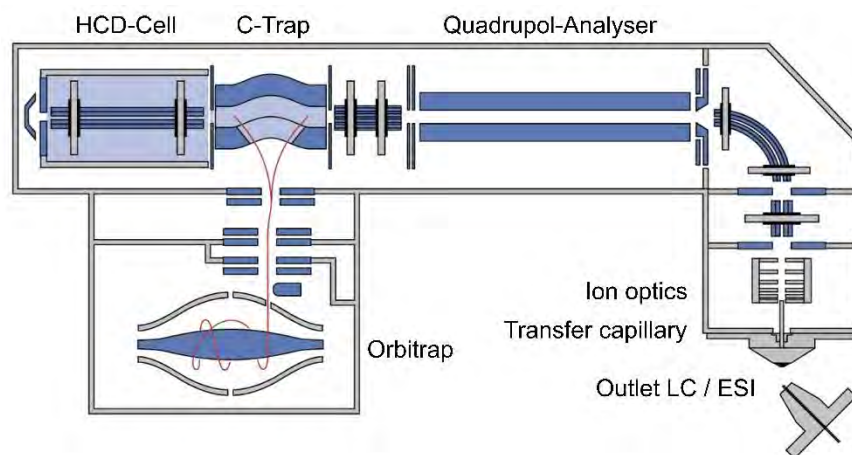


Figure 1.19. Schematic of a Q-Exactive Hybrid Quadrupole-Orbitrap mass spectrometer. Adapted from Thermo Fisher Scientific (2019).¹⁴²

The ions produced in the ESI source pass through a heated transfer capillary to the ion optics, which focus the ion beam before it enters a quadrupole analyser. A quadrupole analyser consists of four hyperbolic cross-sectioned rods positioned on the corners of a square, with equal poles facing each other. By superimposing a DC voltage on an AC voltage in the radio frequency (RF) range, only ions with a certain m/z ratio can pass through the quadrupole

without colliding with the rods. Therefore, quadrupole analysers are often called mass filters. By varying the frequency of the AC voltage, all m/z ratios can be scanned in succession.^{103,131,143}

After selecting the desired ions in the quadrupole, they are stored in a C-trap, a c-shaped ion trap. This temporary storage is necessary because quadrupole analysers work continuously, but the orbitrap analyser is pulsed. The principle of an ion trap is the same as that of a quadrupole, but the high-frequency field is three-dimensional so that the ions can be stored on stable orbits. The C-trap is filled with low pressure nitrogen to moderate the kinetic energy of the analytes through collisions. From the C-trap, the ions can either be directed into an HCD (higher-energy collisional dissociation) cell or they are injected into the orbitrap. In the HCD cell, collisions of the ions with inert gas molecules (N_2) result in bond cleavage due to the conversion of kinetic energy into internal energy, leading to fragmentation of the analytes. The fragments then re-enter the C-trap, from which they are injected into the Orbitrap analyser.^{103,144,145}

The Orbitrap analyser consists of a spindle-shaped inner electrode and a two-part, barrel-shaped outer electrode, between which a DC voltage is applied. An electric field results, the field lines of which are shown schematically in Figure 1.20. The injection of the ion packets from the C-trap takes place perpendicular to the electric field. The injected ions start to migrate back and forth between the right and left side of the electrode without further excitation. As illustrated in Figure 1.19, stable trajectories involve both a rotation around the inner electrode and a migration along the z-axis. This axial oscillation is independent of the initial properties of the ions, such as their kinetic energy, so that the axial frequency is used to determine the m/z ratios.^{103,146,147}

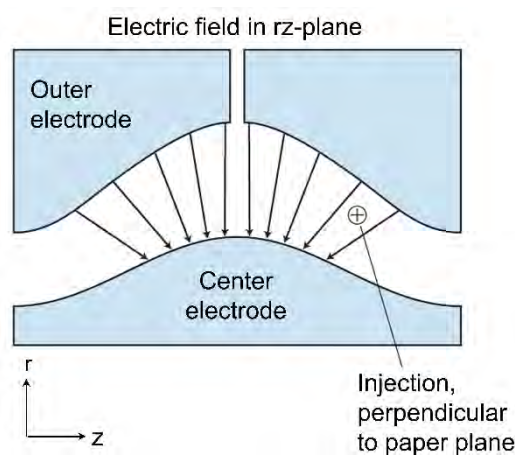


Figure 1.20. Schematic of the electric field in the rz -plane of an Orbitrap mass analyser. Adapted from Harris et al. (2014).¹⁰³

The oscillation of the ions generates a proportional mirror charge in the outer electrode, which results in an image current. This time-dependent signal is transformed into a frequency spectrum by means of a Fourier transformation, from which the mass spectrum is generated. The relationship between frequency ν and the m/z ratio is described by Equation 1.6.^{103,146,147}

$$v \sim \frac{1}{\sqrt{m/z}}$$

*Equation 1.6*¹⁰³

v : Axial frequency

m/z : Mass-to-charge-ratio

2. Development of a method for anodic degradation of lignin for the analysis of paleo-vegetation proxies in speleothems

This chapter has been published in *ChemElectroChem*:¹⁴⁸

ChemElectroChem

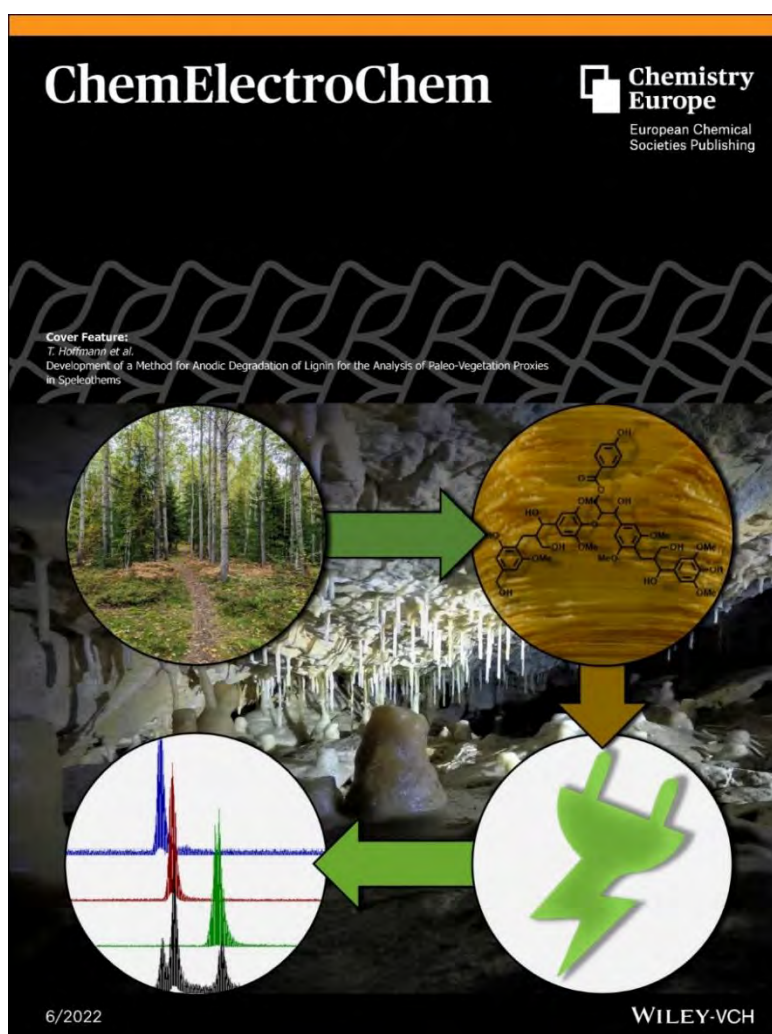
Articles
doi.org/10.1002/celec.202101312

**Chemistry
Europe**
European Chemical
Societies Publishing

www.chemelectrochem.org

Development of a Method for Anodic Degradation of Lignin for the Analysis of Paleo-Vegetation Proxies in Speleothems

Julia Homann,^[a] Michael Zirbes,^[a] Meiko Arndt-Engelbart,^[a] Denis Scholz,^[b] Siegfried R. Waldvogel,^[a] and Thorsten Hoffmann*^[a]



2.1. Abstract

Here we present an electrochemical method for the anodic oxidation and subsequent degradation of lignin in speleothems to utilise the resulting lignin oxidation products (LOPs) as paleo-vegetation markers. LOPs were analysed using an ultra-high performance liquid chromatography (UHPLC) system coupled to a high-resolution mass spectrometer (HRMS). The method presented here achieved comparable or even higher LOP concentrations than established CuO and CuSO₄ oxidation methods. The method represents a new tool for the analysis and reconstruction of paleo-vegetation and has the potential to be applied to other climate archives.

2.2. Introduction

Speleothems are well established climate archives because they can grow continuously over thousands of years and can be dated with unprecedented precision using the ²³⁰Th/U method.^{3,4,16} Due to the stable conditions in caves, speleothems undergo only minor physical and chemical changes over time.^{5,6} Traditionally, speleothem research mainly used inorganic climate proxies, such as $\delta^{13}\text{C}$ or $\delta^{18}\text{O}$ values or trace elements, while organic proxies played only a minor role.^{21,26} However, with the improvement of techniques for organic trace analysis, more and more organic compounds have been investigated as potential proxies.³⁸

One of them is lignin, a biopolymer found exclusively in vascular plants. The main constituents are sinapyl-, coniferyl-, and coumaryl alcohol units linked by stable ether and C-C bonds.⁴⁹ To analyse the lignin, it is broken down into monomeric units by oxidative digestion. The resulting lignin oxidation products (LOPs) can be divided into three groups according to their phenolic: the guajacyl moiety (V), the syringyl group (S) and the cinnamyl group (C).⁵² The composition of the polymer with respect to these groups allows conclusions to be drawn about the different types of vegetation from which the lignin originates. According to a study by Hedges and Mann,⁵⁴ it is possible to distinguish between angiosperms (flowering plants, enclosed seed-bearing plants) and gymnosperms ("naked seed"-bearing plants) as well as woody and non-woody lignin by comparing the two parameters C/V and S/V. Here, C is the sum of all lignin oxidation products in the C-group, etc. This is possible because only non-woody plant parts produce substantial amounts of cinnamyl units and only angiosperms produce substantial amounts of syringyl units. Guajacyl moieties are ubiquitous. The origin of lignin and the pathway of the polymer into the speleothem is shown in Figure 2.1 Hedges and Mann visualised their results with scatter plots and define limits for each result (Figure 2.4). However, their data were limited to a small number of samples and are further constrained by the method used for digestion and analysis. Therefore, their results may rather be considered as a guideline and only applied to the variations between individual samples in a consecutive set of samples. In addition, the parameter $\sum 8$, representing the sum of the concentration of all 8 analysed LOPs, is used as a general measure for the amount of lignin in the sample.

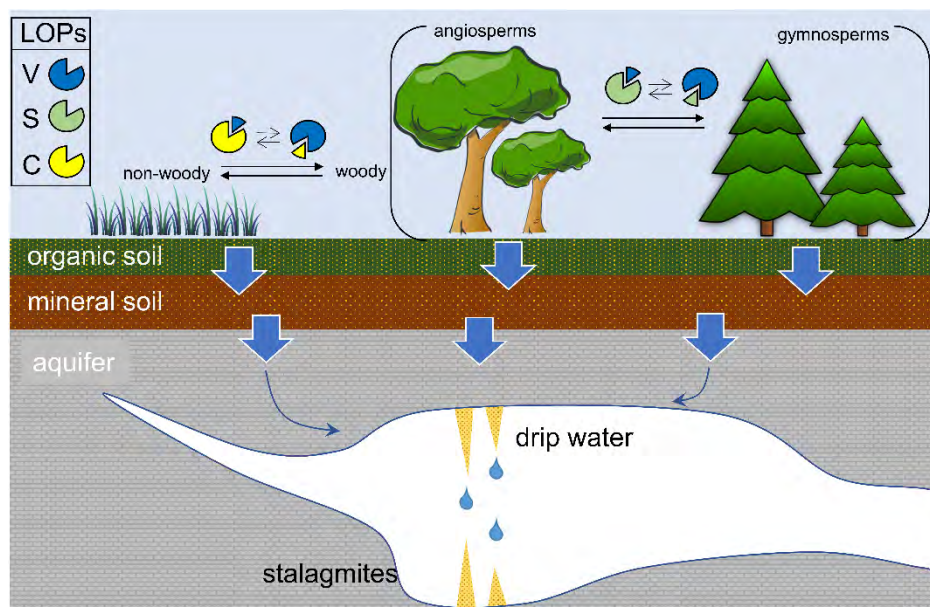


Figure 2.1. Schematic representation of the origin of lignin and the pathway of the polymer into the speleothem.

Traditionally, CuO ,^{55,149} nitrobenzene,¹⁵⁰ or tetramethyl-ammonium hydroxide (TMAH)¹⁵¹ were used for the oxidative/ thermal degradation. However, large sample volumes, impurities of the chemicals used, or a variety of possible reaction products make it difficult to adapt to analytical purposes.^{53,152} More recently, Yan and Kaiser introduced a method based on alkaline CuSO_4 oxidation, which is particularly suitable for small sample volumes.⁵⁶

However, all established methods result in toxic waste, are costly and time consuming, and can cause relatively high blank values. In addition, the composition of the reaction mixture and thus the resulting quantity of LOPs depends on several factors, such as the organic carbon content and the presence of oxygen. A new approach is highly desired to simplify the procedure and obtain more reproducible results.

Electrosynthesis seems to be a promising alternative for the conversion of lignocellulose biomass.¹⁵³⁻¹⁵⁵ Since only electricity serves as oxidizing and/or reducing agent, the generation of reagent waste is avoided, and the atomic efficiency increased. In addition, electric current is an inherently safe, renewable, and cost-efficient reagent.¹⁵⁴⁻¹⁵⁷ Thus, it meets the criteria of "green chemistry".¹⁵⁸⁻¹⁶⁰ In recent decades, electrochemical degradation of lignin has been investigated to produce low molecular fine chemicals in a sustainable manner.¹⁵³ Several applications for the electrochemical conversion of lignosulfonate,¹⁶¹⁻¹⁶⁴ Kraft lignin,¹⁶⁵⁻¹⁸⁰ organosolv lignin,¹⁸¹⁻¹⁸³ and native(-like) lignin¹⁸⁴⁻¹⁹⁰ have been published here. High temperature electrolysis ($>100\text{ }^\circ\text{C}$) has been established for efficient electrochemical depolymerization of technical lignins, such as lignosulfonate, Kraft and organosolv lignin, into valuable aromatic fine chemicals (mainly vanillin).^{162,180,183} In general, nickel-based anodes were commonly used for the electrochemical production of monoaromatics from lignin.^{162,170-176,180,183} For example, the Waldvogel laboratory reported the anodic degradation of lignin to produce vanillin using Ni electrodes in a simple undivided set-up.^{170-172,180,183} Detailed mechanistic studies of the electrocatalytic anodic conversion of lignin utilising nickel anodes

were provided by Utey *et al.* Here, the formation of low molecular weight products, such as vanillin, was associated with the oxidation of phenolic structures in the lignin *via* oxygenated Ni(III) species at the anode surface.^{162,191}

In this study, we developed a new electrochemical degradation method using nickel anodes for the analysis of lignin in speleothems and present the results in comparison with the established CuO and CuSO₄ degradation methods.

2.3. Results and Discussion

Two different temperatures and three different amounts of electric charge applied were tested. The results are summarised in Table 2.1 and illustrated in Figure 2.3 A. All conditions tested lead to a noticeable formation of LOPs with $\Sigma 8$ values ranging from 425.3 ng · g⁻¹ to 753.7 ng · g⁻¹. The $\Sigma 8$ stays at the same level with the increase of the applied charge from 0.1 C to 0.15 C per g speleothem. When the amount of charge is further increased to 0.2 C per g speleothem, the $\Sigma 8$ value drops significantly at 30 °C, while it remains at the same level at 50 °C.

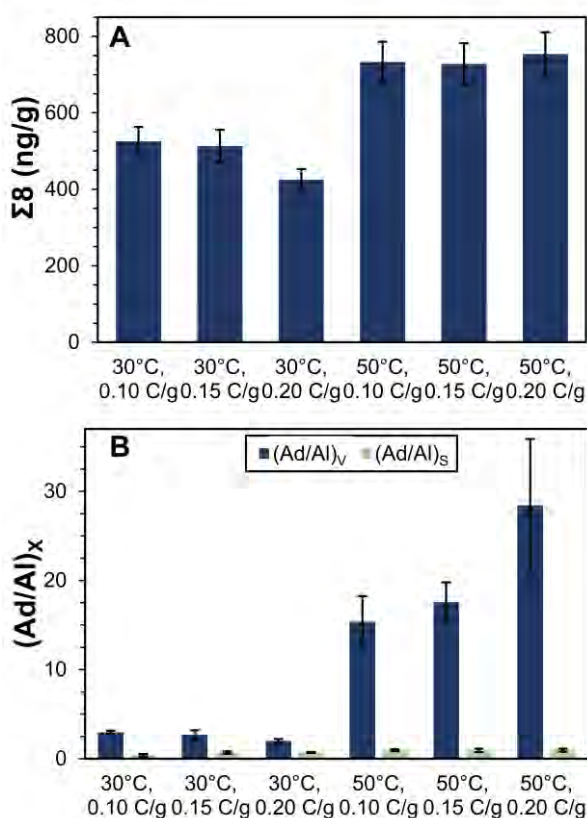


Figure 2.2. A: Comparison of LOP concentration obtained for different anodic oxidation conditions. B: Comparison of the acid-to-aldehyde ratios (Ad/Al) for the V- and S-group obtained for different anodic oxidation conditions.

The decreasing concentration can be explained by over-oxidation of the polymer leading to the formation of units, which were not investigated in this study. This implies that if such

highly oxidised compounds are a desired product, the application of higher charge amounts might be advisable. At 50 °C, the $\Sigma 8$ value is significantly higher, even at $0.1 \text{ C} \cdot \text{g}^{-1}$. This is due to the fact that as the electrolysis temperature increases, the (oxidative) degradation of the polymer is also enhanced.¹⁸⁰ Therefore, a larger amount of low molecular weight compounds is generated. However, these monoaromatic compounds are often more prone to anodic conversion, resulting in highly oxidized species. This is evident from our data, as the main contribution to the $\Sigma 8$ value comes from the V-group, more precisely from vanillic acid (Figure 2.3 B). Moreover, an increasing ratio between vanillic acid and vanillin ((Ad/Al)_v) is observed, applying higher amounts of charge, indicating the over-oxidation of the polymer and/or LOPs. Although the $\Sigma 8$ values for oxidation at 50 °C are all significantly increased compared to the reaction at 30 °C, these conditions are considered unsuitable for analytical purposes because monomeric units of the V-group appear to be formed preferentially over all other LOPs. This would distort the S/V and C/V ratios, making the analytical technique unsuitable to provide reliable results. This behaviour be due to the partial degradation and over-oxidation of the polymer and LOPs at the higher electrolysis temperature, where the corresponding vanillyl units (V) are partially more stable to over-oxidation and/or more easily anodically depolymerised. Therefore, the electrolysis temperature of 30 °C and an applied charge amount of $0.15 \text{ C} \cdot \text{g}^{-1}$ were chosen for all further experiments and comparisons since these conditions gave the highest $\Sigma 8$ value at relatively low (Ad/Al) values.

Table 2.1. Concentrations of the V-, S-, and C-group LOPs, the sum of all eight LOPs ($\Sigma 8$), and the ratios C/V and S/V of the speleothem sample determined using different oxidation methods.

Sample	$\Sigma S [\mu\text{g} \cdot \text{g}^{-1}]$	$\Sigma V [\mu\text{g} \cdot \text{g}^{-1}]$	$\Sigma C [\mu\text{g} \cdot \text{g}^{-1}]$	$\Sigma 8 [\mu\text{g} \cdot \text{g}^{-1}]$	C/V	S/V
30°C, 0.10 C/g	194.8 ± 9.6	242.7 ± 21.7	88.4 ± 6.0	526.0 ± 37.3	0.45 ± 0.05	1.25 ± 0.17
30°C, 0.15 C/g	334.6 ± 30.2	121.4 ± 10.6	56.8 ± 2.1	512.8 ± 42.9	0.17 ± 0.02	0.36 ± 0.06
30°C, 0.20 C/g	154.6 ± 11.4	203.4 ± 14.9	67.3 ± 1.2	425.3 ± 27.6	0.44 ± 0.04	1.32 ± 0.19
50°C, 0.10 C/g	407.1 ± 28.0	241.8 ± 23.0	83.8 ± 2.0	732.8 ± 53.0	0.21 ± 0.02	0.59 ± 0.10
50°C, 0.15 C/g	385.9 ± 34.8	253.2 ± 18.0	88.7 ± 1.8	727.7 ± 54.6	0.23 ± 0.03	0.66 ± 0.11
50°C, 0.20 C/g	475.4 ± 33.8	191.5 ± 20.2	86.8 ± 3.0	753.7 ± 57.1	0.18 ± 0.02	0.40 ± 0.07
Set 1	69.6 ± 10.1	86.0 ± 9.0	13.3 ± 0.6	168.9 ± 19.7	0.19 ± 0.04	1.24 ± 0.31
Set 2	63.2 ± 2.7	12.0 ± 0.9	4.5 ± 0.2	83.6 ± 4.7	0.07 ± 0.01	0.20 ± 0.04
CuO	135.5 ± 1.7	195.1 ± 5.4	21.9 ± 0.9	349.5 ± 8.0	0.17 ± 0.01	1.47 ± 0.06
CuSO ₄	341.7 ± 24.1	79.7 ± 28.9	46.0 ± 0.5	467.4 ± 53.5	0.13 ± 0.01	0.23 ± 0.10

To demonstrate the effectiveness of the anodic oxidation, a set of samples was prepared that was only thermally degraded (Set 1). In addition, a set of samples was prepared that was subjected to anodic conversion only, but not to subsequent thermal degradation (Set 2). The results are shown in Table 2.1. The $\Sigma 8$ value for Set 1 is at $168.9 \text{ ng} \cdot \text{g}^{-1}$ and the $\Sigma 8$ value for Set 2 is at $83.6 \text{ ng} \cdot \text{g}^{-1}$. Thus, both values are significantly lower than the $\Sigma 8$ value of the anodic oxidation and subsequent thermal degradation of $512.8 \text{ ng} \cdot \text{g}^{-1}$. The results illustrate that

both steps are necessary for the successful formation of LOPs from lignin. The anodic oxidation converts the strong ether and C-C bonds of lignin into weaker oxidised bonds, which undergo cleavage by the subsequent thermal degradation.¹⁹²

To compare the anodic oxidation method with established methods, both the CuSO_4 and CuO oxidation method were performed. The results are shown in Table 2.1 and Figure 2.4. The $\Sigma 8$ values obtained (CuSO_4 : $467.4 \text{ ng} \cdot \text{g}^{-1}$; CuO : $349.5 \text{ ng} \cdot \text{g}^{-1}$) are comparable to those obtained by the anodic oxidation method ($512.8 \text{ ng} \cdot \text{g}^{-1}$). The S/V and C/V ratios are also similar, and all lie approximately in the same region of the scatter plot (see Figure 2.4). Minor differences in the results are to be expected and result from the different mechanisms involved in the formation of the LOPs and the general large variability in the composition of natural lignin. Overall, these results indicate that the newly developed anodic oxidation method provides robust LOP values that allow for sound interpretation of the S/V and C/V ratios.

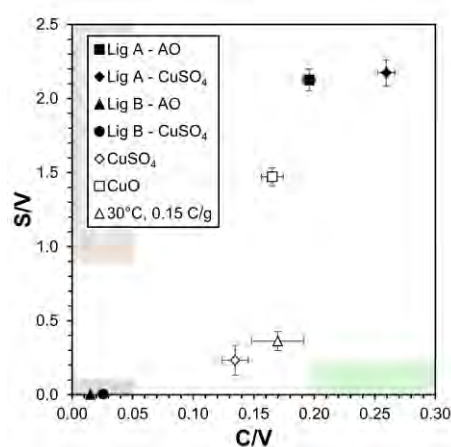


Figure 2.3. S/V versus C/V values of the speleothem sample, and lignin samples determined using anodic oxidation (AO), CuSO_4 oxidation, or CuO mediated oxidation.

The method was applied to two different types of commercial lignin powder to verify that the C/V and S/V ratios obtained agreed with the literature, and again to verify that the results were comparable to those obtained by the CuSO_4 oxidation method. The results are listed in Table 2.2 and illustrated in Figure 2.4. Application of the anodic oxidation method to both wheat straw and mixed woods lignin (Lignin A) and conifer wood lignin (Lignin B) results in $\Sigma 8$ values of about $1\,600 \mu\text{g} \cdot \text{g}^{-1}$, corresponding to a conversion factor of 0.16% (w/w). The $\Sigma 8$ values resulting from the CuSO_4 oxidation method are only $1\,176 \mu\text{g} \cdot \text{g}^{-1}$ for Lignin A and $588 \mu\text{g} \cdot \text{g}^{-1}$ for Lignin B, respectively. These values correspond to conversion factors of about 0.12% and 0.06% (w/w). This shows that the anodic oxidation method can degrade various lignins more effectively than the established CuSO_4 oxidation method. Again, the C/V and S/V ratios of the two different methods are very similar, and the ratios for each of the two different lignin species fall within the regions of the scatter plot expected according to the regions defined by Hedges and Mann.⁵⁴ This last test also confirmed the suitability of anodic oxidation for the analytical degradation of lignin.

Table 2.2. Concentrations of the V-, S-, and C-group LOPs, the sum of all eight LOPs ($\Sigma 8$), and the ratios C/V and S/V of the lignin samples determined using different anodic oxidation (AO) or CuSO₄ oxidation.

Sample		$\Sigma S [\mu\text{g} \cdot \text{g}^{-1}]$	$\Sigma V [\mu\text{g} \cdot \text{g}^{-1}]$	$\Sigma C [\mu\text{g} \cdot \text{g}^{-1}]$	$\Sigma 8 [\mu\text{g} \cdot \text{g}^{-1}]$	C/V	S/V
Lignin A	AO	492.8 ± 8.9	1047.3 ± 17.4	96.4 ± 0.9	1636.5 ± 27.2	0.20 ± 0.01	2.13 ± 0.07
	CuSO ₄	342.4 ± 5.6	744.5 ± 17.6	88.8 ± 1.0	1175.7 ± 24.2	0.26 ± 0.01	2.17 ± 0.09
Lignin B	AO	1573.9 ± 22.6	4.4 ± 0.2	23.7 ± 0.1	1602.0 ± 22.8	0.02 ± 0.00	0.00 ± 0.00
	CuSO ₄	570.6 ± 6.8	2.8 ± 0.3	14.6 ± 0.2	588.0 ± 7.2	0.03 ± 0.00	0.00 ± 0.00

2.4. Conclusion

We developed an electrochemical method for the anodic oxidation and subsequent degradation of lignin in speleothems to analyse the resulting LOPs as paleo-vegetation markers. The new method achieved comparable or even higher LOP concentrations than the established CuO and CuSO₄ oxidation methods. The method also speeds up sample preparation and reduces the risk of contamination input from the chemicals used. In addition, the use of electricity as the terminal oxidant avoids the use of stoichiometric amounts of heavy metals. Furthermore, the oxidation step can be easily adopted to the particular sample matrix, e.g., organic carbon content, and thus could be useful for the analysis of other environmental samples such as soils or sediments. However, the method has so far only been applied to a homogenised speleothem sample and should therefore be further tested with a variety of different speleothem samples to confirm the presented results.

2.5. Experimental Section

Analytical standards of acetosyringone (97 %), acetovanillone (≥ 98 %), para-coumaric acid (≥ 98 %), ethylvanillin (99 %), ferulic acid (99 %), syringaldehyde (98 %), and syringic acid (> 95 %), as well as L-ascorbic acid (SigmaUltra), copper(II) oxide (> 99 %) and ammonium iron(II) sulfate (99 %) were purchased from Sigma-Aldrich. An analytical standard of vanillin (99 %) was obtained from Acros Organics, and an analytical standard of vanillic acid (98 %) was obtained from Alfa Aesar. Sodium hydroxide (pellets, ≥ 99 %), hydrochloric acid (HCl, suprapure, 30%), and water (LC-MS-Grade) were purchased from Merck KGaA. Mixed lignin from wheat straw and various kinds of wood (Lignin A) was purchased from Bonding Chemical. Lignin from mainly coniferous wood (Lignin B) was obtained from BASF SE. Ammonium hydroxide solution (NH₃, analytical grade, 25%) was obtained from Honeywell Fluka. Solid-phase extraction columns (Oasis HLB, 6 mL tubes, 200 mg packing material, Oasis HLB, 3 mL tubes, 60 mg packing material, and Oasis HLB, 1 mL tubes, 30 mg packing material) were purchased from Waters. Ultrapure solvents (LC/MS grade) acetonitrile (ACN) and methanol (MeOH) were obtained from VWR and Carl Roth, respectively. Ultrapure water with 18.2 M Ω resistance was produced using a Milli-Q water system from Merck Millipore (Darmstadt, Germany).

For all experiments, aliquots of powder standard prepared from a speleothem from Ifri Inouqben cave, northern Morocco, were used. The age of this stalagmite is beyond the limit of the $^{230}\text{Th}/\text{U}$ -dating method. Therefore, it is not suited for paleoclimate reconstruction, but is ideal as a standard.¹⁹³ The speleothem was ground coarsely and then homogenised to create a standard material with uniform analyte distribution.

Aliquots of 3 g of the standardised speleothem sample were dissolved in 3 mL HCl (30%) per g speleothem and then diluted 1:1 with ultrapure water. To ensure repeatability, every experiment was conducted fourfold and one blank sample was treated the same way.

The 200 mg HLB cartridges were preconditioned with 6 mL each of MeOH and ultrapure water, acidified to pH 1-2 with HCl (30%). The speleothem solution was filtered through paper filters (Whatman, Grade 40, 8 μm pore size) to prevent undissolved materials from clogging the cartridges and was loaded onto the cartridges using sample reservoirs. The cartridges were washed twice with 6 mL of acidified ultrapure water and then dried by drawing air through the cartridges with a vacuum pump. The lignin was eluted with 10 portions of 500 μL MeOH. The solvent was subsequently evaporated under a gentle stream of nitrogen at 30 $^{\circ}\text{C}$.

The residue was dissolved in 2.5 mL NaOH ($1 \text{ mol} \cdot \text{mL}^{-1}$) by sonification for 10 min at 45 $^{\circ}\text{C}$. The solution was transferred into undivided reaction cells with a capacity of 10 mL made from PTFE (see Figure 2.2). The procedure was repeated, and the sample solutions were combined. Nickel anodes with an active surface area of 1.5 cm^2 were used. A magnetic stirrer ensured homogeneous mixing. Electrolysis was performed at either 30 $^{\circ}\text{C}$ or 50 $^{\circ}\text{C}$ in galvanostatic mode with a current of 17 mA, a current density of 11.3 $\text{mA} \cdot \text{cm}^{-2}$, and a terminal voltage of 1.7-1.8 V. The applied electric charge was varied between 0.10 C, 0.15 C, and 0.20 C per g speleothem.

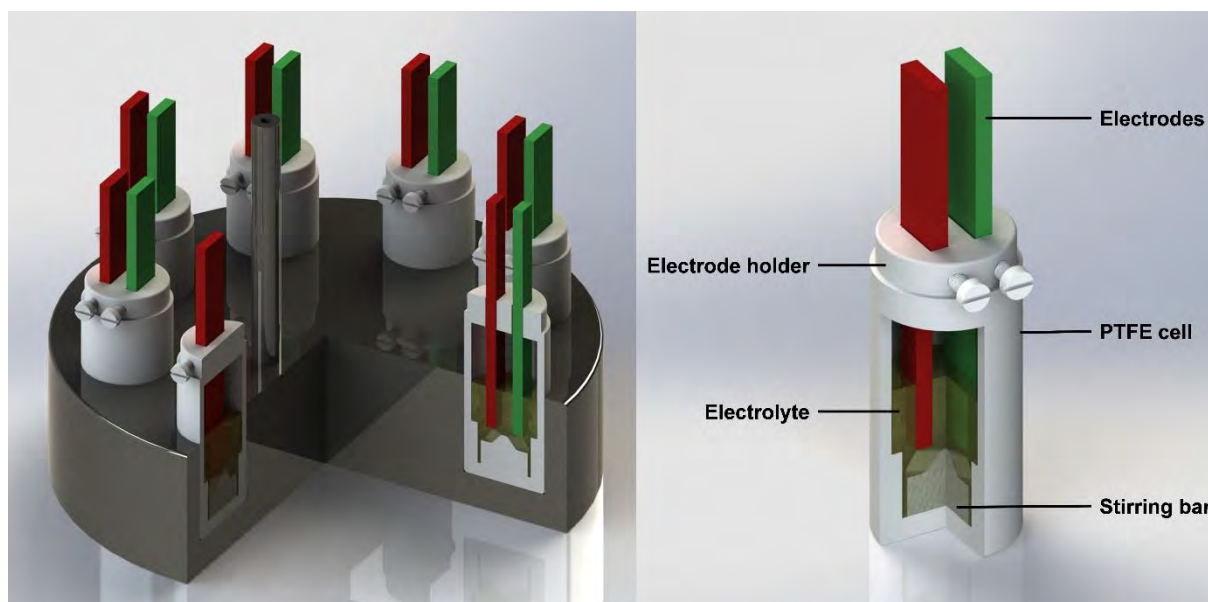


Figure 2.4. Schematic view of the reaction cells.¹⁹⁴

For experiments with pure lignin, about 50 mg of lignin powder was weighed into the reaction cells and dissolved in 5 mL NaOH ($1 \text{ mol} \cdot \text{mL}^{-1}$). Electrolysis was performed at 30 °C in galvanostatic mode with a current of 17 mA, a current density of $11.3 \text{ mA} \cdot \text{cm}^{-2}$, and a terminal voltage of 1.7-1.8 V. The applied charge was set to 30.6 C per g lignin powder.

After electrolysis, the solution was transferred into microwave digestion vessels with a capacity of 30 mL made of PTFE. The vessels were heated to 155 °C in 5 min and held at that temperature for 90 min using a 5890A Gas Chromatograph (Hewlett Packard, USA). Immediately after opening the vessels, 10 μL of a $1 \mu\text{g} \cdot \text{mL}^{-1}$ standard solution of ethyl vanillin in ACN was added as an internal standard, and the oxidised sample solution was acidified to pH 1-2 with HCl (30%).

The CuSO_4 oxidation procedure was developed based on the method described by Yan and Kaiser (2018).⁵⁶ The residue was dissolved in 200 μL MeOH and sonicated at 45 °C for 10 min. The solution was transferred to a PTFE microwave digestion vessel with a capacity of 500 μL . The procedure was repeated with 100 μL MeOH and the combined solutions were evaporated to dryness under a gentle stream of nitrogen at 30 °C. The residue was dissolved in 200 μL NaOH ($1 \text{ mol} \cdot \text{mL}^{-1}$) by sonification for 10 min at 45 °C. To each, 10 μL of each CuSO_4 solution ($10 \text{ mmol} \cdot \text{L}^{-1}$ in H_2O) and a solution of L-ascorbic acid ($0.2 \text{ mol} \cdot \text{L}^{-1}$ in H_2O) were added. The vessels were each purged with nitrogen for 20 s each and quickly sealed to ensure inert gas atmosphere. The digestion vessels were packed 5 at a time into a larger Teflon vessel and covered with 7 mL of NaOH ($1 \text{ mol} \cdot \text{mL}^{-1}$) to ensure better heat transfer. These vessels were also purged with nitrogen for 1 min.

For experiments with pure lignin, about 50 mg of lignin powder was weighed into microwave digestion vessels with a capacity of 30 mL made of PTFE. For oxidation, 126 μL of CuSO_4 solution ($10 \text{ mmol} \cdot \text{L}^{-1}$ in H_2O), 315 μL of L-ascorbic acid solution ($0.2 \text{ mol} \cdot \text{L}^{-1}$), and 1060 μL NaOH ($1 \text{ mol} \cdot \text{mL}^{-1}$) were added. The vessels were purged with nitrogen for 1 min and quickly sealed.

The vessels were heated to 155 °C in 5 min using a gas chromatographic oven (5890A Gas Chromatograph, Hewlett Packard, USA) and held at that temperature for 90 min. Immediately after opening the vials, 10 μL of a $1 \mu\text{g} \cdot \text{mL}$ standard solution of ethyl vanillin in acetonitrile was added as an internal standard and the oxidised sample solution was acidified to pH 1-2 with HCl (30%).

The residue was dissolved in 2 mL NaOH ($2 \text{ mol} \cdot \text{mL}^{-1}$) by sonification for 10 min at 45 °C. The solution was added into a 100 mL Teflon microwave reaction vessel. The sample vial was sonicated again with 2 mL of NaOH ($2 \text{ mol} \cdot \text{mL}^{-1}$) and the solutions were combined. The microwave-assisted CuO-mediated oxidation procedure was performed as described by Heidke et al. (2018).⁵³ An Ethos Plus Microwave Labstation (MLS GmbH, Germany) was used with an HPR-1000/10S high-pressure segment rotor, which can hold up to 10 reaction vessels, and an ATC-CE temperature sensor to measure the temperature inside one reaction vessel. Immediately after opening the vessels, 50 μL of a $1 \mu\text{g} \cdot \text{mL}$ standard solution of ethyl vanillin in acetonitrile was added as an internal standard and after clean-up, the oxidised sample solution was acidified to pH 1-2 with HCl (30%).

The 60 mg HLB cartridges were preconditioned with 3 mL each of MeOH and ultrapure water, acidified to pH 1-2 with HCl (30%). The 30 mg HLB cartridges were preconditioned with 1 mL each of MeOH and ultrapure water, which was acidified to pH 1-2 with HCl (30%), twice. The acidified oxidised sample solutions were loaded onto the 60 mg cartridges using sample reservoirs. Only the speleothem samples prepared by the CuSO₄ oxidation method were loaded directly onto the 30 mg cartridges. The cartridges were washed twice with their void volume of 3 mL or 1 mL, respectively, and then dried by sucking air through the cartridges with a vacuum pump. The LOPs were eluted with 8 portions of 125 µL acetonitrile to which 2% NH₃ was added to reach a basic pH of 8-9. The eluate was evaporated under a gentle stream of nitrogen at 30 °C, and the residue was dissolved in 200 µL acetonitrile/H₂O (1:9) by sonification at 45 °C for 10 min.

The analysis of the LOPs was carried out on a Dionex UltiMate 3000 ultrahigh-performance liquid chromatography system (UHPLC) that was coupled to a heated electrospray ionization source (ESI) and a Q Exactive Orbitrap HRMS (all by Thermo Fisher Scientific). To separate the LOPs, a Acquity UPLC CSH Fluoro Phenyl (PFP) column, 100mm x 2.1mm with 1.7 µm particle size (Waters), was used. The injection volume was 5 µL. A H₂O/acetonitrile gradient program was applied with a flow rate of 0.5 mL · min⁻¹. The gradient started with 5% eluent B (consisting of 98% acetonitrile and 2% H₂O) and 95% eluent A (consisting of 98% H₂O, 2% acetonitrile, and 400 µL · L⁻¹ formic acid). Eluent B was increased to 10% within 0.5 min and held for 4.5 min. It was then increased to 15% within 1 min and further increased to 30% in 1 min and to 50% in 0.5 min, respectively. Finally, it was increased to 99% within 0.5 min, held for 1.5 min, and then eluent B was decreased to the initial value of 5%. The ESI source was operated in negative mode so that deprotonated molecular ions [M-H]⁻ were formed. ESI and MS conditions were the same as reported by Heidke et al. (2018).⁵³

2.6. Acknowledgements

Julia Homann acknowledges support by the Max Planck Graduate Center with the Johannes Gutenberg-Universität Mainz (MPGC). Michael Zirbes gratefully acknowledges the financial support by the Federal Ministry of Food and Agriculture (BMEL, Grant 22409717). Support by the Forschungsinitiative Rheinland-Pfalz in frame of SusInnoScience is highly appreciated. We thank Jenny Klose for assistance during preparation of the speleothem sample.

3. Linked fire activity and climate whiplash in California during the early Holocene

This chapter has been published in Nature communications:⁴⁰

Article

<https://doi.org/10.1038/s41467-022-34950-x>

Linked fire activity and climate whiplash in California during the early Holocene

Received: 25 May 2022

Julia Homann¹, Jessica L. Oster²✉, Cameron B. de Wet²,
Sebastian F. M. Breitenbach³ & Thorsten Hoffmann¹

Accepted: 11 November 2022

3.1. Abstract

Recent wildfire activity in semi-arid regions like western North America exceeds the range of historical records. High-resolution paleoclimate archives such as stalagmites could illuminate the link between hydroclimate, vegetation change, and fire activity in pre-anthropogenic climate states beyond the timescale of existing tree-ring records. Here we present an analysis of levoglucosan, a combustion-sensitive anhydrosugar, and lignin oxidation products (LOPs) in a stalagmite, reconstructing fire activity and vegetation composition in the California Coast Range across the 8.2 kyr event. Elevated levoglucosan concentrations suggest increased fire activity while altered LOP compositions indicate a shift toward more woody vegetation during the event. These changes are concurrent with increased hydroclimate volatility as shown by carbon and calcium isotope proxies. Together, these records suggest that climate whiplash (oscillations between extreme wetness and aridity) and fire activity in California, both projected to increase with anthropogenic climate change, were tightly coupled during the early Holocene.

3.2. Introduction

Increasingly, observations suggest that California's hydroclimate is shifting toward shorter rainy seasons driven in particular by a decline in autumn precipitation.^{195,196} The delayed wet season enhances moisture stress on living vegetation and further decreases moisture levels in dormant and dead vegetation, increasing flammability in a critical season when offshore winds intensify across the state.^{196,197} These observations are corroborated by climate models which project further "sharpening" of the winter rainy season with anthropogenic warming^{196,198,199}, and increases in year-to-year precipitation volatility, or "climate whiplash", with extreme wetness following extended droughts.²⁰⁰ These trends can exacerbate fire recurrence by intensifying autumn dryness and promoting the growth of fast-responding grasses and brush during wet winter peaks that provide fuel to subsequent autumn

wildfires.^{201–203} Likewise, extreme rainfall events following fires are also projected to increase in high emissions scenarios, exacerbating threats of debris flows and vegetation loss.²⁰⁴

Speleothems host numerous isotopic and geochemical proxies that are capable of recording changes in precipitation amount, source, and seasonality that can shed light on hydroclimatic variability during key intervals of Earth's past. Stalagmite-based multi-proxy records have documented a highly dynamic hydroclimate in California across the last several thousand years.^{205–209} At White Moon Cave (WMC) in the California Coast Range, published stable carbon isotope ($d^{13}C$), calcium isotope ($d^{44}Ca$), and trace element ratios (P/Ca) in stalagmite WMC1 records suggest an interval of enhanced precipitation volatility occurred between ~8,250 and 8,100 years BP (where present is 1950 CE), during the 8.2 kyr event, a pronounced Holocene cold period first noted in Greenland ice cores.^{13,15} Further, these proxies record a precursor event at 8,300 years BP, potentially associated with an earlier pulse of freshwater from glacial Lake Agassiz²¹⁰ when precipitation exceeded the wet and dry extremes of the last 60 years in coastal California.^{13,15,23} Thus, hydroclimatically-sensitive proxies from fast-growing stalagmites can provide evidence of changes in climate whiplash, but our understanding of how wildfires may be recorded in stalagmites is just beginning to emerge.^{28,30,35} New proxies are necessary to document wildfire activity to investigate the relationship between climate whiplash and wildfire in the past.

We analysed levoglucosan and lignin as indicators of fire activity and vegetation composition in the portion of stalagmite WMC1 that brackets the 8.2 kyr event (from ~8,600 to 6,900 years BP) where previously analysed proxies suggest increased climate whiplash.^{207,209} The anhydrosugar levoglucosan naturally originates only from the combustion of cellulose⁶⁰, where it is emitted into the particle phase and constitutes a fingerprint of biomass burning.^{63,211} While already used in other paleoclimate archives, especially in aerosols^{60,68–70,212}, neither levoglucosan nor its isomers are typically analysed in speleothems. Lignin, a biopolymer found exclusively in vascular plants, consists of sinapyl-, coniferyl-, and coumaryl alcohol units linked by stable ether and C-C bonds.⁴⁹ For analysis, lignin is broken into monomeric units by oxidative digestion. The resulting lignin oxidation products (LOPs) can be divided into three groups according to their phenolic structures: the vanillyl group (V), the syringyl group (S), and the cinnamyl group (C) (Supplementary Fig. 1).⁵² Through comparison of the C/V and S/V ratios, we can determine if the lignin originated from angiosperms or gymnosperms and distinguish woody and non-woody vegetation.⁵⁴

White Moon Cave, located in the Santa Cruz Mountains east of Davenport, CA (N37°00', W122°11') experiences a warm-summer Mediterranean climate. Local climate and geology of the site are fully described in ref. ²⁰⁹. Vegetation directly above WMC consists of mixed evergreen forest composed of coastal Redwood and Douglas Fir with interspersed Coyote Bush and grasses. The site burned in August 2020 during the CZU Lightning Complex Fire which covered 350 km² and began as the Warnella Fire near Davenport, CA.²¹³ Smaller fires frequently occur in the surrounding coast range during most fire seasons.

Here we demonstrate a link between fire activity, vegetation change, and climate whiplash in California during the early Holocene. We also provide an analysis of levoglucosan and LOPs in

modern dripwater and calcite to place constraints on how surface signals of fire and vegetation move through the modern cave system.

3.3. Results

3.3.1. Stalagmite-based fire and vegetation proxies

Speleothem calcite deposited between 8217 ± 23 and 7847 ± 20 years BP shows elevated levoglucosan levels relative to the remaining stalagmite record (Figure 3.1 d; Table S1), with the highest concentrations found between $8,167 \pm 20$ and $8,019 \pm 15$ years BP. This suggests that fire activity in the vicinity of White Moon Cave was elevated during the 8.2 kyr event relative to the rest of this-early to mid-Holocene record (8,500 to 6,900 years BP). Unlike levoglucosan concentrations, we find no clear pattern in the concentration of LOPs across the speleothem record (Figure S2 and Figure S4; Table S1). However, when plotted by their C/V and S/V ratios (Figure 3.2) the speleothem samples fall into three distinct zones suggesting that the vegetation community surrounding the cave changed over time. Most prominently, between 8,300 and 8,200 years BP, we observe a shift from non-woody to woody vegetation. This is followed by a shift back to more non-woody vegetation between 7,800 and 7,700 years BP. The period of more woody vegetation (specifically $8,271 \pm 23$ to $7,793 \pm 25$ years BP) includes the interval of elevated levoglucosan concentrations ($8,217 \pm 23$ to $7,847 \pm 20$ years BP).

The recovery of the $^{13}\text{C}_6$ -levoglucosan spike for all but one stalagmite sample fall within the standard deviation of the average recovery of the whole sample set (Figure S2). This includes the samples with the highest measured levoglucosan concentrations, indicating that there is no divergent recovery rate and that these high values are unlikely to be an analytical artefact. Theoretically, stalagmite levoglucosan concentrations could also reflect changes in subsurface seepage water flow pathways that would route water from different locations on the surface to the stalagmite. Changes in subsurface water routing would also likely bring water into contact with different mineral phases within the host rock, and thus should be recorded by stalagmite strontium isotope ratios ($^{87}\text{Sr}/^{86}\text{Sr}$) which reflect the balance of water interactions with soils and host rocks with different $^{87}\text{Sr}/^{86}\text{Sr}$ fingerprints. Although we do observe host rock and soil phases with different $^{87}\text{Sr}/^{86}\text{Sr}$ values above WMC, we do not find a shift in stalagmite $^{87}\text{Sr}/^{86}\text{Sr}$ during the 8.2 kyr event²⁰⁹ concurrent with the levoglucosan peak. This indicates that a sustained change in seepage water routing very unlikely during this interval. Thus, the observed changes in levoglucosan concentrations and LOP ratios across the WMC1 record most likely reflect shifts in fire activity and vegetation community in the vicinity of the cave across the 8.2 kyr event.

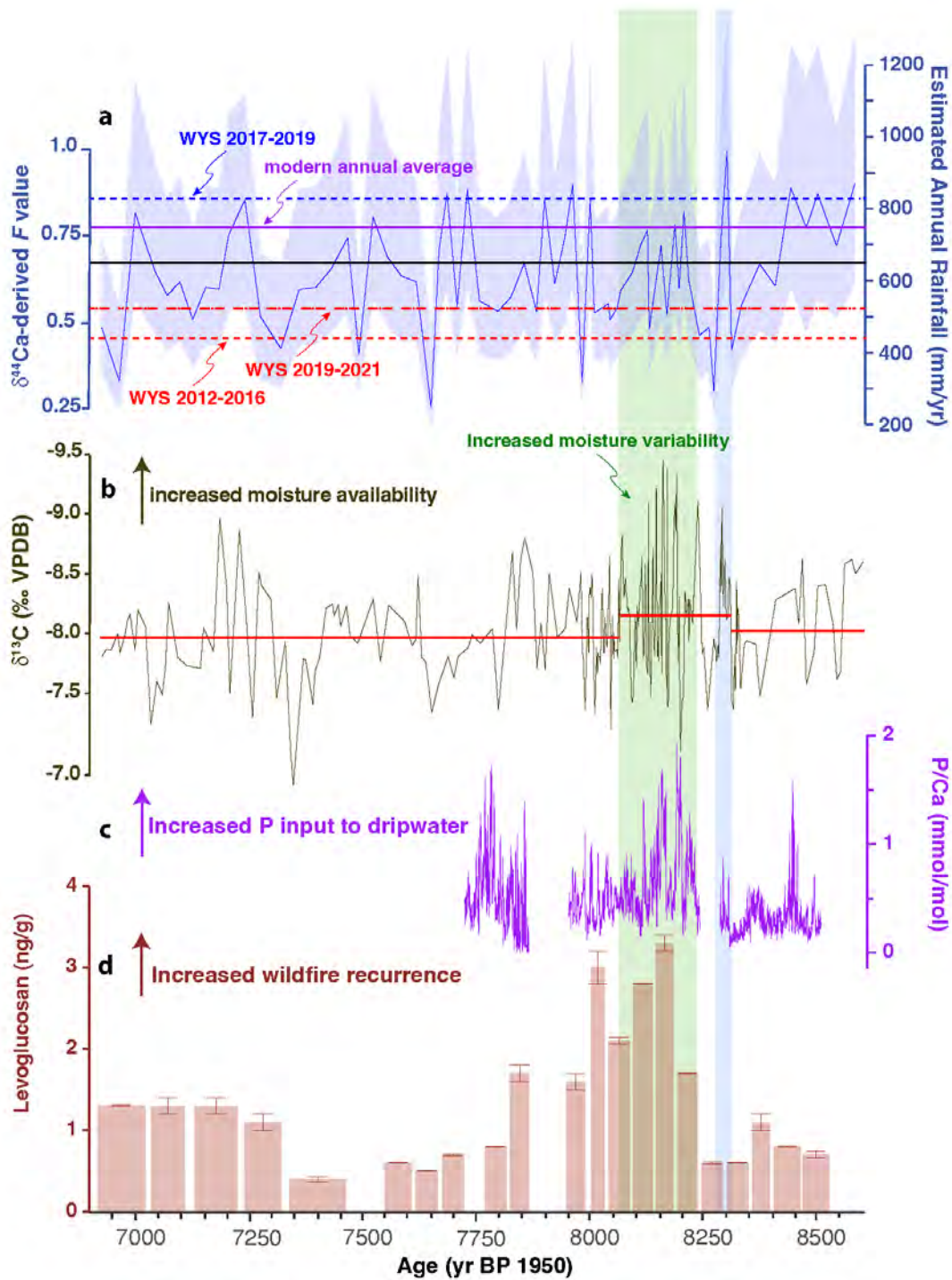


Figure 3.1. Proxy records for White Moon Cave (WMC) stalagmite. a: Fraction of calcite remaining in solution (F) computed from speleothem $\delta^{44}Ca$ using Rayleigh fractionation model²⁰⁹ and translated to estimated rainfall using modern cave system $\delta^{44}Ca$ values and modern rainfall. Horizontal lines provide a comparison to rainfall amounts in the last decade: WYs (water years; 12-month period from October 1st to September 30th designated by the calendar year in which it ends) 2012-2016 (red dashed, 58% modern); WYs 2017-2019 (blue dash-dot, 109% modern); WYs 2019-2021 (red dash-dot, 69% of modern) modern average annual (1950-2021, purple); WMC1 record average computed rainfall (black). b: $\delta^{13}C$ (‰ Vienna Pee Dee Belemnite (VPDB)), red lines highlight mean values of segments between changepoints identified based on mean and variance. c: P/Ca (mmol mol⁻¹). d: Levoglucosan concentrations (ng g⁻¹). Error bars represent the standard deviation of samples measured in duplicate. Vertical shading delineates the duration of the 8.2 kyr event (green) and pre-cursor event (blue).

Increased fire activity coincident with higher proportions of woody vegetation is also evident in Holocene charcoal and pollen records from across the Pacific Northwest²¹⁴, reflecting a potential feedback of increased woody fuel driving fire dynamics or a climate driver that affects both vegetation type and fire activity. The vegetation change noted in WMC1 is broadly consistent with regional changes in vegetation as recorded by pollen from the marine sediment core ODP 1018 off the coast of Santa Cruz which indicates increased redwood and decreased herbs and chaparral species just prior to 8000 years BP.²¹⁵ Lake sediment records from California and southern Oregon suggest increasing fire activity under progressively more intense aridity from the early to middle Holocene^{216–219}, with lakes in the Klamath Mountains suggesting enhanced fire activity at 8400 years BP and the growth of a chaparral understory through the mid-Holocene.²²⁰ However, challenging chronologies and low sediment accumulation rates preclude investigation of fire-vegetation relationships at these sites at temporal resolution comparable to the WMC speleothem.

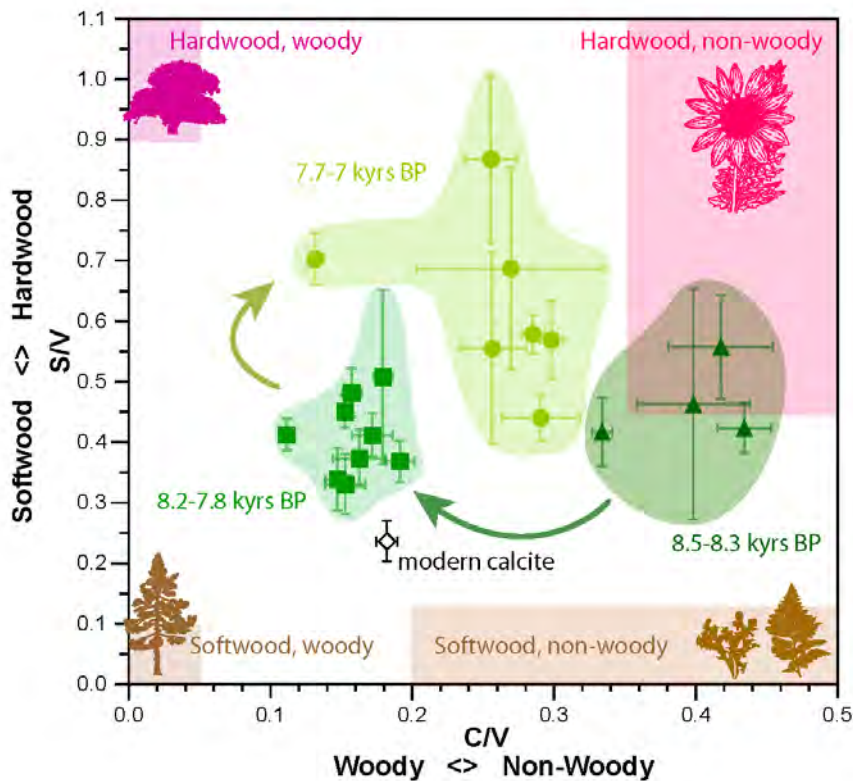


Figure 3.2. Lignin oxidation product (LOP) ratios (S/V versus C/V) for speleothem samples and modern calcite. Shown are speleothem samples with ages from 8.5–8.3 kiloyears before present (kyrs BP) (triangles), 8.2–7.8 kyrs BP (squares), and 7.7–7.0 kyrs BP (circles). The combined modern calcite samples are shown as an open diamond. The area shaded in dark brown corresponds to lignin originating from gymnosperm woody plants, as defined by Hedges and Mann.⁵⁴ The orange area is associated with gymnosperm non-woody plants, the purple area corresponds to angiosperm woody samples, and the pink area is associated with angiosperm non-woody plant parts. Error bars represent the standard deviation of samples measured in duplicate. The arrows highlight the changes over time. Plant icons available from phyloPic.org²²¹ (lower left) and freesvg.org²²² (others) and are licensed under Creative Commons.²²³

3.3.2. Fire and vegetation proxies in the modern cave environment

To explore the behaviour of levoglucosan and LOPs in the modern cave environment in support of our interpretations of the paleoenvironmental record, we analysed glass plate

calcites and dripwaters from several locations within the cave. Glass plates containing ~3 years of calcite growth (see Methods section) were analysed from sites WMC1 and WMC2 in the upper level of the cave (Figure S3). Levoglucosan concentrations in these modern calcites ($3.6 \pm 0.3 \text{ ng} \cdot \text{g}^{-1}$ and $6.6 \pm 0.3 \text{ ng} \cdot \text{g}^{-1}$) are higher than all early to mid-Holocene speleothem samples. Additionally, we analysed portions of the speleothem younger than 6,900 years BP, and these showed higher levoglucosan concentrations up to $4.7 \pm 0.3 \text{ ng} \cdot \text{g}^{-1}$ (Table S1). This increase towards the present may be indicative of higher levoglucosan input into the soil through increased fire activity in the mid to late Holocene, consistent with regional lake records.^{216,218,219} However, we do not have precise age constraints on this part of the stalagmite and can only estimate their ages to be between 6,900 and ~240 years BP. Like levoglucosan, modern calcite samples show higher LOP concentrations than speleothem samples (Figure S2 and Figure S4). This might reflect a denser present-day vegetation above the cave compared to the early Holocene. The C/V and S/V ratios for modern calcite samples are consistent with the current mixed evergreen forest above the cave and are most similar to the speleothem values from ~8,200 to 7,800 years BP when the plant community above the cave consisted of more woody vegetation (Figure 3.2).

To investigate in-cave spatial and temporal patterns in levoglucosan concentrations and their relationships to recent fire activity, we analysed dripwater from four sites collected during the wet seasons (December to February) of 2019, 2020, and 2021 (Figure 3.3). Waters from sites WMC1 and 3 in the upper level of the cave had higher levoglucosan concentrations than waters collected from sites WMC4 and 6, which are approximately 55 m deeper below the surface (Figure S3). These differences may reflect increased adsorption of levoglucosan to rock surfaces along longer seepage water flow paths. Notably, levoglucosan levels of all samples obtained in February 2020 are significantly higher than in samples from February 2019 and December 2021. Smaller ($<1 \text{ km}^2$) fires occurred within 30 km of the cave in autumn 2019.²²⁴ Levoglucosan can easily be transported in the particle phase over such distances^{69,225} although it is currently unclear how signal intensity changes in relation to the distance to the fire. Winter rainfall prior to dripwater collection (January-February) was much higher in 2019 than in 2020 (430 vs. 75 mm).²²⁶ This might have supported leaching of levoglucosan from the soil in 2019 and resulting loss of signal from previous fire seasons. The samples collected in December 2021, after the August 2020 fire, do not show elevated levoglucosan levels relative to other years. Like 2019, the interval prior to water sampling in December 2021 was particularly wet (280 mm, October – December 2021) and more than one rainy season had passed between fire occurrence and dripwater collection. This suggests that the levoglucosan signal in WMC dripwater may only reflect the fire activity of the most recent fire season, and that high rainfall intervals rapidly leach the signal from the soil. Further investigation into the persistence of the levoglucosan signal in cave environments and the required proximity of fires for influencing dripwater chemistry is warranted to better understand the dynamics of this proxy. Given a growth rate of $\sim 0.1 \text{ mm} \cdot \text{yr}^{-1}$ of stalagmite WMC1 and the sampling resolution of the levoglucosan analyses (5-9 mm or ca. 50-90 years), we are not able to evaluate interannual variability in fire activity in the early Holocene. However, peak levoglucosan levels over 4 samples in stalagmite WMC1 indicates that periods of elevated fire activity persisted above the cave over ~150 years during the 8.2 kyr event and

that fire activity in this interval exceeded that in the remaining record from 8,600 to 6,900 years BP.

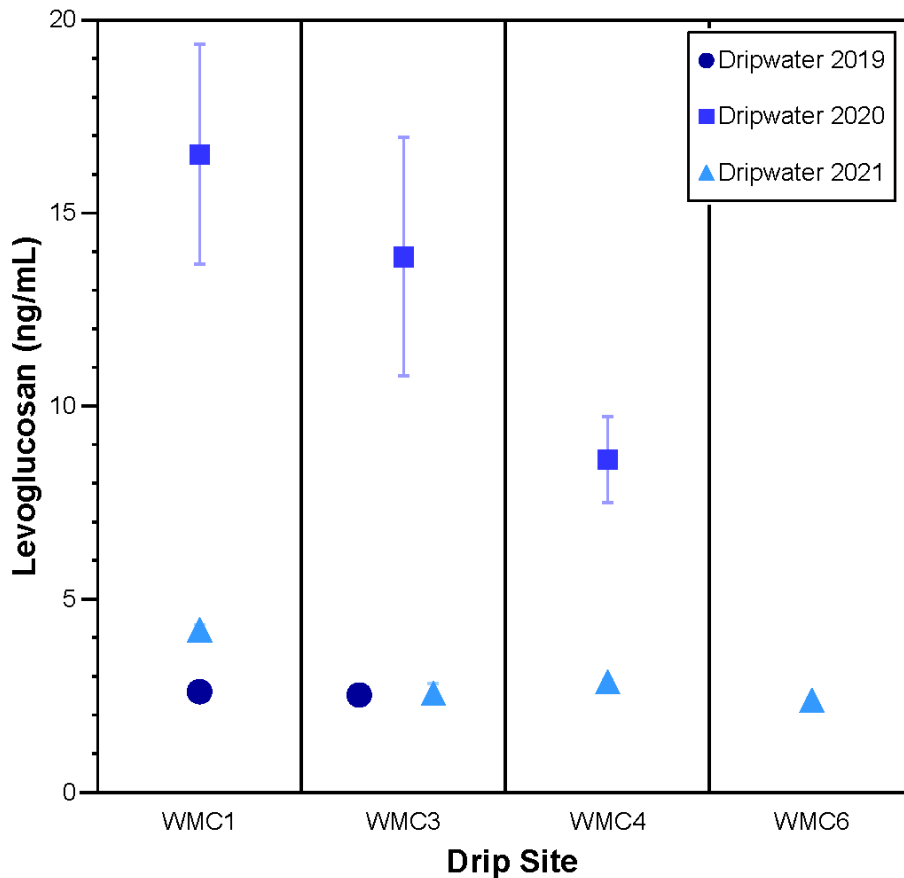


Figure 3.3. Levoglucosan concentrations in dripwater. Water samples were collected in February 2019, February 2020, and December 2021. Error bars represent the standard deviation of samples measured in duplicate and may be smaller than the symbols.

3.4. Discussion

Tree-ring data from western North America reveal strong sensitivity of fire activity to summer temperatures and hydrological drought since the late Holocene.^{227–229} In the southern Cascades²²⁹ and Sierra Nevada²³⁰, variations in fire activity have been associated with changes in the magnitude of interannual fluctuations in rainfall amount, with enhanced fire activity occurring when high interannual variations in the Palmer Drought Severity Index (PDSI) coincide with higher temperatures.²²⁹ Similar relationships are evident in the early to mid-Holocene record of the Pacific Northwest, where pollen and charcoal reconstructions link increased fire activity to summer drought^{214,216}, while lacustrine oxygen isotope records document wetter winters.²³¹

Winter rainfall accounts for >80% of annual precipitation at WMC.²⁰⁹ Thus, stalagmite precipitation proxies will provide a record of winter rainfall changes, while the levoglucosan record likely reflects fire activity from the preceding summer. During the 8.2 kyr event and a “precursor” event at 8,300 years BP, stalagmite isotope and trace element proxies all indicate

overall wetter winters and a potentially more volatile hydroclimate relative to the rest of the record (Figure 3.1 and Figure 3.4).^{207,209} Semi-quantitative estimates of precipitation determined using $d^{44}\text{Ca}$, a proxy that is uniquely sensitive to prior carbonate precipitation (PCP), suggest that during the 8.2 kyr event rainfall oscillated between dry and wet periods with similar magnitude as over the instrumental record (1950-2020) (Figure 3.1 a). However, during the precursor event, these oscillations exceeded modern multi-year droughts and precipitation excesses, including the recent 2012-2015 multi-year drought²³² and ensuing 2016-2017 wet interval.²⁰⁹ Similarly, the higher resolution $d^{13}\text{C}$ record is sensitive to changes in PCP via preferential removing of ^{12}C during CO_2 degassing from seepage waters and changes in soil respiration driven by precipitation or temperature changes.^{7,207} Change point analysis conducted on the $d^{13}\text{C}$ record (Figure 3.1 b) suggests a shift in mean and variance at the onset of the precursor event, and another shift at the end of the 8.2 kyr event interval at $\sim 8,070$ years BP. This indicates the combined precursor and 8.2 kyr event were characterised by higher variance and lower mean $d^{13}\text{C}$ compared to the Holocene. This agrees with overall wetter (lower $d^{13}\text{C}$) but more volatile winter conditions. The change point identified in the $d^{13}\text{C}$ record just predates the rise in levoglucosan near the onset of the 8.2 kyr event at $8,217 \pm 23$ years BP (Figure 3.1 and Figure 3.4). The vegetation shift indicated by LOP ratios also occurs at $8,271 \pm 23$ years BP, just after the precursor event but preceding the rise in levoglucosan. This indicates that abrupt changes from wet to dry extremes during the precursor event may have initiated a shift towards more woody vegetation that persisted as fire activity increased and may have provided increased fire fuel.²¹⁴ Notably, stalagmite P/Ca (Figure 3.1 c), which reflects inputs of soil colloidal material to dripwater²⁰⁹ and has been linked with enhanced fire activity in Australian stalagmites³⁵, also increases at this time.

These proxy comparisons describe a link between hydroclimate volatility, vegetation change, and fire occurrence during the 8.2 kyr event similar to that observed in modern tree-ring records, that are of higher temporal resolution than the stalagmite, and in Holocene lake sediments, that are of lower resolution.^{214,216,229,230} Seasonality was enhanced in the early Holocene including during the 8.2 kyr event, with increased summer insolation leading to higher summer temperatures and vice versa.^{219,231} Although freshwater forcing led to cooling in the North Atlantic region, modelling indicates only a small ($<0.5^\circ\text{C}$) reduction in average annual temperatures associated with the 8.2 kyr event in western North America.²³³ Similar to other instances of freshwater release to the North Atlantic^{205,234,235} the effect of the 8.2 kyr event on California climate was primarily through hydroclimatic change. The WMC1 $d^{13}\text{C}$ record resolves precipitation changes internal to the 8.2 kyr event and suggests that the interval was characterized by heightened interannual precipitation volatility even though the mean shift in precipitation was small. Similar to links between modern PDSI variability and summer temperatures²²⁹, we propose that this heightened volatility coupled with the enhanced early Holocene summer temperatures²¹⁹ drove the shift to more woody vegetation and elevated fire activity.

Our method for the quantification of levoglucosan and LOPs in small speleothem samples (<1 g) and dripwater offers a pathway for reconstructing wildfire activity and paleo-vegetation, respectively in paleoclimate archives on longer pre-instrumental timescales than what is offered by tree-ring records and at higher temporal resolution than what is offered by

lake sediments. Further information from cave monitoring studies along geologic, ecologic, and hydrologic gradients is necessary to evaluate the degree to which levoglucosan records more distal fires, the longevity of the levoglucosan signals in soils, and how the signals are transported through the epikarst and embedded in speleothems. Study sites with a known fire history or with adjacent paleoclimate archives containing other fire and vegetation markers like fire scars in tree-rings, or charcoal, pollen, or polycyclic aromatic hydrocarbons (PAHs) in lake sediments should be prioritised to better restrict the parameters that influence the levoglucosan and LOP signal in speleothems. Techniques to analyse PAHs in dripwaters²³⁶ and speleothems^{90,91} are also in development. Combined analysis of levoglucosan and PAHs within the same speleothem would offer another powerful tool for disentangling the relationships between climate, fire, and vegetation change on multiple timescales.

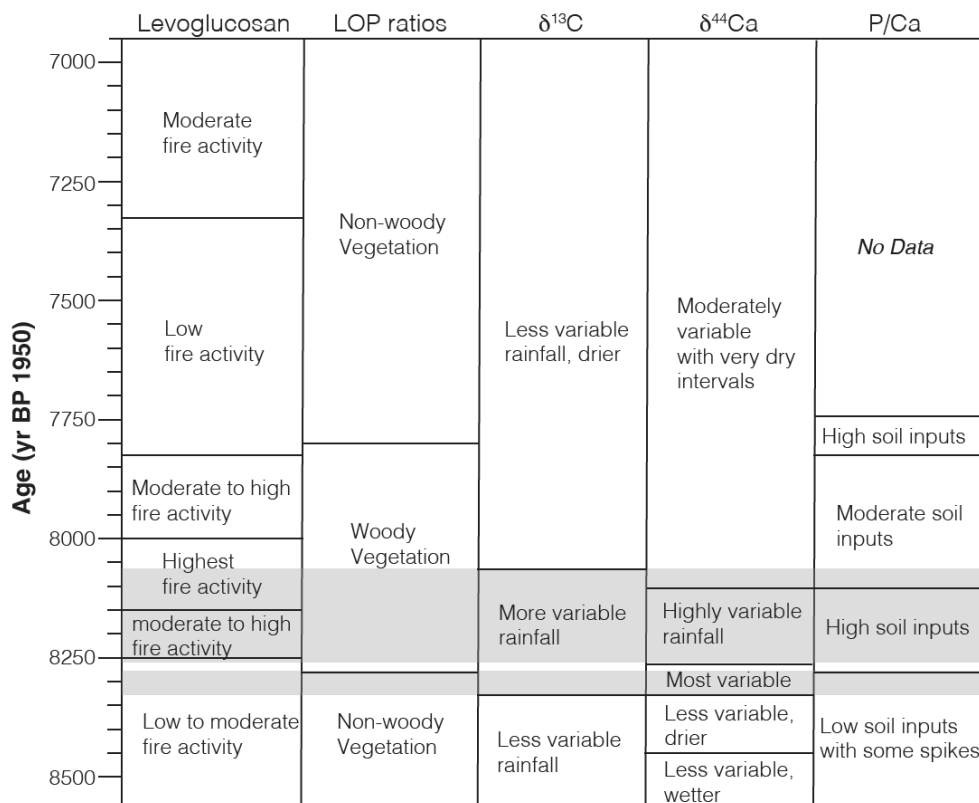


Figure 3.4. Summary of proxy interpretations for stalagmite WMC1 with time. Gray shading denotes the precursor event (centered on 8,300 years BP) and the 8.2 kyr event. See Fig. 1 for proxy time series.

The combined records of hydroclimatic change, wildfire, and vegetation community from White Moon Cave support the link between precipitation volatility and fire activity in western North America that has been observed in tree ring records in the late Holocene, inferred from mid-Holocene lake records, and predicted for future warming scenarios.^{7,8} Our record provides evidence for this climate-fire relationship under early Holocene boundary conditions prior to substantial forcing from anthropogenic greenhouse gas emissions and land use changes such as fire suppression.²³⁷ Further, our records suggest enhanced volatility and fire activity during the 8.2 kyr event, an interval of freshwater forcing and abrupt cooling in the North Atlantic. The incorporation of paleo-fire and vegetation proxies into the WMC1

record demonstrates the potential for fast growing speleothems from fire-prone regions to illuminate the drivers behind in precipitation volatility and the relationship between "climate whiplash" and fire under a range of background climate states.

3.5. Methods

3.5.1. Statistical analysis of previously sampled proxy records

In order to statistically identify changes in the amplitude and frequency of proxy variability, and thus to pinpoint the potential onset and cessation of changes in hydroclimate volatility, we conducted changepoint analysis on the previously published stalagmite $d^{13}C$ record¹⁴ using the changepoint package in R.²³⁸ Changepoints were identified in the $d^{13}C$ record as changes in mean and variance using the PELT algorithm²³⁹ and the modified Bayes Information Criterion (MBIC) penalty.²⁴⁰ The $d^{13}C$ timeseries was chosen for this analysis because of its continuity (trace element records for this stalagmite have gaps) and high resolution (the $d^{44}Ca$ record is of much lower temporal resolution).

An age model was constructed for the levoglucosan and LOP samples using the Stalage algorithm in R¹⁷ and the previously collected stalagmite $^{230}Th/U$ dates.²⁰⁷ The ages of the upper and lower surfaces of the segments collected for levoglucosan and LOP analysis were modelled separately and presented as the upper and lower bounds of the sample ages.

3.5.2. Chemicals and materials

Analytical standards of levoglucosan (99 %), acetosyringone (97 %), acetovanillone (≥ 98 %), para-coumaric acid (≥ 98 %), ethylvanillin (99 %), ferulic acid (99 %), syringaldehyde (98 %), and syringic acid (>95 %), as well as L-ascorbic acid (SigmaUltra) were purchased from Sigma-Aldrich. An analytical standard of $^{13}C_6$ levoglucosan (98 %) was obtained from Cambridge Isotope Laboratories. An analytical standard of vanillin (99 %) was obtained from Acros Organics, and an analytical standard of vanillic acid (98 %) was obtained from Alfa Aesar. An analytical standard of ammonium acetate (≥ 99 %) and ultrapure acetonitrile (ACN, LC/MS grade) were obtained from VWR Chemicals. Sodium hydroxide (pellets, ≥ 99 %), hydrochloric acid (HCl, suprapure, 30 %), and water (LC-MS grade) were purchased from Merck KGaA. Ammonium hydroxide solution (NH_3 , analytical grade, 25 %) was obtained from Honeywell Fluka. Ultrapure methanol (MeOH, LC/MS grade) was obtained Carl Roth while ultrapure dichloromethane (DCM, LC-MS grade, ≥ 99.8 %) was purchased from Fisher Scientific. Ultrapure water with 18.2 M Ω resistance was produced using a Milli-Q water system from Merck Millipore (Darmstadt, Germany). Solid-phase extraction columns (Oasis HLB, 6 mL tubes, 200 mg packing material and Oasis HLB, 1 mL tubes, 30 mg packing material) were purchased from Waters.

3.5.3. Speleothem and modern calcite sample preparation

Stalagmite samples were obtained by using a tile saw to sequentially slice 0.5 to 0.9 cm segments along a section of the WMC1 growth axis. This resulted in calcite samples that ranged in weight from 0.5 to 1.3 g. The 20 speleothem samples were first cleaned in DCM/MeOH 9:1 by 10 min of sonification and subsequently washed with Milli-Q water. Afterwards, the samples were bedecked with HCl (0.6 %) for 5 min to remove any adhesive contaminations, washed again with Milli-Q water, and dried at 150 °C. Thereafter, the sample blocks were pulverised using an electric coffee grinder (Grundig CM 4760 GMS2070).

Samples of modern calcite were scraped from the surface of artificial substrates (glass plates) that were placed in the cave underneath active drip sites. Artificial substrates were placed under drip site WMC2 in December 2015 and WMC1 in March 2016 in the upper level of the cave (see Supplementary Fig. 3). Both plates were recollected in June 2018.

For the extraction of levoglucosan, the pulverised speleothem and modern calcite samples were spiked with 100 µL of a solution of $^{13}\text{C}_6$ levoglucosan (100 ng · g⁻¹ in ACN) and extracted twice with 5 mL or 2.5 mL of MeOH, respectively. The extraction was assisted by ultrasonic sound and lasted 45 min at a time. After sonification the samples were allowed to rest for 10-20 min to improve phase separation. Then, the supernatant was removed, filtered over a 1.0 µm glass fibre fabric filter (Macherey Nagel), and evaporated under a gentle stream of nitrogen at 30 °C. The residue was taken up in 200 µL of ACN/H₂O (95:5) by 10 min of sonification at 45 °C. The solution was filtered with a 0.2 µm PA-filter (Altman-Analytik) and stored in the freezer at -25 °C.

For the analysis of LOPs, the extracted speleothem powder was dried over night at 50 °C and dissolved in 3 mL HCl (30 %) per g sample and then diluted 1:1 with Milli-Q water. The two modern calcite samples were combined to assure that the resulting LOP concentrations would be above LOD. The 200 mg HLB cartridges were preconditioned with 6 mL of each MeOH and ultrapure water, which was acidified to pH 1-2 with HCl (30%). The speleothem solution was filtered through paper filters (Whatman, Grade 40, 8 µm pore size) to prevent undissolved materials from clogging the cartridges and was loaded onto the cartridges using sample reservoirs. The Cartridges were washed twice with 6 mL of acidified ultrapure water and then dried by sucking air through the cartridges using a vacuum pump. The lignin was eluted using 10 portions of 500 µL MeOH. The solvent was subsequently evaporated under a gentle stream of nitrogen at 30 °C. The CuSO₄ oxidation procedure was developed based on the method described by Yan and Kaiser (2018).⁵⁶ The residue was dissolved in 200 µL MeOH and sonicated for 10 min at 45 °C. The solution was added to a PTFE microwave digestion vessel with a capacity of 500 µL. The procedure was repeated with 100 µL MeOH and the combined solutions evaporated to dryness under a gentle stream of nitrogen at 30 °C. The residuum was dissolved in 200 µL NaOH (1 mol · mL⁻¹) through sonification for 10 min at 45 °C. To this, 10 µL each of CuSO₄ solution (10 mmol · L⁻¹ in H₂O) and a solution of L-ascorbic acid (0.2 mol · L⁻¹ in H₂O) were added. The vessels were purged with nitrogen for 20 s each and quickly capped to ensure inert gas atmosphere. The digestion vessels were packed into a bigger Teflon vessel 5 at a time and covered with 7 mL of NaOH (1 mol · mL⁻¹) to ensure better heat transfer. These vessels were also purged with nitrogen for 1 min. The vessels were heated to 155 °C in 5 min and held at that temperature for 90 min using a 5890A Gas

Chromatograph (Hewlett Peckard, USA). Immediately after opening the vessels, 10 μL of a 1 $\mu\text{g} \cdot \text{mL}^{-1}$ standard solution of ethyl vanillin in ACN was added as an internal standard and the oxidised sample solution was acidified to pH 1-2 with HCl (30 %). The 30 mg HLB cartridges were preconditioned with two times 1 mL of each MeOH and ultrapure water, which was acidified to pH 1-2 with HCl (30 %). The acidified oxidised sample solutions were loaded onto the cartridges and the vessels were washed with acidified water twice. Subsequently, the cartridges were washed twice with their void volume and then then dried by sucking air through the cartridges using a vacuum pump. The LOPs were eluted using 8 portions of 125 μL of ACN with 2% NH_3 added to reach a basic pH of 8-9. The eluate was evaporated under a gentle stream of nitrogen at 30 $^{\circ}\text{C}$ and the residue was dissolved in 200 μL ACN/ H_2O (1:9) by 10 min of sonification at 45 $^{\circ}\text{C}$. The solution was filtered with a 0.2 μm PA-filter (Altman-Analytik) and stored in the freezer at -25 $^{\circ}\text{C}$.

Cave drip water samples were collected from four active drip sites at different depths within the cave in February 2019 and 2020 and December 2021 (Supplementary Fig. 3). The samples were passed over a preconditioned 200 mg HLB cartridge (see above). The flow-through was collected and subsequently evaporated using a vacuum centrifuge (Eppendorf Concentrator plus, 248 g) at 30 $^{\circ}\text{C}$. The centrifuge tubes were washed with two portions of 1.5 mL ACN each by 10 min of sonification at 30 $^{\circ}\text{C}$. The combined solutions were evaporated under a gentle stream of nitrogen and the residue was taken up in 200 μL of ACN/ H_2O (95:5) by 10 min of sonification at 45 $^{\circ}\text{C}$. The solution was filtered with a 0.2 μm PA-filter (Altman-Analytik) and stored in the freezer at -25 $^{\circ}\text{C}$.

The loaded SPE cartridges were handled following the same procedure described for the speleothem samples in Preparation for lignin analysis.

3.5.4. Levoglucosan Analysis

All samples were analysed for levoglucosan and LOPs. For this, they were each measured in duplicate. The analysis was carried out on a Dionex UltiMate 3000 ultrahigh-performance liquid chromatography system (UHPLC) that was coupled to a heated electrospray ionisation source (HESI) and a Q Exactive Orbitrap high-resolution mass spectrometer (HRMS) (all by Thermo Fisher Scientific). To retard the analytes, an iHILIC-Fusion (+) column, 100mm x 2.1mm with 1.8 μm particle size (Hilicon), was used. The injection volume was 10 μL . A H_2O /ACN gradient program was applied at a flow of 0.4 $\text{mL} \cdot \text{min}^{-1}$. The gradient started with 97 % eluent B (100 % ACN) and 3 % eluent A (consisting of 5 $\text{mmol} \cdot \text{L}^{-1}$ ammonium acetate in H_2O). Eluent B was held at 97 % for 0.5 min and then decreased to 90 % within 0.5 min. Afterwards, eluent B was further decreased to 85 % in 5 min and 60 % in 1.5 min, respectively. Finally, it was decreased to 50 % within 1.5 min, held for 2.0 min, and then eluent B was increased to the initial value of 97 %. This was held for 8.5 min to re-equilibrate the column. To improve ionisation, a post-column flow of 50 $\text{mmol} \cdot \text{L}^{-1}$ NH_4OH in MeOH was applied with a flow rate of 0.1 $\text{mL} \cdot \text{min}^{-1}$. The ESI source was operated in negative mode so that deprotonated molecular ions $[\text{M}-\text{H}]^-$ were formed. The spray voltage was -4.0 kV, the ESI probe was heated to 150 $^{\circ}\text{C}$, and the capillary temperature was 350 $^{\circ}\text{C}$. The sheath gas

pressure was 60 psi and the auxiliary gas pressure was 20 psi. The mass spectrometer was operated in full scan mode with a resolution of 70,000 and a scan range of m/z 80–500. At the respective retention time windows, the full scan mode was alternated with a targeted MS² mode with a resolution of 17,500. For the MS² mode (i.e., parallel reaction monitoring mode in the software Xcalibur, provided by Thermo Fisher Scientific), higher-energy collisional dissociation (HCD) was used with 35% normalised collision energy (NCE).

3.5.5. LOP Analysis

The analysis of the LOPs was carried out on a Dionex UltiMate 3000 UHPLC system that was coupled to a HESI and a Q Exactive Orbitrap HRMS (all by Thermo Fisher Scientific). To separate the LOPs, a Acquity UPLC CSH Fluoro Phenyl (PFP) column, 100mm x 2.1mm with 1.7 μm particle size (Waters), was used. The injection volume was 5 μL . A H₂O/ACN gradient program was applied with a flow of 0.5 mL · min⁻¹. The gradient started with 5 % eluent B (consisting of 98 % ACN and 2 % H₂O) and 95 % eluent A (consisting of 98 % H₂O, 2% ACN, and 400 $\mu\text{L} \cdot \text{L}^{-1}$ formic acid). Eluent B was increased to 10 % within 0.5 min and held for 4.5 min. It was then increased to 15 % within 1 min and further increased to 30 % in 1 min and to 50 % in 0.5 min, respectively. Finally, it was increased to 99 % within 0.5 min, held for 1.5 min, and then eluent B was decreased to the initial value of 5 %. The ESI source was operated in negative mode so that deprotonated molecular ions [M-H]⁻ were formed. The spray voltage was -4.0 kV, the ESI probe was heated to 150 °C, and the capillary temperature was 350 °C. The sheath gas pressure was 60 psi and the auxiliary gas pressure was 20 psi. The mass spectrometer was operated in full scan mode with a resolution of 70,000 and a scan range of m/z 80–500. At the respective retention time windows, the full scan mode was alternated with a targeted MS² mode with a resolution of 17,500. For the MS² mode (i.e., parallel reaction monitoring mode in the software Xcalibur, provided by Thermo Fisher Scientific), HCD was used with 35% NCE for all analytes.

3.6. Data availability

The levoglucosan and LOP data generated for this study are provided in the supplementary information in Supplementary Table 1 and are publicly archived with the National Centers for Environmental Information at <https://www.ncei.noaa.gov/access/paleo-search/study/37018>. Previously published proxy data are archived at <https://www.ncei.noaa.gov/access/paleo-search/study/32012> and <https://www.ncei.noaa.gov/access/paleo-search/study/22270>.

3.7. Acknowledgments

This work was supported by funding from NSF (AGS1554998) and the National Geographic Society (NGS-39815) to J.O. and the Karst Waters Institute to C.d. J.H. acknowledges financial support by the Max Planck Graduate Center Mainz. We thank Mike Davies and Bruce Rogers of the Western Cave Conservancy for guidance in the field and Susan Petrie of the Peninsula Open Space Trust for cave access.

3.8. Author contributions

J.H., J.O., C.d., S.B., and T.H. designed the study. J.H. conducted the sample preparation and data analysis for levoglucosan and LOPs. C.d. and J.O. subsampled the stalagmite for analysis, constructed the age model, and performed the changepoint analysis on $d^{13}C$. All co-authors participated in discussions, interpretation of the data, and writing of the manuscript.

3.9. Competing Interests Statement

The authors declare no competing interests.

4. Past fire dynamics inferred from polycyclic aromatic hydrocarbons and monosaccharide anhydrides in a stalagmite from the archaeological site of Mayapan, Mexico

This chapter has been accepted for publication in Biogeosciences:²⁴¹

<https://doi.org/10.5194/bg-2023-63>
Preprint. Discussion started: 12 April 2023
© Author(s) 2023. CC BY 4.0 License.



Past fire dynamics inferred from polycyclic aromatic hydrocarbons and monosaccharide anhydrides in a stalagmite from the archaeological site of Mayapan, Mexico

Julia Homann¹, Niklas Karbach¹, Stacy A. Carolin^{2,3}, Daniel H. James², David Hodell², Sebastian F. M. Breitenbach⁴, Ola Kwiecien⁴, Mark Brenner⁵, Carlos Peraza Lope⁶, Thorsten Hoffmann¹

4.1. Abstract

Speleothems (cave stalagmites) contain inorganic and organic substances that can be used to infer past changes in local and regional paleoenvironmental conditions. Specific biomarkers can be employed to elucidate the history of past fires, caused by interactions among climate, regional hydrology, vegetation, humans, and fire activity. We conducted a simple solid-liquid extraction on pulverised carbonate samples to prepare them for analysis of 16 polycyclic aromatic hydrocarbons (PAHs) and three monosaccharide anhydrides (MAs). The preparation method requires only small samples (0.5-1.0 g); PAHs and MAs were measured by GC-MS and LC-HILIC-MS, respectively. Detection limits range from 0.05-2.1 ng for PAHs and 0.01-0.1 ng for MAs. We applied the method to 10 samples from a ~400-year-old stalagmite from Cenote Ch'en Mul, at Mayapan (Mexico), the largest Postclassic Maya capital of the Yucatán Peninsula. We found a strong correlation ($r=0.75$, $p < 0.05$) between the major MA (levoglucosan) and non-alkylated PAHs ($\Sigma 15$). We investigated multiple diagnostic PAH and MA ratios and found that although not all were applicable as paleo-fire proxies, ratios that combine PAHs with MAs are promising tools for identifying different fire regimes and inferring the type of fuel burned. In the 1950s and 1960s, levoglucosan and $\Sigma 15$ concentrations roughly doubled compared to other times in the last 400 years, suggesting greater fire activity at Mayapan during these two decades. The higher concentrations of fire markers may have been a consequence of land clearance at the site and exploration of the cave by Carnegie Institution archaeologists.

4.2. Introduction

Speleothems are valuable continental paleoenvironmental archives. They can grow continuously over long time periods^{1,242} and can provide very high-resolution (sub-annual) proxy time series of past climate and environment.^{243,244} Most can be reliably dated using uranium series isotopes.^{4,10} Well-established inorganic proxies such as $\delta^{18}\text{O}$ and $\delta^{13}\text{C}$ are increasingly complemented by organic biomarkers that record more specific aspects of the paleoenvironmental conditions.³⁶⁻⁴⁰ One important aspect of past environments is the occurrence and dynamics of fires, whether natural or anthropogenic. The development of fire-sensitive proxies in paleoenvironmental archives can help elucidate interactions among climate, regional hydrology, vegetation, and fire activity.³² Two such fire proxies are polycyclic aromatic hydrocarbons (PAHs) and monosaccharide anhydrides (MAs). PAHs are products of incomplete combustion of biomass and petrogenic fuels over a wide temperature range (200-700 °C).^{73,74,87,94}

The presence of specific biomarkers is indicative of the fuel source. Retene, for example, is a PAH that is a unique marker for the combustion of gymnosperm biomass.^{98,99} MAs are formed only during combustion of biomass at lower temperatures (150-350 °C). The predominant MA is levoglucosan, which is formed during combustion of cellulose.^{60,211} Both PAHs and MAs can be present in the gas and the particle phase^{245,246} and have been reported to undergo long-range transport.^{81,247} Their atmospheric residence times, however, differ widely, ranging from 1-3 hours (gas phase) to 4-5 days (particulate phase) for PAHs and 2-26 days for MAs.⁶³⁻⁶⁵ This difference in atmospheric longevity may explain why Denis et al. (2012)⁸⁶ found PAHs to record only very local (≤ 0.5 km) fires, whereas known fires that occurred 1-2 km from the sampling site were not recorded.

These different behaviours of PAHs and MAs are the rationale for analysis of both fire proxies in tandem, not only to detect the presence of fire but also to explore changes in fire regime (e.g. fire frequency, intensity, and fuel source). Whereas PAHs and MAs have been measured simultaneously in lake sediment cores¹⁰⁰⁻¹⁰², they have not yet been investigated jointly in speleothems, although both have been extracted individually from stalagmites.^{40,90,91} Another motivation to survey different markers simultaneously is to better understand their transport and incorporation mechanisms in speleothem carbonate. In principle, PAHs and MAs can be transported into a stalagmite either via infiltrating water, and/or via deposited aerosol particles, delivered via cave ventilation or by cave-internal sources (e.g. campfires, torched, candles, or petroleum lamps). Whereas samples from caves without substantial ventilation (i.e. with no or very narrow entrances) would only archive a dripwater-derived signal, it is likely that in caves with substantial ventilation and easy human access, markers would be introduced via both dripping water and externally introduced or cave internally formed aerosol particles.

Here we focus on the extraction of PAHs and MAs from speleothem carbonate. We report the results of sequential extraction of 16 PAHs and three MAs from a speleothem and their analysis using GC-MS and LC-HILIC-MS, respectively. We applied the new, simple method to a young (~400-year-old) stalagmite (MAYA-22-7) collected in August 2022 from Cenote Ch'en Mul, Mayapan, Yucatán Peninsula, Mexico. Several smaller stalagmites from the same cave

contained charcoal inclusions, indicating that the studied stalagmite was a promising candidate for this proof-of-concept study. We used the measured PAH and MA concentrations and selected diagnostic ratios to interpret past aspects of fire dynamics in the cave and surrounding area. Even though some of the biomarkers were below the limit of detection (LOD), the analysed stalagmite samples provided valuable hints about past fire dynamics.

4.3. Methods

4.3.1. Materials

Ultrapure methanol (MeOH, LC/MS grade) was obtained from Carl Roth, ultrapure dichloromethane (DCM, LC/MS grade, $\geq 99.8\%$) and water (LC/MS grade) were purchased from Fisher Scientific. Ultrapure acetonitrile (ACN, LC/MS grade) and ammonium formate (99%) were obtained from VWR Chemicals. Analytical standards of levoglucosan (1,6-Anhydro- β -D-glucopyranose, 99%), *p*-terphenyl ($\geq 99\%$), naphthalene- d_8 (2000 $\mu\text{g mL}^{-1}$ in DCM), acenaphthene- d_{10} (2000 $\mu\text{g mL}^{-1}$ in DCM), phenanthrene- d_{10} (2000 $\mu\text{g mL}^{-1}$ in DCM), and a standard of 16 PAHs (QTM PAH Mix, 2000 $\mu\text{g mL}^{-1}$ in DCM), as well as ultrapure ethyl acetate (EA, GC/MS grade) were purchased from Sigma-Aldrich. An analytical standard of $^{13}\text{C}_6$ -levoglucosan (98%) was obtained from Cambridge Isotope Laboratories. An analytical standard of retene (10 $\mu\text{g mL}^{-1}$ in cyclohexane) was purchased from LGC and analytical standards of mannosan (1,6-Anhydro- β -D-mannopyranose) and galactosan (1,6-Anhydro- β -D-galactopyranose) were obtained from Carbosynth Ltd. Ultrapure water with 18.2 M Ω resistance was produced using a Milli-Q water system from Merck Millipore. Solid-phase extraction columns (CHROMABOND SiOH, 3 mL tubes, 45 μm particle size) were purchased from Macherey-Nagel.

The developed extraction and measurement methods were tested on stalagmite MAYA-22-7, collected in 2022 from Cenote Ch'en Mul at the Postclassic Maya archaeological site of Mayapan in northern Yucatan (Mexico), with permission granted by the Instituto Nacional de Antropología e Historia (INAH). The stalagmite was retrieved from a narrow passage in the south-east sector of the cave (Figure S5). The growth surface of stalagmite MAYA-22-7 was wet from drip water prior to collection. The stalagmite was cut in half lengthwise, i.e. along the growth axis, and cut again to produce a central working slab and an off-axis working piece, using a Diamond WireTec DSW175 wire saw with a 0.35-mm-diameter diamond-studded steel wire at Northumbria University, UK. Powdered samples for biomarker analysis and U-Th dating were drilled at the University of Cambridge along exposed growth layers on the working half (Figure 4.1), using a handheld Dremel drill with a 0.8-mm-diameter tungsten carbide dental drill bit. The bench surface, drill, drill bit, and aluminium tools for powder collection were all sprayed with compressed air and wiped down with a Kimwipe™ and methanol between sample drilling. Sample pit vertical heights along the growth axis differed depending on the sample pit size, with a range of 3 to 8 mm (Figure 4.1). The stalagmite surface was also wiped with a Kimwipe™ and methanol before each pit was drilled. Powder sample weights ranged from 500 to 1200 mg and were stored in methanol-cleaned glass sample vials with a plastic screw cap.

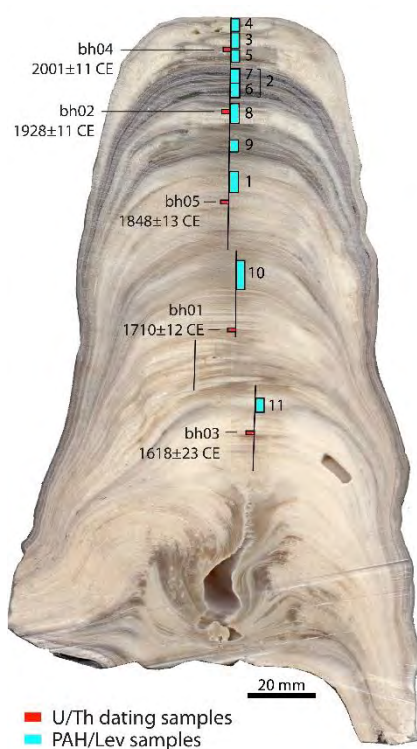


Figure 4.1. Scan of stalagmite MAYA-22-7 with samples taken for U-Th dating and biomarker analysis indicated in red and cyan, respectively. For simplicity, rectangles indicate the position of the samples projected onto the central growth axis, whereas samples were drilled off-axis, along growth layers. Black vertical lines indicate the growth axis along which grey values were measured. Ages are given in calendar years (C.E. = Common Era) with 95% confidence intervals.

The chronology of MAYA-22-7 was determined with a U-Th age model constructed from five U-Th ages drilled from the central working slab (Figure 4.1). Sample preparation and analytical chemistry for dating were conducted at the Department of Earth Sciences, University of Oxford. Samples were dissolved in distilled concentrated nitric acid and spiked with a mixed ^{229}Th - ^{236}U solution. U and Th were separated using column chemistry, following procedures adapted from Edwards et al. (1987).²⁴⁸ U and Th isotopes were measured using a Nu Plasma II Multi-ion-counting, Multi-collector Inductively Coupled Plasma Mass Spectrometer (MC-ICP-MS), following procedures adapted from Hoffman (2008).¹⁴ Ages were calculated iteratively using the $^{230}\text{Th}/^{238}\text{U}$ age equation²⁴⁹, derived in Richards and Dorale (2003).²⁵⁰ The ^{234}U and ^{230}Th half-lives used for age calculations are those reported in Cheng et al. (2013).¹³ Age uncertainty was calculated using a Monte Carlo method, which accounts for instrument measurement, chemical blank, and initial detrital $^{230}\text{Th}/^{232}\text{Th}$ activity ratio uncertainty. The initial detrital $^{230}\text{Th}/^{232}\text{Th}$ activity ratio is set as a uniform distribution of values between 0.1 and 2.0, which encompasses the bulk earth value ($^{230}\text{Th}/^{232}\text{Th}$ activity = 0.82) and the median detritus value determined from a collection of speleothem studies ($^{230}\text{Th}/^{232}\text{Th}$ activity = 1.5)²⁵¹. All U-Th ages are in sequential order, with the corrected youngest date (9.3 mm from stalagmite top) 2001 ± 11 (2σ) CE.

The interpolated age model for the stalagmite central growth axis was produced using the OxCal version 4.4 Poisson-process Deposition model, with the stalagmite vertical growth rate constrained using model inputs $k_0 = 0.1 \text{ mm}^{-1}$ and $\log_{10}(k/k_0) = U(-2, 2)$.^{18,252,253} Because

sample pits in this study were drilled off the central axis, visible laminae were tracked to connect the sample pit locations to the central growth axis to determine the mean age range and 95% confidence age range of the sample pits. The OxCal Deposition model input code, an age-depth plot (Figure S6), U-Th isotope activity ratios and calculated age of U-Th samples (Table S3), as well as ages and their respective errors of the biomarker samples (Table S4) are found in the supplement.

4.3.2. PAH and MA extraction

The sample preparation procedure is illustrated in Figure S7. The PAH extraction method was adapted from Shahpoury et al. (2018).²⁵⁴ Powdered speleothem samples were weighed into baked-out (>8 h at 450 °C) 20 mL glass vials and spiked with 100 µL of a solution of 100 ng mL⁻¹ naphthalene-d₈, acenaphthene-d₁₀, and phenanthrene-d₁₀ in ethyl acetate (EA). Subsequently, each sample was extracted twice with 5 mL g⁻¹ dichloromethane (DCM) in an ultrasonic bath for 45 min. After sonication, samples were allowed to stand for 10-20 minutes to improve phase separation. The supernatant was removed, filtered through a 1 µm glass fibre filter (Macherey Nagel), and loaded onto the preconditioned (3 mL each of EA and DCM) SPE cartridges. The flow-through was collected in baked-out 20 mL glass vials with tapered bottoms. The cartridge was rinsed with 3 mL each of DCM and EA and dried by blowing air through the cartridge. Subsequently, the solution was evaporated under a gentle stream of nitrogen at 30 °C to a volume of approximately 500 µL. The walls of the vial were washed with 3 mL EA, the solution was once again evaporated to approximately 500 µL, and the walls were washed again with another portion of 3 mL EA. Then the sample solution was evaporated to approximately 200 µL, the walls were washed a last time with 500 µL EA, and the solution was finally evaporated to a volume of ~100 µL. This solution was transferred into a baked-out 250 µL vial. The evaporation vial was washed with 100 µL EA and the solution was added to the sample. To enable volume calculation and corrections during measurement, 2 µL of a solution of *p*-terphenyl (7.5 µg mL⁻¹ in EA) were added. The sample solution was stored in the freezer at -25 °C.

The extracted speleothem carbonate powder was dried in an oven at 50 °C overnight and then spiked with 100 µL of a solution of 100 ng mL⁻¹ ¹³C₆-levoglucosan in acetonitrile (ACN). The extraction procedure is described in Homann et al. (2022).⁴⁰ In brief, two 45 min ultrasonic extractions were performed using 5 mL g⁻¹ methanol (MeOH) as an extraction agent. The supernatant was filtered with a 1 µm glass fibre fabric filter and evaporated to dryness under a gentle stream of nitrogen at 30 °C. The residue was redissolved in ACN/H₂O (95:5) and filtered through a 0.2 µm PA-filter (Altman-Analytik) prior to storage at -25 °C.

4.3.3. PAH analysis

The analysis was performed using a Thermo Fisher Scientific Orbitrap Exploris GC system. Analytes were separated on a TG-5-SILMS column (30 m, 0.25 mm inner diameter, 0.25 µm film thickness, Thermo Fisher Scientific). A volume of 1 µL was injected in splitless mode at

an injector temperature of 320 °C, a transfer-line temperature of 320 °C, and an oven temperature of 50 °C. The carrier-gas (helium, 5.0, Nippon Gases) flow was set to 1 mL min⁻¹. The initial temperature was held for 2 min, then increased to 160 °C at a rate of 10 °C min⁻¹ (1 min hold), then to 270 °C at 3 °C min⁻¹, then to 300 °C at 30 °C min⁻¹ (5 min hold), and finally to 320 °C at 30 °C min⁻¹ (2.7 min hold). The injector was cleaned after each injection for 5 min at 330 °C with a flow rate of 150 mL min⁻¹. The mass spectrometer was operated in positive electron ionisation mode (EI+) using selected ion monitoring mode (SIM). The SIM *m/z* ratios and retention times of the respective PAHs are found in Table 4.1. Analytes were quantified via the ratio of the peak area of the analyte to the peak area of the internal standard.

Table 4.1. Common name, acronym, sum formula, retention time, *m/z* value, limit of detection, repeatability, and accuracy of all *d*-PAHs, internal standards, and PAHs determined by the GC-MS method.

	Analyte	Acronym	Sum formula	<i>t_R</i> (min)	<i>m/z</i> [M] ⁺	LOD (ng)	Repeat-ability (%)	Accuracy (%)
Spiked <i>d</i> -PAHs and internal standard	Napthalene- <i>d</i> ₈	d-NAP	C ₁₀ D ₈	9.49	136.1128	0.97	4.5	8.3
	Acenaphthene- <i>d</i> ₁₀	d-ACE	C ₁₂ D ₁₀	13.67	164.1410 [†]	1.37	4.6	1.5
	Phenanthrene- <i>d</i> ₁₀	d-PHE	C ₁₄ D ₁₀	19.40	188.1410	1.29	11.4	2.6
	p-Terphenyl	PTP	C ₁₈ H ₁₄	29.90	230.1096	/	6.6	/
Investigated PAHs	Napthalene	NAP	C ₁₀ H ₈	9.53	128.0626	1.41	5.7	0.6
	Acenaphthylene	ACY	C ₁₂ H ₈	13.28	152.0626	0.07	7.0	0.2
	Acenaphthene	ACE	C ₁₂ H ₁₀	13.77	154.0783	0.14	5.1	0.3
	Fluorene	FLN	C ₁₃ H ₁₀	15.43	166.0783	0.17	25.6	0.1
	Phenanthrene	PHE	C ₁₄ H ₁₀	19.50	178.0783	2.07	17.6	4.8
	Anthracene	ANT	C ₁₄ H ₁₀	19.77	178.0783	0.04	3.3	0.1
	Fluoranthene	FLT	C ₁₆ H ₁₀	26.45	202.0783	0.67	6.2	1.0
	Pyrene	PYR	C ₁₆ H ₁₆	27.81	202.0777 [†]	0.34	2.2	0.5
	Retene	RET	C ₁₈ H ₁₈	30.48	234.1409	0.36	19.4	0.7
	Benzo(a)anthracene	BAA	C ₁₈ H ₁₂	36.53	228.0939	1.09	3.7	1.2
	Chrysene	CHR	C ₁₈ H ₁₂	36.75	228.0939	1.14	8.9	0.9
	Benzo(b)fluoranthene	BBF	C ₂₀ H ₁₂	44.02	252.0939	1.30	8.7	0.2
	Benzo(a)pyrene	BAP	C ₂₀ H ₁₄	45.99	252.0939 [†]	0.55	9.6	1.5
	Indeno(1,2,3- <i>c,d</i>)pyrene	INP	C ₂₂ H ₁₄	52.00	276.0939 [†]	0.51	10.2	1.1
	Dibenz(a,h)anthracene	DBA	C ₂₂ H ₁₄	52.18	278.1096	NA	12.0	1.0
	Benzo(g,h,i)perylene	DPE	C ₂₂ H ₁₂	52.73	276.0939	0.47	12.4	1.5

†: Detection of fragment.

4.3.4. MA analysis

Analysis of MAs was carried out on a Dionex UltiMate 3000 ultrahigh-performance liquid chromatography system (UHPLC), coupled to a heated electrospray ionisation source (HESI) and a Q Exactive Orbitrap high-resolution mass spectrometer (HRMS) (all by Thermo Fisher Scientific) equipped with an iHILIC-Fusion column, 100 mm x 2.1 mm with 1.8 μm particle size (Hilicon). The injection volume was 10 μL. A H₂O/ACN isocratic program was applied at a flow of 0.3 mL min⁻¹ with a run time of 5 min. The eluent composition was 97 % eluent B (100 % ACN) and 3 % eluent A (consisting of 5 mmol L⁻¹ ammonium formate in H₂O). To

improve ionisation, a post-column flow of 50 mmol L⁻¹ NH₄OH in MeOH was applied with a flow rate of 0.1 mL min⁻¹. The HESI source was operated in negative mode to form deprotonated molecular ions [M-H]⁻. The HESI probe was heated to 150 °C, the capillary temperature was set to 350 °C, and the spray voltage was -4.0 kV. The sheath gas pressure was 60 psi and the auxiliary gas pressure was 20 psi. The mass spectrometer was operated in full scan mode with a resolution of 70,000 and a scan range of *m/z* 80–500. During the expected retention times (Table 4.2), the full scan mode was alternated with a targeted MS² mode with a resolution of 17,500. For the MS² mode (i.e. parallel reaction monitoring mode in the software Xcalibur, provided by Thermo Fisher Scientific), higher-energy collisional dissociation (HCD) was used with 35% normalised collision energy (NCE).

Table 4.2. Common name, acronym, sum formula, retention time, *m/z* value, limit of detection, repeatability, and accuracy of ¹³C-MAs and MAs determined in the MA LC-MS method.

Analyte	Acronym	Sum formula	t _R (min)	<i>m/z</i> [M-H] ⁻	LOD (ng)	Repeat-ability (%)	Accuracy (%)
¹³ C ₆ -levoglucosan	¹³ C-LEV	¹³ C ₆ H ₁₀ O ₅	3.28	167.0657	NA	11.5	0.1
Mannosan	MAN	C ₆ H ₁₀ O ₅	2.65	161.0455 129.0193 [†]	0.05	4.4	0.3
Galactosan	GAL	C ₆ H ₁₀ O ₅	2.77	161.0455 113.0245 [†]	0.01	11.0	0.2
Levoglucosan	LEV	C ₆ H ₁₀ O ₅	3.30	161.0455 113.0245 [†] 101.0244 [†]	0.09	6.4	0.1

†: Fragments resulting from targeted MS².

4.4. Results and discussion

4.4.1. Method validation

Detection limits (LODs) were calculated using Equation 4.1 where B is the blank and SD_B the corresponding standard deviation.¹¹²

$$LOD = B + 3 SD_B \quad \text{Equation 4.1}^{112}$$

Recovery was calculated by spiking samples with known amounts of naphthalene-d₈ (42-102 %), acenaphthene-d₁₀ (41-120 %), phenanthrene-d₁₀ (46-137 %), and ¹³C₆-levoglucosan (62-83 %). The comparatively low PAH recovery rates were likely a consequence of volatilisation during the evaporation step. A comprehensive overview of all recoveries is found in Table S3. The sample set data were not corrected for recovery to acknowledge that the three deuterated PAHs examined do not necessarily reflect the properties of all 16 analysed PAHs. A 25 ng mL⁻¹ (PAHs) or a 2.5 ng mL⁻¹ (MAs) standard was used to calculate the accuracy of the method (percent relative deviation with respect to the standard concentration). Repeatability was calculated as the standard deviation of nine measurements of 25 ng mL⁻¹ (PAHs) or 2.5 ng mL⁻¹ (MAs) standards. Results are summarised in Table 4.1 and Table 4.2.

4.4.2. Speleothem MAs and PAHs

Levoglucosan (LEV) and $\Sigma 15$ (sum of non-alkylated PAHs) concentrations are presented in Figure 4.2. Concentrations of individual MAs and PAHs are found in Table S5, whereas calculated sums and ratios are shown in Table 4.3. The LEV and $\Sigma 15$ concentrations range from 0.6 to 5.7 ng g⁻¹ and 3.8 to 16.9 ng g⁻¹, respectively. The $\Sigma 15$ concentrations are greater than values presented by Argiriadis et al. (2019)⁹⁰ but lower than those reported by Perrette et al. (2008).⁹¹ $\Sigma 15$ concentrations and to a lesser extent, LEV concentrations, track the colour (grey value) of the stalagmite (Figure 4.2), suggesting a link between grey scale value and fire activity (soot).

Table 4.3: Calculated sums and diagnostic ratios of the 10 samples from stalagmite MAYA-22-7 from Cenote Ch'en Mul, Mayapan.

Age (Year CE)*	2010-2015	2000-2010	1995-2000	1945-1985	1945-1965	1920-1935	1890-1905	1855-1875	1760-1790	1640-1650
Sample #	4	3	5	2	6	8	9	1	10	11
$\Sigma 15^\dagger$	6.44	6.2	9.95	14.7	15.4	3.8	11.9	6.7	10.3	5.4
LMW \ddagger	6	5.6	9	13.8	14.5	3.7	11.3	6	9.7	5.04
HMW $^\circ$	0.4	0.5	0.9	0.9	0.9	0.02	0.6	0.7	0.5	0.3
LMW/HMW	13.6	10.4	10.33	14.9	15.8	175.5	19.3	8.5	18.9	14.7
PHE/ANT	74.7	4	43	3.4	NA	NA	NA	4.8	NA	NA
ANT/(ANT+PHE)	0.01	0.2	0.02	0.2	NA	NA	NA	0.2	NA	NA
RET/(RET+PHE+ANT)	NA	NA	0.16	NA	NA	NA	0.1	NA	NA	NA
LEV/(LEV+ $\Sigma 15$)	0.5	0.2	0.4	0.4	0.5	0.6	0.3	0.3	0.4	0.5
LEV/MAN	5.9	9.7	8	9.5	18.8	7.4	NA	9.1	8.8	6
LEV/(MAN+GAL)	3.3	4.7	4.6	4.8	5.9	3.7	18.6	5.4	4.7	3.1

*: Start and end dates have errors of $\pm 6-20$ years (95 % confidence interval) † : Sum of non-alkylated PAHs; ‡ : Sum of two and three-ring PAHs; $^\circ$: Sum of four and five-ring PAHs. Errors of sums and diagnostic ratios are reported in Table S6.

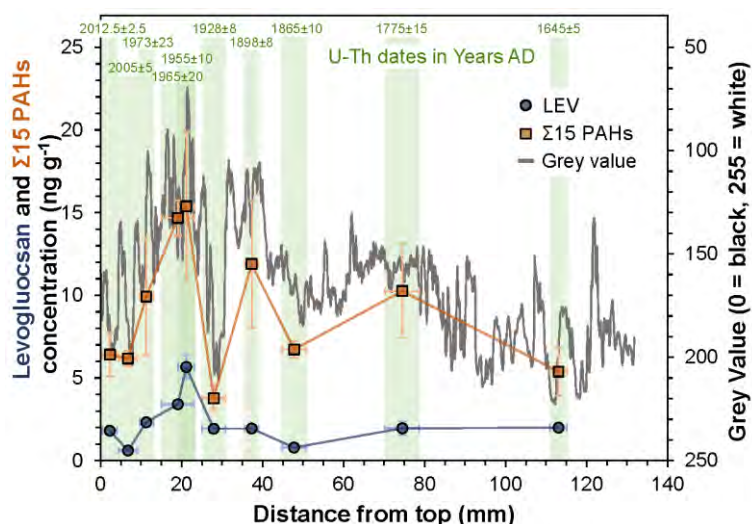


Figure 4.2. Concentrations of levoglucosan (dark blue) and $\Sigma 15$ (sum of non-alkylated PAHs; orange) in the 10 analysed samples from stalagmite MAYA-22-7. Symbols are centred on the middle of their respective sample pit (Figure 4.1). Error bars in the x-axis reflect the lengths of the sample pits. Error bars on the y-axis represent one standard deviation and may be smaller than the symbols. The grey line shows the grey value of stalagmite MAYA-22-7, measured along the growth axis. A value of 0 = black and 250 = white. Green shading represent the width of the sample pits and their respective U-Th dates are given at the top.

Overall, a strong correlation ($r = 0.75$, $p < 0.05$) between LEV and $\Sigma 15$ is observed (Figure 4.3). This correlation changes only slightly ($r=0.76$, $p < 0.05$) when solely low-molecular-weight PAHs (LMW, sum of two- and three-ring PAHs) are considered. This is consistent with the findings of Battistel et al. (2017)¹⁰¹ and suggests a common origin for LEV and smaller PAHs. The three most abundant PAHs (phenanthrene (PHE), naphthalene (NAP), and fluorene (FLN)) constitute an average of 82 ± 7 % of $\Sigma 15$ in the analysed samples. However, PHE, the most abundant PAH, does not show a significant correlation with LEV ($r=0.60$, $p < 0.1$, Figure 4.3, green circles). This is likely caused by different sources of PHE and LEV; it is possible that PHE is generated by higher-intensity fires than required to produce LEV.

Most high molecular weight PAHs (HMW, four- and five-ring PAHs) are below LOD in the analysed sample set. This is consistent with the results of Argiriadis et al. (2019)⁹⁰ and Perrette et al. (2008)⁹¹ and is likely a consequence of a filtering by the overlying soil and epikarst, as discussed by Perrette et al. (2013).²³⁶ They found that HMW PAHs accumulate in soils and only LMW PAHs are transferred into the ground water under steady state conditions. No literature addresses the inclusion of airborne PAHs into speleothems or whether fractionation between HMW and LMW PAHs might be expected. However, it is plausible that LMW PAHs are more readily dissolved in the water-film that covers actively growing speleothems, than are HMW PAHs. This is supported by the respective n-octanol/water partition coefficient (K_{ow}) and air/water partition coefficient (K_{aw}) values, according to which, for instance, NAP is 1-2 orders of magnitude more likely to enter the aqueous phase than BAA.^{255,256} HMW PAHs adsorbed to particles could also be incorporated into the growing speleothem. However, Dickson et al. (2023)²⁵⁷ demonstrated that microscopic particles are situated on the flanks of a stalagmite rather than at the centre. As the samples analysed in this study were drilled along the growth axis, particulate PAHs would very likely not be encountered.

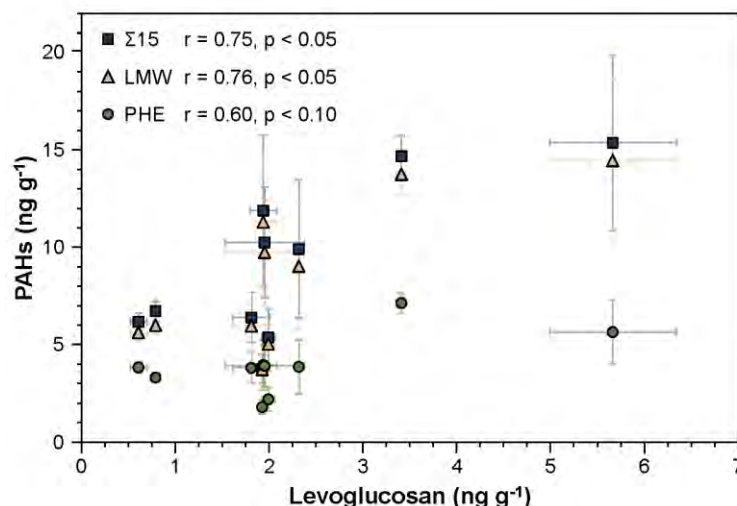


Figure 4.3. Correlation of levoglucosan and PAHs in the 10 samples analysed from stalagmite MAYA-22-7. Blue squares: $\Sigma 15$ (sum of non-alkylated PAHs); beige triangles: LMW (sum of two and three-ring PAHs); green circles: PHE. Error bars represent one standard deviation and may be smaller than the symbols.

Table 4.4. Typically reported values of diagnostic ratios of PAHs and MAs, and respective interpretations.

Ratio	Values	Interpretation	Reference	Medium applied to
LMW/HMW	< 1	Pyrogenic	Zhang et al. (2008) ²⁵⁸	Water
	> 1	Petrogenic		
PHE/ANT	< 10	Pyrogenic	Zhang et al. (2008) ²⁵⁸	Water
	> 15	Petrogenic		
ANT/(PHE+ANT)	< 0.1	Petrogenic	Yunker et al. (2002a) ⁸⁸	River sediment
	> 0.1	Pyrogenic		
RET/(RET+CHR)	0.15-0.50	Petrol combustion	Yan et al. (2005) ⁹⁵	Lake sediment
	0.30-0.45	Coal combustion		
	0.83-0.96	Softwood combustion		
RET/(RET+PHE+ANT)	> 0.1	Gymnosperm combustion	Karp et al. (2020) ⁹⁷	Aerosols
	< 0.1	Angiosperm combustion		
LEV/(LEV+ $\Sigma 15$) [†]	< 0.5	High-intensity fires	Ruan et al. (2020) ²⁵⁹	Marine Sediment
	0.5	Boundary		
	> 0.5	Low-intensity fires		
LEV/MAN	0.5-14	Softwoods	Fabbri et al. (2009) ⁶⁷ and references therein; Kuo et al. (2011) ⁶⁶	Aerosols; Chars
	3-32	Hardwoods		
	4-55	Grasses		
	30-90	Lignite		
LEV/(MAN+GAL)	0.5-6	Softwoods	Fabbri et al. (2009) ⁶⁷ and references therein; Kuo et al. (2011) ⁶⁶	Aerosols; Chars
	1.5-10	Hardwoods		
	4-55	Grasses		
	30-90	Lignite		

[†]: LEV and $\Sigma 15$ are normalised to the highest value of the series.

The lack of HMW PAHs means that some PAH ratios normally used to characterise PAH profiles (Table 4.4) may not apply to speleothems. An example of such a ratio is LMW/HMW; for directly deposited samples such as aerosols or sediments, a ratio > 1 indicates a petrogenic origin of PAHs.^{258,260} The artificially lowered HMW levels observed in speleothems

results in very high LMW/HMW ratios (Table 4.3), rendering this ratio insensitive to the origin of the PAHs. More promising diagnostic metrics in speleothem analysis could be individual PAHs. For this purpose, we studied the ratios of two or more compounds with similar molecular formulas but different molecular structures, assuming that the compounds have comparable physicochemical properties (i.e. volatility, solubility, atmospheric lifetime, adsorption, and transport mechanisms) but different predominant origins.⁸⁷ At high temperatures, a less stable, “kinetic” isomer is formed, which has more aromatic rings and less alkyl substitutes compared to the product at lower combustion temperatures or of petrogenic origin.^{73,74,94} Phenanthrene (PHE) and anthracene (ANT) form one pair, where PHE is the thermodynamic and ANT the kinetic isomer.²⁶⁰ The resulting PHE/ANT and ANT/(ANT+PHE) ratios can also be used to distinguish between pyrogenic (PHE/ANT < 10; ANT/(ANT+PHE) > 0.1) and petrogenic (> 10; < 0.1) origins of the PAHs and appear to apply to our stalagmite samples. The PHE-ANT ratios of samples #1-3 indicate pyrogenic origin; for the remainder of the samples, ANT is very close to or below the LOD. Therefore, we cannot conclude with certainty a petrogenic origin of the PAHs in samples #4-11.

Retene (RET) is an alkylated PAH and a molecular marker of gymnosperm combustion.^{98,99,261} Unfortunately, RET was below the LOD for all but two samples. Literature suggests that gymnosperm vegetation is not common in the study area.^{262–265} Nevertheless, RET might provide a promising marker of fire dynamics in speleothems if it is present in sufficient concentrations. RET is also used in various diagnostic ratios. For instance, in combination with chrysene (CHR), where RET/(RET + CHR) helps to determine fuel type.⁹⁵ Because CHR is one of the HMW PAHs, it is below the LOD for all samples in this study, but this ratio could potentially be utilised in other samples. In addition, Karp et al. (2020)⁹⁷ suggested the use of a ratio that includes three 3-ring PAHs, RET, PHE, and ANT, where RET/(RET+PHE+ANT) is used to distinguish between gymnosperm (softwood, > 0.1) and angiosperm (hardwood, < 0.1) combustion. As mentioned above, in our sample set, RET is above the LOD in only two samples. For one of these (1995-2000 CE) the ratio points towards gymnosperm fuel, whereas the result for the other sample (1890-1905 CE) falls right on the boundary between angiosperm and gymnosperm fuel. This ratio could be particularly useful in combination with the MAs, which can also be used to determine fuel type.

MA ratios, LEV MAN⁻¹ and LEV (MAN + GAL)⁻¹, respectively, have been shown to capture the type of biomass burned (Fabbri et al. (2009)⁶⁷ and references therein; Kuo et al. (2011)⁶⁶). According to Fabbri et al. (2009)⁶⁷, the use of LEV (MAN + GAL)⁻¹ is even more sensitive and discriminating. The ratios in our study are shown in Figure 4.4 (a) and indicate combustion of predominantly mixed hardwoods and softwoods. Kuo et al. (2011)⁶⁶, however, showed that high combustion temperatures may shift the MA ratios to higher values because hemicellulose is less thermally stable than cellulose. This means that MAN and GAL are not emitted at higher temperatures, whereas LEV can still be formed. This could be the case for our sample from 1890-1905 CE (light orange in Figure 4.4 (a)), in which no MAN could be detected and the resulting LEV (MAN + GAL)⁻¹ is very high. Therefore, it might be useful to combine the MA ratios with an indicator of fire intensity.

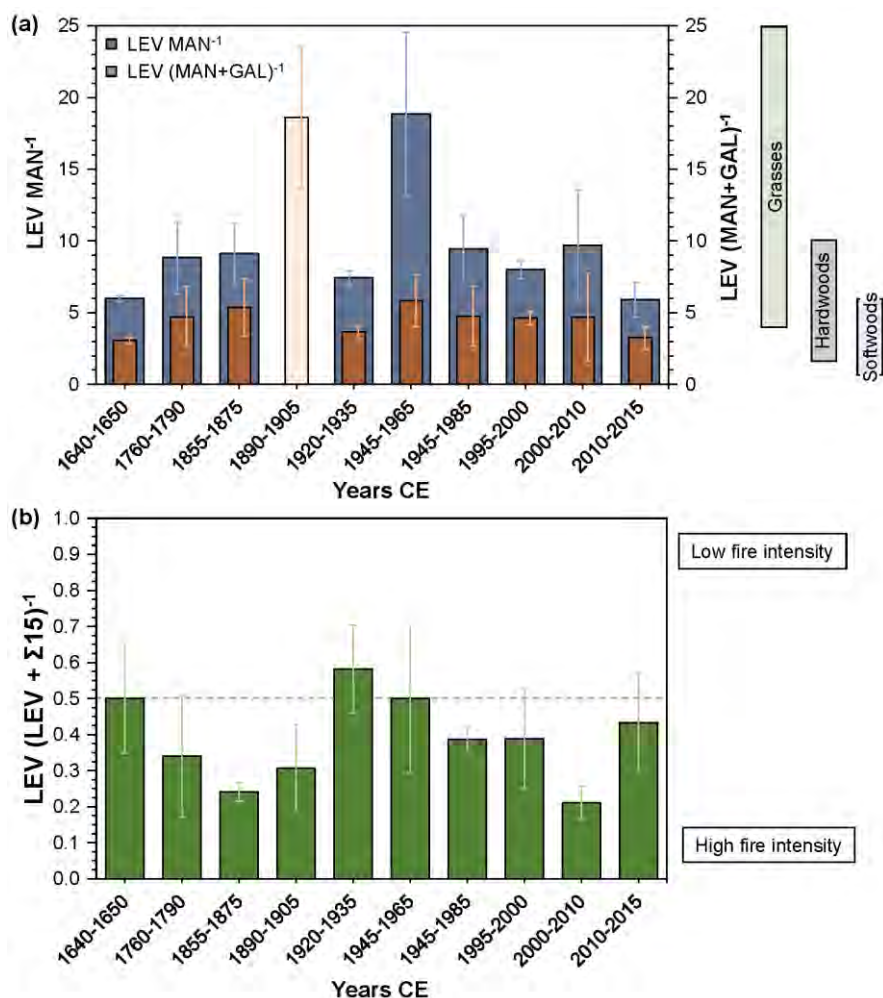


Figure 4.4: (a) $LEV\ MAN^{-1}$ (dark blue) and $LEV\ (MAN + GAL)^{-1}$ (orange) ratios of the 10 samples analysed from stalagmite MAYA-22-7. Coloured bars on the right indicate the burned fuel based on the $LEV\ (MAN + GAL)^{-1}$ ratio according to Fabbri et al. (2009)⁶⁷ and Kuo et al. (2011).⁶⁶ Green: grasses; grey: hardwoods; blue: softwoods. Age range listed is the OxCal modelled mean age at the top and bottom of each sample pit. Start and end dates have errors of $\pm 6-20$ years (95 % confidence interval; see Table S3). Error bars represent one standard deviation. (b) $LEV\ (LEV + \Sigma 15)^{-1}$ ratios of the 10 samples analysed. The dashed line represents the boundary between MA-dominated fire regimes (low intensity) and PAH-dominated fire regimes (high intensity). Age range listed is the OxCal modelled mean age at the top and bottom of each sample pit. Start and end dates have errors of $\pm 6-20$ years (95 % confidence interval; see Table S3). Error bars represent one standard deviation.

Ruan et al. (2020)²⁵⁹ suggested the use of $LEV\ (LEV + \Sigma 15)^{-1}$, with both LEV and $\Sigma 15$ normalised to the highest value in the series. Values > 0.5 indicate a predominance of PAHs and high fire intensity, whereas values < 0.5 indicate low intensity fires with dominant MA emission. Figure 4.4 (b) shows two distinct peaks in fire intensity (i.e. low LEV contribution) in the 1855-1875 CE and 2000-2010 CE samples. The 1890-1905 CE sample mentioned above also shows high-intensity fires, supporting the interpretation that the $LEV\ (MAN + GAL)^{-1}$ ratio may have been artificially increased. The 1920-1935 CE sample is the only one that clearly indicates low fire intensity, whereas the remaining samples fall into the high-intensity fire regime. We note however, the relatively large analytical uncertainties make a definitive interpretation difficult.

4.4.3. LEV and PAHs as indicators of fire activity at Cenote Ch'en Mul

We applied our results to infer past fire activity in and around Cenote Ch'en Mul. Mayapan was the last capital of the Late Postclassic Maya period and was abandoned in the mid-15th century.^{266,267} Its ruins, including the round temple and the Kukulcan temple, were first reported to the English-speaking world in 1841 by John Stephens. Although preliminary excavations were conducted in the early 20th century, major archaeological work only took place in the 1950s under the auspices of the Carnegie Institution.²⁶⁷ These archaeological activities are relevant to the present study, because human-induced fires related to the excavations (land-clearing, use of kerosene lamps or open fires, etc.) produced LEV and PAH that should be recorded in our dataset. Activities like water collection or ritual incense burning have a very long history in Yucatan and are still conducted to this day. Any open flame combustion thus adds to the overall PAH and MA load in the cave, and potentially in speleothems. The signal observed in a stalagmite represents the integral of all accumulated PAHs and MAs, and in-depth research is required to differentiate the relative contribution of each pathway.

Stalagmite MAYA-22-7 grew fast (growth rate of 200-300 $\mu\text{m}/\text{year}$ before the dark layer at a distance of 15-23 mm from the top, and 500-600 $\mu\text{m}/\text{year}$ after that dark layer) and covers only the last ~ 400 years, i.e. the period after the site was abandoned by the Postclassic Maya. The fire history inferred from the stalagmite is likely related to both natural fires in the low-stature, thorny, deciduous tropical forest that characterised the area, and land-clearing activities that preceded archaeological excavation at the site. Early and middle 20th century archaeological efforts likely used kerosene lamps for work in Cenote Ch'en Mul. Parts of the Mayapan site might have been cleared of vegetation using fire, although it is difficult to find evidence for this practice in archaeological field reports. The Carnegie excavations might have used both kerosene and battery powered lights. Either way, it is plausible that LEV and PAHs from human-induced fires might be recorded in the stalagmite.

This is in accordance with our findings, in that the samples covering the period 1945-1985 show the highest LEV and PAH concentrations in the whole sample set. Finding elevated PAH and MA concentrations in speleothem carbonate that dates to a time of higher human-induced fire activity is encouraging and suggests that speleothems are sensitive recorders of combustion products.

4.5. Conclusions

We used a sequential extraction preparation method for analysis of 16 PAHs and three MAs in samples from a stalagmite collected at the Postclassic Maya archaeological site of Mayapan, Yucatán, Mexico. Sample preparation involved solid-liquid extraction of pulverised carbonate samples. To our knowledge, this is one of only a few methods for analysis of PAHs in speleothems and the only one that also enables analysis of MAs. The new method requires relatively small sample amounts (0.5-1.0 g) and simple instrumentation, i.e. an ultrasonic

bath and a sample concentrator. PAHs and MAs were measured by GC-MS and LC-HILIC-MS, respectively.

We applied the method to 10 samples from the MAYA-22-7 stalagmite, collected at Cenote Ch'en Mul, directly below the site of Mayapan. We used concentrations and selected ratios of PAHs and MAs described in the literature to explore fire history in this area of the Yucatán Peninsula. We found a positive correlation between the major MA, levoglucosan, and non-alkylated PAHs ($\Sigma 15$), or two- and three-ring PAHs (LMW), ($r = 0.75$, $p < 0.05$, and $r = 0.76$, $p < 0.05$, respectively). Not all diagnostic PAH ratios were applicable, but the ratios combining PAHs with MAs appear to have promise for discriminating among different fire regimes and inferring the source of burned fuel. Furthermore, retene (RET) can be used as a molecular marker for gymnosperm combustion, if present in high enough concentrations. However, it has to be noted that the HMW PAHs were often below LOD, probably because of a filtering effect of the overlying soil. This limited our ability to fully exploit the data set to interpret past fire dynamics at Mayapan.

Our analyses suggest that within the analysed time series, the period 1945-1985 stands out in terms of high fire activity. We tentatively interpret this result to indicate clearing of the site prior to and during mid-20th-century archaeological excavation. A longer record of the two biochemical proxies from older stalagmites from Che'Mul Cave could document the history of cave use by the Maya for ceremonial and practical purposes - burning undoubtedly occurred within the cave (e.g. torches for lighting).

4.6. Future Work

Future work should be directed towards i) refinement of methods to delineate dripwater- and aerosol-derived fire proxies, ii) deciphering transport mechanisms and potential scavenging effects in the soil and epikarst, and iii) interplay with other proxies. The PAH extraction method should be improved to optimise recovery and reduce its variance. One possible approach is to perform a systematic solvent screening to improve the extraction efficiency. Alternatively, the extraction method could be modified, e.g. by utilisation of microwave extraction or accelerated solvent extraction. Another route is the addition of a keeper (e.g. nonane) during evaporation, to reduce losses to volatilisation, similar to the method described by Wietzoreck et al. (2022).⁸⁴ To correct the data for recovery, additional deuterated PAH standards could be added.

In addition, monitoring rainfall and dripwater at the sample site would be useful to track changes in PAH and MA patterns and to gain a deeper understanding of site-specific transport mechanisms. It would also be beneficial to apply our method to other speleothems from the same cave and other sites, to test whether our results are generally applicable. The two biochemical proxies studied here should be combined with other, established proxies such as carbon and oxygen isotope ratios as well as trace elements described by Campbell et al. (2023),³² to gain further insights into the interplay among fire, hydrology, vegetation, and human activities. Finally, other source-specific PAH species could be added to enhance the interpretation of the PAH patterns. Potentially suitable PAHs include 1,2- and

1,7-dimethylphenanthrene (1,2- and 1,7-DMP). Kappenberg et al. (2019)²⁶⁸ suggested that their ratio could be used as an alternative to distinguish among different types of burned biomass.

4.7. Data availability

All data from our study are presented numerically in the paper and in the Supplement.

4.8. Author contributions

JH and TH designed the study. JH and NK conducted the method development, sample preparation, and data analysis for PAHs and MAs. CL and MB enabled sampling in Cenote Ch'en Mul. DJ, OK, DH, and SB collected stalagmite MAYA-22-7. OK and SB surveyed Cenote Ch'en Mul and prepared the cave map. SC and DJ subsampled the stalagmite for analysis and constructed the age model. All co-authors participated in discussions, interpretation of the data, and writing of the manuscript.

4.9. Competing interests

The contact author has declared that none of the authors has any competing interests.

4.10. Acknowledgements

The authors thank Drs. Susan Milbrath and Marilyn Masson for insights on the history of the archaeological excavations. JH gratefully acknowledges financial support from the Max Planck Graduate Center Mainz. Some of the analytical developments included here were developed with financial support from DFG Project HO 1748/20-1 (Organic trace analysis of atmospheric marker substances in ice cores). DH acknowledges financial support from the Leverhulme Trust Award RPG-2019-228.

5. Conclusion and outlook

In this work, selective and sensitive methods for the analysis of different organic marker species in speleothem samples have been developed or adapted from previous works. Existing sample preparation procedures for the extraction and oxidation of lignin and the extraction of three monosaccharide anhydrides (MAs; levoglucosan, mannosan, and galactosan) have been optimised. New procedures for the electrochemical oxidation and degradation of lignin and the extraction of polycyclic aromatic hydrocarbons (PAHs) from speleothem samples have been developed. The methods have subsequently been applied to real-world samples.

An electrochemical method for the anodic oxidation and subsequent degradation of lignin in speleothems was developed. The new method achieved comparable or even higher lignin oxidation product (LOP) concentrations than the established CuO and CuSO₄ oxidation methods. The method sped up sample preparation and reduced the risk of contamination input from the chemicals used. The use of electricity as the terminal oxidant avoided the use of stoichiometric amounts of heavy metals. The oxidation step can easily be adapted to the particular sample matrix (e.g. organic carbon content) and thus could be useful for the analysis of other environmental samples such as soils or sediments.

The established CuSO₄ oxidation method for lignin and the solid-liquid-extraction method for levoglucosan were applied to samples from White Moon Cave (WMC) in the California Coast Range. A portion of stalagmite WMC1 that brackets the 8.2 kyr event (an interval of freshwater forcing and abrupt cooling in the North Atlantic) and modern dripwater were analysed. During the 8.2 kyr event and a “precursor” event at 8,300 years BP, stalagmite isotope and trace element proxies all indicate overall wetter winters and a potentially more volatile hydroclimate relative to the rest of the record.^{207,209} During the event, elevated levoglucosan concentrations suggest increased fire activity while altered LOP compositions indicate a shift toward more woody vegetation. Together, these records suggest that climate whiplash (oscillations between extreme wetness and aridity) and fire activity in California, both projected to increase with anthropogenic climate change, were tightly coupled during the early Holocene. The dripwater analysis suggest that the levoglucosan signal in WMC dripwater may only reflect the fire activity of the most recent fire season, and that high rainfall intervals rapidly leach the signal from the soil. This study successfully demonstrated that LOPs and levoglucosan can be used jointly in a suitable speleothem to reconstruct climatic changes on a timescale of a few decades to centuries. The extension of the marker substances to include levoglucosan as a biomass burning marker enables a more differentiated view of which environmental and climatic conditions may drive vegetation changes and vice versa.

The developed sequential extraction preparation method for the analysis of 16 PAHs and three MAs was applied to 10 samples from a stalagmite collected at the Postclassic Maya archaeological site of Mayapan, Yucatán, Mexico. Determined PAH and MA concentrations and selected ratios of PAHs and MAs described in the literature were used to explore the fire history in this area of the Yucatán Peninsula. The results revealed a positive correlation between the major MA, levoglucosan, and non-alkylated PAHs ($\Sigma 15$), or two- and three-ring

PAHs (LMW), ($r = 0.75$, $p < 0.05$, and $r = 0.76$, $p < 0.05$, respectively). Not all diagnostic PAH ratios were applicable, but the ratios combining PAHs with MAs appear to have promise for discriminating among different fire regimes and inferring the source of burned fuel. Furthermore, retene (RET) can be used as a molecular marker for gymnosperm combustion, if present in high enough concentrations. The analyses suggests that within the analysed time series, the period 1945-1985 stands out in terms of high fire activity. This could be due to the clearing of the site prior to and during mid-20th-century archaeological excavation. A longer record of the two biochemical proxies from older stalagmites from Che'Mul Cave could document the history of cave use by the Maya for ceremonial and practical purposes as burning undoubtedly occurred within the cave (e.g. torches for lighting).

In addition to the projects presented in this thesis, further speleothem samples were analysed from Siberia (Botovskaya Cave and Taba Bastaakh), Scotland (Rana Hole and Uamh Mhor), Germany (Bleßberg Cave), Spain (Cueva Victoria) and Brazil (Cuíca Cave and Lage Branca Cave). Some of these results are currently being prepared for publication.

For future work, the described methods should be further optimised with regards to recovery and required sample size. Recovery of the PAH extraction method may be increased through the addition of a keeper (e.g. nonane) during the evaporation steps to avoid loss by evaporation; a similar procedure is described by Wietzoreck et al. (2022).⁸⁴ In addition, a variety of solvents should be systematically tested for their suitability as extraction agents for PAHs. The simplest way to reduce the sample size would be to use a more sensitive analysis technique. This could be achieved by using a triple quadrupole mass spectrometer.

The three biochemical proxies studied here should be combined with other, established proxies such as carbon and oxygen isotope ratios as well as trace elements similar to the study described by Campbell et al. (2023)³² to gain further insights into the interplay among fire, hydrology, vegetation, and human activities. Further information from cave monitoring studies along geologic, ecologic, and hydrologic gradients is necessary to evaluate the degree to which MAs and PAHs record more distal fires, the longevity of their signals in soils, and how the proxies are transported through the epikarst and embedded in speleothems. Study sites with a known fire history or with adjacent paleoclimate archives containing other fire and vegetation markers like fire scars in tree-rings, charcoal, or pollen should be prioritised to better restrict the parameters that influence the MA, PAH, and LOP signal in speleothems. It would also be beneficial to apply the described methods to multiple speleothems from one cave covering the same timeframes and samples from various sites, to test the repeatability and restraints of the methods.

Finally, other biochemical proxies should be investigated. Another source-specific PAH species could be added to enhance the interpretation of the PAH patterns. Potentially suitable PAHs include 1,2- and 1,7-dimethylphenanthrene (1,2- and 1,7-DMP). Kappenberg et al. (2019)²⁶⁸ suggested that their ratio could be used to distinguish among different types of burned biomass. Faecal sterols could be investigated to mark the presence of humans and grazing animals. This analysis is already applied to sediment cores¹⁰⁰⁻¹⁰² and holds the potential to provide information on the interplay of climatic and vegetal conditions and human activity. The additional analysis of GDGTs (glycerol dialkyl glycerol tetraethers) as

indicators of paleo-temperature would also add another helpful component to the interpretation. Several procedures for their analysis in speleothems have already been published and could easily be adapted. ^{37,41-43}

6. References

1. Fairchild, I. J. & Baker, A. *Speleothem Science* (John Wiley & Sons, Ltd, Chichester, UK, 2012).
2. Bradley, R. S. *Paleoclimatology. Reconstructing climates of the quaternary*. 3rd ed. (Academic Press/Elsevier, Amsterdam, 2015).
3. Fairchild, I. J. *et al.* Modification and preservation of environmental signals in speleothems. *Earth-Science Reviews* **75**, 105–153; 10.1016/j.earscirev.2005.08.003 (2006).
4. Scholz, D. & Hoffmann, D. $^{230}\text{Th}/\text{U}$ -dating of fossil corals and speleothems. *Quaternary Science Journal*, 52–76; 10.23689/figeo-1056 (2008).
5. Ford, T. D. & Cullingford, C. H. D. (eds.). *The science of speleology*. 2nd ed. (Academic Press, London, 1978).
6. Blyth, A. J. *et al.* Molecular organic matter in speleothems and its potential as an environmental proxy. *Quaternary Science Reviews* **27**, 905–921; 10.1016/j.quascirev.2008.02.002 (2008).
7. Fohlmeister, J. *et al.* Main controls on the stable carbon isotope composition of speleothems. *Geochimica et Cosmochimica Acta* **279**, 67–87; 10.1016/j.gca.2020.03.042 (2020).
8. Fairbanks, R. G. *et al.* Radiocarbon calibration curve spanning 0 to 50,000 years BP based on paired $^{230}\text{Th}/^{234}\text{U}/^{238}\text{U}$ and ^{14}C dates on pristine corals. *Quaternary Science Reviews* **24**, 1781–1796; 10.1016/j.quascirev.2005.04.007 (2005).
9. Hua, Q. Radiocarbon: A chronological tool for the recent past. *Quaternary Geochronology* **4**, 378–390; 10.1016/J.QUAGEO.2009.03.006 (2009).
10. Mason, A. J., Vaks, A., Breitenbach, S. F. M., Hooker, J. N. & Henderson, G. M. A simplified isotope dilution approach for the U–Pb dating of speleogenic and other low- ^{232}Th carbonates by multi-collector ICP-MS. *Geochronology* **4**, 33–54; 10.5194/gchron-4-33-2022 (2022).
11. Ivanovich, M. & Harmon, R. S. (eds.). *Uranium Series Disequilibrium. Applications to Earth, Marine and Environmental Sciences*. 2nd ed. (1992).
12. Obert, J. C. *et al.* $^{230}\text{Th}/\text{U}$ dating of Last Interglacial brain corals from Bonaire (southern Caribbean) using bulk and theca wall material. *Geochimica et Cosmochimica Acta* **178**, 20–40; 10.1016/j.gca.2016.01.011 (2016).
13. Cheng, H. *et al.* Improvements in ^{230}Th dating, ^{230}Th and ^{234}U half-life values, and U–Th isotopic measurements by multi-collector inductively coupled plasma mass spectrometry. *Earth and Planetary Science Letters* **371–372**, 82–91; 10.1016/j.epsl.2013.04.006 (2013).
14. Hoffmann, D. L. ^{230}Th isotope measurements of femtogram quantities for U-series dating using multi ion counting (MIC) MC-ICPMS. *International Journal of Mass Spectrometry* **275**, 75–79; 10.1016/j.ijms.2008.05.033 (2008).

15. Hoffmann, D. L. *et al.* Procedures for accurate U and Th isotope measurements by high precision MC-ICPMS. *International Journal of Mass Spectrometry* **264**, 97–109; 10.1016/j.ijms.2007.03.020 (2007).
16. Chiang, H.-W., Lu, Y., Wang, X., Lin, K. & Liu, X. Optimizing MC-ICP-MS with SEM protocols for determination of U and Th isotope ratios and ²³⁰Th ages in carbonates. *Quaternary Geochronology* **50**, 75–90; 10.1016/j.quageo.2018.10.003 (2019).
17. Scholz, D. & Hoffmann, D. L. StalAge – An algorithm designed for construction of speleothem age models. *Quaternary Geochronology* **6**, 369–382; 10.1016/j.quageo.2011.02.002 (2011).
18. Ramsey, C. B. & Lee, S. Recent and Planned Developments of the Program OxCal. *Radiocarbon* **55**, 720–730; 10.1017/S0033822200057878 (2013).
19. Breitenbach, S. F. M. *et al.* COConstructing Proxy Records from Age models (COPRA). *Clim. Past* **8**, 1765–1779; 10.5194/cp-8-1765-2012 (2012).
20. McDermott, F. Palaeo-climate reconstruction from stable isotope variations in speleothems: a review. *Quaternary Science Reviews* **23**, 901–918; 10.1016/j.quascirev.2003.06.021 (2004).
21. Lachniet, M. S. Climatic and environmental controls on speleothem oxygen-isotope values. *Quaternary Science Reviews* **28**, 412–432; 10.1016/j.quascirev.2008.10.021 (2009).
22. Bajnai, D. *et al.* Dual clumped isotope thermometry resolves kinetic biases in carbonate formation temperatures. *Nat Commun* **11**, 4005; 10.1038/s41467-020-17501-0 (2020).
23. Demény, A. *et al.* Paleotemperature reconstructions using speleothem fluid inclusion analyses from Hungary. *Chemical Geology* **563**, 120051; 10.1016/j.chemgeo.2020.120051 (2021).
24. Matthews, A., Affek, H. P., Ayalon, A., Vonhof, H. B. & Bar-Matthews, M. Eastern Mediterranean climate change deduced from the Soreq Cave fluid inclusion stable isotopes and carbonate clumped isotopes record of the last 160 ka. *Quaternary Science Reviews* **272**, 107223; 10.1016/j.quascirev.2021.107223 (2021).
25. Affolter, S. *et al.* Central Europe temperature constrained by speleothem fluid inclusion water isotopes over the past 14,000 years. *Science advances* **5**, eaav3809; 10.1126/sciadv.aav3809 (2019).
26. Fairchild, I. J. & Treble, P. C. Trace elements in speleothems as recorders of environmental change. *Quaternary Science Reviews* **28**, 449–468; 10.1016/j.quascirev.2008.11.007 (2009).
27. Gascoyne, M. Trace-element partition coefficients in the calcite-water system and their paleoclimatic significance in cave studies. *Journal of Hydrology* **61**, 213–222; 10.1016/0022-1694(83)90249-4 (1983).
28. Bian, F. *et al.* Hydrological and geochemical responses of fire in a shallow cave system. *Science of The Total Environment* **662**, 180–191; 10.1016/j.scitotenv.2019.01.102 (2019).

29. Coleborn, K. *et al.* Effects of wildfire on long-term soil CO₂ concentration: implications for karst processes. *Environ Earth Sci* **75**, 125; 10.1007/s12665-015-4874-9 (2016).
30. Nagra, G. *et al.* A post-wildfire response in cave dripwater chemistry. *Hydrol. Earth Syst. Sci.* **20**, 2745–2758; 10.5194/hess-20-2745-2016 (2016).
31. Treble, P. C. *et al.* Roles of forest bioproductivity, transpiration and fire in a nine-year record of cave dripwater chemistry from southwest Australia. *Geochimica et Cosmochimica Acta* **184**, 132–150; 10.1016/j.gca.2016.04.017 (2016).
32. Campbell, M. *et al.* A Review of Speleothems as Archives for Paleofire Proxies, With Australian Case Studies. *Reviews of Geophysics* **61**; 10.1029/2022RG000790 (2023).
33. Coleborn, K. *et al.* The impact of fire on the geochemistry of speleothem-forming drip water in a sub-alpine cave. *The Science of the total environment* **642**, 408–420; 10.1016/j.scitotenv.2018.05.310 (2018).
34. Coleborn, K. *et al.* Corrigendum to "The impact of fire on the geochemistry of speleothem-forming drip water in a sub-alpine cave" *Sci. Total Environ.* (2018) 408-420. *The Science of the total environment* **668**, 1339–1340; 10.1016/j.scitotenv.2019.02.350 (2019).
35. McDonough, L. K. *et al.* Past fires and post-fire impacts reconstructed from a southwest Australian stalagmite. *Geochimica et Cosmochimica Acta*; 10.1016/j.gca.2022.03.020 (2022).
36. Heidke, I., Scholz, D. & Hoffmann, T. Lignin oxidation products as a potential proxy for vegetation and environmental changes in speleothems and cave drip water – a first record from the Herbstlabyrinth, central Germany. *Clim. Past* **15**, 1025–1037; 10.5194/cp-15-1025-2019 (2019).
37. Baker, A. *et al.* Glycerol dialkyl glycerol tetraethers (GDGT) distributions from soil to cave: Refining the speleothem paleothermometer. *Organic Geochemistry* **136**, 103890; 10.1016/j.orggeochem.2019.06.011 (2019).
38. Blyth, A. J., Hartland, A. & Baker, A. Organic proxies in speleothems – New developments, advantages and limitations. *Quaternary Science Reviews* **149**, 1–17; 10.1016/j.quascirev.2016.07.001 (2016).
39. Bosle, J. M., Mischel, S. A., Schulze, A.-L., Scholz, D. & Hoffmann, T. Quantification of low molecular weight fatty acids in cave drip water and speleothems using HPLC-ESI-IT/MS - development and validation of a selective method. *Analytical and bioanalytical chemistry* **406**, 3167–3177; 10.1007/s00216-014-7743-6 (2014).
40. Homann, J., Oster, J. L., Wet, C. B. de, Breitenbach, S. F. M. & Hoffmann, T. Linked fire activity and climate whiplash in California during the early Holocene. *Nat Commun* **13**, 1–9; 10.1038/s41467-022-34950-x (2022).
41. Blyth, A. J. & Schouten, S. Calibrating the glycerol dialkyl glycerol tetraether temperature signal in speleothems. *Geochimica et Cosmochimica Acta* **109**, 312–328; 10.1016/j.gca.2013.02.009 (2013).

42. Yang, H. *et al.* Occurrence of tetraether lipids in stalagmites: Implications for sources and GDGT-based proxies. *Organic Geochemistry* **42**, 108–115; 10.1016/j.orggeochem.2010.11.006 (2011).
43. Blyth, A. J., Jex, C. N., Baker, A., Khan, S. J. & Schouten, S. Contrasting distributions of glycerol dialkyl glycerol tetraethers (GDGTs) in speleothems and associated soils. *Organic Geochemistry* **69**, 1–10; 10.1016/j.orggeochem.2014.01.013 (2014).
44. Blyth, A. J., Baker, A., Thomas, L. E. & van Calsteren, P. A 2000-year lipid biomarker record preserved in a stalagmite from north-west Scotland. *J. Quaternary Sci.* **26**, 326–334; 10.1002/jqs.1457 (2011).
45. Hitzemann, I. Entwicklung einer Methode zur Analyse von Fettsäuren und Ligninphenolen in Speläothemen mittels HPLC-ESI-MS. Diplomarbeit. Johannes Gutenberg-Universität, April 2015.
46. Blyth, A. J. *et al.* A new approach to detecting vegetation and land-use Change using high-resolution lipid biomarker records in stalagmites. *Quat. res.* **68**, 314–324; 10.1016/j.yqres.2007.08.002 (2007).
47. Xie, S. *et al.* Lipid distribution in a subtropical southern China stalagmite as a record of soil ecosystem response to paleoclimate change. *Quat. res.* **60**, 340–347; 10.1016/j.yqres.2003.07.010 (2003).
48. Andreae, M. O. Atmospheric Aerosols: Biogeochemical Sources and Role in Atmospheric Chemistry. *Science* **276**, 1052–1058; 10.1126/science.276.5315.1052 (1997).
49. Boerjan, W., Ralph, J. & Baucher, M. Lignin biosynthesis. *Annual review of plant biology* **54**, 519–546; 10.1146/annurev.arplant.54.031902.134938 (2003).
50. Brown, S. A. Biochemistry of Lignin Formation. *BioScience* **19**, 115–121; 10.2307/1294669 (1969).
51. Vanholme, R., Demedts, B., Morreel, K., Ralph, J. & Boerjan, W. Lignin biosynthesis and structure. *Plant Physiology* **153**, 895–905; 10.1104/pp.110.155119 (2010).
52. Jex, C. N. *et al.* Lignin biogeochemistry: from modern processes to Quaternary archives. *Quaternary Science Reviews* **87**, 46–59; 10.1016/j.quascirev.2013.12.028 (2014).
53. Heidke, I., Scholz, D. & Hoffmann, T. Quantification of lignin oxidation products as vegetation biomarkers in speleothems and cave drip water. *Biogeosciences* **15**, 5831–5845; 10.5194/bg-15-5831-2018 (2018).
54. Hedges, J. I. & Mann, D. C. The characterization of plant tissues by their lignin oxidation products. *Geochimica et Cosmochimica Acta* **43**, 1803–1807; 10.1016/0016-7037(79)90028-0 (1979).
55. Goñi, M. A. & Montgomery, S. Alkaline CuO oxidation with a microwave digestion system: lignin analyses of geochemical samples. *Anal. Chem.* **72**, 3116–3121; 10.1021/ac991316w (2000).

56. Yan, G. & Kaiser, K. Ultralow Sample Volume Cupric Sulfate Oxidation Method for the Analysis of Dissolved Lignin. *Anal. Chem.* **90**, 9289–9295; 10.1021/acs.analchem.8b01867 (2018).
57. Beschnitt, A. Development and application of analytical methods for trace analysis of organic marker species in climate archives using liquid chromatography and high-resolution mass spectrometry. Dissertation. Johannes Gutenberg-Universität Mainz, 2022.
58. Heidke, I. *et al.* Lignin oxidation products in soil, dripwater and speleothems from four different sites in New Zealand. *Biogeosciences* **18**, 2289–2300; 10.5194/bg-18-2289-2021 (2021).
59. Blyth, A. J. & Watson, J. S. Thermochemolysis of organic matter preserved in stalagmites: A preliminary study. *Organic Geochemistry* **40**, 1029–1031; 10.1016/j.orggeochem.2009.06.007 (2009).
60. Elias, V. O., Simoneit, B. R., Cordeiro, R. C. & Turcq, B. Evaluating levoglucosan as an indicator of biomass burning in Carajás, amazônia: a comparison to the charcoal record. *Geochimica et Cosmochimica Acta* **65**, 267–272; 10.1016/S0016-7037(00)00522-6 (2001).
61. Janoszka, K. & Czaplicka, M. Methods for the determination of levoglucosan and other sugar anhydrides as biomass burning tracers in environmental samples - A review. *Journal of separation science* **42**, 319–329; 10.1002/jssc.201800650 (2019).
62. Yan, C. *et al.* Residential Coal Combustion as a Source of Levoglucosan in China. *Environmental science & technology* **52**, 1665–1674; 10.1021/acs.est.7b05858 (2018).
63. Fraser, M. P. & Lakshmanan, K. Using Levoglucosan as a Molecular Marker for the Long-Range Transport of Biomass Combustion Aerosols. *Environ. Sci. Technol.* **34**, 4560–4564; 10.1021/es991229l (2000).
64. Bai, J., Sun, X., Zhang, C., Xu, Y. & Qi, C. The OH-initiated atmospheric reaction mechanism and kinetics for levoglucosan emitted in biomass burning. *Chemosphere* **93**, 2004–2010; 10.1016/j.chemosphere.2013.07.021 (2013).
65. Slade, J. H. & Knopf, D. A. Heterogeneous OH oxidation of biomass burning organic aerosol surrogate compounds: assessment of volatilisation products and the role of OH concentration on the reactive uptake kinetics. *Physical chemistry chemical physics : PCCP* **15**, 5898–5915; 10.1039/c3cp44695f (2013).
66. Kuo, L.-J., Louchouart, P. & Herbert, B. E. Influence of combustion conditions on yields of solvent-extractable anhydrosugars and lignin phenols in chars: implications for characterizations of biomass combustion residues. *Chemosphere* **85**, 797–805; 10.1016/j.chemosphere.2011.06.074 (2011).
67. Fabbri, D. *et al.* Levoglucosan and other cellulose and lignin markers in emissions from burning of Miocene lignites. *Atmospheric Environment* **43**, 2286–2295; 10.1016/j.atmosenv.2009.01.030 (2009).

68. Simoneit, B. *et al.* Levoglucosan, a tracer for cellulose in biomass burning and atmospheric particles. *Atmospheric Environment* **33**, 173–182; 10.1016/S1352-2310(98)00145-9 (1999).
69. Schreuder, L. T., Hopmans, E. C., Stuut, J.-B. W., Sinninghe Damsté, J. S. & Schouten, S. Transport and deposition of the fire biomarker levoglucosan across the tropical North Atlantic Ocean. *Geochimica et Cosmochimica Acta* **227**, 171–185; 10.1016/j.gca.2018.02.020 (2018).
70. Yao, P. *et al.* Levoglucosan concentrations in ice-core samples from the Tibetan Plateau determined by reverse-phase high-performance liquid chromatography–mass spectrometry. *J. Glaciol.* **59**, 599–612; 10.3189/2013JøG12J157 (2013).
71. Mackay, R. Method Development for the Detection of Levoglucosan, Mannosan, and Galactosan in Speleothems. MChem Project. University of Aberdeen, 2016.
72. Homann, J. Methodenentwicklung zur Bestimmung von Levoglucosan und Lignin-Oxidationsprodukten in Speläothemen mittels UHPLC-ESI-HRMS. Masterarbeit. Johannes Gutenberg-Universität, August 2019.
73. Han, Y. *et al.* Different formation mechanisms of PAH during wood and coal combustion under different temperatures. *Atmospheric Environment* **222**, 117084; 10.1016/j.atmosenv.2019.117084 (2020).
74. McGrath, T. E., Chan, W. & Hajaligol, M. R. Low temperature mechanism for the formation of polycyclic aromatic hydrocarbons from the pyrolysis of cellulose. *Journal of Analytical and Applied Pyrolysis* **66**, 51–70; 10.1016/S0165-2370(02)00105-5 (2003).
75. Baek, S. O. *et al.* A review of atmospheric polycyclic aromatic hydrocarbons: Sources, fate and behavior. *Water Air Soil Pollut* **60**, 279–300; 10.1007/BF00282628 (1991).
76. Haritash, A. K. & Kaushik, C. P. Biodegradation aspects of polycyclic aromatic hydrocarbons (PAHs): a review. *Journal of Hazardous Materials* **169**, 1–15; 10.1016/j.jhazmat.2009.03.137 (2009).
77. Williams, P. T. & Horne, P. A. Analysis of aromatic hydrocarbons in pyrolytic oil derived from biomass. *Journal of Analytical and Applied Pyrolysis* **31**, 15–37; 10.1016/0165-2370(94)00814-H (1995).
78. Horne, P. A. & Williams, P. T. Influence of temperature on the products from the flash pyrolysis of biomass. *Fuel* **75**, 1051–1059; 10.1016/0016-2361(96)00081-6 (1996).
79. Evans, R. J. & Milne, T. A. Molecular characterization of the pyrolysis of biomass. *Energy Fuels* **1**, 123–137; 10.1021/ef00002a001 (1987).
80. U.S. EPA. *Method 610: Polynuclear Aromatic Hydrocarbons. APPENDIX A TO PART 136: METHODS FOR ORGANIC CHEMICAL ANALYSIS OF MUNICIPAL AND INDUSTRIAL WASTEWATER* (1984).
81. Luo, J. *et al.* Effect of northern boreal forest fires on PAH fluctuations across the arctic. *Environmental pollution (Barking, Essex : 1987)* **261**, 114186; 10.1016/j.envpol.2020.114186 (2020).

82. Wietzoreck, M. *et al.* Polycyclic aromatic hydrocarbons (PAHs) and their alkylated, nitrated and oxygenated derivatives in the atmosphere over the Mediterranean and Middle East seas. *Atmos. Chem. Phys.* **22**, 8739–8766; 10.5194/acp-22-8739-2022 (2022).
83. Vergnoux, A., Malleret, L., Asia, L., Doumenq, P. & Theraulaz, F. Impact of forest fires on PAH level and distribution in soils. *Environmental research* **111**, 193–198; 10.1016/j.envres.2010.01.008 (2011).
84. Wietzoreck, M. *et al.* Nitro- and oxy-PAHs in grassland soils from decade-long sampling in central Europe. *Environmental geochemistry and health* **44**, 2743–2765; 10.1007/s10653-021-01066-y (2022).
85. Argiriadis, E. *et al.* Multi-proxy biomarker determination in peat: Optimized extraction and cleanup method for paleoenvironmental application. *Microchemical Journal* **156**, 104821; 10.1016/j.microc.2020.104821 (2020).
86. Denis, E. H. *et al.* Polycyclic aromatic hydrocarbons (PAHs) in lake sediments record historic fire events: Validation using HPLC-fluorescence detection. *Organic Geochemistry* **45**, 7–17; 10.1016/j.orggeochem.2012.01.005 (2012).
87. Yunker, M. B. *et al.* PAHs in the Fraser River basin: a critical appraisal of PAH ratios as indicators of PAH source and composition. *Organic Geochemistry* **33**, 489–515; 10.1016/S0146-6380(02)00002-5 (2002).
88. Yunker, M. B., Backus, S. M., Graf Pannatier, E., Jeffries, D. S. & Macdonald, R. W. Sources and Significance of Alkane and PAH Hydrocarbons in Canadian Arctic Rivers. *Estuarine, Coastal and Shelf Science* **55**, 1–31; 10.1006/ecss.2001.0880 (2002).
89. Vecchiato, M. *et al.* The Great Acceleration of fragrances and PAHs archived in an ice core from Elbrus, Caucasus. *Sci Rep* **10**, 10661; 10.1038/s41598-020-67642-x (2020).
90. Argiriadis, E., Denniston, R. F. & Barbante, C. Improved Polycyclic Aromatic Hydrocarbon and n-Alkane Determination in Speleothems through Cleanroom Sample Processing. *Anal. Chem.* **91**, 7007–7011; 10.1021/acs.analchem.9b00767 (2019).
91. Perrette, Y. *et al.* Polycyclic Aromatic Hydrocarbons in stalagmites: Occurrence and use for analyzing past environments. *Chemical Geology* **251**, 67–76; 10.1016/j.chemgeo.2008.02.013 (2008).
92. Centre for Environment & Health. Human health effects of polycyclic aromatic hydrocarbons as ambient air pollutants - Report of the Working Group on Polycyclic Aromatic Hydrocarbons of the Joint Task Force on the Health Aspects of Air Pollution. *World Health Organization* (2021).
93. Directive 2004/107/EC of the European Parliament and of the Council of 15 December 2004 relating to arsenic, cadmium, mercury, nickel and polycyclic aromatic hydrocarbons in ambient air. 2004/107/EC (2004).
94. Tobiszewski, M. & Namieśnik, J. PAH diagnostic ratios for the identification of pollution emission sources. *Environmental pollution (Barking, Essex : 1987)* **162**, 110–119; 10.1016/j.envpol.2011.10.025 (2012).

95. Yan, B. *et al.* Molecular tracers of saturated and polycyclic aromatic hydrocarbon inputs into Central Park Lake, New York City. *Environ. Sci. Technol.* **39**, 7012–7019; 10.1021/es0506105 (2005).
96. Lawal, A. T. Polycyclic aromatic hydrocarbons. A review. *Cogent Environmental Science* **3**, 1339841; 10.1080/23311843.2017.1339841 (2017).
97. Karp, A. T., Holman, A. I., Hopper, P., Grice, K. & Freeman, K. H. Fire distinguishers: Refined interpretations of polycyclic aromatic hydrocarbons for paleo-applications. *Geochimica et Cosmochimica Acta* **289**, 93–113; 10.1016/j.gca.2020.08.024 (2020).
98. Ramdahl, T. Retene—a molecular marker of wood combustion in ambient air. *Nature* **306**, 580–582; 10.1038/306580a0 (1983).
99. Wakeham, S. G., Schaffner, C. & Giger, W. Poly cyclic aromatic hydrocarbons in Recent lake sediments—II. Compounds derived from biogenic precursors during early diagenesis. *Geochimica et Cosmochimica Acta* **44**, 415–429; 10.1016/0016-7037(80)90041-1 (1980).
100. Argiriadis, E. *et al.* Lake sediment fecal and biomass burning biomarkers provide direct evidence for prehistoric human-lit fires in New Zealand. *Sci Rep* **8**, 12113; 10.1038/s41598-018-30606-3 (2018).
101. Battistel, D. *et al.* Fire and human record at Lake Victoria, East Africa, during the Early Iron Age: Did humans or climate cause massive ecosystem changes? *The Holocene* **27**, 997–1007; 10.1177/0959683616678466 (2017).
102. Callegaro, A. *et al.* Fire, vegetation, and Holocene climate in a southeastern Tibetan lake: a multi-biomarker reconstruction from Paru Co. *Clim. Past* **14**, 1543–1563; 10.5194/cp-14-1543-2018 (2018).
103. Harris, D. C., Werner, G. & Werner, T. *Lehrbuch der Quantitativen Analyse*. 8th ed. (Springer Spektrum, Berlin, 2014).
104. Camel, V. Solid phase extraction of trace elements. *Spectrochimica Acta Part B: Atomic Spectroscopy* **58**, 1177–1233; 10.1016/S0584-8547(03)00072-7 (2003).
105. Hennion, M.-C. Graphitized carbons for solid-phase extraction. *Journal of Chromatography A* **885**, 73–95; 10.1016/S0021-9673(00)00085-6 (2000).
106. Poole, C. F. New trends in solid-phase extraction. *TrAC Trends in Analytical Chemistry* **22**, 362–373; 10.1016/S0165-9936(03)00605-8 (2003).
107. Dąbrowski, Ł. Review of use of keepers in solvent evaporation procedure during the environmental sample analysis of some organic pollutants. *TrAC Trends in Analytical Chemistry* **80**, 507–516; 10.1016/j.trac.2015.10.014 (2016).
108. Marek, R. & Straub, J. Analysis of the evaporation coefficient and the condensation coefficient of water. *International Journal of Heat and Mass Transfer* **44**, 39–53; 10.1016/S0017-9310(00)00086-7 (2001).
109. Langmuir, I. Vapor Pressure, Evaporation, Condensation and Adsorption. *J. Am. Chem. Soc.* **54**, 2798–2832; 10.1021/ja01346a022 (1932).

110. Malisch, R., Lippold, R., Metschies, M. & Moats, W. A. Application of centrifugal vacuum concentrators in residue analysis. *Fresenius J Anal Chem* **341**, 449–456; 10.1007/BF00321537 (1991).
111. Ontko, J. A. & Jones, R. F. Centrifugal evaporation of organic solvents from a series of solutions. *J Am Oil Chem Soc* **42**, 462–464; 10.1007/BF02635593 (1965).
112. Otto, M. *Analytische Chemie*. 4th ed. (Wiley-VCH, Weinheim, 2014).
113. Nováková, L., Matysová, L. & Solich, P. Advantages of application of UPLC in pharmaceutical analysis. *Talanta* **68**, 908–918; 10.1016/j.talanta.2005.06.035 (2006).
114. Meyer, V. *Practical high-performance liquid chromatography*. 5th ed. (Wiley, Chichester, U.K, 2010).
115. Snyder, L. R., Kirkland, J. J. & Dolan, J. W. *Introduction to modern liquid chromatography*. 3rd ed. (Wiley, Hoboken, NJ, 2010).
116. Kahsay, G., Song, H., van Schepdael, A., Cabooter, D. & Adams, E. Hydrophilic interaction chromatography (HILIC) in the analysis of antibiotics. *Journal of pharmaceutical and biomedical analysis* **87**, 142–154; 10.1016/j.jpba.2013.04.015 (2014).
117. Przybyciel, M. Fluorinated HPLC Phases — Looking Beyond C18 for Reversed-Phase HPLC. *LCGC Europe* **19**, 19–27 (2006).
118. Sadek, P. C. & Carr, P. W. Study of solute retention in reversed-phase high-performance liquid chromatography on hydrocarbonaceous and three fluorinated bonded phases. *Journal of Chromatography A* **288**, 25–41; 10.1016/S0021-9673(01)93679-9 (1984).
119. Alpert, A. J. Hydrophilic-interaction chromatography for the separation of peptides, nucleic acids and other polar compounds. *Journal of Chromatography* **499**, 177–196; 10.1016/S0021-9673(00)96972-3 (1990).
120. Buszewski, B. & Noga, S. Hydrophilic interaction liquid chromatography (HILIC)--a powerful separation technique. *Analytical and bioanalytical chemistry* **402**, 231–247; 10.1007/s00216-011-5308-5 (2012).
121. Jandera, P. Stationary and mobile phases in hydrophilic interaction chromatography: a review. *Analytica chimica acta* **692**, 1–25; 10.1016/j.aca.2011.02.047 (2011).
122. Guo, Y. & Gaiki, S. Retention behavior of small polar compounds on polar stationary phases in hydrophilic interaction chromatography. *Journal of Chromatography A* **1074**, 71–80; 10.1016/j.chroma.2005.03.058 (2005).
123. HILICON AB. iHILIC®-Fusion. advances HILIC separation in UHPLC and HPLC (2018).
124. Guo, Y. Recent progress in the fundamental understanding of hydrophilic interaction chromatography (HILIC). *The Analyst* **140**, 6452–6466; 10.1039/c5an00670h (2015).
125. Hemström, P. & Irgum, K. Hydrophilic interaction chromatography. *Journal of separation science* **29**, 1784–1821; 10.1002/jssc.200600199 (2006).
126. Dinh, N. P., Jonsson, T. & Irgum, K. Probing the interaction mode in hydrophilic interaction chromatography. *Journal of chromatography. A* **1218**, 5880–5891; 10.1016/j.chroma.2011.06.037 (2011).

127. McCalley, D. V. Study of the selectivity, retention mechanisms and performance of alternative silica-based stationary phases for separation of ionised solutes in hydrophilic interaction chromatography. *Journal of chromatography. A* **1217**, 3408–3417; 10.1016/j.chroma.2010.03.011 (2010).
128. Vogel, F. Leitfaden für eine erfolgreiche HILIC-Trennung. Available at www.analytik-news.de (2012).
129. Bartle, K. D. & Myers, P. History of gas chromatography. *TrAC Trends in Analytical Chemistry* **21**, 547–557; 10.1016/S0165-9936(02)00806-3 (2002).
130. McNair, H. M., Miller, J. M. & Snow, N. H. *Basic gas chromatography* (Wiley, Hoboken, New Jersey, 2019).
131. Gross, J. H. *Massenspektrometrie. Spektroskopiekurs kompakt* (Springer Berlin Heidelberg, Berlin, Heidelberg, 2019).
132. Mann, M. & Kelleher, N. L. Precision proteomics: the case for high resolution and high mass accuracy. *Proceedings of the National Academy of Sciences of the United States of America* **105**, 18132–18138; 10.1073/pnas.0800788105 (2008).
133. Cech, N. B. & Enke, C. G. Practical implications of some recent studies in electrospray ionization fundamentals. *Mass spectrometry reviews* **20**, 362–387; 10.1002/mas.10008 (2001).
134. Kebarle, P. & Tang, L. From ions in solution to ions in the gas phase - the mechanism of electrospray mass spectrometry. *Anal. Chem.* **65**, 972A-986A; 10.1021/ac00070a001 (1993).
135. Huang, E. C., Wachs, T., Conboy, J. J. & Henion, J. D. ATMOSPHERIC PRESSURE IONIZATION MASS SPECTROMETRY. *Anal. Chem.* **62**, 713A-725A; 10.1021/ac00212a727 (1990).
136. Konermann, L., Ahadi, E., Rodriguez, A. D. & Vahidi, S. Unraveling the mechanism of electrospray ionization. *Analytical chemistry* **85**, 2–9; 10.1021/ac302789c (2013).
137. Iribarne, J. V. On the evaporation of small ions from charged droplets. *J. Chem. Phys.* **64**, 2287; 10.1063/1.432536 (1976).
138. Dole, M. *et al.* Molecular Beams of Macroions. *The Journal of Chemical Physics* **49**, 2240–2249; 10.1063/1.1670391 (1968).
139. Kebarle, P. & Verkerk, U. H. Electrospray: from ions in solution to ions in the gas phase, what we know now. *Mass spectrometry reviews* **28**, 898–917; 10.1002/mas.20247 (2009).
140. Maciel, E. V. S., Pereira Dos Santos, N. G., Vargas Medina, D. A. & Lanças, F. M. Electron ionization mass spectrometry: Quo vadis? *Electrophoresis* **43**, 1587–1600; 10.1002/elps.202100392 (2022).
141. Santos, F. J. & Galceran, M. T. Modern developments in gas chromatography-mass spectrometry-based environmental analysis. *Journal of Chromatography A* **1000**, 125–151; 10.1016/S0021-9673(03)00305-4 (2003).

142. Thermo Fisher Scientific. Schematic of the Q Exactive. Available at <http://planetorbitrap.com/q-exactive#tab:schematic> (2019).
143. Miller, P. E. & Denton, M. B. The quadrupole mass filter: Basic operating concepts. *J. Chem. Educ.* **63**, 617; 10.1021/ed063p617 (1986).
144. Olsen, J. V. *et al.* Higher-energy C-trap dissociation for peptide modification analysis. *Nature methods* **4**, 709–712; 10.1038/nmeth1060 (2007).
145. Makarov, A. & Scigelova, M. Coupling liquid chromatography to Orbitrap mass spectrometry. *Journal of chromatography. A* **1217**, 3938–3945; 10.1016/j.chroma.2010.02.022 (2010).
146. Hu, Q. *et al.* The Orbitrap: a new mass spectrometer. *Journal of mass spectrometry : JMS* **40**, 430–443; 10.1002/jms.856 (2005).
147. Perry, R. H., Cooks, R. G. & Noll, R. J. Orbitrap mass spectrometry: instrumentation, ion motion and applications. *Mass spectrometry reviews* **27**, 661–699; 10.1002/mas.20186 (2008).
148. Homann, J. *et al.* Development of a method for anodic degradation of lignin for the analysis of paleo-vegetation proxies in speleothems. *ChemElectroChem*; 10.1002/celec.202101312 (2021).
149. Hedges, J. I. & Ertel, J. R. Characterization of lignin by gas capillary chromatography of cupric oxide oxidation products. *Anal. Chem.* **54**, 174–178; 10.1021/ac00239a007 (1982).
150. Freudenberg, K., Lautsch, W. & Engler, K. Die Bildung von Vanillin aus Fichtenlignin. *Ber. dtsh. Chem. Ges. A/B* **73**, 167–171; 10.1002/cber.19400730302 (1940).
151. Filley, T. R., Minard, R. D. & Hatcher, P. G. Tetramethylammonium hydroxide (TMAH) thermochemolysis: proposed mechanisms based upon the application of ¹³C-labeled TMAH to a synthetic model lignin dimer. *Organic Geochemistry* **30**, 607–621; 10.1016/S0146-6380(99)00040-6 (1999).
152. Heidke, I. Dissertation. Johannes Gutenberg-Universität, April 2021.
153. Zirbes, M. & Waldvogel, S. R. Electro-conversion as sustainable method for the fine chemical production from the biopolymer lignin. *Current Opinion in Green and Sustainable Chemistry* **14**, 19–25; 10.1016/j.cogsc.2018.05.001 (2018).
154. Möhle, S. *et al.* Modern Electrochemical Aspects for the Synthesis of Value-Added Organic Products. *Angewandte Chemie (International ed. in English)* **57**, 6018–6041; 10.1002/anie.201712732 (2018).
155. Pollok, D. & Waldvogel, S. R. Electro-organic synthesis - a 21st century technique. *Chemical science* **11**, 12386–12400; 10.1039/D0SC01848A (2020).
156. Wiebe, A. *et al.* Electrifying Organic Synthesis. *Angewandte Chemie (International ed. in English)* **57**, 5594–5619; 10.1002/anie.201711060 (2018).
157. Horn, E. J., Rosen, B. R. & Baran, P. S. Synthetic Organic Electrochemistry: An Enabling and Innately Sustainable Method. *ACS central science* **2**, 302–308; 10.1021/acscentsci.6b00091 (2016).

158. Schäfer, H. J. Contributions of organic electrosynthesis to green chemistry. *Comptes Rendus Chimie* **14**, 745–765; 10.1016/j.crci.2011.01.002 (2011).
159. Frontana-Urbe, B. A., Little, R. D., Ibanez, J. G., Palma, A. & Vasquez-Medrano, R. Organic electrosynthesis: a promising green methodology in organic chemistry. *Green Chem.* **12**, 2099; 10.1039/C0GC00382D (2010).
160. Anastas, P. & Eghbali, N. Green chemistry: principles and practice. *Chemical Society reviews* **39**, 301–312; 10.1039/B918763B (2010).
161. Bjørsvik, H.-R. & Minisci, F. Fine Chemicals from Lignosulfonates. 1. Synthesis of Vanillin by Oxidation of Lignosulfonates. *Org. Process Res. Dev.* **3**, 330–340; 10.1021/op9900028 (1999).
162. Smith, C. Z., Utey, J. H. P. & Hammond, J. K. Electro-organic reactions. Part 60[1]. The electro-oxidative conversion at laboratory scale of a lignosulfonate into vanillin in an FM01 filter press flow reactor: preparative and mechanistic aspects. *J Appl Electrochem* **41**, 363–375; 10.1007/s10800-010-0245-0 (2011).
163. Lu, Z., Tu, B. & Chen, F. Electro-Degradation of Sodium Lignosulfonate. *J. of Wood Chem. & Tech.* **23**, 261–277; 10.1081/WCT-120026933 (2003).
164. Shao, D., Liang, J., Cui, X., Xu, H. & Yan, W. Electrochemical oxidation of lignin by two typical electrodes: Ti/SbSnO₂ and Ti/PbO₂. *Chemical Engineering Journal* **244**, 288–295; 10.1016/j.cej.2014.01.074 (2014).
165. Luo, J., Melissa, P., Zhao, W., Wang, Z. & Zhu, Y. Selective Lignin Oxidation towards Vanillin in Phenol Media. *ChemistrySelect* **1**, 4596–4601; 10.1002/slct.201600758 (2016).
166. Limosin, D., Pierre, G. & Cauquis, G. Oxydation Electrochimique de quelques Echantillons de Lignine en Solution Aqueuse Basique. *Holzforschung* **40**, 31–36; 10.1515/hfsg.1986.40.1.31 (1986).
167. Parpot, P., Bettencourt, A. P., Carvalho, A. M. & Belgsir, E. M. Biomass conversion: attempted electrooxidation of lignin for vanillin production. *J Appl Electrochem* **30**, 727–731; 10.1023/A:1004003613883 (2000).
168. Rauber, D., Dier, T. K., Volmer, D. A. & Hempelmann, R. Electrochemical Lignin Degradation in Ionic Liquids on Ternary Mixed Metal Electrodes. *Zeitschrift für Physikalische Chemie* **232**, 189–208; 10.1515/zpch-2017-0951 (2018).
169. Reichert, E., Wintringer, R., Volmer, D. A. & Hempelmann, R. Electro-catalytic oxidative cleavage of lignin in a protic ionic liquid. *Physical chemistry chemical physics : PCCP* **14**, 5214–5221; 10.1039/c2cp23596j (2012).
170. Schmitt, D., Regenbrecht, C., Hartmer, M., Stecker, F. & Waldvogel, S. R. Highly selective generation of vanillin by anodic degradation of lignin: a combined approach of electrochemistry and product isolation by adsorption. *Beilstein journal of organic chemistry* **11**, 473–480; 10.3762/bjoc.11.53 (2015).

171. Schmitt, D., Regenbrecht, C., Schubert, M., Schollmeyer, D. & Waldvogel, S. R. Treatment of black liquor (BL) by adsorption on AE resins and a subsequent electrochemical degradation of BL to obtain vanillin. *Holzforschung* **71**, 35–41; 10.1515/hf-2015-0210 (2017).
172. Zirbes, M. *et al.* Anodic Degradation of Lignin at Active Transition Metal-based Alloys and Performance-enhanced Anodes. *ChemElectroChem* **6**, 155–161; 10.1002/celec.201801218 (2019).
173. Di Marino, D., Stöckmann, D., Kriescher, S., Stiefel, S. & Wessling, M. Electrochemical depolymerisation of lignin in a deep eutectic solvent. *Green Chem.* **18**, 6021–6028; 10.1039/C6GC01353H (2016).
174. Stiefel, S., Lölsberg, J., Kipshagen, L., Möller-Gulland, R. & Wessling, M. Controlled depolymerization of lignin in an electrochemical membrane reactor. *Electrochemistry Communications* **61**, 49–52; 10.1016/j.elecom.2015.09.028 (2015).
175. Stiefel, S., Schmitz, A., Peters, J., Di Marino, D. & Wessling, M. An integrated electrochemical process to convert lignin to value-added products under mild conditions. *Green Chem.* **18**, 4999–5007; 10.1039/C6GC00878J (2016).
176. Di Marino, D., Aniko, V., Stocco, A., Kriescher, S. & Wessling, M. Emulsion electro-oxidation of kraft lignin. *Green Chem.* **19**, 4778–4784; 10.1039/C7GC02115A (2017).
177. Tolba, R., Tian, M., Wen, J., Jiang, Z.-H. & Chen, A. Electrochemical oxidation of lignin at IrO₂-based oxide electrodes. *Journal of Electroanalytical Chemistry* **649**, 9–15; 10.1016/j.jelechem.2009.12.013 (2010).
178. Tian, M., Wen, J., MacDonald, D., Asmussen, R. M. & Chen, A. A novel approach for lignin modification and degradation. *Electrochemistry Communications* **12**, 527–530; 10.1016/j.elecom.2010.01.035 (2010).
179. Cui, X., Liang, J. & Wang, D. Optimization of integrated electrochemical oxidation and biodegradation (EO-BD) for Kraft lignin. *J. Chem. Technol. Biotechnol.* **90**, 747–753; 10.1002/jctb.4370 (2015).
180. Zirbes, M. *et al.* High-Temperature Electrolysis of Kraft Lignin for Selective Vanillin Formation. *ACS Sustainable Chem. Eng.* **8**, 7300–7307; 10.1021/acssuschemeng.0c00162 (2020).
181. Dier, T. K. F., Rauber, D., Durneata, D., Hempelmann, R. & Volmer, D. A. Sustainable Electrochemical Depolymerization of Lignin in Reusable Ionic Liquids. *Scientific reports* **7**, 5041; 10.1038/s41598-017-05316-x (2017).
182. Schutyser, W. *et al.* Revisiting alkaline aerobic lignin oxidation. *Green Chem.* **20**, 3828–3844; 10.1039/C8GC00502H (2018).
183. Breiner, M., Zirbes, M. & Waldvogel, S. R. Comprehensive valorisation of technically relevant organosolv lignins via anodic oxidation. *Green Chem.*; 10.1039/d1gc01995c (2021).

184. Bosque, I., Magallanes, G., Rigoulet, M., Kärkäs, M. D. & Stephenson, C. R. J. Redox Catalysis Facilitates Lignin Depolymerization. *ACS central science* **3**, 621–628; 10.1021/acscentsci.7b00140 (2017).
185. MAHDAVI, B. *et al.* Electrocatalytic hydrogenolysis of lignin model dimers at Raney nickel electrodes. *J Appl Electrochem* **27**, 605–611; 10.1023/A:1018463131891 (1997).
186. Zhu, H. *et al.* Lignin depolymerization via an integrated approach of anode oxidation and electro-generated H₂O₂ oxidation. *RSC Adv.* **4**, 6232; 10.1039/c3ra47516f (2014).
187. Zhu, H. *et al.* Electrochemical depolymerization of lignin into renewable aromatic compounds in a non-diaphragm electrolytic cell. *RSC Adv.* **4**, 29917; 10.1039/C4RA03793F (2014).
188. Wang, Y., Yang, F., Liu, Z., Yuan, L. & Li, G. Electrocatalytic degradation of aspen lignin over Pb/PbO₂ electrode in alkali solution. *Catalysis Communications* **67**, 49–53; 10.1016/j.catcom.2015.03.033 (2015).
189. Liu, M., Wen, Y., Qi, J., Zhang, S. & Li, G. Fine Chemicals Prepared by Bamboo Lignin Degradation through Electrocatalytic Redox between Cu Cathode and Pb/PbO₂ Anode in Alkali Solution. *ChemistrySelect* **2**, 4956–4962; 10.1002/slct.201700881 (2017).
190. Nguyen, B. H., Perkins, R. J., Smith, J. A. & Moeller, K. D. Solvolysis, Electrochemistry, and Development of Synthetic Building Blocks from Sawdust. *J. Org. Chem.* **80**, 11953–11962; 10.1021/acs.joc.5b01776 (2015).
191. Pardini, V. L., Smith, C. Z., Utley, J. H. P., Vargas, R. R. & Viertler, H. Electroorganic reactions. 38. Mechanism of electrooxidative cleavage of lignin model dimers. *J. Org. Chem.* **56**, 7305–7313; 10.1021/jo00026a022 (1991).
192. Kim, S. *et al.* Computational Study of Bond Dissociation Enthalpies for a Large Range of Native and Modified Lignins. *J. Phys. Chem. Lett.* **2**, 2846–2852; 10.1021/jz201182w (2011).
193. e-Forschungsberichte des Deutschen Archäologischen Instituts 2014, Faszikel 1. *e-Forschungsberichte des Deutschen Archäologischen Instituts* (2014).
194. Gütz, C., Klöckner, B. & Waldvogel, S. R. Electrochemical Screening for Electroorganic Synthesis. *Org. Process Res. Dev.* **20**, 26–32; 10.1021/acs.oprd.5b00377 (2016).
195. Luković, J., Chiang, J. C. H., Blagojević, D. & Sekulić, A. A Later Onset of the Rainy Season in California. *Geophys. Res. Lett.* **48**; 10.1029/2020GL090350 (2021).
196. Swain, D. L. A Shorter, Sharper Rainy Season Amplifies California Wildfire Risk. *Geophys. Res. Lett.* **48**; 10.1029/2021GL092843 (2021).
197. Goulden, M. L. & Bales, R. C. California forest die-off linked to multi-year deep soil drying in 2012–2015 drought. *Nat. Geosci.* **12**, 632–637; 10.1038/s41561-019-0388-5 (2019).
198. Dong, L., Leung, L. R., Lu, J. & Song, F. Mechanisms for an Amplified Precipitation Seasonal Cycle in the U.S. West Coast under Global Warming. *Journal of Climate* **32**, 4681–4698; 10.1175/JCLI-D-19-0093.1 (2019).

199. Mahoney, K. *et al.* Cool season precipitation projections for California and the Western United States in NA-CORDEX models. *Clim Dyn* **56**, 3081–3102; 10.1007/s00382-021-05632-z (2021).
200. Swain, D. L., Langenbrunner, B., Neelin, J. D. & Hall, A. Increasing precipitation volatility in twenty-first-century California. *Nature Clim Change* **8**, 427–433; 10.1038/s41558-018-0140-y (2018).
201. Abatzoglou, J. T., Williams, A. P., Boschetti, L., Zubkova, M. & Kolden, C. A. Global patterns of interannual climate-fire relationships. *Global change biology* **24**, 5164–5175; 10.1111/gcb.14405 (2018).
202. Williams, A. P. *et al.* Observed Impacts of Anthropogenic Climate Change on Wildfire in California. *Earth's Future* **7**, 892–910; 10.1029/2019EF001210 (2019).
203. Goss, M. *et al.* Climate change is increasing the likelihood of extreme autumn wildfire conditions across California. *Environ. Res. Lett.* **15**, 94016; 10.1088/1748-9326/ab83a7 (2020).
204. Touma, D. *et al.* Climate change increases risk of extreme rainfall following wildfire in the western United States. *Science advances* **8**, eabm0320; 10.1126/sciadv.abm0320 (2022).
205. Oster, J. L., Montañez, I. P., Sharp, W. D. & Cooper, K. M. Late Pleistocene California droughts during deglaciation and Arctic warming. *Earth and Planetary Science Letters* **288**, 434–443; 10.1016/j.epsl.2009.10.003 (2009).
206. Oster, J. L. *et al.* Stalagmite records of hydroclimate in central California during termination 1. *Quaternary Science Reviews* **127**, 199–214; 10.1016/j.quascirev.2015.07.027 (2015).
207. Oster, J. L. *et al.* Climate response to the 8.2 ka event in coastal California. *Sci Rep* **7**, 3886; 10.1038/s41598-017-04215-5 (2017).
208. Oster, J. L., Weisman, I. E. & Sharp, W. D. Multi-proxy stalagmite records from northern California reveal dynamic patterns of regional hydroclimate over the last glacial cycle. *Quaternary Science Reviews* **241**, 106411; 10.1016/j.quascirev.2020.106411 (2020).
209. Wet, C. B. de *et al.* Semiquantitative Estimates of Rainfall Variability During the 8.2 kyr Event in California Using Speleothem Calcium Isotope Ratios. *Geophys. Res. Lett.* **48**; 10.1029/2020GL089154 (2021).
210. Dominguez-Villar, D. *et al.* Oxygen isotope precipitation anomaly in the North Atlantic region during the 8.2 ka event. *Geology* **37**, 1095–1098; 10.1130/G30393A.1 (2009).
211. Simoneit, B. R. Biomass burning — a review of organic tracers for smoke from incomplete combustion. *Applied Geochemistry* **17**, 129–162; 10.1016/S0883-2927(01)00061-0 (2002).
212. Bhattarai, H. *et al.* Levoglucosan as a tracer of biomass burning: Recent progress and perspectives. *Atmospheric Research* **220**, 20–33; 10.1016/j.atmosres.2019.01.004 (2019).

213. State of California. CZU Lightning Complex (Including Warnella Fire) Incident. Available at <https://www.fire.ca.gov/incidents/2020/8/16/czu-lightning-complex-including-warnella-fire/> (2020).
214. Marlon, J., Bartlein, P. J. & Whitlock, C. Fire-fuel-climate linkages in the northwestern USA during the Holocene. *The Holocene* **16**, 1059–1071; 10.1177/0959683606069396 (2006).
215. Lyle, M. *et al.* Pleistocene water cycle and eastern boundary current processes along the California continental margin. *Paleoceanography* **25**, n/a-n/a; 10.1029/2009PA001836 (2010).
216. Whitlock, C. *et al.* Long-term relations among fire, fuel, and climate in the northwestern US based on lake-sediment studies. *Int. J. Wildland Fire* **17**, 72; 10.1071/WF07025 (2008).
217. Street, J. H., Anderson, R. S. & Paytan, A. An organic geochemical record of Sierra Nevada climate since the LGM from Swamp Lake, Yosemite. *Quaternary Science Reviews* **40**, 89–106; 10.1016/j.quascirev.2012.02.017 (2012).
218. MacDonald, G. M. *et al.* Prolonged California aridity linked to climate warming and Pacific sea surface temperature. *Sci Rep* **6**, 33325; 10.1038/srep33325 (2016).
219. Palmer, H. M., Vriesman, V. P., Livsey, C. M., Fish, C. R. & Hill, T. M. *Holocene climate and oceanography of the coastal Western United States and California Current System* (2021).
220. Mohr, J. A., Whitlock, C. & Skinner, C. N. Postglacial vegetation and fire history, eastern Klamath Mountains, California, USA. *The Holocene* **10**, 587–601; 10.1191/095968300675837671 (2000).
221. PhyloPic. Available at <http://phylopic.org/> (2019).
222. Free SVG vector files. Available at <https://freesvg.org/> (2019-2020).
223. Creative Commons. Available at <https://creativecommons.org/publicdomain/zero/1.0/>.
224. State of California. 2019 Incident Archive. Available at <https://www.fire.ca.gov/incidents/2019/>.
225. Swap, R. *et al.* The long-range transport of southern African aerosols to the tropical South Atlantic. *J. Geophys. Res.* **101**, 23777–23791; 10.1029/95JD01049 (1996).
226. National Oceanic and atmospheric administration. Daily Summaries Station Details. SANTA CRUZ, CA US. Available at www.ncdc.noaa.gov/cdo-web/datasets/GHCND/stations/GHCND:USC00047916/detail.
227. Trouet, V., Taylor, A. H., Wahl, E. R., Skinner, C. N. & Stephens, S. L. Fire-climate interactions in the American West since 1400 CE. *Geophys. Res. Lett.* **37**; 10.1029/2009GL041695 (2010).

228. Marlon, J. R. *et al.* Long-term perspective on wildfires in the western USA. *Proceedings of the National Academy of Sciences of the United States of America* **109**, E535-43; 10.1073/pnas.1112839109 (2012).
229. Taylor, A. H., Trouet, V. & Skinner, C. N. Climatic influences on fire regimes in montane forests of the southern Cascades, California, USA. *Int. J. Wildland Fire* **17**, 60; 10.1071/WF07033 (2008).
230. Swetnam, T. W. Fire history and climate change in giant sequoia groves. *Science (New York, N.Y.)* **262**, 885–889; 10.1126/science.262.5135.885 (1993).
231. Steinman, B. A. *et al.* Oxygen isotope records of Holocene climate variability in the Pacific Northwest. *Quaternary Science Reviews* **142**, 40–60; 10.1016/j.quascirev.2016.04.012 (2016).
232. Griffin, D. & Anchukaitis, K. J. How unusual is the 2012-2014 California drought? *Geophys. Res. Lett.* **41**, 9017–9023; 10.1002/2014GL062433 (2014).
233. Renssen, H., Goosse, H. & Fichefet, T. Simulation of Holocene cooling events in a coupled climate model. *Quaternary Science Reviews* **26**, 2019–2029; 10.1016/j.quascirev.2007.07.011 (2007).
234. Munroe, J. S. & Laabs, B. J. C. Temporal correspondence between pluvial lake highstands in the southwestern US and Heinrich Event 1. *J. Quaternary Sci.* **28**, 49–58; 10.1002/jqs.2586 (2013).
235. McGee, D., Moreno-Chamarro, E., Marshall, J. & Galbraith, E. D. Western U.S. lake expansions during Heinrich stadials linked to Pacific Hadley circulation. *Science advances* **4**, eaav0118; 10.1126/sciadv.aav0118 (2018).
236. Perrette, Y. *et al.* Atmospheric sources and soil filtering of PAH content in karst seepage waters. *Organic Geochemistry* **65**, 37–45; 10.1016/j.orggeochem.2013.10.005 (2013).
237. Knight, C. A. *et al.* Land management explains major trends in forest structure and composition over the last millennium in California's Klamath Mountains. *Proceedings of the National Academy of Sciences of the United States of America* **119**, e2116264119; 10.1073/pnas.2116264119 (2022).
238. Killick, R., Hayes, K., Eckley, I., Fearnhead, P., Lee, J. Methods for changepoint detection. R package. Available at <https://github.com/rkillick/changepoint/> (2016).
239. Killick, R., Fearnhead, P. & Eckley, I. A. Optimal detection of changepoints with a linear computational cost. *Journal of the American Statistical Association* **107**, 1590–1598; 10.1080/01621459.2012.737745 (2012).
240. Zhang, N. R. & Siegmund, D. O. A modified Bayes information criterion with applications to the analysis of comparative genomic hybridization data. *Biometrics* **63**, 22–32; 10.1111/j.1541-0420.2006.00662.x (2007).
241. Homann, J. *et al.* Past fire dynamics inferred from polycyclic aromatic hydrocarbons and monosaccharide anhydrides in a stalagmite from the archaeological site of Mayapan, Mexico (2023).

242. Gałuszka, A., Migaszewski, Z. M. & Namieśnik, J. The role of analytical chemistry in the study of the Anthropocene. *TrAC Trends in Analytical Chemistry* **97**, 146–152; 10.1016/j.trac.2017.08.017 (2017).
243. Ridley, H. E. *et al.* Aerosol forcing of the position of the intertropical convergence zone since ad 1550. *Nat. Geosci.* **8**, 195–200; 10.1038/ngeo2353 (2015).
244. Braun, T. *et al.* Decline in seasonal predictability potentially destabilized Classic Maya societies. *Commun Earth Environ* **4**, 1–12; 10.1038/s43247-023-00717-5 (2023).
245. Lammel, G., Sehili, A. M., Bond, T. C., Feichter, J. & Grassl, H. Gas/particle partitioning and global distribution of polycyclic aromatic hydrocarbons--a modelling approach. *Chemosphere* **76**, 98–106; 10.1016/j.chemosphere.2009.02.017 (2009).
246. Xie, M., Hannigan, M. P. & Barsanti, K. C. Gas/particle partitioning of 2-methyltetrols and levoglucosan at an urban site in Denver. *Environ. Sci. Technol.* **48**, 2835–2842; 10.1021/es405356n (2014).
247. Zennaro, P. *et al.* Fire in ice: two millennia of boreal forest fire history from the Greenland NEEM ice core. *Clim. Past* **10**, 1905–1924; 10.5194/cp-10-1905-2014 (2014).
248. Edwards, R. L., Chen, J. H., Ku, T. L. & Wasserburg, G. J. Precise timing of the last interglacial period from mass spectrometric determination of thorium-230 in corals. *Science (New York, N.Y.)* **236**, 1547–1553; 10.1126/science.236.4808.1547 (1987).
249. Kaufman, A. & Broecker, W. Comparison of Th 230 and C 14 ages for carbonate materials from lakes Lahontan and Bonneville. *J. Geophys. Res.* **70**, 4039–4054; 10.1029/JZ070i016p04039 (1965).
250. Richards, D. A. & Dorale, J. A. Uranium-series Chronology and Environmental Applications of Speleothems. *Reviews in Mineralogy and Geochemistry* **52**, 407–460; 10.2113/0520407 (2003).
251. Hellstrom, J. U–Th dating of speleothems with high initial ²³⁰Th using stratigraphical constraint. *Quaternary Geochronology* **1**, 289–295; 10.1016/j.quageo.2007.01.004 (2006).
252. Ramsey, C. B. Deposition models for chronological records. *Quaternary Science Reviews* **27**, 42–60; 10.1016/j.quascirev.2007.01.019 (2008).
253. Ramsey, C. B. Bayesian Analysis of Radiocarbon Dates. *Radiocarbon* **51**, 337–360; 10.1017/S0033822200033865 (2009).
254. Shahpoury, P., Kitanovski, Z. & Lammel, G. Snow scavenging and phase partitioning of nitrated and oxygenated aromatic hydrocarbons in polluted and remote environments in central Europe and the European Arctic. *Atmos. Chem. Phys.* **18**, 13495–13510; 10.5194/acp-18-13495-2018 (2018).
255. Lu, G.-N., Tao, X.-Q., Dang, Z., Yi, X.-Y. & Yang, C. Estimation of n-octanol/water partition coefficients of polycyclic aromatic hydrocarbons by quantum chemical descriptors. *Open Chemistry* **6**, 310–318; 10.2478/s11532-008-0010-y (2008).

256. Rayne, S. & Forest, K. Air-water partition coefficients for a suite of polycyclic aromatic and other C10 through C20 unsaturated hydrocarbons. *Journal of environmental science and health. Part A, Toxic/hazardous substances & environmental engineering* **51**, 938–953; 10.1080/10934529.2016.1191812 (2016).
257. Dickson, B., Sniderman, J. K., Korasidis, V. A. & Woodhead, J. The distribution of fossil pollen and charcoal in stalagmites. *Quat. res.*, 1–13; 10.1017/qua.2023.11 (2023).
258. Zhang, W. *et al.* Source diagnostics of polycyclic aromatic hydrocarbons in urban road runoff, dust, rain and canopy throughfall. *Environmental Pollution* **153**, 594–601; 10.1016/j.envpol.2007.09.004 (2008).
259. Ruan, Y. *et al.* Interaction of Fire, Vegetation, and Climate in Tropical Ecosystems: A Multiproxy Study Over the Past 22,000 Years. *Global Biogeochem. Cycles* **34**; 10.1029/2020GB006677 (2020).
260. Soclo, H., Garrigues, P. & Ewald, M. Origin of Polycyclic Aromatic Hydrocarbons (PAHs) in Coastal Marine Sediments: Case Studies in Cotonou (Benin) and Aquitaine (France) Areas. *Marine Pollution Bulletin* **40**, 387–396; 10.1016/S0025-326X(99)00200-3 (2000).
261. Muri, G., Wakeham, S. G. & Faganeli, J. Polycyclic aromatic hydrocarbons and black carbon in sediments of a remote alpine Lake (Lake Planina, northwest Slovenia). *Environ Toxicol Chem* **22**, 1009–1016; 10.1002/etc.5620220508 (2003).
262. Contreras-Medina, R., Vega, I. L. & Morrone, J. J. Gymnosperms and cladistic biogeography of the Mexican Transition Zone. *Taxon* **56**, 905–916; 10.2307/25065872 (2007).
263. Douglas, P. M., Pagani, M., Brenner, M., Hodell, D. A. & Curtis, J. H. Aridity and vegetation composition are important determinants of leaf-wax δD values in southeastern Mexico and Central America. *Geochimica et Cosmochimica Acta* **97**, 24–45; 10.1016/j.gca.2012.09.005 (2012).
264. *Etnoflora Yucatanense* (Xalapa, Veracruz, México, 1994).
265. Tellez, O. *et al.* Native trees of Mexico: diversity, distribution, uses and conservation. *PeerJ* **8**, e9898; 10.7717/peerj.9898 (2020).
266. Kennett, D. J. *et al.* Drought-Induced Civil Conflict Among the Ancient Maya. *Nat Commun* **13**, 3911; 10.1038/s41467-022-31522-x (2022).
267. Milbrath, S. & Peraza Lope, C. REVISITING MAYAPAN: Mexico's last Maya capital. *Ancient Mesoam* **14**, 1–46; 10.1017/S0956536103132178 (2003).
268. Kappenberg, A., Braun, M., Amelung, W. & Lehndorff, E. Fire condensates and charcoals: Chemical composition and fuel source identification. *Organic Geochemistry* **130**, 43–50; 10.1016/j.orggeochem.2019.01.009 (2019).
269. Brown, C. T. Water Sources at Mayapan, Yucatan, Mexico. In *Precolumbian Water Management. Ideology, Ritual, and Power*, edited by L. J. Lucero. 1st ed. (University of Arizona Press, Washington, D. C., 2006), pp. 171–186.

270. Weeks, J. M. & Masson, M. *The Carnegie Maya. II: Carnegie Institution of Washington current reports, 1952-1957* (University Press of Colorado, Boulder, Colo, 2009).
271. Homann, J., Hoffmann, T., Scholz, D. & Breitenbach, S. *Levoglucosan in speleothems: An evaluation of various sample preparation methods* (2021).
272. Piot, C. *et al.* Quantification of levoglucosan and its isomers by High Performance Liquid Chromatography - Electrospray Ionization tandem Mass Spectrometry and its applications to atmospheric and soil samples. *Atmos. Meas. Tech.* **5**, 141–148; 10.5194/amt-5-141-2012 (2012).
273. Caseiro, A. *et al.* Determination of saccharides in atmospheric aerosol using anion-exchange high-performance liquid chromatography and pulsed-amperometric detection. *Journal of chromatography. A* **1171**, 37–45; 10.1016/j.chroma.2007.09.038 (2007).
274. Hopmans, E. C., dos Santos, R. A. L., Mets, A., Sinninghe Damsté, J. S. & Schouten, S. A novel method for the rapid analysis of levoglucosan in soils and sediments. *Organic Geochemistry* **58**, 86–88; 10.1016/j.orggeochem.2013.02.003 (2013).
275. Cordell, R. L., White, I. R. & Monks, P. S. Validation of an assay for the determination of levoglucosan and associated monosaccharide anhydrides for the quantification of wood smoke in atmospheric aerosol. *Analytical and bioanalytical chemistry* **406**, 5283–5292; 10.1007/s00216-014-7962-x (2014).
276. Oros, D. R. & Simoneit, B. R. Identification and emission factors of molecular tracers in organic aerosols from biomass burning Part 1. Temperate climate conifers. *Applied Geochemistry* **16**, 1513–1544; 10.1016/S0883-2927(01)00021-X (2001).
277. Mackay, R. Method Development for the Detection of Levoglucosan, Mannosan, and Galactosan in Speleothems. MChem Project. University of Aberdeen, 2016.
278. van Eijck, A. Atmospheric degradation of reactive biogenic VOCs and their role in aerosol formation: Modelling activities, laboratory experiments and field studies in different vegetation zones. Dissertation. Johannes Gutenberg-Universität, October 2013.

7. Appendix

A. Supplementary material chapter 3

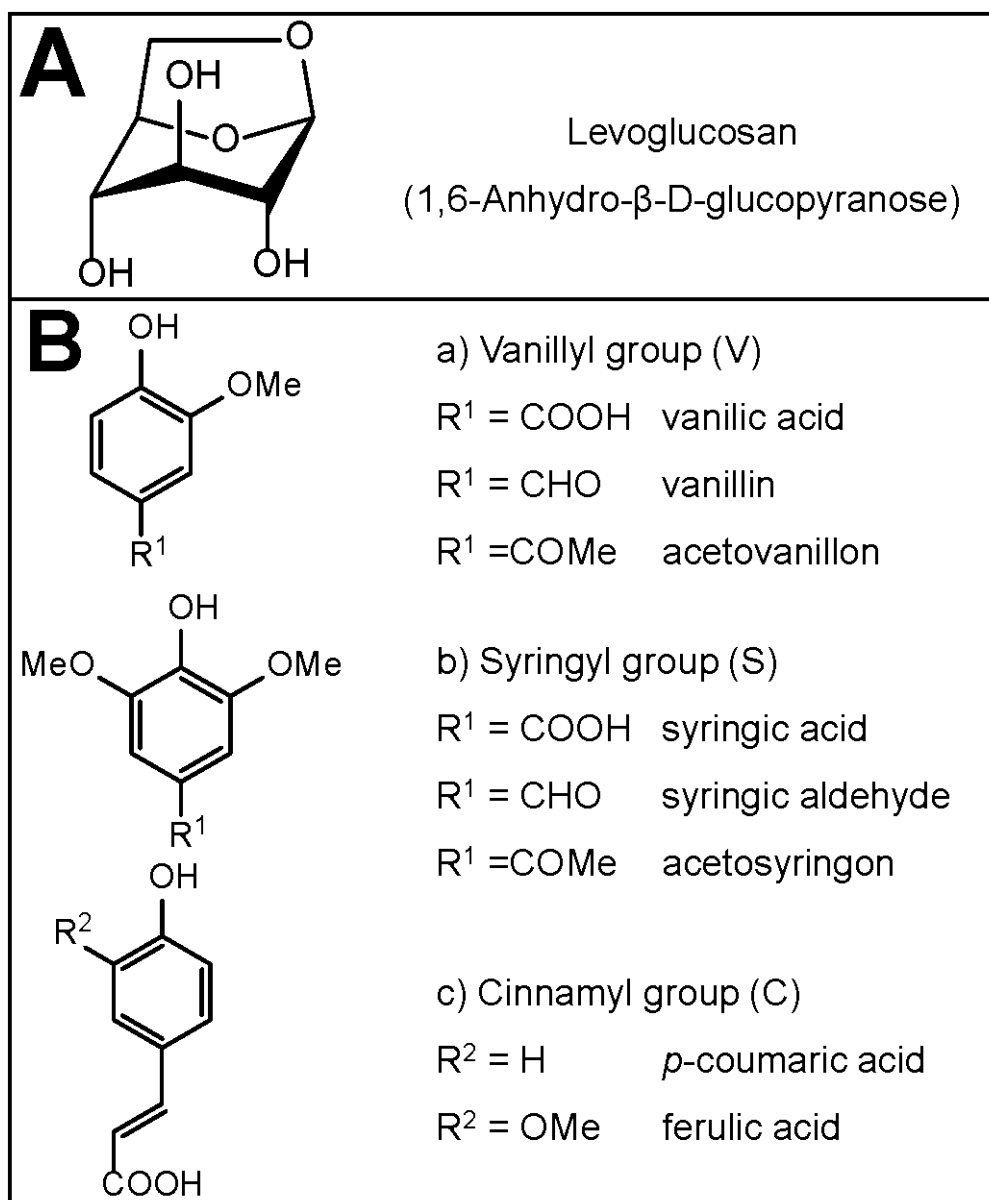


Figure S1. Structural formulas of levoglucosan (A) and the eight investigated lignin oxidation products (LOPs) (B), sorted by structural group.

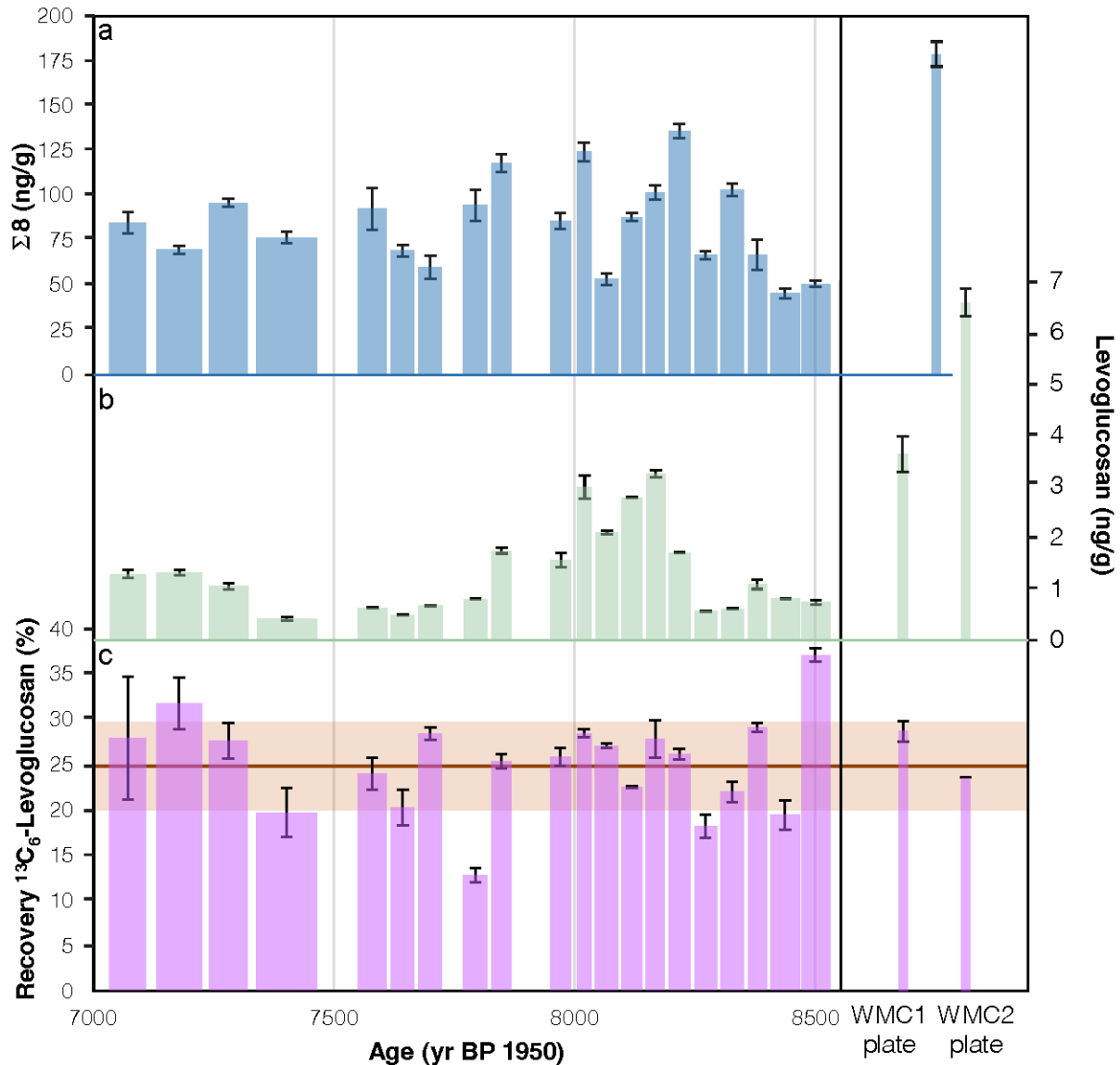


Figure S2. Determined lignin oxidation products (LOPs), levoglucosan concentrations, and recovery rates of $^{13}\text{C}_6$ levoglucosan. a: Determined concentration of the sum of all 8 LOPs ($\Sigma 8$; blue); b: Levoglucosan (light green); c: Determined recovery rates of $^{13}\text{C}_6$ levoglucosan (pink) of the 20 speleothem samples and the modern calcite samples. WMC1 plate was in place from March 2016 – June 2018 and WMC2 plate from December 2015 – June 2018. Width of the lines represent the time range for each sample. Error bars represent the standard deviation of samples measured in duplicate. Modern calcite samples were combined for the LOP measurements. The horizontal brown line indicates the average recovery for all speleothem samples and the shaded area represents the error, calculated as the standard deviation.

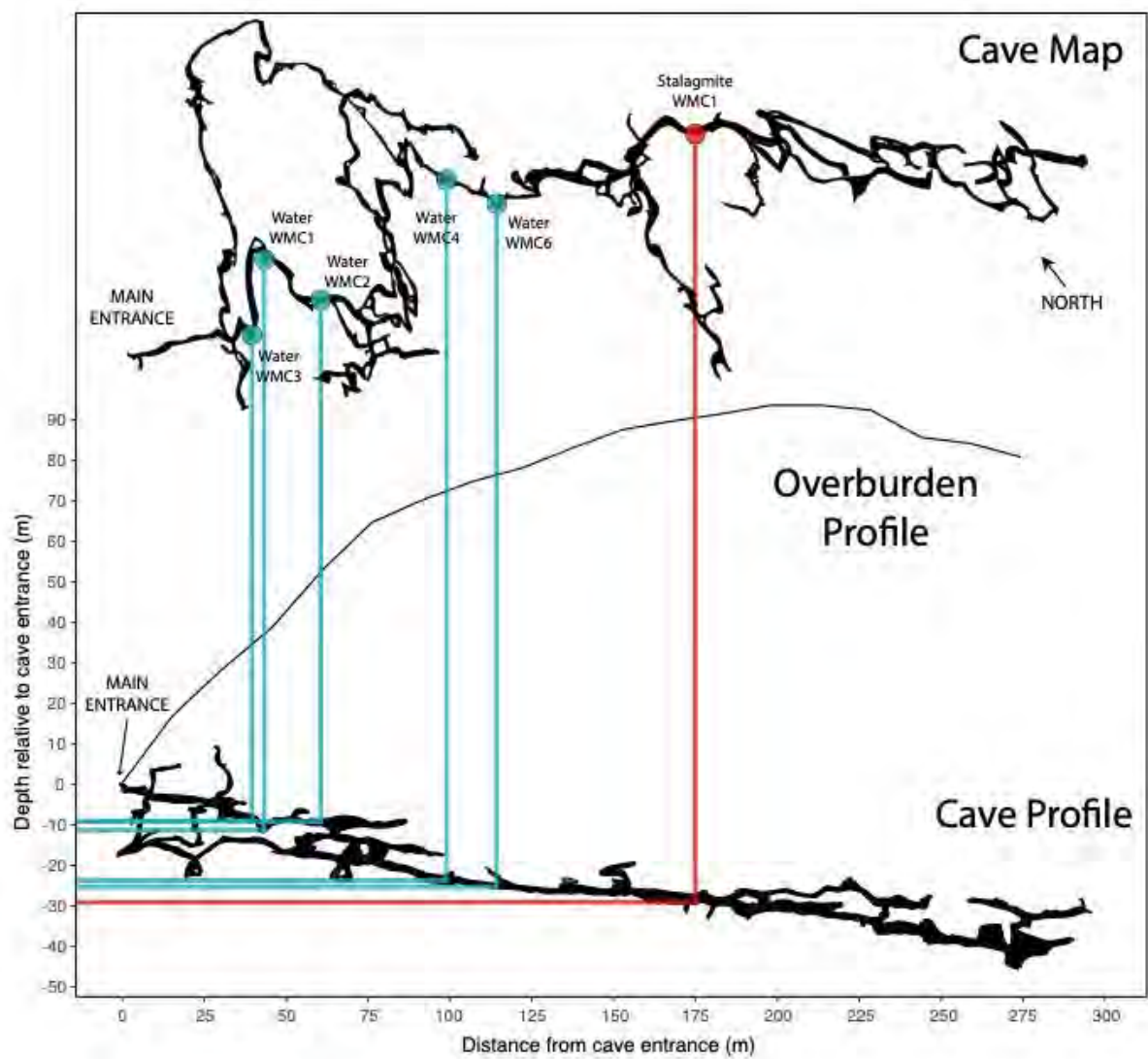


Figure S3. Map of White Moon Cave (WMC) and approximated overburden profile. Water and modern calcite sampling sites are marked in blue; site of the investigated speleothem is marked in red. The overburden at the sample WMC1 is ca. 120 m.

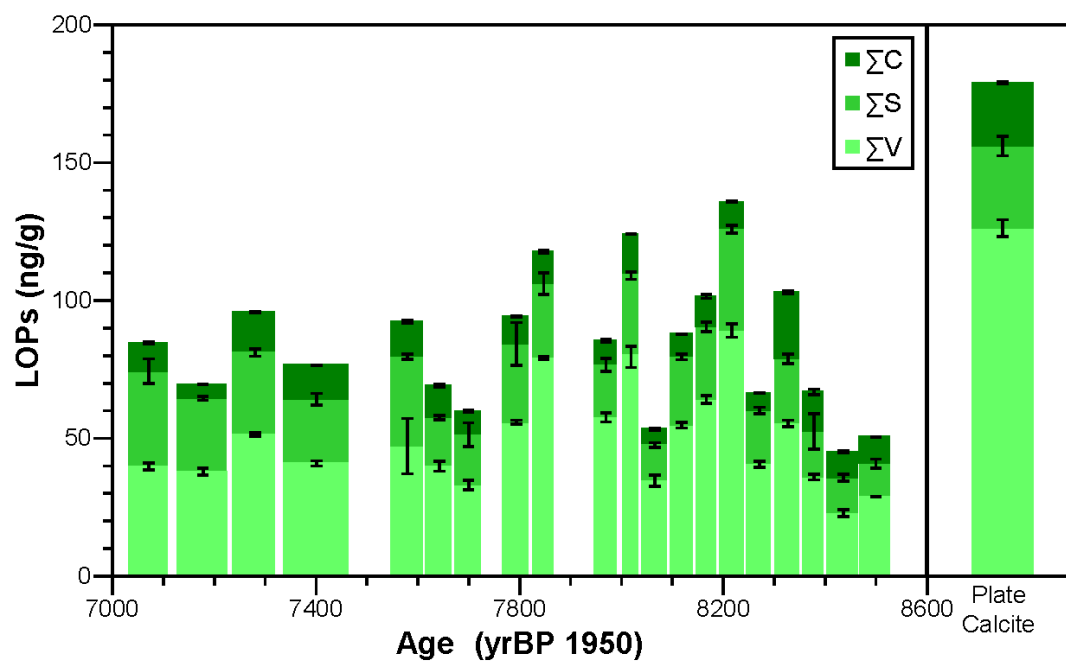


Figure S4. Determined lignin oxidation products (LOPs) concentrations of the 20 speleothem samples and combined modern calcite samples shown by structural group. Light green: sum of the V-group LOPs; Green: sum of the S-group LOPs; Dark green: sum of the C-group LOPs. Error bars represent the standard deviation of samples measured in duplicate.

Table S1. Ages of the speleothem and modern calcite samples, as well as determined levoglucosan concentration, $^{13}\text{C}_6$ -levoglucosan recovery, and LOP concentrations.

Sample	Depth from top (cm)	Age $\pm 2\sigma$ uncert. (cal yr BP 1950) [†]	Levoglucosan \pm SD (ng/g)	$^{13}\text{C}_6$ -levoglucosan recovery \pm SD (%)	$\Sigma\text{V} \pm$ SD (ng/g)	$\Sigma\text{S} \pm$ SD (ng/g)	$\Sigma\text{C} \pm$ SD (ng/g)	$\Sigma 8 \pm$ SD (ng/g)
a*	5 to 5.5	<6900	4.74 \pm 0.28	49.6 \pm 1.8	95.78 \pm 10.64	69.94 \pm 11.12	27.26 \pm 0.99	192.97 \pm 22.75
b*	5.5 to 6.2		2.80 \pm 0.13	45.6 \pm 2.6	98.02 \pm 2.81	54.80 \pm 2.52	25.18 \pm 1.46	178.00 \pm 6.79
c*	6.25 to 6.9		2.21 \pm 0.14	38.8 \pm 0.1	77.41 \pm 2.76	57.37 \pm 5.99	19.64 \pm 0.48	154.43 \pm 9.24
d*	7 to 8		1.31 \pm 0.01	36.9 \pm 16.2	12.02 \pm 0.29	8.40 \pm 0.90	3.76 \pm 0.11	24.19 \pm 1.30
e	8 to 8.6	7071 \pm 37	1.29 \pm 0.08	27.9 \pm 6.8	39.83 \pm 1.23	34.58 \pm 4.45	10.17 \pm 0.43	84.58 \pm 6.11
f	8.75 to 9.4	7178 \pm 48	1.32 \pm 0.06	31.7 \pm 2.9	37.89 \pm 1.28	26.65 \pm 0.72	4.99 \pm 0.06	69.53 \pm 2.06
g	9.5 to 10.1	7280 \pm 40	1.06 \pm 0.06	27.6 \pm 2.0	51.37 \pm 0.58	29.70 \pm 1.31	14.64 \pm 0.25	95.71 \pm 2.14
h	10.25 to 11.5	7401 \pm 62	0.41 \pm 0.03	19.7 \pm 2.7	40.89 \pm 0.93	23.28 \pm 2.10	12.19 \pm 0.07	76.37 \pm 3.10
i	12.5 to 13.25	7579 \pm 30	0.63 \pm 0.01	24.0 \pm 1.8	47.19 \pm 10.04	32.42 \pm 0.96	12.71 \pm 0.44	92.32 \pm 11.44
j	13.25 to 13.9	7642 \pm 24	0.49 \pm 0.01	20.2 \pm 1.9	39.91 \pm 1.82	17.59 \pm 0.76	11.60 \pm 0.57	69.10 \pm 3.15
k	13.9 to 14.5	7700 \pm 24	0.67 \pm 0.01	28.4 \pm 0.7	33.02 \pm 1.76	18.33 \pm 4.26	8.47 \pm 0.33	59.81 \pm 6.36
l	15 to 15.6	7793 \pm 25	0.81 \pm 0.003	12.7 \pm 0.8	55.90 \pm 0.64	28.39 \pm 7.71	10.03 \pm 0.25	94.31 \pm 8.60
m	15.6 to 16.1	7847 \pm 20	1.74 \pm 0.06	25.3 \pm 0.8	79.24 \pm 0.48	26.84 \pm 3.95	11.67 \pm 0.60	117.74 \pm 5.03
n	17 to 17.5	7970 \pm 22	1.56 \pm 0.14	25.8 \pm 1.0	57.63 \pm 1.64	19.07 \pm 2.30	8.80 \pm 0.57	85.50 \pm 4.51
o	17.65 to 18	8019 \pm 15	2.99 \pm 0.22	28.4 \pm 0.5	79.61 \pm 3.88	29.37 \pm 1.30	15.23 \pm 0.09	124.21 \pm 5.28
p	18.1 to 18.7	8066 \pm 24	2.10 \pm 0.04	27.1 \pm 0.2	34.66 \pm 2.01	12.94 \pm 0.87	5.64 \pm 0.32	53.24 \pm 3.20
q	18.8 to 19.4	8118 \pm 21	2.79 \pm 0.004	22.5 \pm 0.1	54.81 \pm 1.01	24.70 \pm 1.01	8.37 \pm 0.10	87.88 \pm 2.13
r	19.4 to 20	8167 \pm 20	3.25 \pm 0.07	27.8 \pm 2.1	64.08 \pm 1.44	26.38 \pm 1.69	11.02 \pm 0.67	101.48 \pm 3.79
s	20 to 20.6	8217 \pm 23	1.72 \pm 0.01	26.2 \pm 0.6	89.11 \pm 2.43	36.78 \pm 1.34	9.93 \pm 0.21	135.82 \pm 3.99
t	20.7. to 21.3	8271 \pm 23	0.57 \pm 0.01	18.2 \pm 1.2	40.59 \pm 1.09	19.56 \pm 1.12	6.38 \pm 0.10	66.53 \pm 2.30
u	21.3 to 21.9	8327 \pm 24	0.62 \pm 0.003	22.0 \pm 1.1	55.37 \pm 1.24	23.44 \pm 1.74	24.05 \pm 0.51	102.87 \pm 3.49
v	22 to 22.5	8379 \pm 19	1.09 \pm 0.09	29.1 \pm 0.5	35.94 \pm 0.98	16.63 \pm 6.38	14.31 \pm 1.04	66.88 \pm 8.41
w	22.5 to 23.25	8436 \pm 30	0.82 \pm 0.01	19.4 \pm 1.6	22.90 \pm 1.32	12.76 \pm 1.25	9.56 \pm 0.29	45.22 \pm 2.85
x	23.3 to 24	8500 \pm 29	0.74 \pm 0.04	37.1 \pm 0.8	28.84 \pm 0.13	12.03 \pm 1.57	9.63 \pm 0.16	50.50 \pm 1.87
Mod A	/	/	3.62 \pm 0.35	28.7 \pm 1.2	126.63 \pm 3.00	29.89 \pm 3.56	23.05 \pm 0.38	179.58 \pm 6.94
Mod B	/	/	6.57 \pm 0.27	23.6 \pm 0.0				

*Results of measurements of these samples were not discussed in the manuscript as the dating on them is uncertain and no other proxy data is available for comparison.

† Ages provided are for the midpoint of the sample depth range.

B. Supplementary material chapter 4

Cave survey and stalagmite sample MAYA-22-7

Because only very rough sketch maps were available, our team surveyed part of Cenote Ch'en Mul in August 2022 (Fig. S1). The cenote is in direct vicinity to the Kukulcan temple and the observatory (structure Q-152).²⁶⁹ The cenote has been targeted in archaeological studies since the Carnegie Maya project 1952-1957.²⁷⁰

The cave extends from the collapse doline in north-easterly then easterly direction and results from an ancient underground stream. The overburden is only between 7 and 8 m thick and facilitates rapid infiltration. Today, the passages are characterised by large breakdown and washed-in silt- and clay-rich unconsolidated sediment. The sediment on the cave floor is rich in organic material that has been washed in during floods. Several trenches have been excavated (and filled in afterwards) in the cenote and in the main cave passage, including a trench in 1953 and two trenches called 'Bernard Trench'.²⁶⁹

Hell Chamber in the north-eastern section of the cave hosts a large colony of bats and manifold centipedes and millipedes, crickets and other cave dwellers. Maya potsherds are widespread in all passages, indicating human activity in the past. While the main passage is largely devoid of secondary cave carbonates (speleothems), the side passages are very well decorated with stalagmites and stalactites. During our visit in 2022 the cave showed active dripping in only few places, especially in the SE, where a small puddle was detected which might be linked to the water table.

Stalagmite MAYA-22-7 (Figure 4.1) was found a few meters above the puddle. It was active (i.e., dripwater was falling onto it) when it was collected. The stalagmite was packed in a large plastic zip-lock bag before being detached from the growth spot to avoid contamination of the youngest surface.

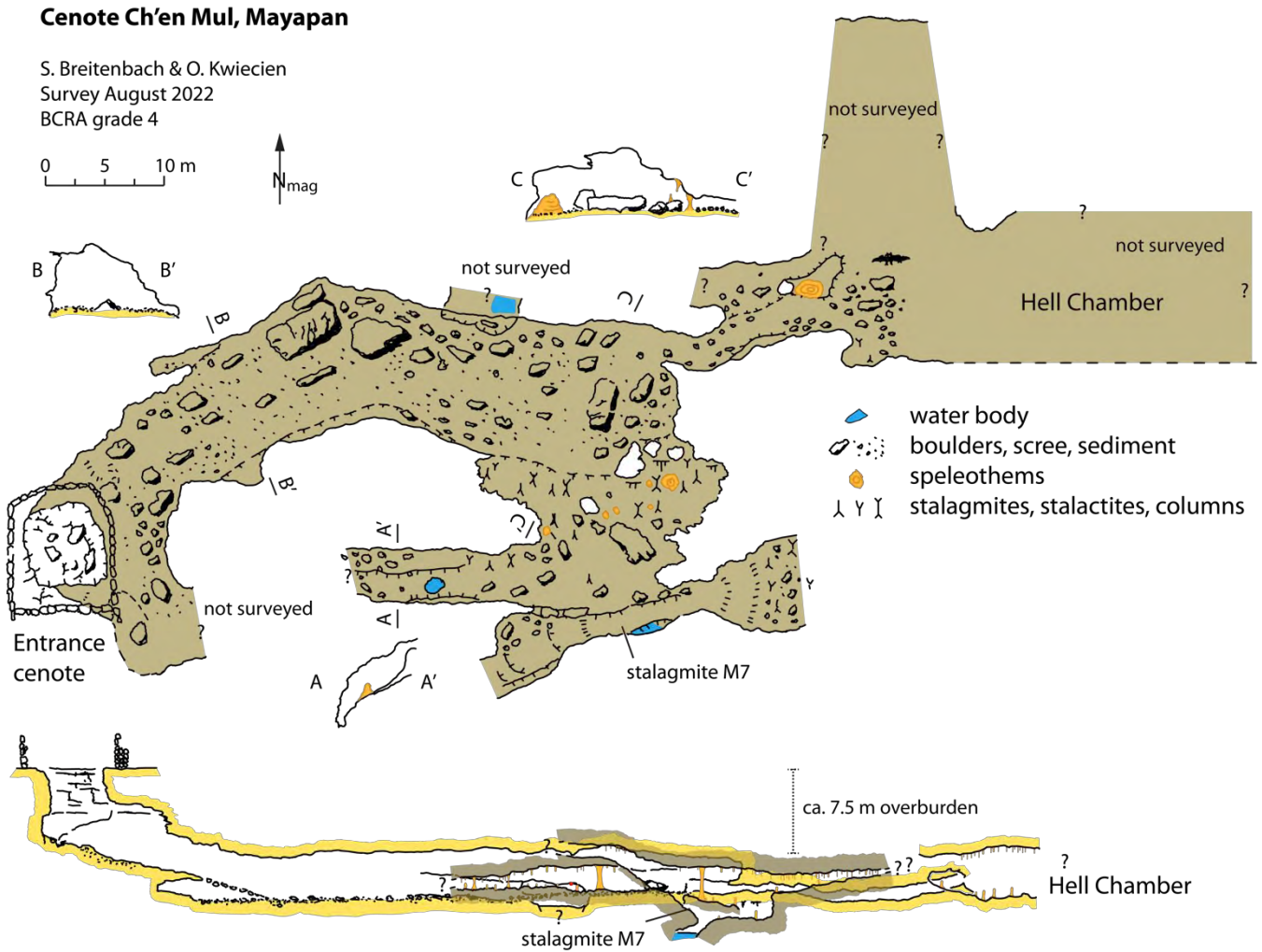


Figure S5. Map and profile of Cenote Ch'en Mul below the Mayapan ruins. The survey, conducted in August 2022, is incomplete due to time constraints. The cave passages extend below the prominent structure Q-152, which is also called Observatory.²⁶⁹ Significant additional passages remain currently unmapped.

OxCal Deposition model input code

Below is the code used to run the OxCal Poisson-Process Deposition model. Boundaries were placed at 14 mm and 24 mm distance from top, where there are clearly visible detrital layers in the stalagmite. A top boundary at 0 mm distance from top was input as a date between 2010-2022 CE, uniform distribution.

```
Plot()
{
P_Sequence("M7",0.1,null,U(-2,2))
{
timescale="UTh";
Boundary();
Date("bh03",N(calBP(332),11.5))
{
z=121;
};
Date("bh01",N(calBP(233),7))
{
z=90.3;
};
Date("bh05",N(calBP(100),6.2))
{
z=53.3;
};
Date("bh02",N(calBP(22),5.4))
{
z=27.3;
};
Boundary("detrital_2")
{
z=24;
};
Boundary("detrital_1")
{
```

```
z=14;
};
Date("bh04",N(calBP(-51),5.3))
{
z=9.3;
};
Date("top",U(calBP(-72),calBP(-60)))
{
z=0;
};
Boundary();
};
};
```

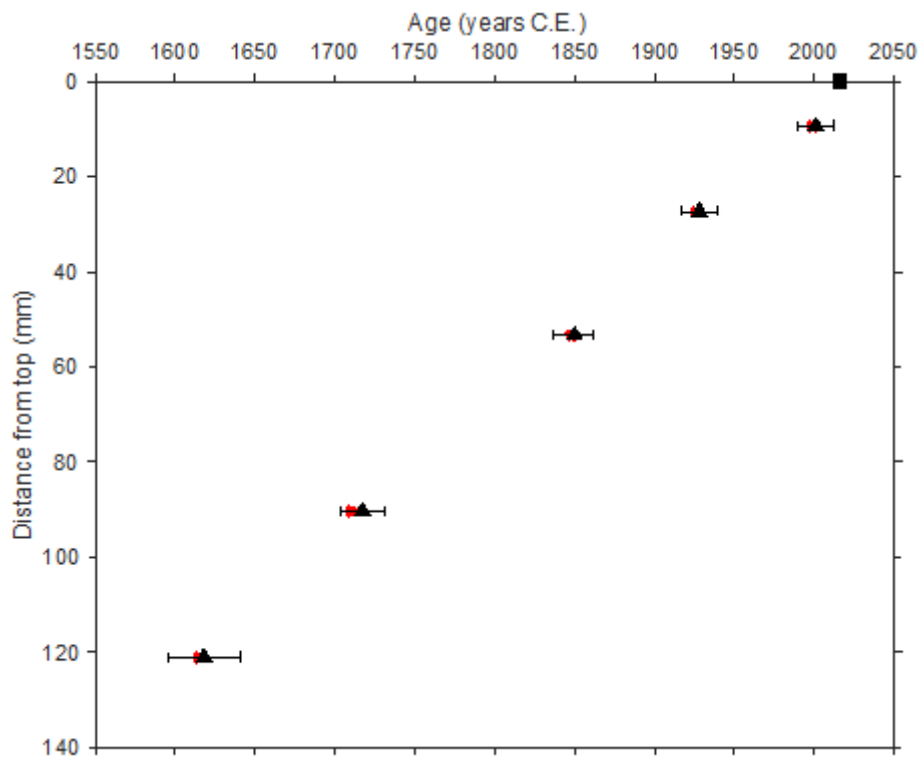


Figure S6. Age-depth plot of stalagmite MAYA-22-7. Black triangles show the mean corrected U-Th age and error bars indicate the 95% confidence interval. Red x's mark the uncorrected U-Th ages. A black rectangle is placed between 2010-2022 C.E., marking the estimated top age of the stalagmite, collected in August 2022.

Table S2. U-Th isotope activity ratios, calculated age (years C.E.), and Monte Carlo derived 95% confidence interval on the age for the five stalagmite MAYA-22-7 U-Th samples. An initial $^{230}\text{Th}/^{232}\text{Th}$ activity ratio range of 0.1-2 (uniform distribution) was used to correct the ages for initial detrital Th contamination. The ^{234}U and ^{230}Th half-lives used to calculate age are provided in Cheng et al. (2013).

Sample ID	Distance from top (mm)	^{238}U (ppb)	^{232}Th (ppb)	$(^{230}\text{Th}/^{232}\text{Th})$ measured	$(^{234}\text{U}/^{238}\text{U})$ measured	$(^{234}\text{U}/^{238}\text{U})$ 1s	$(^{230}\text{Th}/^{238}\text{U})$ measured	$(^{230}\text{Th}/^{238}\text{U})$ 1s	$(^{232}\text{Th}/^{238}\text{U})$ measured	$(^{232}\text{Th}/^{238}\text{U})$ 1s
bh04	9.3	1097	0.04	17	1.0236	0.0004	0.00022	0.00005	1.254E-05	3E-08
bh02	27.3	1322	0.09	43	1.0369	0.0006	0.00092	0.00005	2.134E-05	3E-08
bh05	53.3	1202	0.07	92	1.0435	0.0005	0.00167	0.00006	1.805E-05	4E-08
bh01	90.3	1181	0.22	50	1.0338	0.0005	0.00296	0.00006	5.905E-05	5E-08
bh03	121.0	1133	0.11	119	1.0330	0.0005	0.00386	0.00011	3.237E-05	7E-08

Sample ID	Year measured (years CE)	Initial $(^{230}\text{Th}/^{232}\text{Th})$	Age uncorrected (years CE)	95% CI lower	95% CI upper	Age corrected (years CE)	95% CI lower	95% CI upper
bh04	2022.83	0.1-2	1999	1989	2010	2001	1990	2011
bh02	2022.83	0.1-2	1926	1915	1936	1928	1918	1939
bh05	2022.83	0.1-2	1848	1836	1861	1850	1838	1863
bh01	2022.83	0.1-2	1710	1698	1722	1717	1703	1731
bh03	2022.83	0.1-2	1615	1592	1637	1618	1595	1641

Table S3. OxCal modelled ages of the 10 biomarker samples.

Sample #	Position	Distance from top (mm)	OxCal modelled mean age (years CE)	Error 2σ (years)
4	pit top	0.5	2015	6
4	pit bottom	4.1	2009	8
3	pit top	4.6	2009	8
3	pit bottom	9.1	2001	10
5	pit top	9.6	2000	11
5	pit bottom	13.0	1994	19
2	pit top	15.0	1986	21
6	pit top	15.0	1986	21
6	pit bottom	19.1	1965	19
2	pit bottom	19.1	1965	19
8	pit top	23.2	1944	17
8	pit bottom	23.2	1944	17
9	pit top	25.1	1936	15
9	pit bottom	30.8	1918	11
1	pit top	35.6	1903	11
1	pit bottom	39.1	1892	11
10	pit top	44.8	1874	11
10	pit bottom	50.8	1855	11
11	pit top	70.3	1788	12
11	pit bottom	78.7	1759	12

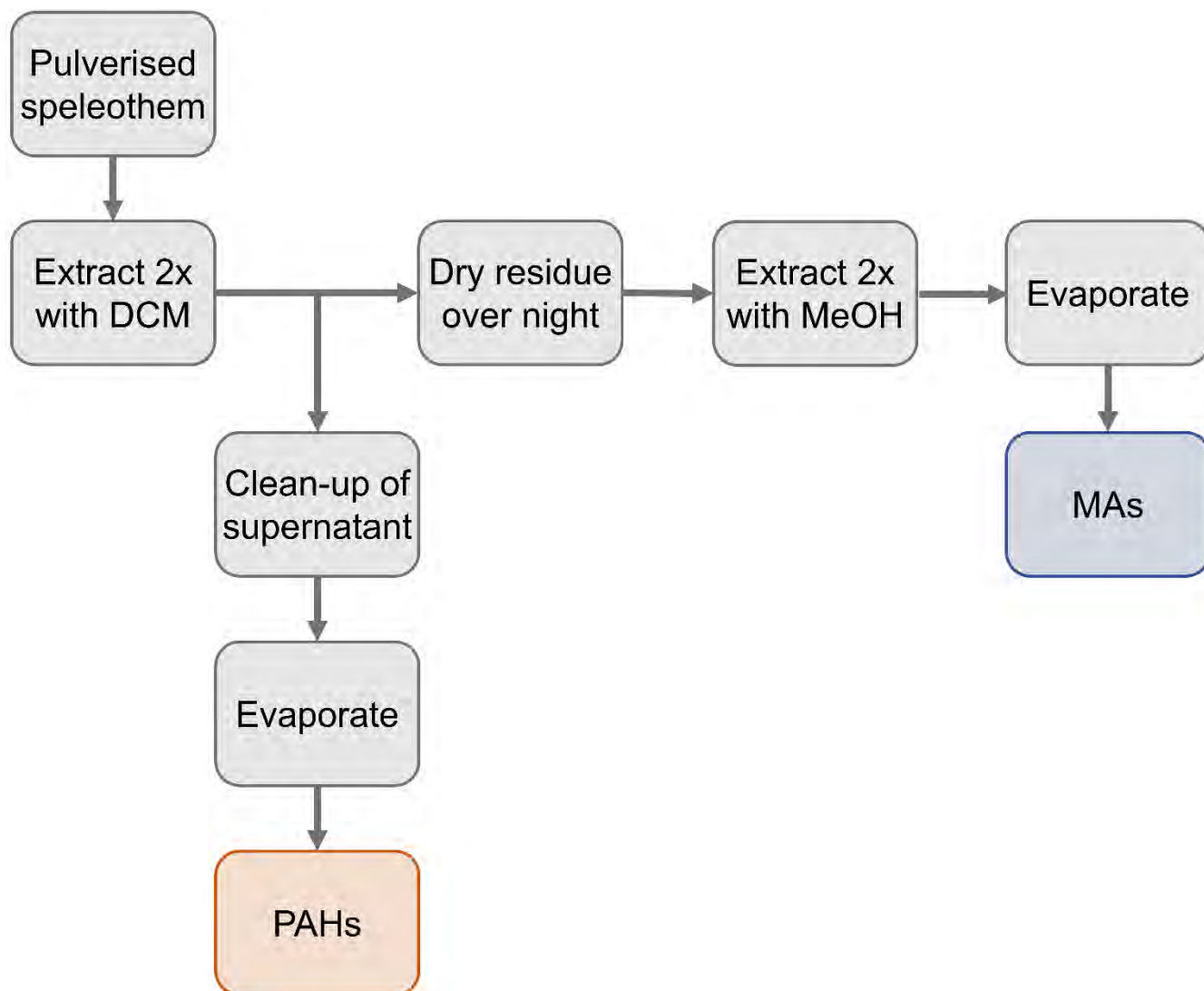


Figure S7. Flow chart of the sample preparation method.

Table S4. Determined d-PAH and ¹³C-levoglucosan recoveries (%) of the 10 samples from stalagmite MAYA-22-7 from Cenote Ch'en Mul, Mayapan.

Age (Year CE)*	2010-2015	2000-2010	1995-2000	1945-1985	1945-1965	1920-1935	1890-1905	1855-1875	1760-1790	1640-1650
Sample #	4	3	5	2	6	8	9	1	10	11
d-NAP	48.1 ±9.8	57.6 ±4.2	101.7 ±36.4	48.9 ±3.5	67.4 ±19.7	41.6 ±8.2	82.8 ±26.8	66.6 ±5.0	97.2 ±27.0	60.8 ±16.5
d-ACE	51.6 ±10.5	47.7 ±3.5	120.7 ±43.1	40.7 ±2.9	77.3 ±22.6	45.5 ±9.0	93.8 ±30.3	56.7 ±4.3	101.1 ±28.0	57.4 ±15.5
d-PHE	66.9 ±13.6	76.8 ±5.6	127.2 ±45.5	66.6 ±4.8	89.6 ±26.2	46.4 ±9.1	100.3 ±32.4	88.7 ±6.7	110.0 ±30.5	69.7 ±18.9
¹³ C-LEV	70.7 ±7.6	66.8 ±6.9	79.2 ±1.8	66.1 ±4.5	74.2 ±6.5	61.8 ±4.7	82.9 ±10.2	80.7 ±2.2	71.4 ±17.2	78.1 ±5.2

*: Start and end dates have errors of ± 6-20 years (95 % confidence interval)

Table S5. Determined PAH and MA concentrations (ng g^{-1}) of the 10 samples from stalagmite MAYA-22-7 from Cenote Ch'en Mul, Mayapan.

Age (Year CE)*	2010-2015	2000-2010	1995-2000	1945-1985	1945-1965	1920-1935	1890-1905	1855-1875	1760-1790	1640-1650
Sample #	4	3	5	2	6	8	9	1	10	11
NAP	1.4 ± 0.3	< LOD	3.2 ± 1.1	2.8 ± 0.2	7.1 ± 2.1	1.4 ± 0.3	5.2 ± 1.7	1.2 ± 0.1	4.0 ± 1.1	2.2 ± 0.6
ACY	0.1 ± 0.02	0.3 ± 0.02	0.1 ± 0.04	0.5 ± 0.04	0.3 ± 0.1	< LOD	0.3 ± 0.1	0.1 ± 0.01	0.2 ± 0.1	< LOD
ACE	0.2 ± 0.05	0.2 ± 0.01	0.5 ± 0.2	0.3 ± 0.02	0.7 ± 0.2	0.2 ± 0.05	0.5 ± 0.2	0.2 ± 0.02	0.4 ± 0.1	0.3 ± 0.1
FLN	0.4 ± 0.1	0.4 ± 0.03	0.6 ± 0.2	0.8 ± 0.1	0.7 ± 0.2	0.2 ± 0.05	0.6 ± 0.2	0.4 ± 0.03	0.5 ± 0.1	0.4 ± 0.1
PHE	3.8 ± 0.8	3.8 ± 0.3	3.9 ± 1.4	7.20 ± 0.5	5.7 ± 1.7	1.8 ± 0.4	4.0 ± 1.3	3.3 ± 0.3	3.9 ± 1.1	2.2 ± 0.6
ANT	0.1 ± 0.01	1.0 ± 0.1	0.1 ± 0.03	2.1 ± 0.2	< LOD	< LOD	< LOD	0.7 ± 0.1	< LOD	< LOD
FLT	< LOD	< LOD	0.7 ± 0.3	< LOD	< LOD	< LOD	0.7 ± 0.2	< LOD	0.7 ± 0.2	< LOD
PYR	0.4 ± 0.1	0.5 ± 0.004	0.6 ± 0.2	0.9 ± 0.1	0.9 ± 0.3	< LOD	0.5 ± 0.2	0.7 ± 0.05	0.5 ± 0.1	0.3 ± 0.1
RET	< LOD	< LOD	0.8 ± 0.3	< LOD	< LOD	< LOD	0.4 ± 0.1	< LOD	< LOD	< LOD
BAA	< LOD	< LOD	< LOD	< LOD	< LOD	< LOD	< LOD	< LOD	< LOD	< LOD
CHR	< LOD	< LOD	< LOD	< LOD	< LOD	< LOD	< LOD	< LOD	< LOD	< LOD
BBF	< LOD	< LOD	< LOD	< LOD	< LOD	< LOD	< LOD	< LOD	< LOD	< LOD
BAP	< LOD	< LOD	< LOD	< LOD	< LOD	< LOD	< LOD	< LOD	< LOD	< LOD
INP	< LOD	< LOD	< LOD	< LOD	< LOD	< LOD	< LOD	< LOD	< LOD	< LOD
DBA	0.1 ± 0.02	0.0 ± 0.001	0.2 ± 0.1	0.1 ± 0.004	< LOD	0.02 ± 0.004	0.1 ± 0.03	0.1 ± 0.004	0.04 ± 0.01	< LOD
DPE	< LOD	< LOD	< LOD	< LOD	< LOD	< LOD	< LOD	< LOD	< LOD	< LOD
MAN	0.3 ± 0.03	0.1 ± 0.02	0.3 ± 0.02	0.4 ± 0.08	0.3 ± 0.06	0.3 ± 0.01	< LOD	0.1 ± 0.02	0.2 ± 0.01	0.3 ± 0.0003

Age (Year CE)*	2010-2015	2000-2010	1995-2000	1945-1985	1945-1965	1920-1935	1890-1905	1855-1875	1760-1790	1640-1650
Sample #	4	3	5	2	6	8	9	1	10	11
GAL	0.3 ±0.1	0.1 ±0.02	0.2 ±0.003	0.4 ±0.07	0.7 ±0-01	0.3 ±0.01	0.1 ±0.02	0.1 ±0.01	0.2 ±0.03	0.3 ±0.01
LEV	1.8 ±0.20	0.6 ±0.09	2.3 ±0.001	3.4 ±0.05	5.7 ±0.67	1.9 ±0.02	1.9 ±0.14	0.8 ±0.02	2.0 ±0.42	2.0 ±0.07

*: Start and end dates have errors of ± 6-20 years (95 % confidence interval)

Table S6. Calculated sums and diagnostic ratios of the 10 samples from stalagmite MAYA-22-7 from Cenote Ch'en Mul, Mayapan.

Age (Year CE)*	2010-2015	2000-2010	1995-2000	1945-1985	1945-1965	1920-1935	1890-1905	1855-1875	1760-1790	1640-1650
Sample #	4	3	5	2	6	8	9	1	10	11
$\Sigma 15^\dagger$	6.4 \pm 1.3	6.2 \pm 0.5	9.9 \pm 3.5	14.7 \pm 1.1	15.4 \pm 4.5	3.8 \pm 0.7	11.9 \pm 3.8	6.7 \pm 0.5	10.3 \pm 2.8	5.4 \pm 1.5
LMW ‡	6.0 \pm 1.2	5.6 \pm 0.4	9.0 \pm 3.2	13.8 \pm 1.0	14.5 \pm 4.2	3.7 \pm 0.7	11.3 \pm 3.7	6.0 \pm 0.5	9.7 \pm 1.4	5.0 \pm 1.4
HMW $^\diamond$	0.4 \pm 0.1	0.5 \pm 0.04	0.9 \pm 0.3	0.9 \pm 0.1	0.9 \pm 0.3	0.02 \pm 0.004	0.6 \pm 0.2	0.7 \pm 0.1	0.5 \pm 0.1	0.3 \pm 0.1
LMW/HMW	13.6 \pm 5.5	10.4 \pm 1.5	10.3 \pm 7.3	14.9 \pm 2.1	15.8 \pm 9.2	175.5 \pm 69.1	19.3 \pm 12.5	8.5 \pm 1.3	18.9 \pm 10.5	14.7 \pm 8.0
PHE/ANT	74.7 \pm 30.3	4.0 \pm 0.6	43.0 \pm 30.7	3.4 \pm 0.5	NA	NA	NA	4.8 \pm 0.7	NA	NA
ANT/(ANT+PHE)	0.01 \pm 0.01	0.2 \pm 0.03	0.02 \pm 0.02	0.2 \pm 0.03	NA	NA	NA	0.2 \pm 0.03	NA	NA
RET/(RET+PHE+ANT)	NA	NA	0.16 \pm 0.18	NA	NA	NA	0.10 \pm 0.06	NA	NA	NA
LEV/(LEV+ $\Sigma 15$)	0.5 \pm 0.1	0.2 \pm 0.04	0.4 \pm 0.1	0.4 \pm 0.04	0.5 \pm 0.2	0.6 \pm 0.1	0.3 \pm 0.1	0.3 \pm 0.03	0.4 \pm 0.2	0.5 \pm 0.2
LEV/MAN	5.9 \pm 1.2	9.7 \pm 3.8	8.0 \pm 0.6	9.5 \pm 2.3	18.8 \pm 5.7	7.4 \pm 0.5	NA	9.1 \pm 2.1	8.8 \pm 2.5	6.0 \pm 0.2
LEV/(MAN+GAL)	3.3 \pm 0.8	4.7 \pm 3.0	4.6 \pm 0.4	4.8 \pm 2.1	5.9 \pm 1.8	3.7 \pm 0.4	18.6 \pm 4.96	5.4 \pm 2.0	4.7 \pm 2.1	3.1 \pm 0.2.

*: Start and end dates have errors of \pm 6-20 years (95 % confidence interval) † : Sum of non-alkylated PAHs; ‡ : Sum of two and three-ring PAHs; $^\diamond$: Sum of four and five-ring PAHs

C. Adaptation of CuSO_4 digestion to other matrices

C.1. Introduction

As mentioned in Chapter 2, a CuSO_4 digestion method for lignin in speleothem samples has been developed following Yan and Kaiser.⁵⁶ A schematic representation of the procedure can be found in Figure S5. Briefly, the speleothem sample is dissolved in 30% HCl and the solution is loaded onto an HLB SPE cartridge to isolate the polymeric lignin. This is eluted and then digested with CuSO_4 to produce the lignin oxidation products (LOPs), which are finally concentrated by another SPE.

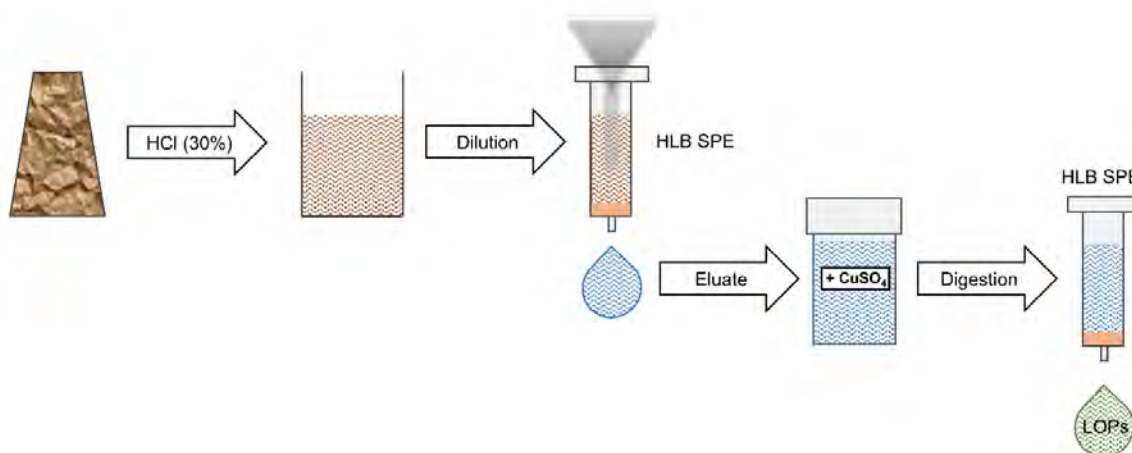


Figure S8. Schematic representation of the CuSO_4 digestion method.

However, to study the polymer's transport through and natural degradation within the soil it is necessary to also analyse lignin from other matrices like soil, leaves, and branches.

To adapt the existing method for the analysis of other natural samples and pure lignin powder, two different approaches were explored based on sample preparation procedures described by Heidke et al. (2018,2019)^{36,53} and Hedges and Mann (1979).⁵⁴

C.2. Solid-liquid extraction prior to CuSO_4 digestion

For the first approach, the different sample types were soaked in solvent for two weeks and the resulting extracts then treated like the speleothem solutions in the original method.

Soil, leaf litter, and small branches were collected from a green corridor at the campus of Johannes Gutenberg-University Mainz. The samples were dried at 130 °C for three days prior to analysis and homogenised. In addition, a lignin powder from wheat straw and various kinds of wood was analysed.

Approximately 100 mg of each natural sample and 50 mg of the lignin powder, respectively, were covered with 2 mL solvent to soak for one to two weeks. HCl (30%), NH_3 (25%), and water were tested as solvents with an initial extraction time of two weeks.

To test the repeatability of the method, each of the samples were prepared in triplicate and extracted with HCl (30%) for a week.

To determine the optimal duration of the extraction, soil samples were extracted for a length of 1 h, 2 h, 3 h, 4 h, 6 h, 8 h, 24 h, 48 h, 70 h, and 143 h.

All samples were filtrated through a Whatman 40 paper filter onto preconditioned 200 mg HLB SPE-cartridges and then processed as described in Chapter 2.

C.2.1. Selection of extraction solvent

The extraction of lignin lead to the highest sum of all 8 investigated lignin oxidation products ($\Sigma 8$) irrespective of the extraction solvent (Figure S6). However, the extraction with water resulted in much higher $\Sigma 8$ concentrations ($1892 \pm 150 \text{ ng} \cdot \text{g}^{-1}$) than the extraction with hydrochloric acid ($1423 \pm 84 \text{ ng} \cdot \text{g}^{-1}$), and ammonia solution ($1039 \pm 126 \text{ ng} \cdot \text{g}^{-1}$). This trend is not found for the other sample types in the same extent. Water extraction also results in the highest $\Sigma 8$ concentration for leaf litter ($883 \pm 94 \text{ ng} \cdot \text{g}^{-1}$) but extraction with the two other solvents do not differ significantly from one another ($518 \pm 39 \text{ ng} \cdot \text{g}^{-1}$ (HCl) and $482 \pm 55 \text{ ng} \cdot \text{g}^{-1}$ (NH₃)). The extraction of branches led to the same $\Sigma 8$ range with all three solvents ($708 \pm 64 \text{ ng} \cdot \text{g}^{-1}$ (H₂O), $632 \pm 128 \text{ ng} \cdot \text{g}^{-1}$ (HCl), and $687 \pm 20 \text{ ng} \cdot \text{g}^{-1}$ (NH₃), respectively) while hydrochloric acid led to the highest $\Sigma 8$ concentrations for the extraction of soil ($148 \pm 13 \text{ ng} \cdot \text{g}^{-1}$), followed by ammonia solution ($92 \pm 8 \text{ ng} \cdot \text{g}^{-1}$) and water ($51 \pm 45 \text{ ng} \cdot \text{g}^{-1}$).

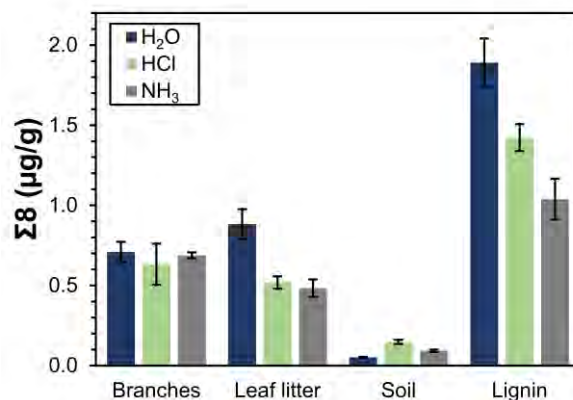


Figure S9. $\Sigma 8$ values of the extraction of branches, leaf litter, soil, and lignin with H₂O (blue), HCl (30 %; green), and NH₃ (25 %; grey), respectively. Extraction time was 14 days in all cases. Error bars represent one standard deviation of samples measured in duplicate.

Interestingly, extraction with the three different solvents results in unique distribution of ΣV , ΣS , and ΣC for each sample type (Figure S7, left) which in turn leads to different positions in the C/V vs. S/V scatter plot (Figure S7, right) for each sample-solvent pair.

Based on the known origin of the investigated samples it was determined that the extraction with HCl (30 %) lead to the most accurate results. Therefore, HCl (30 %) was chosen as the solvent for further extraction experiments.

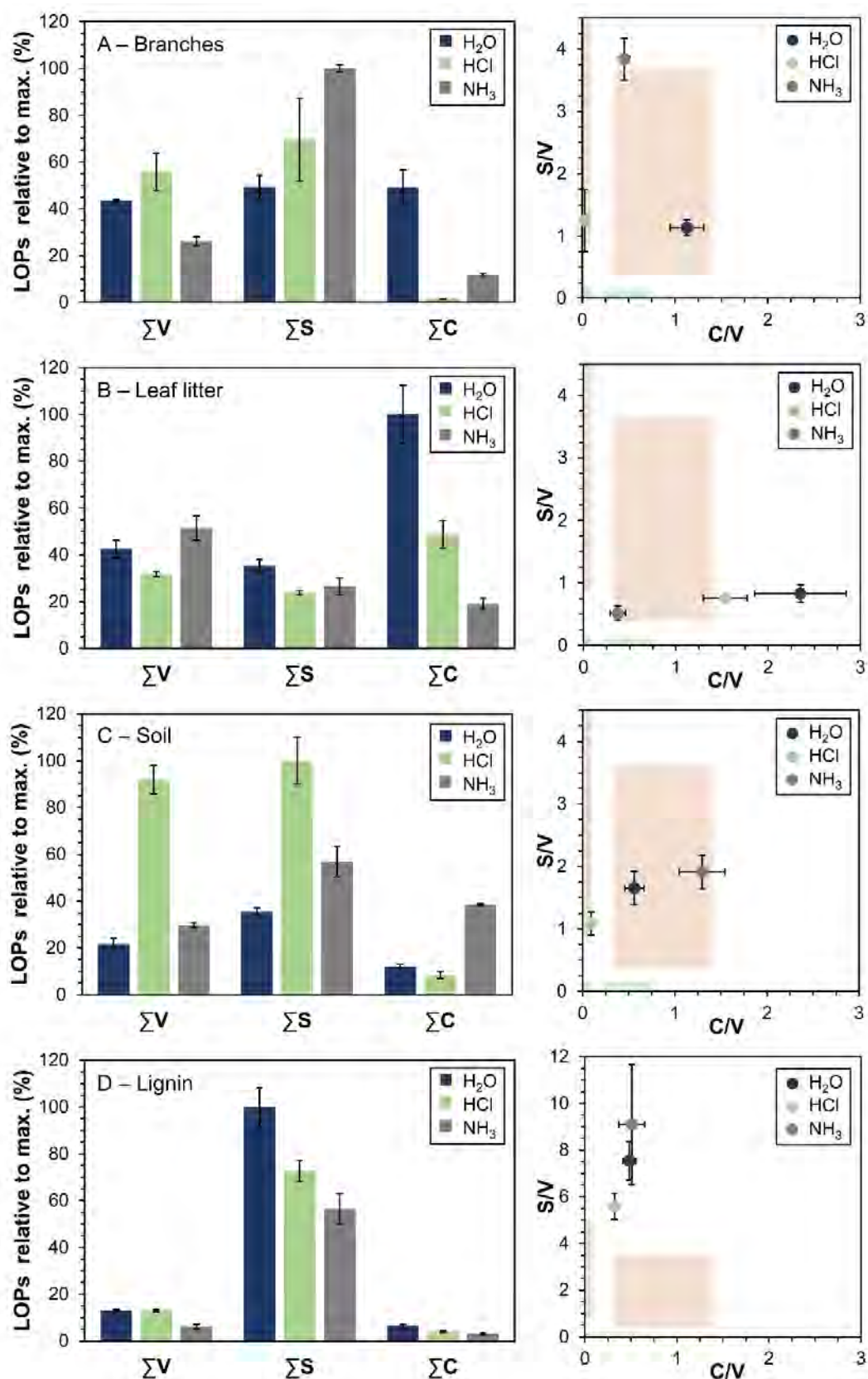


Figure S10. ΣV , ΣS , and ΣC values (left) and S/V versus C/V ratios (right) of the extraction of branches (A), leaf litter (B), soil (C), and lignin (D) with H₂O (blue), HCl (30%; green), and NH₃ (25%; grey), respectively. ΣV , ΣS , and ΣC values are normalised to the highest value for each sample type. Shaded areas in the scatter plots correspond to different vegetation sources as defined by Hedges and Mann (1979).⁵⁴ Extraction time was 14 days in all cases. Error bars represent one standard deviation of samples measured in duplicate.

C.2.2. Repeatability of extraction

To test the repeatability of the HCl extraction, every sample type was extracted three times for 7 days each. The resulting $\Sigma 8$ and RSD values are shown in Figure S8.

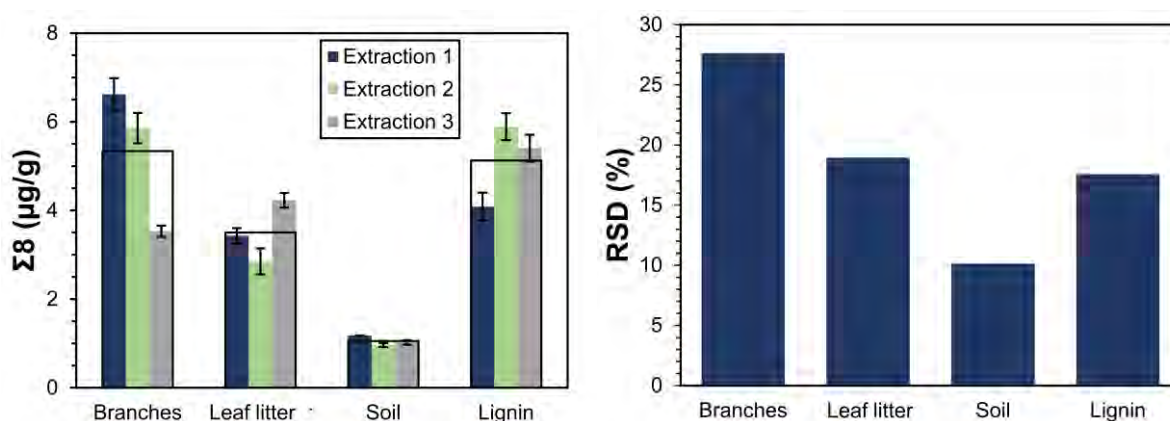


Figure S11. $\Sigma 8$ values of individual extractions (blue, green, and grey) and mean of three extraction (black) (left) and RSD (right) of the extraction of branches, leaf litter, soil, and lignin with HCl (30 %) for 7 days. Error bars represent one standard deviation of samples measured in duplicate.

The determined $\Sigma 8$ values are significantly higher than the corresponding concentrations found in chapter C.2.1 (e.g. $1.05 \pm 0.11 \mu\text{g} \cdot \text{g}^{-1}$ vs. $0.15 \pm 0.01 \mu\text{g} \cdot \text{g}^{-1}$ for soil) but the distribution is the same with branches and lignin powder resulting in the highest $\Sigma 8$ values, followed by leaf litter, and soil displaying the lowest concentrations. The higher concentrations might be caused by inhomogeneity of the sample material. For this reason, the influence of the extraction time on the determined lignin oxidation products (LOP) concentrations should be investigated.

The repeatability experiments displayed reasonable RSD values with 27.6 % for branches, 19.0 % for leaf litter, 17.6 % for lignin powder, and 10.1 % for soil, respectively. As all sample types are of natural origin, a higher variation of lignin constitution is expected^{53,54} and RSDs of under 30 % are well acceptable.

C.2.3. Determination of optimal extraction time

As mentioned above, the influence of the extraction time on the determined LOP concentrations need to be investigated to retrieve maximal $\Sigma 8$ values while maintaining reasonable C/V and S/V values. For this reason, soil samples were extracted for various time periods.

Figure S9 shows the obtained ΣV , ΣS , and ΣC values plotted versus the extraction time. While ΣV and ΣS decrease after the first three hours of extraction before building up again after 24 – 48 hours, ΣC starts off with very low concentrations and only approaches the reference concentration (chapter C.2.2) after 24 – 48 hours. After an extraction time of 48 hours, the obtained values for both ΣV and ΣC lie within the error of the reference concentration. ΣS also stabilises after 48 hours but only at about 60 % of the reference. This effect could be due to a methodological error due to which syringic acid (SA) could not be detected in the latter half of the sample set. This is also reflected in the Acid-to-Aldehyde ratio of the S-group ((Ad/Al)_S) which is significantly lower than the comparison while the respective ratio of the V-group ((Ad/Al)_V) falls within the error of the reference (Figure S10). However, this does not necessarily mean, that the samples did not contain any SA as the calibration solutions

were likewise affected. It is possible that SA is degraded in solution over time, however this issue remains unsolved.

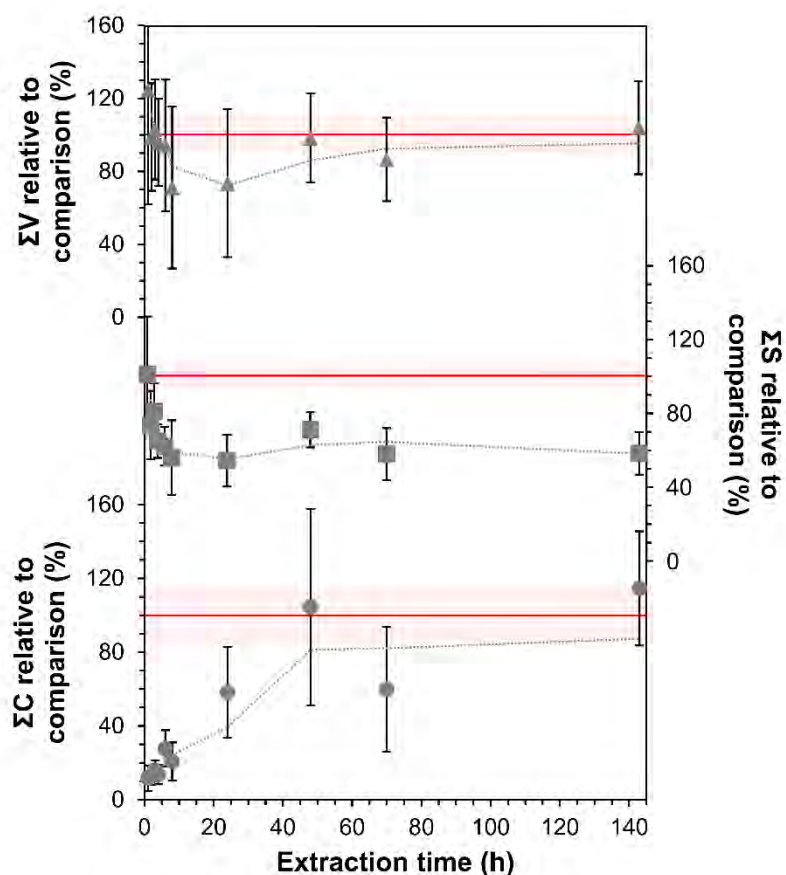


Figure S12. ΣV (triangles), ΣS (squares), and ΣC (circles) values of the extraction of soil with HCl (30 %) in dependence on the extraction time. Results are normalised to the results from the repeatability experiment (chapter C.2.2). Error bars represent one standard deviation of samples prepared in triplicate and measured in duplicate. The red lines represent the respective results from the repeatability experiment with one standard deviation shown by the shaded areas. The grey dotted lines represent the moving average.

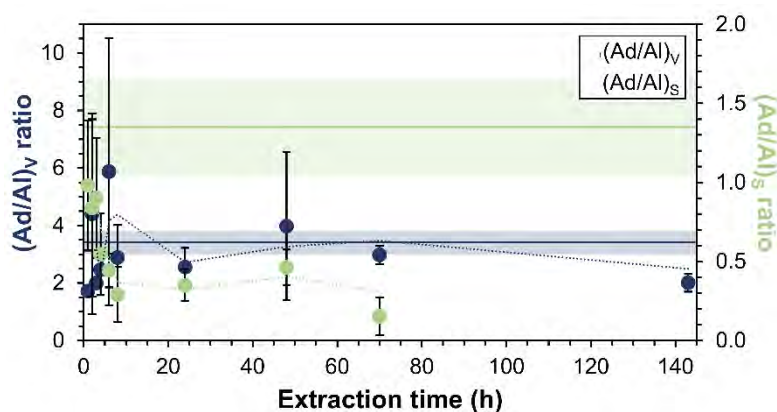


Figure S13. Acid-to-Aldehyde ratios (Ad/Al) for the V- (blue) and the S-group (green) LOPs of the extraction of soil with HCl (30 %) in dependence on the extraction time. Error bars represent one standard deviation of samples prepared in triplicate and measured in duplicate. The dark lines represent the respective results from the repeatability experiment with one standard deviation shown by the shaded areas. The dotted lines represent the moving average.

Irrespective of the unclear results for SA, the experiment shows that a saturation is reached after an extraction time of 24 – 48 hours. While, an extraction time of up to 143 hours does not lead to higher concentrations it also does not lead to an overoxidation which would be visible in increased (Ad/Al) values. Therefore, it can be concluded that an extended extraction time of over 48 hours is neither useful nor harmful.

C.3. Direct CuSO₄ digestion

As an extraction adds an additional step to the sample preparation making it more time consuming and increasing the possibility of analyte loss or contamination, a direct digestion (Figure S11) of the sample materials would be preferred. In this case, the dried and pulverised sample is directly fed to the CuSO₄ digestion and the LOPs are isolated on a HLB SPE cartridge.

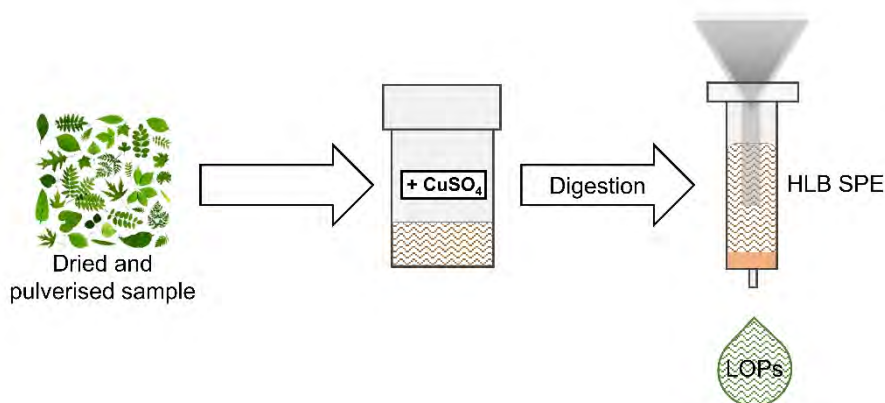


Figure S14. Schematic representation of the newly developed direct digestion using CuSO₄ as the oxidising agent.

As a proof of principle, the different sample types (soil, leaf litter, branches, and lignin powder) were digested with two different oxidant- (CuSO₄) to-antioxidant (ascorbic acid) ratios (O/AO) representing the ratios used in the original CuSO₄ (1:56) and CuO (1:20) digestion methods, respectively.

Approximately 100 mg of each natural sample and 50 mg the lignin powder, respectively, were used for the digestion. The samples were mixed with respective volumes of CuSO₄- and ascorbic acid solutions and covered with 1.25 mL of degassed NaOH. The digestion and subsequent sample processing was conducted as described in Chapter 2.

To test the repeatability of the method, each of the sample types was prepared in triplicate with an oxidant-to-antioxidant ratio (O/AO) of 1:20.

To systematically optimise the O/AO ratio, six ratios (no AO, 1:1, 1:5, 1:10:1:20, 1:50) were investigated using two different kinds of lignin powder (A: wheat straw and various kinds of wood; B: softwood). This was done by keeping the volume of oxidant constant (126 µL 10 mM CuSO₄-solution) while varying the amount of added antioxidant.

C.3.1. Proof of principle

Both O/AO ratios resulted in successful digestions of all sample types. The achieved $\Sigma 8$ values and the S/V and C/V ratios are displayed in Figure S12.

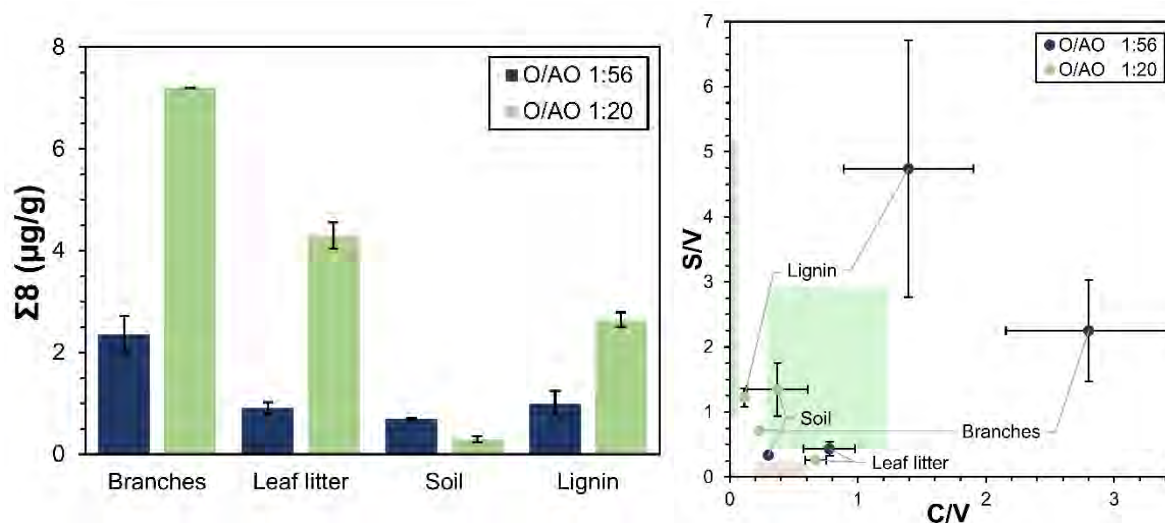


Figure S15. $\Sigma 8$ values (left) and S/V versus C/V ratios (right) of the digestion of branches, leaf litter, soil, and lignin with an oxidant-to-antioxidant ratio (O/AO) of 1:56 (blue) and 1:20 (green), respectively. Shaded areas in the scatter plots correspond to different vegetation sources as defined by Hedges and Mann (1979).⁵⁴ Error bars represent one standard deviation of samples measured in duplicate.

The digestion with an O/AO ratio of 1:20 led to significantly higher $\Sigma 8$ concentrations for branches, leaf litter, and lignin powder ($7.2 \pm 0.0 \mu\text{g} \cdot \text{g}^{-1}$, $4.3 \pm 0.3 \mu\text{g} \cdot \text{g}^{-1}$, and $2.6 \pm 0.1 \mu\text{g} \cdot \text{g}^{-1}$, respectively) than the digestion with an O/AO ratio of 1:56 ($2.4 \pm 0.4 \mu\text{g} \cdot \text{g}^{-1}$, $0.9 \pm 0.1 \mu\text{g} \cdot \text{g}^{-1}$, and $1.0 \pm 0.2 \mu\text{g} \cdot \text{g}^{-1}$, respectively). The latter method only led to higher concentrations for the soil sample ($0.7 \pm 0.0 \mu\text{g} \cdot \text{g}^{-1}$ versus $0.3 \pm 0.1 \mu\text{g} \cdot \text{g}^{-1}$). The resulting positions in the S/V versus C/V scatter plot were reasonable for all samples, although the branches and lignin samples of the digestion with an O/AO ratio of 1:56 led to high values in both LOP ratios. These two data points therefore differ a lot from the corresponding samples with an O/AO ratio of 1:20.

Because of the higher $\Sigma 8$ values achieved through an O/AO ratio of 1:20, this method was used for the determination of the repeatability of the direct digestion.

C.3.2. Repeatability of digestion

To test the repeatability of the direct digestion, every sample types was digested three times with an O/AO ratio of 1:20. The resulting $\Sigma 8$ and RSD values are shown in Figure S13.

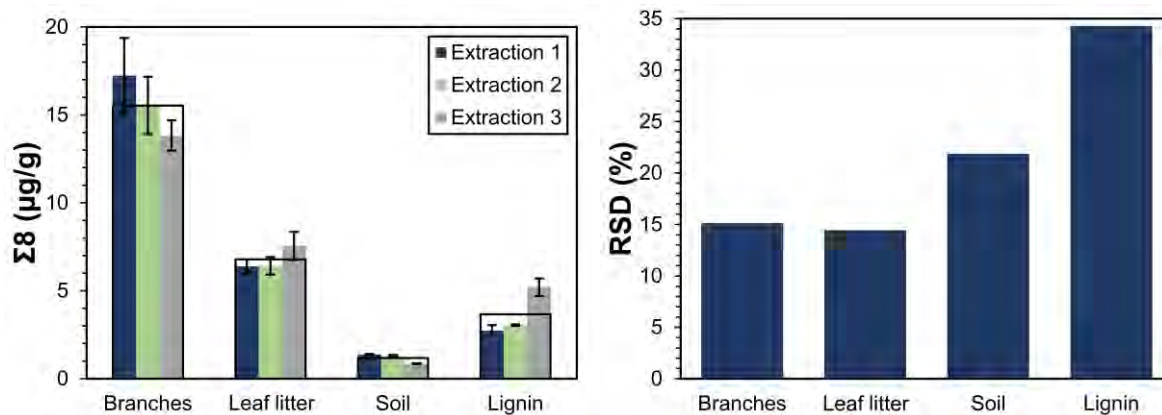


Figure S16. $\Sigma 8$ values of individual extractions (blue, green, and grey) and mean of three extraction (black) (left) and RSD (right) of the digestion of branches, leaf litter, soil, and lignin with an oxidant-to-antioxidant ratio (O/AO) of 1:20. Error bars represent one standard deviation of samples prepared in triplicate and measured in duplicate.

The repeatability experiments displayed reasonable RSD values with 21.9 % for soil, 15.1 % for branches, 15.5 % for leaf litter, respectively. Only the digestion of lignin powder led to an RSD of over 30 % at 34.3 %.

Overall, the digestion displays a good repeatability which renders the method suitable for routine analysis.

C.3.3. Optimisation of oxidant-to-antioxidant ratio

The first experiments in chapter C.3.1 showed that the oxidant-to-antioxidant ratio (O/AO) has a large impact on the achievable $\Sigma 8$ values and the resulting position in the C/V vs. S/V scatter plot. For this purpose, two different lignins of known origin (A: wheat straw and various kinds of wood; B: softwood) were each digested with six different O/AO ratios to optimise the direct digestion method.

The digestion without the addition of an antioxidant resulted in the highest $\Sigma 8$ values for both kinds of lignin (Figure S13, left). However, the resulting datapoint in the C/V vs. S/V scatter plot for lignin A lay apart from the cluster of the other lignin A datapoints (Figure S13, right). In addition, the corresponding acid-to-aldehyde (Ad/Al) ratios were elevated in comparison to the results of the other O/AO ratios (Figure S15) which is an indicator for over-oxidation. This is reasonable, as the addition of antioxidant to the digestion is meant to prevent just that.

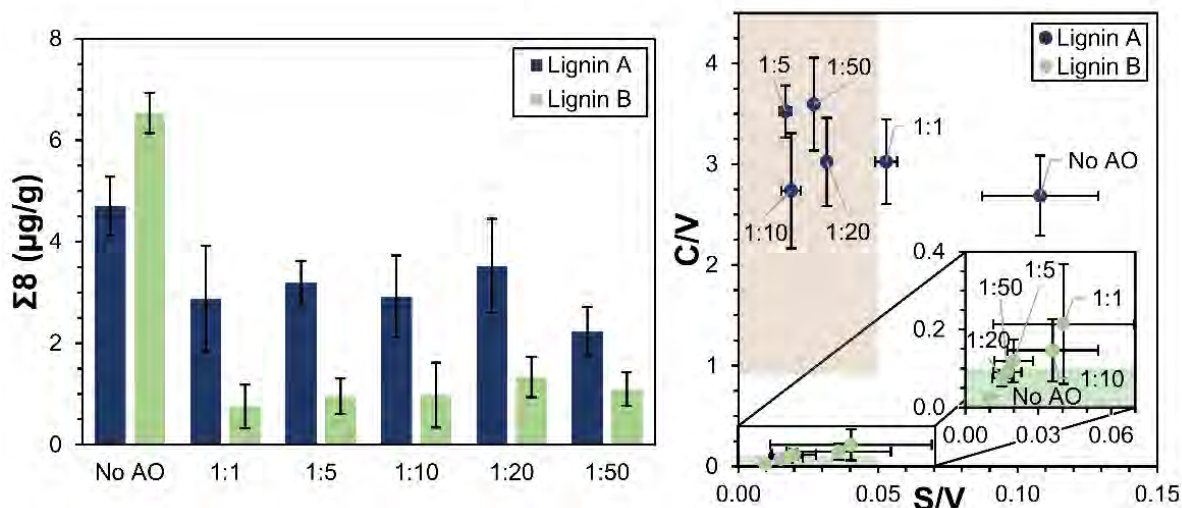


Figure S17. Influence of the oxidant-to-antioxidant ratio (O/AO) on the obtained $\Sigma 8$ (left) and S/V versus C/V ratios (right) of two different lignin powders (A: wheat straw and various kinds of wood, blue; B: softwood, green). Shaded areas in the scatter plots correspond to different vegetation sources as defined by Hedges and Mann (1979).⁵⁴ Error bars represent one standard deviation of samples prepared four times and measured in duplicate.

The $\Sigma 8$ values for the remaining O/AO ratios show a gradual increase from 1:1 up to 1:20 and then a slight decline towards 1:50 for both types of lignins (Figure S14, left). However, the differences between the individual ratios are within one standard deviation of each other. The datapoints of the two lignins also each cluster very closely together in the C/V vs. S/V scatter plot (Figure S13, right), indicating that a digestion with any of the O/AO ratios could possibly be used for vegetation reconstruction. As there is no other trend visible in the Ad/Al ratios, an O/AO ratio of 1:20 is recommended for further experiments. This ratio is equivalent to the ratio used in the original CuO method.

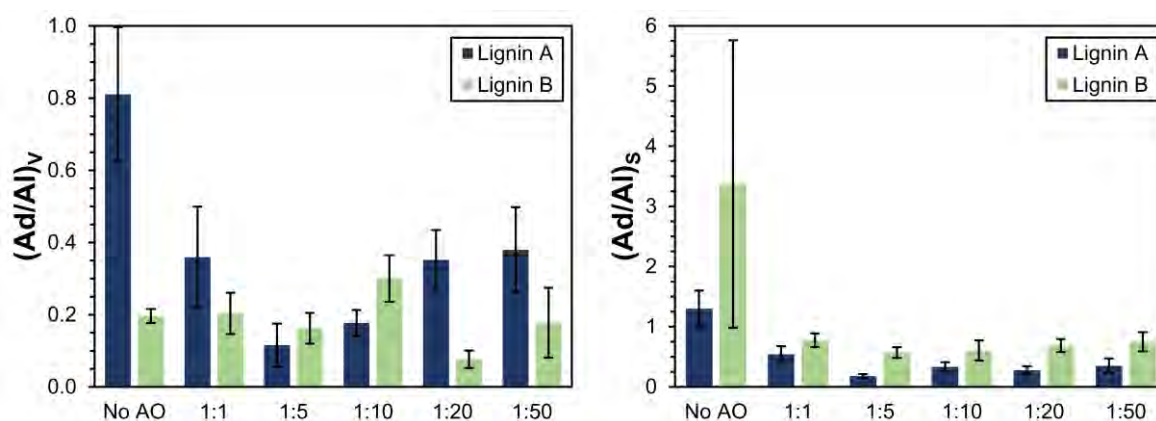


Figure S18. Influence of the oxidant-to-antioxidant ratio (O/AO) on the obtained Acid/Aldehyde ratios (Ad/Al) for the V- (left) and the S-group (right) of two different lignin powders (A: wheat straw and various kinds of wood, blue; B: softwood, green). Error bars represent one standard deviation of samples prepared four times and measured in duplicate.

C.4. Comparison and conclusion

Both the extraction with HCl (30 %) and the $CuSO_4$ digestion (O/AO 1:20) were shown to lead to high LOP concentrations and sensible vegetation reconstructions based on the data's position in a C/V vs. S/V scatter plot.

In an immediate comparison, the $\Sigma 8$ values of the digestion surpass those of the extraction for all natural sample types while the concentrations obtained from the analysis of lignin powder are of comparable magnitude with both methods (Figure S16).

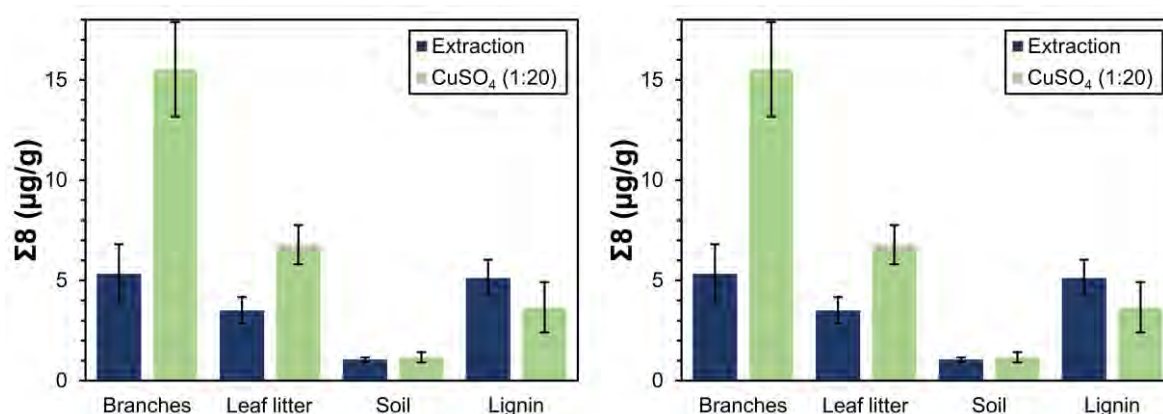


Figure S19. Comparison of the $\Sigma 8$ values (left) and RSD (right) of branches, leaf litter, soil, and lignin when prepared with a 7-day HCl (30 %) extraction (blue) and a CuSO₄ digestion (O/AO 1:20, green). Error bars represent one standard deviation of samples prepared in triplicate and measured in duplicate.

As the RSDs for both methods are also in an acceptable range for all sample types and both methods, no clear preference can be stated based on the data alone. However, if the sample preparation procedure is also taken into account, the CuSO₄ digestion is clearly preferable as it omits the extraction and pre-concentration steps before the digestion. Thus, the digestion method is less time consuming and resource intensive than the extraction method.

D. Levoglucosan in speleothems: An evaluation of various sample preparation methods

The results discussed in this chapter have been presented as a poster during *EGU General Assembly 2021*.²⁷¹

D.1. Abstract

Secondary mineral deposits in caves, such as stalagmites or flowstones, are valuable paleoclimate archives and they have several advantages over other environmental archives. These include stable in-cave conditions, protecting the speleothems from external influences, and the potential to precisely date samples up to 600,000 years using $^{230}\text{Th}/\text{U}$ -dating.⁴ Supplementing established climate proxies, such as stable isotopes and trace elements, organic proxies have been increasingly used in recent years to inform on local vegetation and soil dynamics.³⁸

Biomass burning events are major sources of atmospheric particulate matter that influence global and local climate.⁷⁰ Investigating fire proxies in paleoclimate archives may therefore help determine the interactions of climate, hydrology, and fire activity. Levoglucosan, an anhydrosugar, naturally only originates from the combustion of cellulose and thus constitutes a biomass burning marker. Analysis of levoglucosan in sediments has shown high correlation with traditional burning markers, such as black charcoal.⁶⁰ Mannosan and galactosan, both stereoisomers of levoglucosan, are formed during combustion of hemicellulose. Previous work suggests that rather than absolute levoglucosan concentrations the ratio of levoglucosan to its isomers should be considered when characterizing burning events.⁶⁷ To date, no data on levoglucosan or its isomers in speleothems has been published, whereas the anhydrosugars are already utilised in other paleoclimate archives, such as sediments and ice cores.^{38,70}

We test three approaches (solid phase extraction (SPE), soxhlet extraction and solid/liquid extraction) for the isolation and quantification of anhydrosugars using HILIC-MS instrumentation. As the anhydrosugars are highly polar molecules, extraction from the calcium carbonate matrix and subsequent sample preparation proved challenging. We evaluate the different approaches and compare the resulting concentrations and assumed recoveries. We find that the anhydrosugars do not show significant retention on any of the evaluated SPE materials. While solid/liquid extractions lead to detectable analyte concentrations, soxhlet extractions with methanol or dichloromethane/methanol mixtures are more efficient.

Levoglucosan in speleothems: An evaluation of various sample preparation methods.



J. Homann¹, T. Hoffmann¹, D. Scholz², S. Breitenbach³

¹ Department of Chemistry, Johannes Gutenberg-Universität Mainz, Germany (✉ juhomann@uni-mainz.de)

² Institute for Geosciences, Johannes Gutenberg-Universität Mainz, Germany

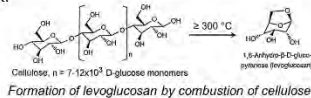
³ Department of Geography and Environmental Sciences, Northumbria University Newcastle, UK



Motivation

Levoglucosan, an anhydrosugar, naturally only originates from the combustion of cellulose and can thus be used as a biomass burning marker in speleothems and other archives. Investigating fire proxies in paleoclimate archives may help determine the interactions of climate, hydrology, and fire activity.

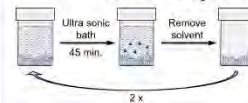
As anhydrosugars are highly polar molecules, extraction from the calcium carbonate matrix of speleothems and subsequent sample preparation proved difficult.



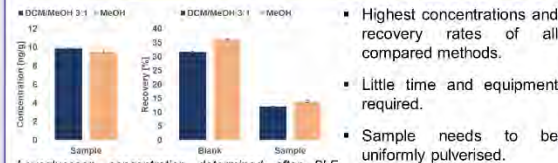
A variety of approaches for the isolation of levoglucosan were evaluated and compared based on the recoveries for ¹³C₆-levoglucosan spiked samples and resulting concentrations from the extraction of 1 g aliquots of a speleothem from Ifri Inouqben cave in northern Morocco. Measurements were conducted using the HILIC-ESI-HRMS method described by Homann et al.²

Pulverised speleothem

Solid-liquid extraction (SLE)



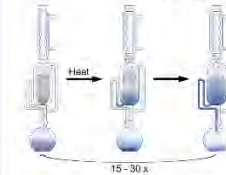
- Compared two different solvents.
- Evaporated solvent (2 x 5 mL).
- Dissolved residual in 200 µL ACN/H₂O 95:5 for measurement.



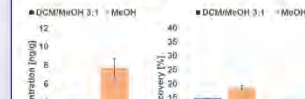
Levoglucosan concentration determined after SLE. Percentage recovery of ¹³C₆-levoglucosan in blanks and spiked sample, n=4.

SLE with either dichloromethane / methanol (DCM/MeOH) 3:1 or MeOH is recommended for the extraction of levoglucosan

Soxhlet extraction



- Compared two different solvents.
- Extraction time of 6 h.
- Evaporated solvent (50 mL).
- Dissolved residual in 200 µL ACN/H₂O 95:5 for measurement.

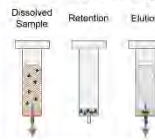


Levoglucosan concentration determined after soxhlet extraction. Percentage recovery of ¹³C₆-levoglucosan in blanks and spiked sample, n=4.

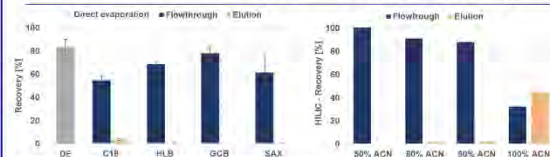
- Lower concentrations and recovery rates than SLE. Levoglucosan seems to be degraded by high temperatures.
- Time intensive and high SD.
- Soxhlet extraction with MeOH is **haltingly recommended** for the extraction of levoglucosan.

Dissolved speleothem

Solid phase extraction (SPE)



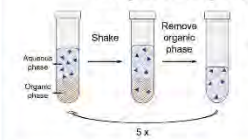
- Structure of solid phase determines retention:
 - C₁₈** – silica based RP
 - HLB** – polymer based RP
 - GCB** – charcoal based RP
 - SAX** – silica bonded quaternary ammonium ions
 - HILIC** – silica bonded zwitterions



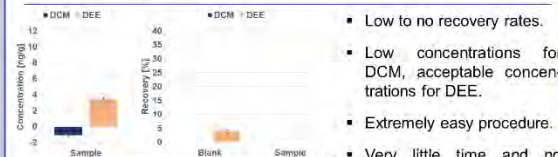
Percentage recovery of levoglucosan after SPE. 100 ng analyte were applied in 10 mL solvent. Elution with 6 x 250 µL H₂O for HILIC and 10 x 500 µL of MeOH for all other phases. HILIC: n=1; C₁₈: n=2; SAX and DE: n=3; HLB and GCB: n=4.

None of the evaluated phases is suitable for the extraction of levoglucosan.

Liquid-liquid extraction (LLE)



- Compared two different solvents.
- Evaporated solvent (5 x 3 mL).
- Dissolved residual in 200 µL ACN/H₂O 95:5 for measurement.

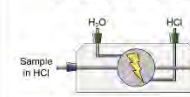


Levoglucosan concentration determined after LLE. Percentage recovery of ¹³C₆-levoglucosan in blanks and spiked sample, n=4.

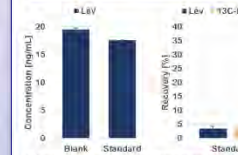
LLE with diethyl ether (DEE) is tentatively recommended for the extraction of levoglucosan due to extreme ease of procedure.

- Low to no recovery rates.
- Low concentrations for DCM, acceptable concentrations for DEE.
- Extremely easy procedure.
- Very little time and no special equipment required.

Electrochemical neutralisation (ECN)



- Neutralisation of HCl (15%) by electrochemical exchange of anions.
- Evaporated aqueous solution
- Dissolved residual in 200 µL ACN/H₂O 95:5 for measurement.



Concentration and percentage recovery of levoglucosan and ¹³C₆-levoglucosan after ECN. 100 ng analyte were dissolved in 6 mL HCl (15%). Blank: n=3; Standard: n=2.

- High blank values and carry over between measurements.
- Low recovery rates. Levoglucosan seems to be degraded by the electric current during neutralisation period (3 h).
- Very time intensive and special instrumentation required.
- Might be suitable for analytes not prone to oxidation.

ECN is not suitable for the extraction of levoglucosan.

Conclusion

- Extraction of pulverised speleothem proved more effective than utilising dissolved speleothem.
- Levoglucosan proved prone to degradation when exposed to elongated periods of high temperature or electric current.
- Sample needs to be uniformly ground to a low grain size to maximise extraction efficiency.



Max Planck Graduate Center
mit der Johannes Gutenberg-Universität



Ref.: [1] Elias et al. *Geochimica et Cosmochimica Acta* 2001, 65 (2), 267–272
 [2] Homann et al. EGU General Assembly 2020, Online, 4–8 May 2020, EGU2020-2413

D.2. Introduction

Investigating fire proxies in paleoclimate archives may help determine the interactions of climate, hydrology, and fire activity. Levoglucosan, an anhydrosugar, naturally only originates from the combustion of cellulose and thus constitutes a biomass burning marker. Analysis of levoglucosan in sediments has shown high correlation with traditional burning markers, such as black charcoal.⁶⁰ Mannosan and galactosan, both stereoisomers of levoglucosan, are formed during combustion of hemicellulose. To date, no data on levoglucosan or its isomers in speleothems has been published, whereas the anhydrosugars are already utilised in other paleoclimate archives, such as sediments and ice cores.^{38,70}

For analysis, levoglucosan has to be extracted from the speleothem matrix. In theory, an extraction from a solution of the dissolved speleothem would be preferable as all analyte should be available for extraction. In contrast, only the molecules at the phase interface are extractable with methods using solid samples. Therefore, the particle size has to be as small as possible to maximise surface area. In literature, multiple different extraction techniques are utilised for the extraction of levoglucosan from sediments and aerosol filter samples. There, mostly H₂O^{272,273}, methanol (MeOH)^{60,67,274,275}, or dichloromethane (DCM)^{211,276} have been used as extraction agents. In a past research project²⁷⁷ and a master thesis⁷² different extraction methods have already been investigated. Based on the results of these two projects, five different sample preparation methods were compared.

D.3. Experimental

For the experiments, aliquots of a speleothem from Ifri Inouqben cave in northern Morocco were used. The speleothem was ground to a particle size of about 60 µm and then homogenised to create a standard material with (ideally) uniform analyte distribution.

D.3.1. Chemicals and materials

An analytical standard of levoglucosan (99 %) and sodium thiosulphate (≥98 %) were purchased from Sigma-Aldrich. An analytical standard of ¹³C₆ levoglucosan (98 %) was obtained from Cambridge Isotope Laboratories. An analytical standard of ammonium acetate (≥99 %) and ultrapure acetonitrile (ACN, LC/MS grade) were obtained from VWR Chemicals. Sodium hydroxide (pellets, ≥ 99 %), hydrochloric acid (HCl, suprapure, 30 %), C18 solid-phase extraction columns (LiChromlut, 3 mL, 200 mg packing material), and water (LC-MS grade) were purchased from Merck KGaA. Ammonium hydroxide solution (NH₃, analytical grade, 25 %) was obtained from Honeywell Fluka. Ultrapure methanol (MeOH, LC/MS grade) was obtained Carl Roth while ultrapure dichloromethane (DCM, LC-MS grade, ≥99.8 %) and diethyl ether (DEE, LC-MS grade, ≥99.5 %) were both purchased from Fisher Scientific. Ultrapure water with 18.2 MΩ resistance was produced using a Milli-Q water system from Merck Millipore (Darmstadt, Germany). HLB solid-phase extraction columns (Oasis HLB, 3 mL tubes, 60 mg packing material) were purchased from Waters. GCB (ENVI-Carb, 3 mL tubes, 250 mg packing material) and SAX solid-phase extraction columns (Discovery DCS-SAX, 3 mL, 500 mg packing material) were both obtained from Supelco. HILIC solid-phase extraction columns (iSPE-HILIC, 3 mL, 200 mg packing material) were purchased from HILICON AB.

D.3.2. Solid-liquid extraction (SLE)

Aliquots of 1 g of speleothem were spiked with 100 μL of a solution of $^{13}\text{C}_6$ levoglucosan (100 $\text{ng} \cdot \text{mL}^{-1}$ in ACN) and extracted twice with 5 mL of MeOH or MeOH/DCM (1:3), respectively. The extraction was assisted by ultrasonic sound and lasted 45 min at a time. For each solvent a blank was prepared in the same manner. After sonication the samples were allowed to rest for 10-20 min to improve phase separation. Then, the supernatant was removed, filtered over a 1.0 μm glass fibre fabric filter (Macherey-Nagel), and evaporated under a gentle stream of nitrogen at 30 $^{\circ}\text{C}$. The residue was taken up in 200 μL of ACN/ H_2O (95:5) by 10 min of sonification at 45 $^{\circ}\text{C}$. The solution was filtered with a 0.2 μm PA-filter (Altmann-Analytik) and stored in the freezer at -25 $^{\circ}\text{C}$.

D.3.3. Soxhlet extraction

Aliquots of 1 g of speleothem were added into a glass extraction thimble and spiked with 100 μL of a solution of $^{13}\text{C}_6$ levoglucosan (100 $\text{ng} \cdot \text{mL}^{-1}$ in ACN). The sample was extracted for 6 h with 50 mL of MeOH or MeOH/DCM (1:3), respectively. For each solvent, a blank was prepared accordingly. The solution was evaporated under a gentle stream of nitrogen at 30 $^{\circ}\text{C}$ and the residue was redissolved in 200 μL of ACN/ H_2O (95:5) by 10 min of sonification at 45 $^{\circ}\text{C}$. The liquid was filtered with a 0.2 μm PA-filter (Altmann-Analytik) and stored in the freezer at -25 $^{\circ}\text{C}$.

D.3.4. Solid-phase extraction (SPE)

The C18, HLB, GCB, and SAX solid-phase extraction cartridges were pre-conditioned with 6 mL of MeOH followed by 6 mL of water. The HILIC SPE columns were pre-conditioned with 6 mL of each water and ACN. The HILIC SPE columns were loaded via reservoirs with solutions of 10 ng levoglucosan (100 μL of 100 $\text{ng} \cdot \text{mL}^{-1}$ in ACN) diluted in 10 mL solvent. The solvent consisted of 50 %, 80 %, 90 %, and 100 % ACN each mixed with water to amount to 100 %. The remaining cartridges were loaded via reservoirs with solutions of 10 ng levoglucosan (100 μL of 100 $\text{ng} \cdot \text{mL}^{-1}$ in ACN) dissolved in 10 mL water that had been acidified to pH 1-2 with HCl (30%). The flowthrough was collected and evaporated under a gentle stream of nitrogen at 30 $^{\circ}\text{C}$. Afterwards, the C18 and HLB cartridges were washed twice with 3 mL of an aqueous solution containing 5% MeOH. GCB columns were washed twice with 3 mL of water. SAX and HILIC columns were not washed. Again, the flowthrough was gathered and evaporated. Subsequently, the HILIC columns were eluted 6 times with 250 μL water. HLB and SAX cartridges were eluted 10 times with 500 μL MeOH each. C18 and GCB cartridges were eluted using 4 and 3 portions of 500 μL MeOH, respectively. The combined eluates were once more evaporated under a gentle stream of nitrogen at 30 $^{\circ}\text{C}$. Finally, all residues were redissolved in 200 μL ACN/ H_2O (95:5) by 10 min of sonification at 45 $^{\circ}\text{C}$. The liquid was filtered with a 0.2 μm PA-filter (Altmann-Analytik) and stored in the freezer at -25 $^{\circ}\text{C}$. For reference, a sample of 100 μL of levoglucosan (100 $\text{ng} \cdot \text{g}^{-1}$ in ACN) was evaporated under a gentle stream of nitrogen at 30 $^{\circ}\text{C}$. The workup of the residue was the same as described above.

D.3.5. Liquid-liquid extraction (LLE)

1 g aliquots of speleothem were weighed into a 15 mL centrifuge tube and dissolved in 2.5 mL HCl (30 %). The solution was diluted 1:1 with water and 100 μL of a solution of $^{13}\text{C}_6$

levoglucosan ($100 \text{ ng} \cdot \text{mL}^{-1}$ in ACN) were added. The sample solution was extracted 5 times with each 3 mL of DEE or DCM, respectively. The organic phases were collected and evaporated under a gentle stream of nitrogen at $30 \text{ }^\circ\text{C}$. For each solvent, a blank was prepared following the same procedure. The residue was taken up in $200 \text{ }\mu\text{L}$ of ACN/ H_2O (95:5) by 10 min of sonification at $45 \text{ }^\circ\text{C}$. The liquid was filtered with a $0.2 \text{ }\mu\text{m}$ PA-filter (Altmann-Analytik) and stored in the freezer at $-25 \text{ }^\circ\text{C}$.

D.3.6. Electrochemical neutralisation (ECN)

For the experiments, a Dionex CERS 500 (2 mm) suppressor (Thermo Fisher Scientific) was used in combination with a peristaltic pump (Perimax 16, Spetec GmbH). The sample solution (6 mL of HCl (15%), or $10 \text{ }\mu\text{L}$ each of solutions of levoglucosan and $^{13}\text{C}_6$ levoglucosan (each $10 \text{ }\mu\text{g} \cdot \text{mL}^{-1}$ in ACN) diluted with 6 mL HCl (15%)) was pumped in a circular flow at a flow rate of $0.25 \text{ mL} \cdot \text{min}^{-1}$. For this a white-white tube (fluoro rubber) was used. For the counter-current flow NaOH ($100 \text{ mmol} \cdot \text{L}^{-1}$) or water was utilised with a flow of $1.4 \text{ mL} \cdot \text{min}^{-1}$ in a double strand of violet-violet tubing (fluoro rubber). The waste was passed into a sodium thiosulphate solution (approximately 10 g in 200 mL water) to neutralise the generated chlorine gas. The reaction was run for about 3 h until the pH of the sample solution was at 2-5. During this time, the sample volume fell to approximately 4.5 mL . Afterwards, the equipment was purged with water which was combined with the sample until its volume was at 6 mL again. In total, 5 samples were prepared, alternating between blanks and spiked solutions starting and ending with blanks. The solution was evaporated with a vacuum centrifuge (Eppendorf Concentrator plus, $1,400 \text{ rpm}$) at $45 \text{ }^\circ\text{C}$ for 6 h to 12 h. The residue was redissolved twice in 1.5 mL ACN each by 10 min of sonification at $45 \text{ }^\circ\text{C}$. These solutions were combined and evaporated under a gentle stream of nitrogen at $30 \text{ }^\circ\text{C}$ and the residue taken up in $200 \text{ }\mu\text{L}$ of ACN/ H_2O (95:5) by 10 min of sonification at $45 \text{ }^\circ\text{C}$. The liquid was filtered with a $0.2 \text{ }\mu\text{m}$ PA-filter (Altmann-Analytik) and stored in the freezer at $-25 \text{ }^\circ\text{C}$.

D.3.7. Analysis

The analysis was carried out on a Dionex UltiMate 3000 ultrahigh-performance liquid chromatography system (UHPLC) that was coupled to a heated electrospray ionisation source (HESI) and a Q Exactive Orbitrap high-resolution mass spectrometer (HRMS) (all by Thermo Fisher Scientific). To retard the analytes, an iHILIC-Fusion(+) column, $100 \text{ mm} \times 2.1 \text{ mm}$ with $1.8 \text{ }\mu\text{m}$ particle size (Hilicon), was used. The injection volume was $10 \text{ }\mu\text{L}$. A $\text{H}_2\text{O}/\text{ACN}$ gradient program was applied at a flow of $0.4 \text{ mL} \cdot \text{min}^{-1}$. The gradient started with 97 % eluent B (100 % ACN) and 3 % eluent A (consisting of $5 \text{ mmol} \cdot \text{L}^{-1}$ ammonium acetate in H_2O). Eluent B was held at 97 % for 0.5 min and then decreased to 90 % within 0.5 min. Afterwards, eluent B was further decreased to 85 % in 5 min and 60 % in 1.5 min, respectively. Finally, it was decreased to 50 % within 1.5 min, held for 2.0 min, and then eluent B was increased to the initial value of 97 %. This was held for 8.5 min to re-equilibrate the column. To improve ionisation, a post-column flow of $50 \text{ mmol} \cdot \text{L}^{-1}$ NH_4OH in MeOH was applied with a flow rate of $0.1 \text{ mL} \cdot \text{min}^{-1}$. The ESI source was operated in negative mode so that deprotonated molecular ions $[\text{M}-\text{H}]^-$ were formed. ESI and MS conditions were the same as reported by Heidke et al. (2018).⁵³

D.4. Results and discussion

D.4.1. Solid-liquid extraction (SLE)

The results of the SLE experiments are visualised in Figure 8.1. Both DCM/MeOH 3:1 and MeOH lead to comparable recoveries, but the values obtained for MeOH are slightly higher. The recovery of $^{13}\text{C}_6$ levoglucosan is elevated for blank samples in comparison to the real samples. This implies some irreversible attachment of the analyte molecules to the sample matrix. Another possible explanation is that in the real samples other extractables are present besides levoglucosan with which the solvent preferably interacts. The recovery for the blank samples is at $31.7 \pm 0.2 \%$ for DCM/MeOH 3:1 and at $36.1 \pm 0.3 \%$ for MeOH. The recovery for the real samples is significantly lower with $12.1 \pm 0.1 \%$ for DCM/MeOH 3:1 and $13.9 \pm 0.5 \%$ for MeOH.

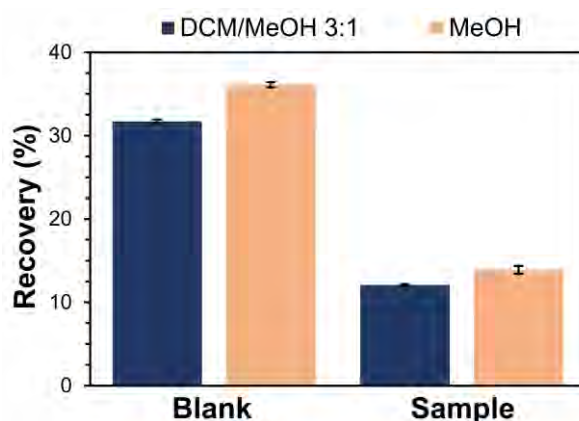


Figure 8.1. Percentage recovery of $^{13}\text{C}_6$ -levoglucosan in blanks and spiked sample after SLE. Error bars represent one standard deviation of samples prepared four times and measured in duplicate.

Because even the recovery for the blank samples is greatly reduced, methods for the increase of recovery should be evaluated. It might be possible to improve the recovery through the utilisation of silanated glassware. The silanisation could reduce adhesion to the glass. Another possible analyte sink are the consecutive evaporation steps. While these are necessary for the sample preparation, the effect should be quantified through appropriate experiments.

D.4.2. Soxhlet extraction

The recovery for the Soxhlet extractions is shown in Figure 8.2. Again, the recovery is higher for the blank samples than for the real samples. However, the difference is not as pronounced as for the SLE experiments. The recovery for the blank samples lies at $14.6 \pm 0.1 \%$ and $18.5 \pm 0.8 \%$ for DCM/MeOH 3:1 and MeOH, respectively. The real sample recoveries amount to $9.7 \pm 0.2 \%$ for DCM/MeOH 3:1 and $12.0 \pm 0.2 \%$ for MeOH. These results confirm the observation from the SLE experiments that the utilisation of MeOH as extraction solvent leads to slightly higher recoveries.

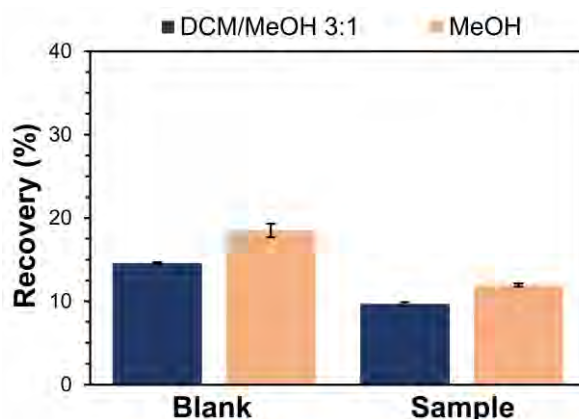


Figure 8.2. Percentage recovery of ¹³C₆-levoglucosan in blanks and spiked sample after Soxhlet extraction. Error bars represent one standard deviation of samples prepared four times and measured in duplicate.

Overall, the results are inferior to the SLE data and furthermore, the sample preparation is more time consuming and more prone to contamination and loss due to the higher solvent volume necessary. Therefore, SLE is preferred over Soxhlet extraction.

D.4.3. Solid phase extraction (SPE)

The results of the HILIC-SPE experiments are visualised in Figure 8.3. It is apparent that only if the analyte is applied in 100 % ACN a significant percentage is retained on the cartridge. This renders the application useless for the present problem because the speleothem sample first has to be dissolved in acid and then either evaporated and redissolved in ACN or must be extremely diluted with ACN. Firstly, the former case is impossible to achieve, as concentrated HCl cannot be fully evaporated and secondly, even if it could, it would be easier to just redissolve the residue in the solvent for measurement directly. The second case, while technically possible, is impractical and expensive as large quantities of ACN would be needed.

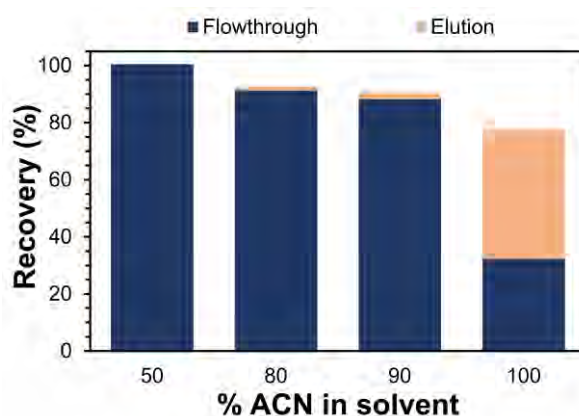


Figure 8.3. Percentage recovery of levoglucosan after HILIC-SPE. 100 ng analyte were applied in 10 mL solvent. The percentage of ACN in the solvent is given in the respective label. Elution with 6 x 250 μ L H₂O.

The results of the other SPE experiments can be found in Figure 8.4. While the C18 and SAX material seem to be able to retain levoglucosan to some degree, MeOH does not seem to be a suitable eluent. This implies that the interaction of the analyte with the solid phase is stronger than the interaction with the solvent. Elution with an aqueous solvent might lead to better

recoveries. However, the evaporation of aqueous solvents is tedious and should be avoided. Therefore, the utilisation of SPE for the present problem was discarded.

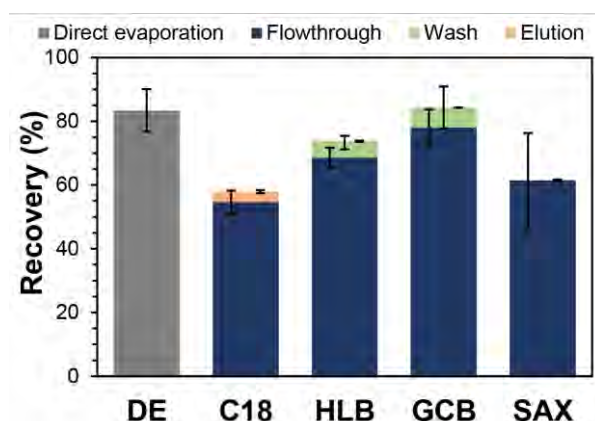


Figure 8.4. Percentage recovery of levoglucosan after SPE. 100 ng analyte were applied in 10 mL solvent. Elution 10 x 500 μ L of MeOH. C18: n=2; SAX and DE: n=3; HLB and GCB: n=4. Error bars represent one standard deviation of n samples.

D.4.4. Liquid-liquid extraction (LLE)

Figure 8.5 visualises the results of the LLE experiments. It is evident, that recoveries could only be calculated for the blank sample that had been extracted with DEE. For all other samples, no $^{13}\text{C}_6$ levoglucosan could be detected. While the procedure is easy to perform and the necessary equipment very cheap, the recovery for the DEE blank sample only lies at 4.1 ± 0.5 %. Therefore, the method proved to be unsuitable for this application.

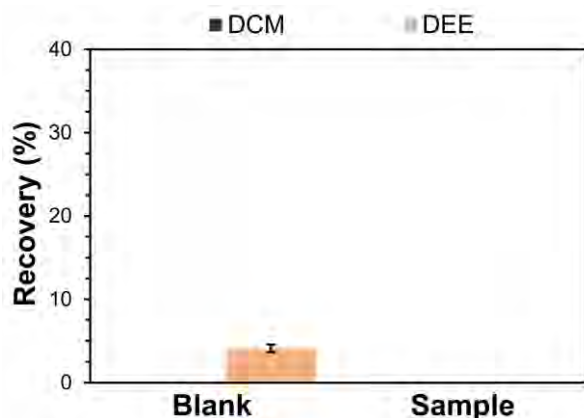


Figure 8.5. Levoglucosan concentration determined after LLE. Percentage recovery of $^{13}\text{C}_6$ -levoglucosan in blanks and spiked sample. Error bars represent one standard deviation of samples prepared four times and measured in duplicate.

D.4.5. Electrochemical neutralisation (ECN)

Figure 8.6 shows the results of the ECN experiments. The recovery of both, levoglucosan and $^{13}\text{C}_6$ levoglucosan, only amount to 3.5 ± 0.9 % and 3.7 ± 0.9 % respectively. A possible explanation for the low recovery is that the analyte might be degraded by the electric current during the sample preparation time of 3 h. Furthermore, the method shows a significant carry-over between measurements, which is apparent in the blank values which are of the

same magnitude as the samples. For these reasons and the very particular equipment needed, the method was discarded.

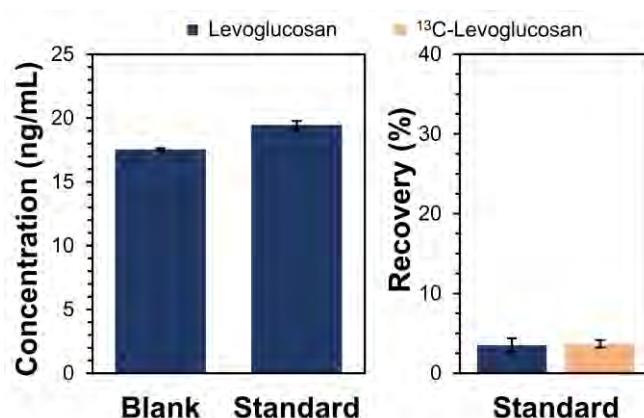


Figure 8.6. Concentration and percentage recovery of levoglucosan and $^{13}\text{C}_6$ -levoglucosan after ECN. 100 ng analyte were dissolved in 6 mL HCl (15 %). Blank: $n=3$; Standard: $n=2$. Error bars represent one standard deviation of samples measured in duplicate.

D.5. Comparison

For a concluding comparison of the discussed methods, the obtained concentrations of the speleothem sample are compared in Figure 8.7. As expected, the LEE led to the lowest concentrations with $-1.1 \pm 0.2 \text{ ng} \cdot \text{g}^{-1}$ and $3.5 \pm 0.2 \text{ ng} \cdot \text{g}^{-1}$ for DCM and DEE, respectively. It should be noted that the negative concentration for the extraction with DCM is an artefact due to the applied calibration and does not correspond to an actual negative concentration. Both Soxhlet extraction and SLE show higher concentrations for the use of MeOH as extraction solvent which is in accordance with the recovery data presented above. However, it is striking that while the concentrations gained from the MeOH extraction are similar for both methods with $9.5 \pm 0.1 \text{ ng} \cdot \text{g}^{-1}$ for SLE and $9.2 \pm 1.2 \text{ ng} \cdot \text{g}^{-1}$ for Soxhlet extraction, the concentrations obtained through the extraction of DCM/MeOH 3:1 differ significantly. Here, the concentrations are determined as $8.4 \pm 0.1 \text{ ng} \cdot \text{g}^{-1}$ and $4.9 \pm 0.1 \text{ ng} \cdot \text{g}^{-1}$ for SLE and Soxhlet extraction, respectively. Furthermore, the Soxhlet extraction with MeOH shows a large standard deviation of $\pm 1.1 \text{ ng} \cdot \text{g}^{-1}$ compared to only $\pm 0.1 \text{ ng} \cdot \text{g}^{-1}$ for the equivalent SLE experiment.

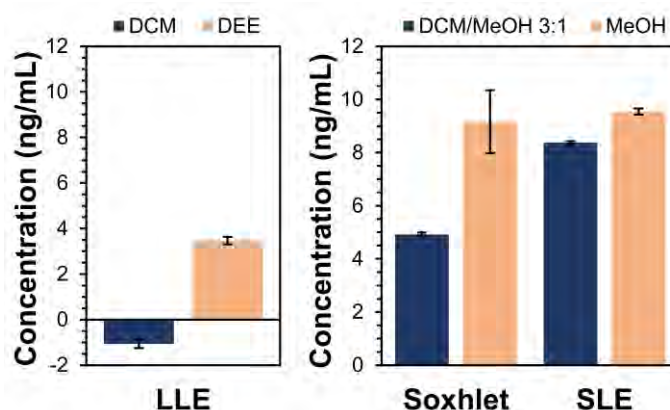


Figure 8.7. Comparison of LLE, Soxhlet extraction, and SLE based on the concentrations found for aliquots of the same speleothem sample. Error bars represent one standard deviation of samples prepared four times and measured in duplicate.

These results validate the former decision to prefer SLE for the extraction of levoglucosan from speleothems and similar matrices.

D.6. Conclusion

Five different sample preparation methods were evaluated for the extraction of levoglucosan from speleothems. Solid-phase extraction (SPE) and electrochemical neutralisation (ECN) did not prove suitable for the desired purpose. It is possible to extract small amounts of levoglucosan via liquid-liquid extraction (LLE) with diethyl ether, but the recovery rate is very low, and the method should only be applied if no other procedure is available. Solid-liquid extraction (SLE) and Soxhlet extraction, both with methanol as the extraction agent, led to similar concentrations, but SLE showed higher recovery rates and an overall easier procedure. Therefore, SLE with MeOH is recommended for the extraction of levoglucosan from speleothems and similar matrices.

E. Further optimisation and validation of the levoglucosan extraction method and lignin digestion

E.1. Silanisation of extraction vessels

As described in Chapter 3, the recovery for $^{13}\text{C}_6$ levoglucosan with the recommended solid-liquid-extraction (SLE) method was quite low. To improve the recovery, silanisation of the 25 mL extraction vials and the 1.5 mL vials used for evaporation was explored by adapting a silanisation procedure as described by Anna van Eijck (2013).²⁷⁸

Aliquots of a speleothem from Ifri Inouqben cave in northern Morocco were used. The speleothem was ground to a particle size of about 60 μm and then homogenised to create a standard material.

E.1.1. Experimental

The glass vials were submerged in a solution of 60 mL nitric acid in 340 mL water over night. Afterwards, they were cleaned with Milli-Q water and dried at 120 °C for 60 min. The vessels were submerged in a solution of 5 % dimethyldichlorosilane in hexane for 5 min while still hot and subsequently cleaned with methanol by sonification for 30 min. Finally, they were dried at 60 °C for 30 min, rinsed with acetonitrile, and once more dried at 60 °C for 60 min.

The subsequent extractions of the standard speleothem were conducted following the procedure described in Chapter 3.

For comparison, samples prepared with silanated vessels (1), samples prepared with a regular extraction vessel and a silanated evaporation vial (2), as well as samples prepared with non-silanated glass ware (3) were analysed.

The analysis was carried out following the procedure described in Chapter 3. However, an iHILIC-Fusion column was used and the analysis was conducted in isocratic mode with an eluent ratio of A/B 3:97 (A: 5 mM ammonium formate in water, B: Acetonitrile (ACN)) and a flow of 300 $\mu\text{L} \cdot \text{min}^{-1}$.

E.1.2. Results

The recoveries of $^{13}\text{C}_6$ -levoglucosan were determined as $3.9 \pm 2.7 \%$ (1), $7.7 \pm 6.1 \%$ (2), and $2.5 \pm 0.4 \%$ (3), respectively (Figure S17, left). The levoglucosan concentrations were determined as $0.13 \pm 0.12 \text{ ng} \cdot \text{g}^{-1}$ (1), $0.27 \pm 0.22 \text{ ng} \cdot \text{g}^{-1}$ (2), and $0.07 \pm 0.02 \text{ ng} \cdot \text{g}^{-1}$ (3) (Figure S17, right).

Experiment (2) yields the highest recoveries and levoglucosan concentrations. However, the standard deviations of both (1) and (2) are almost of the same magnitude as the determined values.

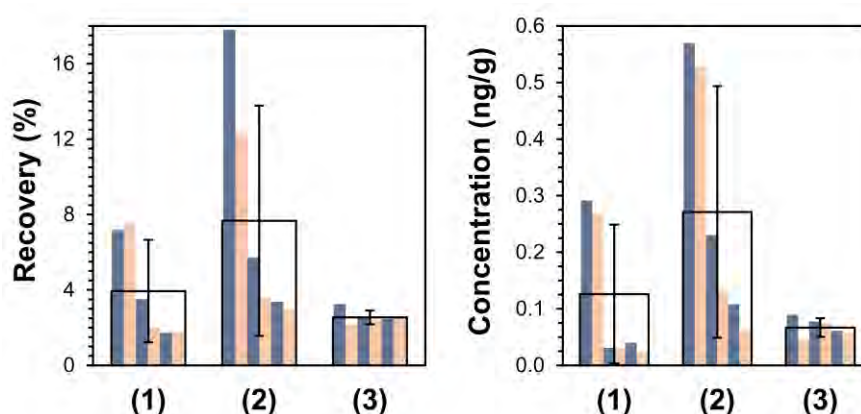


Figure S20. Comparison of recoveries of $^{13}\text{C}_6$ levoglucosan (left) and levoglucosan concentration (right) after extraction in silanated vessels (1), regular extraction vessel and a silanated evaporation vial (2) and normal glass vessels (3). Black frames represent the averages of samples prepared in triplicate and measured in duplicate with the error bars representing one standard deviation.

Figure S17 also shows the individual measurements. From these it is apparent that for both experiment (1) and (2), the first two measurements (corresponding to the first of three samples) seem to cause the high standard deviation. Upon excluding these values from the results, the new recoveries can be calculated as $2.2 \pm 0.9 \%$ (1) and $3.9 \pm 1.24 \%$ (2). The levoglucosan concentrations then amount to $0.05 \pm 0.04 \text{ ng} \cdot \text{g}^{-1}$ (1) and $0.13 \pm 0.07 \text{ ng} \cdot \text{g}^{-1}$ (2). Taking into account the errors, these values are still within the same range as the results from experiment (3), meaning that no significant difference can be observed between them.

All in all, no sound proof could be found that the silanisation of the extraction vessels and/or the vials used for evaporation results in higher yields of levoglucosan during the extraction of speleothem. Therefore, this practice is not recommended for future use.

E.2. Extraction efficiency for different sample amounts

To assure the same extraction efficiency for different sample amounts, the extraction procedure was carried out for 1 g and 2 g aliquots of the standard speleothem.

E.2.1. Experimental

Sets of 4 samples for each 1 g and 2 g aliquots were prepared. The extraction of the standard speleothem was conducted following the procedure described in Chapter 3 using 5 mL of methanol (MeOH) per g speleothem for extraction. The samples were analysed as described above (Chapter E.1.1).

E.2.2. Results

The obtained concentrations for the three isomers are illustrated in Figure S18. It is apparent, that the concentrations found for the 1 g aliquots are in good agreement with the concentrations determined for the 2 g samples. This implies that the extraction efficiency is independent of the sample amount for the investigated range.

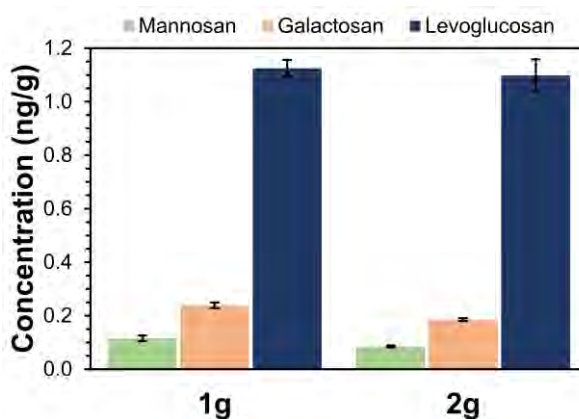


Figure S21. Comparison of anhydrosugar concentrations for extraction of 1 g and 2 g sample. Error bars represent one standard deviation of samples prepared four times and measured in duplicate.

It is further visible that levoglucosan is by far the biggest contributor to the overall anhydrosugar concentration with $1.13 \pm 0.03 \text{ ng} \cdot \text{g}^{-1}$ to $0.12 \pm 0.01 \text{ ng} \cdot \text{g}^{-1}$ and $0.24 \pm 0.01 \text{ ng} \cdot \text{g}^{-1}$ for mannosan and galactosan, respectively. Therefore, and because the application of the iHILIC-Fusion column which allows for the separation of the isomers proved instrumentally challenging, only levoglucosan was quantified in some experiments with mannosan and galactosan contributing to the peak area.

E.3. Impact of extraction of levoglucosan on retrieved LOP concentration

To investigate whether the prior extraction of levoglucosan has a negative impact on the obtained lignin oxidation products (LOP) concentration and to assure the linearity of the method, sample sets of 1 g and 2 g aliquots of the standard speleothem material from Ifri Inouqben cave were analysed for LOPs, both before and after extraction of levoglucosan.

E.3.1. Experimental

Sets of 4 samples for each 1 g and 2 g aliquots, before (b) and after (a) extraction of levoglucosan, were prepared. The extracted speleothem samples from Chapter E.2 were dried at 60 °C over night and then treated the same way as the other samples.

The speleothem powder was dissolved in 3 mL HCl (30 %) per g sample and then diluted 1:1 with Milli-Q water. The 200 mg HLB cartridges were preconditioned with 6 mL of each MeOH and ultrapure water, which was acidified to pH 1-2 with HCl (30%). The speleothem solution was filtered through paper filters (Whatman, Grade 40, 8 µm pore size) to prevent undissolved materials from clogging the cartridges and was loaded onto the cartridges using sample reservoirs. The Cartridges were washed twice with 6 mL of acidified ultrapure water and then dried by sucking air through the cartridges using a vacuum pump. The lignin was eluted using 10 portions of 500 µL MeOH. The solvent was subsequently evaporated under a gentle stream of nitrogen at 30 °C.

The residue was dissolved in 200 µL MeOH and sonicated for 10 min at 45 °C. The solution was added to a PTFE microwave digestion vessel with a capacity of 500 µL. The procedure was repeated with 100 µL MeOH and the combined solutions evaporated to dryness under a gentle stream of nitrogen at 30 °C. The residual was dissolved in 200 µL NaOH (1 mol · L⁻¹) through sonification for 10 min at 45 °C. To this, 10 µL of each CuSO₄ solution (10 mmol · L⁻¹ in H₂O) and a solution of L-ascorbic acid (0.2 mol · L⁻¹ in H₂O) were added. The vessels were purged with nitrogen for 20 s each and quickly capped to ensure inert gas atmosphere. The digestion vessels were packed into a bigger Teflon vessel five at a time and covered with 7 mL of NaOH (1 mol · L⁻¹) to ensure better heat transfer. These vessels were also purged with nitrogen for 1 min. The vessels were heated to 155 °C in 5 min and held at that temperature for 90 min using a 5890A Gas Chromatograph (Hewlett Packard, USA). Immediately after opening the vessels, 10 µL of a 1 µg · mL⁻¹ standard solution of ethyl vanillin in acetonitrile was added as an internal standard and the oxidised sample solution was acidified to pH 1-2 with HCl (30 %).

30 mg HLB cartridges were preconditioned with two times 1 mL of each MeOH and ultrapure water, which was acidified to pH 1-2 with HCl (30 %). The acidified oxidised sample solutions were loaded onto the cartridges. The cartridges were washed twice with 1 mL and then then dried by sucking air through the cartridges using a vacuum pump. The LOPs were eluted using 8 portions of 125 µL of acetonitrile with 2% NH₃ added to reach a basic pH of 8-9. The eluate was evaporated under a gentle stream of nitrogen at 30 °C and the residue was dissolved in 200 µL acetonitrile/H₂O (1:9) by 10 min of sonification at 45 °C. The solution was filtered with a 0.2 µm PA-filter and stored in the freezer at -25 °C.

The analysis of the LOPs was carried out on a Dionex UltiMate 3000 ultrahigh-performance liquid chromatography system (UHPLC) that was coupled to a heated electrospray ionization source (ESI) and a Q Exactive Orbitrap high-resolution mass spectrometer (HRMS) (all by Thermo Fisher Scientific). To separate the LOPs, a Acquity UPLC CSH Fluoro Phenyl (PFP) column, 100mm x 2.1mm with 1.7 μm particle size (by Waters), was used. The injection volume was 10 μL . A H_2O /acetonitrile gradient program was applied with a flow of 0.5 $\text{mL} \cdot \text{min}^{-1}$. The gradient started with 5 % eluent B (consisting of 98 % acetonitrile and 2 % H_2O) and 95 % eluent A (consisting of 98 % H_2O , 2% acetonitrile, and 400 $\mu\text{L} \cdot \text{L}^{-1}$ formic acid). Eluent B was increased to 10 % within 0.5 min and held for 4.5 min. It was then increased to 15 % within 1 min and further increased to 30 % in 1 min and to 50 % in 0.5 min, respectively. Finally, it was increased to 99 % within 0.5 min, held for 1.5 min, and then eluent B was decreased to the initial value of 5 %. The ESI source was operated in negative mode so that deprotonated molecular ions $[\text{M}-\text{H}]^-$ were formed. ESI and MS conditions were the same as reported by Heidke et al. (2018).⁵³

E.3.2. Results

Figure S19 (left) illustrates the obtained LOP concentrations and it is striking that the concentrations after the extraction of levoglucosan are significantly higher than for the analysis before the extraction ($185.5 \pm 10.4 \text{ ng} \cdot \text{g}^{-1}$ versus $932.4 \pm 45.4 \text{ ng} \cdot \text{g}^{-1}$ and $118.8 \pm 6.3 \text{ ng} \cdot \text{g}^{-1}$ versus $827.3 \pm 40.6 \text{ ng} \cdot \text{g}^{-1}$ for the sum of all 8 LOPs ($\Sigma 8$)). A possible explanation for this phenomenon is that other organic compounds present in the speleothem are also removed from the calcium carbonate matrix during the initial methanol extraction. These compounds might be oxidised preferentially during the digestion of lignin. Therefore, the extraction step leads to a more targeted oxidation of lignin and thus results in higher LOP concentration.

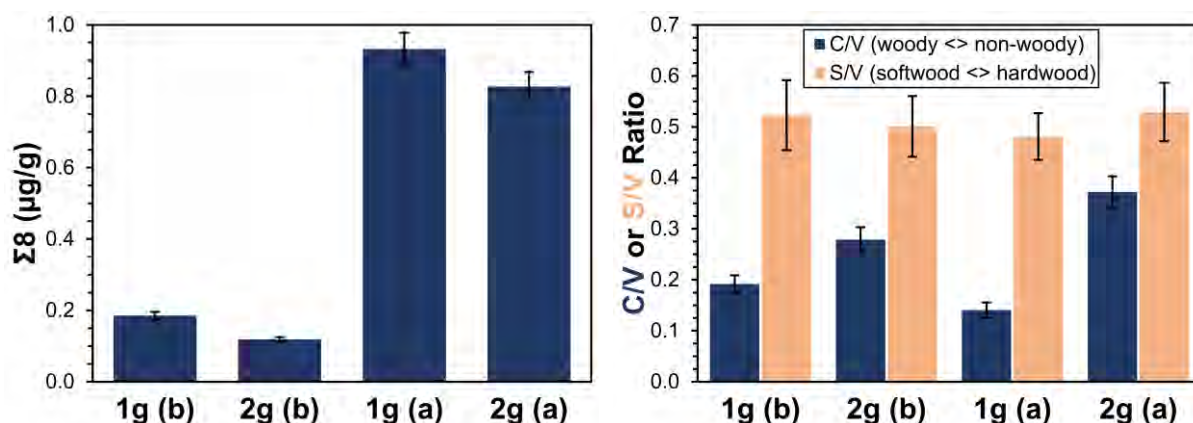


Figure S22. Comparison of the $\Sigma 8$ values (left) and the C/V and S/V ratios (right) in 1 g and 2 g aliquots, before (b) and after (a) the extraction of levoglucosan. Error bars represent one standard deviation of samples prepared four times and measured in duplicate.

Figure S19 illustrates that the concentrations obtained for the 1 g sample sets are elevated in comparison to the 2 g sample sets ($185.5 \pm 10.4 \text{ ng} \cdot \text{g}^{-1}$ versus $118.8 \pm 6.3 \text{ ng} \cdot \text{g}^{-1}$ and $932.4 \pm 45.4 \text{ ng} \cdot \text{g}^{-1}$ versus $827.3 \pm 40.6 \text{ ng} \cdot \text{g}^{-1}$ for $\Sigma 8$). However, the LOP ratios (Figure S19, right) are comparable. These findings imply that the lignin oxidation is more efficient in smaller sample amounts. Therefore, results should only be compared directly if the original samples had the same weight.

F. List of Abbreviations

^{13}C -LEV	$^{13}\text{C}_6$ -levoglucosan
ACE	Acenaphthene
ACN	Acetonitrile
ACY	Acenaphthylene
Ad/Al	Acid-to-aldehyde-ratio
ANT	Anthracene
BAA	Benzo(a)anthracene
BAP	Benzo(a)pyrene
BBF	Benzo(b)fluoranthene
BP	Before present
C-group / ΣC	Monomers of the cinnamyl-group
CHR	Chrysene
CRM	Charge residue model
d-ACE	Acenaphthene- d_{10}
DBA	Dibenz(a,h)anthracene
DCM	Dichloromethane
DEE	Diethyl ether
d-NAP	Napthalene- d_8
DPE	Benzo(g,h,i)perylene
d-PHE	Phenanthrene- d_{10}
EA	Ethyl acetate
ECN	Electrochemical neutralisation
EI	Electron ionisation
ESI	Electrospray ionisation
ESI-MS	Electrospray ionisation mass spectrometry
FID	Flame ionisation detector
FLN	Fluorene
FLT	Fluoranthene

List of Abbreviations

GAL	Galactosan
GC	Gas chromatography
GCB	Graphitised carbon black
GDGTs	Glycerol dialkyl glycerol tetraethers
HCD	Higher-energy collisional dissociation
HESI	Heated electrospray ionisation
HETP	Height equivalent of a theoretical plate
HILIC	Hydrophilic interaction chromatography
HLB	Hydrophilic-lipophilic-balanced
HMW	High molecular weight
HPLC	High performance liquid chromatography
HRMS	High-resolution mass spectrometry
ICP-MS	Inductively coupled plasma mass spectrometry
IEM	Ion emission model
INP	Indeno(1,2,3-c,d)pyrene
LA	Laser ablation
LC	Liquid chromatography
LEV	Levoglucosan
LLE	Liquid-liquid extraction
LMW	Low molecular weight
LOD	Limit of detection
LOPs	Lignin oxidation products
M	Molecule
<i>m/z</i>	Mass-to-charge-ratio
MAN	Mannosan
MAs	Monosaccharide anhydrides
MBIC	Modified Bayes Information Criterion
MC-ICP-MS	Multi-collector inductively coupled plasma mass spectrometry
MeOH	Methanol

MS	Mass spectrometry
NAP	Naphthalene
NCE	Normalised collision energy
NP-LC	Normal phase liquid chromatography
O/AO	Oxidant-to-antioxidant-ratio
PA	Polyamide
PAHs	Polycyclic aromatic hydrocarbon
pCO ₂	Partial pressure of CO ₂
PCP	Prior calcite precipitation
PDSI	Palmer Drought Severity Index
PFP	Pentafluorophenyl residues
PHE	Phenanthrene
PTFE	Polytetrafluorethylen
PTP	p-Terphenyl
PYR	Pyrene
RET	Retene
RF	Radio frequency
RP-LC	Reversed phase liquid chromatography
RSD	Relative standard deviation
Σ8 / S8	Sum of all 8 LOP monomers
Σ15	Sum of 15 non-alkylated PAHs
SA	Syringic acid
SAX	Strong anion exchange
SD	Standard deviation
S-group / ΣS	Monomers of the syringyl-group
SIM	selected ion monitoring mode
SLE	Solid-liquid extraction
SPE	Solid phase extraction
TMAH	Tetramethyl-ammonium hydroxide

List of Abbreviations

UHPLC	Ultra-high performance liquid chromatography
V-group / ΣV	Monomers of the vanillyl-group

G. List of related publications and presentations

Peer-reviewed publications:

J. Homann, M. Zirbes, M. Arndt-Engelbart, D. Scholz, S. R. Waldvogel, and T. Hoffmann: Development of a method for anodic degradation of lignin for the analysis of paleo-vegetation proxies in speleothems, *ChemElectroChem*, 9, e20210131, (2022) DOI: [0.1002/celec.202101312](https://doi.org/10.1002/celec.202101312)

J. Homann, J. Oster, C. de Wet, S. F. M. Breitenbach, and T. Hoffmann: Linked fire activity and climate whiplash in California during the early Holocene, *Nature communications*, 13, 7175 (2022) DOI: [10.1038/s41467-022-34950-x](https://doi.org/10.1038/s41467-022-34950-x)

Accepted:

J. Homann, N. Karbach, S. A. Carolin, D. H. James, D. Hodell, S. F. M. Breitenbach, O. Kwiecien, M. Brenner, C. Peraza Lope, and T. Hoffmann: Past fire dynamics inferred from polycyclic aromatic hydrocarbons and monosaccharide anhydrides in a stalagmite from the archaeological site of Mayapan, Mexico, *Biogeosciences*, DOI: [10.5194/bg-2023-63](https://doi.org/10.5194/bg-2023-63)

Oral presentations:

J. Homann, A. Beschnitt, and T. Hoffmann: Trace analysis of levoglucosan and lignin-phenols in speleothems by HILIC-UHPLC-ESI-HRMS: A new method, *European Geoscience Union General Assembly*, Online, May 2020, DOI: [10.5194/egusphere-egu2020-2413](https://doi.org/10.5194/egusphere-egu2020-2413)

J. Homann, D. Scholz, S. F. M. Breitenbach, and T. Hoffmann: Levoglucosan in speleothems: An evaluation of various sample preparation methods, *European Geoscience Union General Assembly*, Online, April 2021, DOI: [10.5194/egusphere-egu21-1065](https://doi.org/10.5194/egusphere-egu21-1065)

J. Homann, J. Oster, C. de Wet, S. F. M. Breitenbach, and T. Hoffmann: Investigation of levoglucosan as proxy for biomass burning events and its relationship with established proxies in a speleothem from White Moon Cave, CA, *American Geoscience Union Fall Meeting*, New Orleans, USA, December 2021

J. Homann: Levoglucosan – Ein Drama in drei Akten, *32. PhD student seminar of the AK Separation Science (GDCh)*, Hohenroda, Germany, January 2023

J. Homann, I. Heidke, M. Weber, D. Scholz, and T. Hoffmann: A new record of environmental proxies for Cueva Victoria, Spain, *European Geoscience Union General Assembly*, Vienna, Austria, May 2022, DOI: [10.5194/egusphere-egu22-960](https://doi.org/10.5194/egusphere-egu22-960)

Poster presentations:

J. Homann, S. F. M. Breitenbach, S. Carolin, D. Hodell, J. Oster, C. de Wet, and T. Hoffmann: Polycyclic aromatic Hydrocarbons (PAHs) in speleothems, *European Geoscience Union General Assembly*, Vienna, Austria, April 2023, DOI: [10.5194/egusphere-egu23-1735](https://doi.org/10.5194/egusphere-egu23-1735)

H. Acknowledgments

First of all, I would like to thank my supervisor Prof. Dr. Thorsten Hoffmann for giving me the opportunity to work in his research group and explore the fascinating world of speleothems. I am thankful for our discussions, his support, and the freedom to explore my own research goals.

My research would not have been possible without the financial support of the Max-Planck-Graduate-Centre. The MPGK enabled me to participate in numerous conferences, a research visit, and a month-long field-trip. These adventures were the highlights of my PhD and I am deeply grateful.

Many thanks to my second supervisor Prof. Dr. Denis Scholz and my two MPGK mentors Dr. Alfredo Martínez García and Dr. Christopher Kampf for their support and the fruitful discussions about the direction of my research.

A huge thank you to Prof. Dr. Sebastian Breitenbach for his boundless enthusiasm, quick email responds, passionate support of my research, and amazing networking skills. Thank you, Seb, for taking me to (and bringing me back from) Siberia, welcoming me into your group and your home, and supplying me with an endless stream of interesting samples and collaborators. I also want to thank the members of the Breitenbach-Group, Jade, Stuart, and Sevi, for providing me with samples, introducing me to the Geologist's side of speleothem analysis, and for amazing shared times in Siberia, Newcastle, and Vienna. I would like to take this opportunity to also thank the members of Speleoclub Arabica from Irkutsk for their hospitality and support during our campaign in Siberia. You made this trip truly unforgettable. МОЩНОСТЬ!

Thank you to all of my other collaborators who provided samples, additional data, and helped me with the interpretation of my results. A huge thanks goes to Prof. Dr. Jessica Oster and Dr. Cameron de Wet who supplied me with samples from White Moon Cave and helped tremendously in putting together the resulting publication. I also want to thank Prof. Dr. David Hodell, Prof. Dr. Mark Brenner, Dr. Stacy Carolin, Dr. Ola Kwiecien, and Carlos Peraza Lope for our successful collaboration on the samples from Mayapan. A big thanks goes to Jenny, Marcela, and Julio from the Scholz-Group for providing me with multiple samples from Germany and Brazil. Thanks to Prof. Dr. Siegfried Waldvogel and Michael Zirbes for the joint project on anodic degradation of lignins.

I want to thank all of the former and current members of the Hoffmann-Group for the great work environment and all the productive discussions we had. Thank you for our daily Skat games, BBQ nights, AK-Ausflüge, and so many more joint activities. You made my time at work truly enjoyable. You were absolutely Präzise. Effizient. Leistungsstark! A special thanks goes to the bachelor and master students who supported my research and everyone who proofread parts of my thesis.

Lastly, I would like to thank my family and friends who's love and support constantly encouraged me and who I could always turn to.

I. Curriculum vitae

Personal Information:

Name: Julia Homann
Date of Birth: 05.09.1994
Place of Birth: Bad Kreuznach

Academic Qualifications:

Since 10/2019 **PhD studies** with Prof. Dr. Thorsten Hoffmann,
Department Chemie, Johannes Gutenberg University Mainz, Germany

04/2022 – 05/2022 **Research visit** with Prof. Dr. Sebastian Breitenbach,
Stable Isotope Laboratory, Northumbria University, Newcastle upon
Tyne, UK

10/2017 – 09/2019 **Master of Science Chemie**,
Johannes Gutenberg University Mainz, Germany

02/2019 – 08/2019 **Master Thesis** with Prof. Dr. Thorsten Hoffmann,
Department Chemie, Johannes Gutenberg University Mainz, Germany

09/2018 – 01/2019 **ERASMUS-Internship** with Prof. Dr. Jörg Feldmann,
Trace Element Speciation Laboratory, University of Aberdeen, UK

10/2014 – 09/2017 **Dual Bachelor programme, Bachelor of Science Chemistry**,
University of applied Sciences Darmstadt

09/2013 – 06/2016 **Apprenticeship as a chemical laboratory worker**,
Boehringer Ingelheim Pharma GmbH & Co. KG, Ingelheim, Germany

03/2013 **Abitur**,
Alfred-Delp-Schule, Hargesheim, Germany

Scholarships and Awards:

Since 07/2020 Member of the Max Planck Graduate Center (MPGC) Mainz

02/2021 – 07/2022 Student speaker Max Planck Graduate Center Mainz

10/2017 – 09/2019 Support through the Deutschlandstipendium